ANALYTICAL AND NUMERICAL STUDIES OF BOSE-EINSTEIN CONDENSATES

LIM FONG YIN
B.SC.(HONS)
NATIONAL UNIVERSITY OF SINGAPORE

A THESIS SUBMITTED FOR THE DEGREE OF
DOCTOR OF PHILOSOPHY

DEPARTMENT OF MATHEMATICS
NATIONAL UNIVERSITY OF SINGAPORE

2008

Acknowledgements

The present thesis is the collection of the studies conducted under the guidance of my Ph.D. advisor Prof. Weizhu Bao from the National University of Singapore. I would like to express my sincere gratitude to my advisor for his supervision and helpful advices throughout the study, as well as for the recommendations and support given to attend a number of conferences and workshops from which I gained valuable experiences in academic research.

I would also like to express grateful thanks to my collaborators, Prof. I-Liang Chern, Dr. Dieter Jaksch, Mr. Matthias Rosenkranz and Dr. Yanzhi Zhang for their substantial help and contribution to the studies. Many thanks to Yanzhi again for the discussions from which I gained deeper understanding in my works. My thanks also go to Alexander, Anders, Hanquan and Yang Li for providing me with useful comments and help in advancing my studies.

Finally, I would like to dedicate this thesis to my family, for the support and encouragement they have been giving to me throughout the years.

Contents

Summary

Bose-Einstein condensation has been a widely studied research topic among physicists and applied mathematicians since its first experimental observation in 1995. Various theories were developed to describe the Bose-Einstein condensates (BECs) subjected to different ranges of temperature and interaction. This thesis focuses on studying the BECs in cold dilute atomic gases, in which the mean field theory is valid and the Gross-Pitaevskii equation (GPE) provides a good description of the macroscopic wavefunction of the condensate atoms at a temperature much lower than the transition temperature. This thesis starts with analytically studying the ground state of a single component BEC in several types of trapping potentials, for both repulsively and attractively interacting atoms. In the strongly repulsively interacting regime, asymptotic ground state solution is found by applying the Thomas-Fermi approximation, i.e. by neglecting the kinetic energy in the Gross-Pitaevskii energy functional; while in the strongly attractively interacting regime, asymptotic solution is found by neglecting the potential energy. One dimensional BEC with weakly attractive interaction is studied in a symmetric double well potential in particular. In this case, the ground state may not be a symmetric state, which is in contrast to a BEC with repulsive interaction. Applying a Gaussian wavepacket ansatz to the GPE, a critical interaction strength at which the symmetry breaking of the ground state taking place can be predicted. The study is followed by the introduction of the normalized gradient flow (NGF) method to solve the GPE numerically for the condensate ground state. The NGF can be solved accurately and effectively, even in three dimensional simulation, through the utilization of the sine-pseudospectral method and the backward/semi-implicit backward Euler scheme with the inclusion of a constant stabilization parameter. The method is then extended to a spin-1 BEC which is described by three-component coupled GPEs. An additional normalization condition is derived, to resolve the problem of insufficient conditions for the normalization of three wavefunctions. Two inherent conditions of the system are the conservation of total particle number and the conservation of total spin. The method is also applicable to a spin-1 BEC subjected to uniform magnetic field, with a proper treatment of different Zeeman energies experienced by different components. Finally, the transport of a strongly repulsively interacting BEC through a shallow optical lattice of finite width is studied numerically, as well as analytically in terms of nonlinear Bloch waves. The development and disappearance of a self-trapped state is observed. Such dynamical self-trapping can be well explained by the nonlinear band structure in a periodic potential, where the nonlinear band structure arises due to the interparticle interaction in the GPE.

Chapter 1

Introduction

The phenomenon of Bose-Einstein condensation was predicted by Albert Einstein in 1925 [58, 59], after generalizing Satyendra Nath Bose's derivation of Planck's distribution for photons [26] to the case of non-interacting massive bosons. The prediction was made in the early stage of development of quantum mechanics, even before the classification of particles into bosons and fermions, which are characterized by zero or integer spin and half-integer spin, respectively.

Particles exhibit particle-wave duality property. Being a point-like particle, each particle at the same time behaves as a wave. At temperature T, the wave properties of a particle of mass m are characterized by the de-Broglie wavelength

$$\lambda_{dB} = \left(\frac{2\pi\hbar^2}{mk_B T} \right)^{1/2} \tag{1.1}$$

which increases as the temperature decreases. $\hbar$ is the Planck constant and k_B is the Boltzmann constant. When the temperature of the system is so low that λ_{dB} is comparable to the average spacing between the particles, their thermal de-Broglie waves overlap and the atoms behave coherently, as a single giant atom. This is when the Bose-Einstein condensation takes place. The coherent atoms all occupy the same single-particle state and they can be viewed as a single collective object occupying a macroscopic wavefunction which is the product of all single-particle wavefunctions. The phenomenon can also be predicted from the Bose-Einstein statistics for bosons. At temperature T, a system of bosons distribute themselves among different energy levels according to the Bose-Einstein distribution,

$$f(\varepsilon_i) = \frac{1}{\exp(\frac{\varepsilon_i - \mu}{k_B T}) - 1}, \tag{1.2}$$

where ε_i is the energy of the ith quantum state and μ is the chemical potential of the system. When the temperature is lowered to the critical temperature T_c, the lowest energy quantum state ε_0 is populated by a large fraction of particles. A phase transition from thermally distributed particles to the Bose-Einstein condensed state takes place. If the temperature is further lowered, a nearly pure condensate, only accompanied by a few thermally excited atoms, can be achieved.

To achieve the condensed state, an extremely low temperature of the order of 100nK is required so that λ_{dB} is of the order of interatomic spacing. At the same time, a gaseous state of the system has to be maintained to avoid collision of particles that leads to the formation of molecules and clusters. This causes great challenges for experimentalists since almost all substances condense into solid state at such low temperature, except ^{4}He, which remains liquid even at absolute zero. For these reasons, the idea of Bose-Einstein condensation was not paid much attention until superfluid ^{4}He was discovered [72] and until the suggestion of superfluid ^{4}He being a system of Bose-Einstein condensate was proposed by London [77], noting that Einstein's formula for the T_c gave a good estimate of the observed transition temperature of superfluidity of ^{4}He. A number of theoretical studies on the superfluid were carried out since its discovery. Tisza, initiated by London, came up with the two-fluid model [108] which stated that ^{4}He consists of two parts: the normal component that moves with friction and the superfluid component that moves without friction. The model was further developed by Landau into the two-fluid quantum hydrodynamics [74] which remains as the basis of modern description of superfluid ^{4}He. Even though at a later time the superfluid ^{4}He was shown not to be a Bose-Einstein condensed system (there is only $< 10\%$ of condensate particles), those theoretical works provided a solid background to the later development of the theories in BEC in dilute atomic gases after 1995.

After 1980's, when the cooling technique became relatively advanced compared to the earlier time, physicists started to seek for a BEC in spin-polarized H atoms, which was predicted to be stable in a gas phase even at $T = 0$K since no bound state can be formed between two spin-polarized H atoms. However, attempts to achieve a BEC failed as the three-body interaction causes the spin flip and the combination of H atoms into molecules. Nevertheless, various cooling techniques further developed over the years in seeking spin-polarized H condensate were applied to other dilute akali gases and the first observation of Bose-Einstein condensation of dilute atomic ^{87}Rb gas was reported in June 1995 by JILA group leaded by E. Cornell and C. Wieman [8]. Two experimental achievements were reported in the same year by the Ketterle's group in MIT for ^{23}Na [48] and Hulet's group in Rice University for ^{7}Li [28]. Atomic H condensate was finally produced in the year 1998 [61]. There are two cooling stages to create the dilute atomic BEC: laser cooling and evaporative cooling. Laser cooling serves as the pre-cooling stage, in which laser beams are used to bombard and slow down the atoms, thereby reducing the energy of the atoms to $T \sim 10\mu$K. However, this temperature is still too high for the atoms to form a condensate. The second cooling stage is to trap the atoms with magnetic field. The magnetic trap creates a thermally isolated and material-free wall that confines the atoms and at the same time prevents the nucleation of atomic cluster on the wall (optical trap created by laser light was developed at a later time that substituted the magnetic trap to hold spinor condensates as well as to create a periodic trapping potential and a box potential). Radio frequency is applied to flip the electronic spin of the atoms with higher energy. These spin-flipped atoms are repelled by the magnetic trap, carrying away the excess energy and thereby achieving the purpose of cooling of the remaining atoms, in a similar way as hot water is cooled through evaporation of the water molecules from the surface. As the temperature is being brought down, the cool atoms in the trap will start occupying the lowest energy state and form the condensate. The evaporative cooling can reduce the temperature down to 50nK-100nK, as reported in the first BEC experiment.

The experiments in 1995 have spurred great excitement and are of tremendous interest in the field of atomic and condensed matter physics. Due to the collective behaviours of the atoms, one can now measure the microscopic quantum mechanical properties in a macroscopic scale by optical means. It also provides a testing ground for exploring the quantum phenomena of interacting many-body system. Plenty of theoretical studies on cold dilute atomic gases were carried out and a number of labs were set up to study the properties of BECs. The quantity of BEC related research articles has been growing at the rate of about 100 per year since then. Early reports studied BEC in ideal gas. However, the interparticle interaction in the dilute atomic gases, despite being very weak, plays an important role and turns the problem into a non-trivial many-body problem. A theoretical model that is widely studied for BEC in a trap is the mean field model. In this model, the interaction that an atom experiences is described by the average interacting potential field caused by other atoms in the system, resulting in a nonlinear term in the Schrödinger equation that describes the condensate atoms at zero temperature. Despite its simplicity, the model is shown to describe many properties of the condensate quite accurately. By taking the effect of temperature into account, the properties of the condensate and the thermal cloud at a temperature much lower than the transition temperature are also well modelled within the mean field approximation. The mean field theory does not work well at a temperature close to the transition temperature, at which the population of thermally excited atoms is high. Several models have been developed beyond the mean field approach for this range of temperature.

1.1 Mean Field Theory

Hamiltonian of the quantum field operators $\hat{\psi}(\boldsymbol{x},t)$ and $\hat{\psi}^\dagger(\boldsymbol{x},t)$ which creates and annihilates a particle at position $\boldsymbol{x}$ at time t, can be expressed as

$$\begin{aligned}\hat{H} &= \int \hat{\psi}^\dagger(\boldsymbol{x},t)\left(-\frac{\hbar^2}{2m}\nabla^2 + V(\boldsymbol{x},t)\right)\hat{\psi}(\boldsymbol{x},t)\,d\boldsymbol{x} \\ &+\frac{1}{2}\int\int \hat{\psi}^\dagger(\boldsymbol{x},t)\hat{\psi}^\dagger(\boldsymbol{x}',t)V_{\text{int}}(\boldsymbol{x}'-\boldsymbol{x})\hat{\psi}(\boldsymbol{x},t)\hat{\psi}(\boldsymbol{x}',t)\,d\boldsymbol{x}'\,d\boldsymbol{x}, \qquad (1.3)\end{aligned}$$

where $V(\boldsymbol{x},t)$ is the external trapping potential and $V_{\text{int}}(\boldsymbol{x}'-\boldsymbol{x})$ is the two-body interatomic interacting potential. The field operators of bosons satisfy the Bose commutation relations

$$\left[\hat{\psi}(\boldsymbol{x},t),\hat{\psi}^\dagger(\boldsymbol{x}',t)\right] = \delta(\boldsymbol{x}-\boldsymbol{x}'), \qquad (1.4)$$

$$\left[\hat{\psi}(\boldsymbol{x},t),\hat{\psi}(\boldsymbol{x}',t)\right] = \left[\hat{\psi}^\dagger(\boldsymbol{x},t),\hat{\psi}^\dagger(\boldsymbol{x}',t)\right] = 0, \qquad (1.5)$$

where $[\hat{A},\hat{B}] = \hat{A}\hat{B} - \hat{B}\hat{A}$ is the commutator of operators $\hat{A}$ and $\hat{B}$. In dilute cold gases, only binary collision is important. The collision is characterized by a single parameter a_s, which is the s-wave scattering length of the atom. Under the condition a_s much smaller than the interparticle spacing, the interacting potential can be effectively replaced by the mean field potential [47, 60]

$$V_{\text{int}}(\boldsymbol{x}'-\boldsymbol{x}) = g\delta(\boldsymbol{x}'-\boldsymbol{x}), \qquad (1.6)$$

where the coupling constant $g = \frac{4\pi\hbar^2 a_s}{m}$. Positive a_s corresponds to repulsive interaction and negative a_s corresponds to attractive interaction. The Heisenberg interpretation for the time evolution of the field operator, with effective potential (1.6), is then given by

$$\begin{aligned}i\hbar\frac{\partial\hat{\psi}(\boldsymbol{x},t)}{\partial t} &= \left[\hat{\psi}(\boldsymbol{x},t),\hat{H}\right] \\ &= \left[-\frac{\hbar^2}{2m}\nabla^2 + V(\boldsymbol{x},t) + g\hat{\psi}^\dagger(\boldsymbol{x},t)\hat{\psi}(\boldsymbol{x},t)\right]\hat{\psi}(\boldsymbol{x},t). \qquad (1.7)\end{aligned}$$

When the system of particles consists of a large fraction of Bose-Einstein condensate, the condensate part can be separated out from the quantum field operator and be represented by a classical field $\psi(\boldsymbol{x},t)$ [23, 25]. That is, the quantum field operator can be expressed as the sum of the condensate order parameter $\psi(\boldsymbol{x},t)$ and the quantum fluctuation field $\tilde{\psi}(\boldsymbol{x},t)$ which represents the non-condensate particles:

$$\hat{\psi}(\boldsymbol{x},t) = \psi(\boldsymbol{x},t) + \tilde{\psi}(\boldsymbol{x},t), \tag{1.8}$$

where

$$\begin{aligned} \left\langle \hat{\psi}(\boldsymbol{x},t) \right\rangle &= \psi(\boldsymbol{x},t), & (1.9) \\ \left\langle \tilde{\psi}(\boldsymbol{x},t) \right\rangle &= 0. & (1.10) \end{aligned}$$

The brackets $\left\langle \hat{A} \right\rangle$ denotes the expectation value of operator $\hat{A}$ on a suitably defined ensemble.

The thesis deals mainly with the zero temperature model, in which the non-condensate atoms are completely neglected, or equivalently, the quantum field $\hat{\psi}(\boldsymbol{x},t)$ is replaced by the classical field $\psi(\boldsymbol{x},t)$. However, in order to provide a detailed physical background to the mean field description of Bose-Einstein condensation, as well as to present the possible extended studies from current research within the context of this thesis, finite temperature mean field models will also be reviewed here.

Applying expression (1.8) with assumptions (1.9)–(1.10), the equation of motion for the condensate part is

$$\begin{aligned} i\hbar\frac{\partial\psi}{\partial t} &= \left[-\frac{\hbar^2}{2m}\nabla^2 + V(\boldsymbol{x},t)\right]\psi + g\left\langle \hat{\psi}^\dagger\hat{\psi}\hat{\psi} \right\rangle \\ &= \left[-\frac{\hbar^2}{2m}\nabla^2 + V(\boldsymbol{x},t) + g(n_c + 2n_T)\right]\psi + g\tilde{m}\psi^* + g\left\langle \tilde{\psi}^\dagger\tilde{\psi}\tilde{\psi} \right\rangle, & (1.11) \end{aligned}$$

where

$$\begin{aligned} & n_c = |\psi|^2 = \text{condensate density}, & (1.12) \\ & n_T = \left\langle \tilde{\psi}^\dagger\tilde{\psi} \right\rangle = \text{non-condensate density}, & (1.13) \\ & \tilde{m} = \left\langle \tilde{\psi}\tilde{\psi} \right\rangle = \text{off-diagonal non-condensate density}, & (1.14) \\ & \left\langle \tilde{\psi}^\dagger\tilde{\psi}\tilde{\psi} \right\rangle = \text{three-field correlation function}. & (1.15) \end{aligned}$$

Here ψ^* denotes the complex conjugate of the wavefunction. The off-diagonal term and the three-field correlation term are called the anomalous terms. If the external trapping potential does not depend of time, separation of variables can be applied to (1.7) and the quantum field operator can be written as

$$\hat{\psi}(\boldsymbol{x},t) = \hat{\phi}(\boldsymbol{x})e^{-i\mu t/\hbar}, \tag{1.16}$$

where μ is the chemical potential of the system. The time-independent quantum field operator $\hat{\phi}(\boldsymbol{x})$ satisfies the time-independent nonlinear Schrödinger equation

$$\mu\hat{\phi}(\boldsymbol{x}) = \left[-\frac{\hbar^2}{2m}\nabla^2 + V(\boldsymbol{x}) + g\hat{\phi}^\dagger(\boldsymbol{x})\hat{\phi}(\boldsymbol{x})\right]\hat{\phi}(\boldsymbol{x}). \tag{1.17}$$

Separating the condensate and non-condensate part of $\hat{\phi}(\boldsymbol{x})$ according to (1.8), we get the time-independent Schrödinger equation for the condensate

$$\mu\phi = \left[-\frac{\hbar^2}{2m}\nabla^2 + V(\boldsymbol{x}) + g(n_c + 2n_T)\right]\phi + g\tilde{m}\phi^* + g\left\langle\tilde{\phi}^\dagger\tilde{\phi}\tilde{\phi}\right\rangle. \tag{1.18}$$

Any solution of (1.18) is called the stationary solution since the probability density of finding a particle at position $\boldsymbol{x}$ and time t, $|\psi(\boldsymbol{x},t)|^2 = |\phi(\boldsymbol{x})|^2$, is independent of time.

The exact equation of motion for the non-condensate particles can be found by subtracting (1.11) from (1.7), which yields

$$i\hbar\frac{\partial\tilde{\psi}}{\partial t} = \left[-\frac{\hbar^2}{2m}\nabla^2 + V(\boldsymbol{x},t)\right]\tilde{\psi} + g\left[\hat{\psi}^\dagger\hat{\psi}\hat{\psi} - \left\langle\hat{\psi}^\dagger\hat{\psi}\hat{\psi}\right\rangle\right]. \tag{1.19}$$

Depending on the temperature of the system, some terms corresponding to the non-condensate may be neglected, resulting in several mean field models for BECs. The term $\hat{\psi}^\dagger\hat{\psi}\hat{\psi}$ in (1.19) can be simplified via the Bogoliubov transformation and different approximations in the mean field models will be introduced in the following parts of this chapter.

1.1.1 Hartree-Fock-Bogoliubov (HFB) model

If the three-field correlation function is ignored, the Bose-Einstein condensed system is described by the Hartree-Fock-Bogoliubov theory (HFB) [64]. Equations (1.11) and (1.18) are reduced to

$$i\hbar\frac{\partial\psi(\boldsymbol{x},t)}{\partial t} = \left[-\frac{\hbar^2}{2m}\nabla^2 + V(\boldsymbol{x},t) + g(n_c + 2n_T)\right]\psi(\boldsymbol{x},t) + g\tilde{m}\psi^*(\boldsymbol{x},t), \tag{1.20}$$

and

$$\mu\phi(\boldsymbol{x}) = \left[-\frac{\hbar^2}{2m}\nabla^2 + V(\boldsymbol{x}) + g(n_c + 2n_T)\right]\phi(\boldsymbol{x}) + g\tilde{m}\phi^*(\boldsymbol{x}). \tag{1.21}$$

For the non-condensate particles, expanding the term $\hat{\psi}^\dagger\hat{\psi}\hat{\psi}$ in (1.19) by applying assumption (1.8) and the following mean field approximations:

$$\tilde{\psi}^\dagger\tilde{\psi} \approx \left\langle\tilde{\psi}^\dagger\tilde{\psi}\right\rangle, \tag{1.22}$$

$$\tilde{\psi}\tilde{\psi} \approx \left\langle\tilde{\psi}\tilde{\psi}\right\rangle, \tag{1.23}$$

$$\tilde{\psi}^\dagger\tilde{\psi}\tilde{\psi} \approx 2\left\langle\tilde{\psi}^\dagger\tilde{\psi}\right\rangle\tilde{\psi} + \tilde{\psi}^\dagger\left\langle\tilde{\psi}\tilde{\psi}\right\rangle, \tag{1.24}$$

we obtain the equation of motion for the fluctuation field operator within the HFB approximation:

$$i\hbar\frac{\partial\tilde{\psi}}{\partial t} = \left[-\frac{\hbar^2}{2m}\nabla^2 + V + 2g(n_c + n_T)\right]\tilde{\psi} + g(\psi^2 + \tilde{m})\tilde{\psi}^\dagger. \tag{1.25}$$

Equation (1.25) can be diagonalized by expressing the field operators in terms of a set of non-interacting quasiparticle creation operator α_j and annihilation operator $\alpha_j^\dagger$. This is done through the Bogoliubov transformation,

$$\tilde{\psi}(\boldsymbol{x}, t) = \sum_j \left[u_j(\boldsymbol{x}, t)\alpha_j + v_j^*(\boldsymbol{x}, t)\alpha_j^\dagger\right], \tag{1.26}$$

where u_j and v_j are the quasiparticle amplitudes. The quasiparticle operators satisfy the Bose commutation relations:

$$\left[\alpha_i, \alpha_j^\dagger\right] = \delta_{ij}, \tag{1.27}$$

$$[\alpha_i, \alpha_j] = \left[\alpha_i^\dagger, \alpha_j^\dagger\right] = 0. \tag{1.28}$$

The Bogoliubov transformation converts (1.25) into the HFB equations at finite temperature,

$$i\hbar\frac{\partial u_j}{\partial t} = \left[-\frac{\hbar^2}{2m}\nabla^2 + V + 2g(n_c + n_T)\right]u_j + g(\psi^2 + \tilde{m})v_j, \tag{1.29}$$

$$-i\hbar\frac{\partial v_j}{\partial t} = \left[-\frac{\hbar^2}{2m}\nabla^2 + V + 2g(n_c + n_T)\right]v_j + g((\psi^*)^2 + \tilde{m}^*)u_j, \tag{1.30}$$

where

$$n_c = |\psi|^2, \tag{1.31}$$

$$n_T = \sum_j \left[|u_j|^2 N_j + |v_j|^2 (N_j + 1)\right], \tag{1.32}$$

$$\tilde{m} = \sum_j u_j v_j^* (1 + 2N_j), \tag{1.33}$$

$$N_j = \left\langle \alpha_j^\dagger \alpha_j \right\rangle = \frac{1}{\exp\left(\frac{\epsilon_j}{k_B T}\right) - 1}. \tag{1.34}$$

N_j is the occupation number of the jth state quasiparticle at temperature T, expressed according to the Bose-Einstein distribution, and ϵ_j is the jth state quasiparticle energy.

If the trapping potential does not depend on time, the quasiparticle amplitudes can be written as

$$\begin{aligned} u_j(\boldsymbol{x}, t) &= u_j(\boldsymbol{x}) e^{-i\epsilon_j t/\hbar} e^{-i\mu t/\hbar}, & (1.35)\\ v_j(\boldsymbol{x}, t) &= v_j(\boldsymbol{x}) e^{-i\epsilon_j t/\hbar} e^{-i\mu t/\hbar}. & (1.36)\end{aligned}$$

The stationary solutions $u_j(\boldsymbol{x})$ and $v_j(\boldsymbol{x})$ satisfy the time-independent HFB equations:

$$\begin{aligned} \epsilon_j u_j &= \left[-\frac{\hbar^2}{2m}\nabla^2 + V - \mu + 2g(n_c + n_T)\right] u_j + g(\phi^2 + \tilde{m}) v_j, & (1.37)\\ -\epsilon_j v_j &= \left[-\frac{\hbar^2}{2m}\nabla^2 + V - \mu + 2g(n_c + n_T)\right] v_j + g((\phi^*)^2 + \tilde{m}^*) u_j. & (1.38)\end{aligned}$$

Equations (1.37)–(1.38) together with (1.21) form a closed set of equations, which describe the Bose-Einstein condensed system at finite temperature T. The quasiparticle amplitudes satisfy the normalization condition

$$\int u_i^* u_j - v_i^* v_j \, d\boldsymbol{x} = \delta_{ij}. \tag{1.39}$$

The number of atoms in the condensed state is given by

$$N_c = \int n_c \, d\boldsymbol{x} = N - N_T = N - \int n_T \, d\boldsymbol{x}, \tag{1.40}$$

where N is the total number of particles and N_T is the number of non-condensate atoms.

1.1.2 Hartree-Fock-Bogoliubov-Popov (HFBP) model

HFB theory is able to produce good predictions of the excitation frequencies of dilute atomic gases measured in laboratory. However, the model suffers from infrared and ultraviolet divergence. Also an unphysical energy gap is predicted in the excitation spectrum. In order to produce a gapless excitation spectrum, the HFB theory with Popov approximation was suggested [64, 69]. For lower values of temperature, the theoretical results agree excellently with the experimental results [56]. Compared to the HFB model, more theoretical studies on the mean field finite temperature models are carried out on the basis of HFBP description [55, 111, 119]. Within the Popov approximation, the off-diagonal non-condensate density m is neglected. The Hartree-Fock-Bogoliubov-Popov (HFBP) equations are obtained easily from the HFB model, as

$$\begin{aligned} i\hbar\frac{\partial\psi}{\partial t} &= \left[-\frac{\hbar^2}{2m}\nabla^2 + V + g(n_c + 2n_T)\right]\psi, && (1.41)\\ i\hbar\frac{\partial u_j}{\partial t} &= \left[-\frac{\hbar^2}{2m}\nabla^2 + V + 2g(n_c + n_T)\right]u_j + g\psi^2 v_j, && (1.42)\\ -i\hbar\frac{\partial v_j}{\partial t} &= \left[-\frac{\hbar^2}{2m}\nabla^2 + V + 2g(n_c + n_T)\right]v_j + g(\psi^*)^2 u_j. && (1.43) \end{aligned}$$

The time-independent HFBP equations read

$$\begin{aligned} \mu\phi &= \left[-\frac{\hbar^2}{2m}\nabla^2 + V + g(n_c + 2n_T)\right]\phi, && (1.44)\\ \epsilon_j u_j &= \left[-\frac{\hbar^2}{2m}\nabla^2 + V + 2g(n_c + n_T)\right]u_j + g\phi^2 v_j, && (1.45)\\ -\epsilon_j v_j &= \left[-\frac{\hbar^2}{2m}\nabla^2 + V + 2g(n_c + n_T)\right]v_j + g(\phi^*)^2 u_j. && (1.46) \end{aligned}$$

The HFBP theory produces excellent results for a Bose-Einstein condensed system under $0.6T_c$ [56, 68]. As the critical temperature is approached, the calculated excitation frequencies diverge from those measured in experiments, and theories beyond mean field approximation should be applied to describe the Bose-Einstein condensed system.

1.1.3 Hartree-Fock (HF) model

For high energy excitations, the quasiparticle amplitude v_j is small and is negligible. In this regime, the coupled equations (1.42)–(1.43) and (1.45)–(1.46) in the HFBP model can be replaced by single particle excitation, that is

$$i\hbar\frac{\partial u_j}{\partial t} = \left[-\frac{\hbar^2}{2m}\nabla^2 + V + 2g(n_c + n_T)\right]u_j \qquad (1.47)$$

for time-dependent case, and

$$\epsilon_j u_j = \left[-\frac{\hbar^2}{2m}\nabla^2 + V + 2g(n_c + n_T) \right] u_j \tag{1.48}$$

for time-independent case. The non-condensate density is given by

$$n_T = \sum_j |u_j|^2 \frac{1}{\exp \frac{\epsilon_j}{k_B T} - 1}. \tag{1.49}$$

1.1.4 Gross-Pitaevskii equation (GPE)

At zero temperature, all anomalous terms and the non-condensate part can be neglected. This is equivalent to replacing the quantum field $\hat{\psi}(\boldsymbol{x}, t)$ in (1.7) by the classical field $\psi(\boldsymbol{x}, t)$. It gives rise to a nonlinear Schrödinger equation, the well-known Gross-Pitaevskii equation (GPE),

$$i\hbar\frac{\partial \psi}{\partial t} = \left[-\frac{\hbar^2}{2m}\nabla^2 + V + g|\psi|^2 \right] \psi, \tag{1.50}$$

for the Bose-Einstein condensed system. The GPE was first developed independently by Gross [65] and Pitaevskii [95] in 1961 to describe the vortex structure in superfluid. The macroscopic wavefunction/order parameter is normalized to the total number of particles in the system, which is conserved over time, i.e.

$$\int |\psi(\boldsymbol{x}, t)|^2 \, d\boldsymbol{x} = N. \tag{1.51}$$

A stationary state satisfies the time-independent GPE

$$\mu\phi = \left[-\frac{\hbar^2}{2m}\nabla^2 + V + g|\phi|^2 \right] \phi, \tag{1.52}$$

under constraint (1.51).

For ideal (non-interacting) gas, all particles occupy the ground state at $T = 0K$ and $\psi(\boldsymbol{x}, t)$ in the GPE describes the properties of all N particles in the system. For interacting gas, owing to the interparticle interaction, not all particles condense into the lowest energy state even at zero temperature. This phenomenon is called the quantum depletion. In a weakly interacting dilute atomic vapor, which is the main concern in this thesis, the non-condensate fraction is very small. The mean field theory can be successfully applied and the quantum depletion can be neglected at zero temperature, assuming a pure BEC in the system. If one is interested in finding the quantum depletion, the HFBP model (1.41)–(1.46) can be applied, in which

$$n_T = n_{\text{depletion}} = \sum_j |v_j|^2 \tag{1.53}$$

is the non-condensate particle number in the depletion, as reduced from (1.32) at $T = 0K$. In the case of strongly correlated system, e.g. superfluid ^{4}He in which the quantum depletion is greater than 90% even at $T = 0K$, the mean field approximation fails to describe the system.

1.2 Other Finite Temperature BEC Models

Mean field models introduced in the previous section are unsuccessful to give a good description of a cold dilute gas at temperature $T > 0.6T_c$, which is populated by a large number of thermally excited particles. Several theories have been developed to study the dynamics of the system in this higher temperature range.

The HFB and HFBP models deal with the BEC in the collisionless regime in which the collisional mean-free-path of excited particles is much larger than the wavelength of excitations. This usually corresponds to a low density and low temperature thermal cloud. In a collision-dominated regime, the problem becomes hydrodynamic in nature and the interparticle collisions should be taken into consideration. The ZGN theory [89, 116, 117], named after the 3 physicists, Zaremba, Griffin, and Nikuni, who developed the theory, describes a finite temperature BEC in the semiclassical limit in which the thermal energy (of the order of k_BT) is much larger than the energy levels of the trapping potential and is much larger than the interaction energy of the particles. The ZGN theory follows the mean field approach (1.11) within the Popov approximation which neglects the off-diagonal non-condensate density m. However, it is different from the HFBP model in a way that the three-field correlation function $\left\langle \tilde{\psi}^\dagger \tilde{\psi} \tilde{\psi} \right\rangle$ in (1.11) is retained. This term contributes to the collision and energy exchange between the condensate and the non-condensate. A semiclassical approximation is applied to the non-condensate, represented by a phase-space distribution function $f(\boldsymbol{p}, \boldsymbol{x}, t)$. The function $f(\boldsymbol{p}, \boldsymbol{x}, t)$ is described by a quantum Boltzmann kinetic equation that couples to the condensate through mean field and interparticle collisions. The final result in the ZGN theory is a closed system of two-fluid hydrodynamic equations in terms of the local densities and velocities of the condensate and non-condensate components. The theory was shown to be consistent with the Landau two-fluid model in the limiting case of complete local equilibrium in the condensate and the non-condensate of a uniform weakly interacting gas.

Another model that simulates the finite temperature BEC dynamics is the projected Gross-Pitaevskii equation (PGPE) proposed by Davis et al. [49, 51, 52]. It is a classical field and non-perturbative approach. The method was developed based on the approximation that the low-lying energy modes of the quantum Bose-field are highly occupied. They can therefore be treated by a classical field evolving according to the modification of the GPE with a projection operator, in which the high energy modes with small number of particles are excluded. The PGPE was shown to be able to evolve randomized initial wavefunction to a state describing the thermal equilibrium, and to assign a temperature to the final configuration. In the cases of small interaction strength or low temperature, the predictions of the PGPE are comparable to the predictions of Bogoliubov theory [50, 51, 52].

1.3 Purpose of Study and Structure of Thesis

Due to success of the HFBP model to describe various properties of a BEC as well as to produce a gapless excitation spectrum, this model has been widely applied in physics literature. However, the complexity of the equations creates high difficulties in the numerical simulation, especially in 3D BEC modelling. Self-consistent scheme has been applied to solve the HFBP equations by several authors. Yet, these studies have been restricted to a BEC in a parabolic trapping potential with radial/spherical symmetry that greatly simplifies the three dimensional problem by reduction to a lower dimensional problem. Even in these studies, the calculation is very time consuming and the numerical methods applied are usually of low order accuracy. Therefore, an efficient algorithm to solve the simplest model, the zero temperature GPE, is a pre-requisite to solving the HFBP equations efficiently. Furthermore, in studying the collective excitations of BEC, one needs to solve the Bogoliubov-de-Gennes (BdG) equations in a form similar to (1.45)–(1.46) but with $n_T = 0$. An accurate approximation to the BEC ground state is required to solve the BdG equations so as to avoid the appearance of any unphysical excitation frequency in the excitation spectrum.

The purpose of this thesis is to develop efficient and accurate algorithms to solve the zero temperature GPE. Such algorithms can provide a good preparatory step in developing efficient numerical schemes to solve other finite temperature mean field models. Furthermore, the PGPE possesses great similarity to the GPE. With an efficient method to solve the GPE, the method may also be applicable to the PGPE with appropriate modification.

This thesis will start with analytically studying the ground state of a single component BEC in several types of trapping potential, for both repulsively and attractively interacting atoms (Chapter 2). In Chapter 3, accurate and efficient numerical methods for the computation of a single component BEC ground state will be proposed, developed on the basis of the imaginary time method. Numerical examples will be provided to show the efficiency of the proposed method. In Chapter 4, the numerical method will be extended to a spin-1 BEC which is described by three-component coupled GPEs. The numerical scheme will further be extended to solve for the spin-1 BEC ground state subjected to uniform magnetic field, which exhibits rich properties due to different Zeeman energies experienced by different components. Finally, the transport of a strongly repulsive BEC through a shallow optical lattice of finite width will be studied in Chapter 5. The study will be carried out numerically via the modelling of the time-dependent GPE as well as analytically in terms of nonlinear Bloch waves. Concluding remarks will be given in Chapter 6.

Chapter 2

Analytical Study of Single Component BEC Ground State

2.1 The Gross-Pitaevskii Equation

Neglecting the quantum depletion, the properties of a Bose-Einstein condensate (BEC) at zero temperature are well described by the macroscopic wavefunction $\psi(\boldsymbol{x}, t)$ whose evolution is governed by the Gross-Pitaevskii equation (GPE) [65, 95], which is a self-consistent mean field nonlinear Schrödinger equation (NLSE):

$$i\hbar\frac{\partial}{\partial t}\psi(\boldsymbol{x}, t) = \left(-\frac{\hbar^2}{2m}\nabla^2 + V(\boldsymbol{x}) + Ng|\psi(\boldsymbol{x}, t)|^2\right)\psi(\boldsymbol{x}, t), \quad \boldsymbol{x} \in \mathbb{R}^3, \ t \geq 0. \tag{2.1}$$

The external trapping potential $V(\boldsymbol{x})$ is taken to be time-independent. It is convenient to normalize the wavefunction by requiring

$$\|\psi(\cdot, t)\|^2 := \int_{\mathbb{R}^3} |\psi(\boldsymbol{x}, t)|^2 \, d\boldsymbol{x} = 1. \tag{2.2}$$

The equations (2.1) and (2.2) are obtained by rescaling $\psi \to \sqrt{N}\psi$ in (1.50) and (1.51).

2.1.1 Different external trapping potentials

In early BEC experiments, quadratic harmonic oscillator well was used to trap the atoms. Recently more advanced and complicated traps have been applied for studying BECs in laboratories [29, 35, 82, 94]. In this section, we will review several typical trapping potentials which are widely used in current experiments.

I. Three-dimensional (3D) harmonic oscillator potential [94]:

$$V_{\rm ho}(\boldsymbol{x}) = V_{\rm ho}(x) + V_{\rm ho}(y) + V_{\rm ho}(z),\ \ \boldsymbol{x} \in \mathbb{R}^3, \qquad V_{\rm ho}(\tau) = \frac{m}{2}\omega_\tau^2 \tau^2,\ \ \tau = x, y, z, \tag{2.3}$$

where ω_x, ω_y, and ω_z are the trapping frequencies in x-, y-, and z-direction respectively.

II. 2D harmonic oscillator + 1D double well potential (Type I) [82]:

$$V_{\rm dw}^{(1)}(\boldsymbol{x}) = V_{\rm dw}^{(1)}(x) + V_{\rm ho}(y) + V_{\rm ho}(z), \quad \boldsymbol{x} \in \mathbb{R}^3, \qquad V_{\rm dw}^{(1)}(x) = \frac{m}{2}\nu_x^4 \left(x^2 - \hat{a}^2\right)^2, \tag{2.4}$$

where $\pm\hat{a}$ are the double well centers along the x-axis, ν_x is a given constant with physical dimension $1/[\mathrm{m\ s}]^{1/2}$.

III. 2D harmonic oscillator + 1D double well potential (Type II) [33, 67]:

$$V_{\rm dw}^{(2)}(\boldsymbol{x}) = V_{\rm dw}^{(2)}(x) + V_{\rm ho}(y) + V_{\rm ho}(z), \quad \boldsymbol{x} \in \mathbb{R}^3, \qquad V_{\rm dw}^{(2)}(x) = \frac{m}{2}\omega_x^2 \left(|x| - \hat{a}\right)^2. \tag{2.5}$$

IV. 3D harmonic oscillator + optical lattice potential [2, 41, 94]:

$$V_{\rm hop}(\boldsymbol{x}) = V_{\rm ho}(\boldsymbol{x}) + V_{\rm opt}(x) + V_{\rm opt}(y) + V_{\rm opt}(z), \quad \boldsymbol{x} \in \mathbb{R}^3, \quad V_{\rm opt}(\tau) = S_\tau\ E_\tau \sin^2(\hat{q}_\tau \tau), \tag{2.6}$$

where $\hat{q}_\tau = 2\pi/\lambda_\tau$ is the angular frequency of the laser beam, with wavelength λ_τ, that creates the stationary 1D periodic lattice, $E_\tau = \hbar^2\hat{q}_\tau^2/2m$ is the recoil energy, and S_τ is a dimensionless parameter characterizing the intensity of the laser beam. The optical lattice potential has periodicity $T_\tau = \pi/\hat{q}_\tau = \lambda_\tau/2$ along the τ-axis ($\tau = x, y, z$).

V. 3D box potential [94]:

$$V_{\text{box}}(\boldsymbol{x}) = \begin{cases} 0, & 0 < x, y, z < L, \\ \infty, & \text{otherwise}. \end{cases} \tag{2.7}$$

where L is the length of the box.

2.1.2 Dimensionless GPE

In order to scale (2.1) under the normalization (2.2), we introduce the following dimensionless parameters [17]:

$$\tilde{t} = \frac{t}{t_0}, \quad \tilde{\boldsymbol{x}} = \frac{\boldsymbol{x}}{x_0}, \quad \tilde{\psi}\left(\tilde{\boldsymbol{x}}, \tilde{t}\right) = x_0^{3/2}\psi\left(\boldsymbol{x}, t\right), \quad \tilde{E}(\tilde{\psi}) = \frac{E(\psi)}{E_0}, \tag{2.8}$$

where t_0, x_0 and E_0 are the scaling parameters of dimensionless time, length and energy units, respectively. Substituting (2.8) into (2.1), multiplying by $t_0^2/mx_0^{1/2}$, and removing all ˜ yield the dimensionless GPE under normalization in 3D,

$$i\frac{\partial\psi(\boldsymbol{x}, t)}{\partial t} = \left(-\frac{1}{2}\nabla^2 + V(\boldsymbol{x}) + \beta|\psi(\boldsymbol{x}, t)|^2\right)\psi(\boldsymbol{x}, t), \qquad \boldsymbol{x} \in \mathbb{R}^3. \tag{2.9}$$

The dimensionless energy functional $E(\psi)$ is defined as

$$E(\psi) = \int_{\mathbb{R}^3} \left[\frac{1}{2}|\nabla\psi|^2 + V(\boldsymbol{x})|\psi|^2 + \frac{\beta}{2}|\psi|^4\right] d\boldsymbol{x}. \tag{2.10}$$

The choices for the scaling parameters t_0 and x_0, the dimensionless potential $V(\boldsymbol{x})$ with $\gamma_y = t_0\omega_y$ and $\gamma_z = t_0\omega_z$, the energy unit $E_0 = \hbar/t_0 = \hbar^2/mx_0^2$, and the interaction parameter $\beta = 4\pi a_s N/x_0$ for different external trapping potentials are given below:

I. 3D harmonic oscillator potential:

$$t_0 = \frac{1}{\omega_x}, \quad x_0 = \sqrt{\frac{\hbar}{m\omega_x}}, \quad V(\boldsymbol{x}) = \frac{1}{2}\left(x^2 + \gamma_y^2 y^2 + \gamma_z^2 z^2\right).$$

II. 2D harmonic oscillator + 1D double well potential (type I):

$$t_0 = \left(\frac{m}{\hbar \nu_x^4}\right)^{1/3}, \; x_0 = \left(\frac{\hbar}{m\nu_x^2}\right)^{1/3}, \; a = \frac{\hat{a}}{x_0}, \; V(\boldsymbol{x}) = \frac{1}{2}\left[\left(x^2 - a^2\right)^2 + \gamma_y^2 y^2 + \gamma_z^2 z^2\right].$$

III. 2D harmonic oscillator + 1D double well potential (type II):

$$t_0 = \frac{1}{\omega_x}, \quad x_0 = \sqrt{\frac{\hbar}{m\omega_x}}, \quad a = \frac{\hat{a}}{x_0}, \quad V(\boldsymbol{x}) = \frac{1}{2}\left[(|x| - a)^2 + \gamma_y^2 y^2 + \gamma_z^2 z^2\right].$$

IV. 3D harmonic oscillator + optical lattice potential:

$$t_0 = \frac{1}{\omega_x}, \quad x_0 = \sqrt{\frac{\hbar}{m\omega_x}}, \quad k_\tau = \frac{2\pi^2 x_0^2 S_\tau}{\lambda_\tau^2}, \quad q_\tau = \frac{2\pi x_0}{\lambda_\tau}, \quad \tau = x, y, z,$$
$$V(\boldsymbol{x}) = \frac{1}{2}(x^2 + \gamma_y^2 y^2 + \gamma_z^2 z^2) + k_x \sin^2(q_x x) + k_y \sin^2(q_y y) + k_z \sin^2(q_z z).$$

V. 3D box potential:

$$t_0 = \frac{mL^2}{\hbar}, \quad x_0 = L, \quad V(\boldsymbol{x}) = \begin{cases} 0, & 0 < x, y, z < 1, \\ \infty, & \text{otherwise.} \end{cases}$$

Under external potentials I–IV, in a disk-shape condensation, i.e. $\omega_y \approx 1/t_0$ and $\omega_z \gg 1/t_0$ ($\Leftrightarrow$ $\gamma_y \approx 1$ and $\gamma_z \gg 1$), following the procedure used in [13, 18, 75], the 3D GPE can be reduced to a 2D GPE. Similarly, in a cigar-shaped condensation, i.e. $\omega_y \gg 1/t_0$ and $\omega_z \gg 1/t_0$ ($\Leftrightarrow \gamma_y \gg 1$ and $\gamma_z \gg 1$), the 3D GPE can be reduced to a 1D GPE. This suggests us to consider a GPE in d dimensions ($d = 1, 2, 3$):

$$i\,\frac{\partial}{\partial t}\psi(\boldsymbol{x}, t) = \left(-\frac{1}{2}\nabla^2 + V_d(\boldsymbol{x}) + \beta_d|\psi(\boldsymbol{x}, t)|^2\right)\psi(\boldsymbol{x}, t), \qquad \boldsymbol{x} \in \Omega \subseteq \mathbb{R}^d, \tag{2.11}$$

$$\psi(\boldsymbol{x}, t) = 0, \qquad \boldsymbol{x} \in \Gamma = \partial\Omega, \tag{2.12}$$

$$\psi(\boldsymbol{x}, 0) = \psi_0(\boldsymbol{x}), \qquad \boldsymbol{x} \in \Omega; \tag{2.13}$$

where β_d is the scaled interacting parameter and $V_d(\boldsymbol{x})$ is the scaled external potential.

There are two important invariants of (2.11), which are the normalization of the wavefunction

$$N(\psi) = \int_\Omega |\psi(\boldsymbol{x},t)|^2 \, d\boldsymbol{x} \equiv N(\psi_0) = \int_\Omega |\psi_0(\boldsymbol{x})|^2 \, d\boldsymbol{x} = 1, \quad t \geq 0 \tag{2.14}$$

and the energy functional

$$E(\psi) = \int_\Omega \left[\frac{1}{2}|\nabla\psi|^2 + V_d(\boldsymbol{x})|\psi|^2 + \frac{\beta_d}{2}|\psi|^4\right] d\boldsymbol{x} \equiv E(\psi_0), \quad t \geq 0. \tag{2.15}$$

The energy functional $E(\psi)$ can be split into three parts, i.e. kinetic energy $E_{\text{kin}}(\psi)$, potential energy $E_{\text{pot}}(\psi)$ and interaction energy $E_{\text{int}}(\psi)$, which are defined as

$$E_{\text{int}}(\psi) = \int_\Omega \frac{\beta_d}{2}|\psi(\boldsymbol{x},t)|^4 d\boldsymbol{x}, \qquad E_{\text{pot}}(\psi) = \int_\Omega V_d(\boldsymbol{x})|\psi(\boldsymbol{x},t)|^2 d\boldsymbol{x}, \tag{2.16}$$

$$E_{\text{kin}}(\psi) = \int_\Omega \frac{1}{2}|\nabla\psi(\boldsymbol{x},t)|^2 \, d\boldsymbol{x}, \quad E(\psi) = E_{\text{kin}}(\psi) + E_{\text{pot}}(\psi) + E_{\text{int}}(\psi). \tag{2.17}$$

2.1.3 Stationary states

The magnitude square of the wavefunction, $|\psi(\boldsymbol{x},t)|^2$, represents the probability density of finding a particle at position $\boldsymbol{x}$ and time t. We are interested to find the stationary states of the Bose-Einstein condensed system, whose probability density is independent of time. To find a stationary solution of (2.11), we write

$$\psi(\boldsymbol{x},t) = e^{-i\mu t}\phi(\boldsymbol{x}), \tag{2.18}$$

where μ is the chemical potential of the condensate and $\phi(\boldsymbol{x})$ is a function independent of time. Substituting (2.18) into (2.11) yields the equation

$$\mu \, \phi(\boldsymbol{x}) = \left(-\frac{1}{2}\nabla^2 + V(\boldsymbol{x}) + \beta_d|\phi(\boldsymbol{x})|^2\right)\phi(\boldsymbol{x}), \quad \boldsymbol{x} \in \Omega \subseteq \mathbb{R}^d, \tag{2.19}$$

for $\phi(\boldsymbol{x})$ under the normalization condition

$$\|\phi\|^2 := \int_\Omega |\phi(\boldsymbol{x})|^2 \, d\boldsymbol{x} = 1. \tag{2.20}$$

This is a nonlinear eigenvalue problem with a constraint. Any eigenvalue μ can be computed from its corresponding eigenfunction ϕ by

$$\begin{aligned}\mu &= \mu(\phi) = \int_\Omega \left[\frac{1}{2}|\nabla\phi(\boldsymbol{x})|^2 + V(\boldsymbol{x})|\phi(\boldsymbol{x})|^2 + \beta_d|\phi(\boldsymbol{x})|^4\right] d\boldsymbol{x} \\ &= E(\phi) + \int_\Omega \frac{\beta_d}{2}|\phi(\boldsymbol{x})|^4 d\boldsymbol{x}. \end{aligned} \tag{2.21}$$

In fact, the eigenfunctions of (2.19) under the constraint (2.20) are equivalent to the critical points of the energy functional $E(\phi)$ over the unit sphere $S = \{\phi \mid \|\phi\| = 1, E(\phi) < \infty\}$.

From mathematical point of view, the ground state of a BEC is defined as the solution of the following minimization problem:

Find $(\mu_g, \phi_g \in S)$ such that

$$E_g := E(\phi_g) = \min_{\phi\in S} E(\phi), \qquad \mu_g = \mu(\phi_g) = E_g + \int_\Omega \frac{\beta_d}{2}|\phi_g(\boldsymbol{x})|^4\, d\boldsymbol{x}. \tag{2.22}$$

When $\beta_d \geq 0$ and $\lim_{|\boldsymbol{x}|\to\infty} V(\boldsymbol{x}) = \infty$, there exists a unique positive solution of the minimization problem (2.22) [76]. It is easy to show that the ground state ϕ_g is an eigenfunction of (2.19). Other eigenfunctions of (2.19) whose energies are larger than E_g are called the excited states in physics literature.

2.2 Condensate Ground State with Repulsive Interaction

2.2.1 Box potential

In this section, we will present the asymptotic approximations for the ground and the excited states, as well as their energy and chemical potential approximations up to $o(1)$ in terms of β_d, for a BEC in a box potential, i.e. $V_d(\boldsymbol{x}) \equiv 0$ and $\Omega = [0,1]^d$ in (2.19) [17]. Approximations will be presented for both weakly interacting regime ($\beta_d \to 0$), and strongly repulsively interacting regime ($\beta_d \to \infty$). In this case, we have the following equalities between the energies and chemical potential:

$$E_{\rm int}(\phi) = \frac{1}{2}\left[\mu(\phi) - E_{\rm kin}(\phi)\right], \qquad E(\phi) = E_{\rm kin}(\phi) + E_{\rm int}(\phi). \tag{2.23}$$

2.2.1.1 Approximations in weakly interacting regime

When $\beta_d = 0$, the problem (2.19)–(2.20) reduces to a linear eigenvalue problem, i.e.

$$\mu\,\phi(\boldsymbol{x}) = -\frac{1}{2}\nabla^2\phi(\boldsymbol{x}), \quad \boldsymbol{x} \in \Omega, \qquad \phi(\boldsymbol{x})|_\Gamma = 0, \qquad \|\phi\| = 1. \tag{2.24}$$

By applying separation of variables, a complete set of orthonormal eigenfunctions can be found as

$$\phi_{\boldsymbol{J}}(\boldsymbol{x}) = \prod_{m=1}^{d} \phi_{j_m}(x_m),\ \phi_l(\tau) = \sqrt{2}\sin(l\pi\tau),\ l \in \mathbb{N},\ \boldsymbol{J} = (j_1, \cdots, j_d) \in \mathbb{N}^d. \tag{2.25}$$

The corresponding eigenvalues are

$$\mu_{\boldsymbol{J}} = \sum_{m=1}^{d} \mu_{j_m}, \qquad \mu_l = \frac{1}{2}l^2\pi^2, \qquad l \in \mathbb{N}. \tag{2.26}$$

From these solutions, we can get the ground state solution $\phi_g(\boldsymbol{x}) = \phi_{(1,\cdots,1)}(\boldsymbol{x})$. The corresponding energy and chemical potential are $E_g = \mu_g = d\pi^2/2$. All the other eigenfunctions are called the excited states. Of course, these solutions can be viewed as approximations for the ground and the excited states when $\beta_d = o(1)$, by dropping the nonlinear term on the right hand side of (2.19).

2.2.1.2 Thomas-Fermi approximation

In the strongly repulsively interacting regime ($\beta_d \gg 1$), the diffusion term, i.e. the first term on the right hand side of the time-independent GPE (2.19), can be dropped. This yields

$$\mu_g^{\mathrm{TF}}\,\phi_g^{\mathrm{TF}}(\boldsymbol{x}) = \beta_d\,\left|\phi_g^{\mathrm{TF}}(\boldsymbol{x})\right|^2 \phi_g^{\mathrm{TF}}(\boldsymbol{x}), \qquad \boldsymbol{x} \in \Omega. \tag{2.27}$$

Such approximation is called the Thomas-Fermi (TF) approximation in physics. From (2.27), we obtain

$$\phi_g^{\mathrm{TF}}(\boldsymbol{x}) = \sqrt{\frac{\mu_g^{\mathrm{TF}}}{\beta_d}}, \qquad \boldsymbol{x} \in \Omega. \tag{2.28}$$

Substituting (2.28) into the normalization condition (2.20) gives

$$1 = \int_\Omega |\phi_g^{\mathrm{TF}}(\boldsymbol{x})|^2\,d\boldsymbol{x} = \int_\Omega \frac{\mu_g^{\mathrm{TF}}}{\beta_d}\,d\boldsymbol{x} = \frac{\mu_g^{\mathrm{TF}}}{\beta_d} \quad \Rightarrow \quad \mu_g^{\mathrm{TF}} = \beta_d. \tag{2.29}$$

Noticing (2.21), we get the Thomas-Fermi energy

$$E_g^{\mathrm{TF}} = \mu_g^{\mathrm{TF}} - \frac{\beta_d}{2}\int_\Omega |\phi_g^{\mathrm{TF}}|^4 \, d\boldsymbol{x} = \frac{\mu_g^{\mathrm{TF}}}{2} = \frac{\beta_d}{2}. \tag{2.30}$$

Therefore, when $\beta_d \gg 1$ the TF approximation for the ground state, the energy, and the chemical potential are given by

$$\phi_g(\boldsymbol{x}) \approx \phi_g^{\mathrm{TF}}(\boldsymbol{x}) = 1, \qquad \boldsymbol{x} \in \Omega, \tag{2.31}$$

$$E_g \approx E_g^{\mathrm{TF}} = \frac{\beta_d}{2}, \qquad \mu_g \approx \mu_g^{\mathrm{TF}} = \beta_d. \tag{2.32}$$

It is easy to see that the TF approximation for the ground state does not satisfy the zero boundary conditions (2.12), due to the removal of the diffusion term in (2.19). This suggests that boundary layers appear in the ground state when $\beta_d \gg 1$. Due to existence of the boundary layers, the kinetic energy does not converge to zero when $\beta_d \to \infty$ and therefore it cannot be neglected. In the next section, we will present a better approximation by applying the matched asymptotic method.

2.2.1.3 Ground state in 1D

When $d = 1$, $V_d(\boldsymbol{x}) \equiv 0$ and $\Omega = [0, 1]$ in the GPE (2.19), boundary layers exist at the two boundaries $x = 0$ and $x = 1$. We therefore solve (2.19) near $x = 0$ and $x = 1$ separately. Firstly, we consider $0 \le x \le 1/2$ and rescale (2.19) by introducing

$$x = \frac{1}{\sqrt{\mu_g}} X, \qquad \phi(x) = \sqrt{\frac{\mu_g}{\beta_1}}\Phi(X), \tag{2.33}$$

where $\mu_g \approx \beta_1$ is the chemical potential of the ground state. Substituting (2.33) into (2.19) yields

$$\Phi(X) = -\frac{1}{2}\Phi_{XX}(X) + \Phi^3(X), \qquad 0 \le X < \infty, \tag{2.34}$$

$$\Phi(0) = 0, \qquad \lim_{X\to\infty} \Phi(X) = 1. \tag{2.35}$$

Solving (2.34)–(2.35), we obtain

$$\Phi(X) = \tanh(X), \qquad 0 \le X < \infty. \tag{2.36}$$

Substituting (2.36) into (2.33), an approximation for $\phi_g(x)$ near $x=0$ when $\beta_1 \gg 1$ is obtained as

$$\phi_g(x) \approx \sqrt{\frac{\mu_g}{\beta_1}} \tanh\left(\sqrt{\mu_g} x\right), \qquad 0 \le x < 1/2. \tag{2.37}$$

Similarly, an approximation for $\phi_g(x)$ near $x=1$ when $\beta_1 \gg 1$ is found to be

$$\phi_g(x) \approx \sqrt{\frac{\mu_g}{\beta_1}} \tanh\left(\sqrt{\mu_g}(1-x)\right), \qquad 1/2 < x \le 1. \tag{2.38}$$

Applying the matched asymptotic method to (2.37) and (2.38), we get an approximation for the ground state when $\beta_1 \gg 1$:

$$\begin{aligned} \phi_g(x) &\approx \phi_g^{\mathrm{MA}}(x) \qquad (2.39)\\ &= \sqrt{\frac{\mu_g^{\mathrm{MA}}}{\beta_1}} \left[\tanh\left(\sqrt{\mu_g^{\mathrm{MA}}} x\right) + \tanh\left(\sqrt{\mu_g^{\mathrm{MA}}}(1-x)\right) - \tanh\left(\sqrt{\mu_g^{\mathrm{MA}}}\right)\right]. \end{aligned}$$

Substituting (2.39) into (2.20), and making an approximation of $e^{-\alpha} \approx 0$ for $\alpha \gg 1$ during the evaluation of integral, we obtain

$$1 = \int_0^1 |\phi_g^{\mathrm{MA}}(x)|^2 \, dx \approx \frac{\mu_g^{\mathrm{MA}}}{\beta_1} - 2\frac{\sqrt{\mu_g^{\mathrm{MA}}}}{\beta_1}. \tag{2.40}$$

Solving (2.40) yields the matched asymptotic chemical potential,

$$\mu_g \approx \mu_g^{\mathrm{MA}} = \beta_1 + 2\sqrt{\beta_1+1} + 2 = \mu_g^{\mathrm{TF}} + 2\sqrt{\beta_1+1} + 2, \qquad \beta_1 \gg 1. \tag{2.41}$$

Substituting (2.39) into (2.16)–(2.17) yields the matched asymptotic energies,

$$\begin{aligned} E_{\mathrm{kin},g} &\approx E_{\mathrm{kin},g}^{\mathrm{MA}} = \frac{2}{3}\sqrt{\beta_1+1} + 2, & (2.42)\\ E_{\mathrm{int},g} &\approx E_{\mathrm{int},g}^{\mathrm{MA}} = \frac{\beta_1}{2} + \frac{2}{3}\sqrt{\beta_1+1}, \qquad \beta_1 \gg 1, & (2.43)\\ E_g &\approx E_g^{\mathrm{MA}} = \frac{\beta_1}{2} + \frac{4}{3}\sqrt{\beta_1+1} + 2. & (2.44) \end{aligned}$$

From the above asymptotic results, we draw the following conclusions:

(i) The width of the boundary layer in the matched asymptotic approximation is $O(1/\sqrt{\beta_1})$.

$1/\beta_1$	4/25	2/25	1/25	1/50	1/100	1/400
$\max\lvert\phi_g-\phi_g^{\text{MA}}\rvert$	8.17E-3	9.24E-4	4.67E-5	8E-7	– –	– –
$\lVert\phi_g-\phi_g^{\text{MA}}\rVert_{L^2}$	6.84E-3	8.05E-4	4.11E-5	6E-7	– –	– –
$\lvert E_{\text{kin},g}-E_{\text{kin},g}^{\text{MA}}\rvert$	1.3018	0.9479	0.6464	0.4340	0.2946	0.1399
Rate		0.4577	0.5523	0.5747	0.5589	0.5372
$\lvert E_{\text{int},g}-E_{\text{int,g}}^{\text{MA}}\rvert$	0.5948	0.4608	0.3218	0.2171	0.1473	0.0701
Rate		0.3683	0.5180	0.5678	0.5596	0.5356
$\lvert E_g-E_g^{\text{MA}}\rvert$	0.7071	0.4871	0.3245	0.2171	0.1472	0.0698
Rate		0.5377	0.5860	0.5799	0.5606	0.5382
$\lvert\mu_g-\mu_g^{\text{MA}}\rvert$	0.1124	0.0263	0.0027	0.0001	– –	– –
E_g/μ_g	0.6854	0.6234	0.5813	0.5543	0.5368	0.5175
$E_{\text{int},g}/E_g$	0.4591	0.6042	0.7204	0.8042	0.8628	0.9323
$E_{\text{kin},g}/E_g$	0.5409	0.3958	0.2796	0.1958	0.1372	0.0677

Table 2.1: Convergence study of the matched asymptotic approximation for the BEC ground state in 1D box potential when $\beta_1 \gg 1$.

(ii) The ratios between the energies satisfy

$$\lim_{\beta_1\to\infty}\frac{E_g}{\mu_g}=\frac{1}{2},\qquad \lim_{\beta_1\to\infty}\frac{E_{\text{int},g}}{E_g}=1,\qquad \lim_{\beta_1\to\infty}\frac{E_{\text{kin},g}}{E_g}=0. \tag{2.45}$$

To verify (2.39), (2.41)–(2.45) numerically, we compute and list the errors between the numerically computed ground state and its matched asymptotic approximation in Table 2.1 (the numerical method will be introduced in Chapter 3). Figure 2.1 (a) shows the numerically computed ground state for different β_1. Here and below, the convergence rate of a function $f(\alpha)$ as $\alpha \to 0$ is computed as: $\ln[f(2\alpha)/f(\alpha)]/\ln 2$.

From Table 2.1 and Figure 2.1 (a), we draw the following conclusions:

(1) The matched asymptotic approximation converges to the ground state, when $\beta_1 \to \infty$, with a convergence rate

$$\max|\phi_g-\phi_g^{\text{MA}}| = O(e^{-3\sqrt{\beta_1}/2}),\qquad \|\phi_g-\phi_g^{\text{MA}}\|_{L^2} = O(e^{-3\sqrt{\beta_1}/2}),\qquad \beta_1 \gg 1.$$

(2) The asymptotic approximations (2.41)–(2.45) are verified. Furthermore, the numerical results suggest the following convergence rates:

$$\begin{aligned} &E_{\text{kin},g}=E_{\text{kin},g}^{\text{MA}}+O(1/\sqrt{\beta_1}),\qquad E_{\text{int},g}=E_{\text{int},g}^{\text{MA}}+O(1/\sqrt{\beta_1}),\\ &E_g=E_g^{\text{MA}}+O(1/\sqrt{\beta_1}),\quad \mu_g=\mu_g^{\text{MA}}+O(e^{-3\sqrt{\beta_1}/2}),\qquad \beta_1\gg 1.\end{aligned}$$

(3) Boundary layers are observed at $x = 0$ and $x = 1$ in the ground state when $\beta_1 \gg 1$, and the width of the layers is about $2/\sqrt{\beta_1}$. The width of the boundary layer is measured numerically from the wavefunction changing from 0 to $1/\sqrt{2} \approx 0.7071$.

2.2.1.4 Excited states in 1D

Applying similar procedure used in approximating the BEC ground state solution, we construct the matched asymptotic approximations for the excited states in 1D box potential in the Thomas-Fermi regime. When $\beta_1 \gg 1$, the kth ($k \in \mathbb{N}$) excited state has two boundary layers located at $x = 0$ and $x = 1$, and k interior layers located at $x = j/(k+1)$ ($j = 1, \cdots, k$). Using the matched asymptotic method, an approximation $\phi_k^{\rm MA}(x)$ for the kth excited state ϕ_k ($k \in \mathbb{N}$) is obtained as

$$\begin{aligned}\phi_k(x) \quad &\approx \quad \phi_k^{\rm MA}(x) = \sqrt{\frac{\mu_k^{\rm MA}}{\beta_1}}\left[\sum_{j=0}^{[(k+1)/2]} \tanh\left(\sqrt{\mu_k^{\rm MA}}\left(x - \frac{2j}{k+1}\right)\right)\right. \\ &\left. + \sum_{j=0}^{[k/2]} \tanh\left(\sqrt{\mu_k^{\rm MA}}\left(\frac{2j+1}{k+1} - x\right)\right) - C_k \tanh\left(\sqrt{\mu_k^{\rm MA}}\right)\right], \quad k \in \mathbb{N}, \qquad (2.46)\end{aligned}$$

where $[\tau]$ is the integer part of the real number τ, and constant C_k is given by

$$C_k = \begin{cases} 1, & k \text{ even}, \\ 0, & k \text{ odd}, \end{cases} \qquad n \in \mathbb{N}.$$

Substituting (2.46) into (2.20), we get

$$1 = \int_0^1 |\phi_k^{\rm MA}(x)|^2 \, dx \approx \frac{\mu_k^{\rm MA}}{\beta_1}\left[1 - \frac{2(k+1)}{\sqrt{\mu_k^{\rm MA}}}\right]. \qquad (2.47)$$

Solving (2.47) yields the chemical potential of the kth excited state,

$$\mu_k \approx \mu_k^{\rm MA} = \beta_1 + 2(k+1)\sqrt{\beta_1 + (k+1)^2} + 2(k+1)^2, \quad k \in \mathbb{N}. \qquad (2.48)$$

Substituting (2.46) into (2.16)–(2.17) gives the matched asymptotic energies,

$$E_{{\rm kin},k} \approx E_{{\rm kin},k}^{\rm MA} = \frac{2}{3}(k+1)\sqrt{\beta_1 + (k+1)^2} + 2(k+1)^2, \qquad (2.49)$$

$$E_{\rm int,k} \approx E_{\rm int,k}^{\rm MA} = \frac{\beta_1}{2} + \frac{2}{3}(k+1)\sqrt{\beta_1 + (k+1)^2}, \quad k \in \mathbb{N}, \quad \beta_1 \gg 1, \qquad (2.50)$$

$$E_k \approx E_k^{\mathrm{MA}} = \frac{\beta_1}{2} + \frac{4}{3}(k+1)\sqrt{\beta_1 + (k+1)^2} + 2(k+1)^2. \tag{2.51}$$

From (2.41)–(2.44) and (2.48)–(2.51), we can formally draw the following conclusion when $\beta_1 \gg 1$:

If all eigenfunctions, i.e. ϕ_g, ϕ_1, ϕ_2, $\cdots$, of the nonlinear eigenvalue problem (2.21) are ranked according to their energies, then the corresponding eigenvalues (or chemical potentials) are ranked in the increasing order, i.e.

$$E(\phi_g) < E(\phi_1) < E(\phi_2) < \cdots \quad \Longrightarrow \quad \mu(\phi_g) < \mu(\phi_1) < \mu(\phi_2) < \cdots. \tag{2.52}$$

This suggests that the two definitions of the ground state used in physics literature, i.e. (1) solution of the minimization problem (2.22), (2) eigenfunction of the nonlinear eigenvalue problem (2.19) with the smallest eigenvalue, are equivalent. Furthermore, we have

$$\lim_{\beta_1\to\infty} \frac{E_k}{E_g} = 1, \qquad \lim_{\beta_1\to\infty} \frac{\mu_k}{\mu_g} = 1, \qquad \lim_{\beta_1\to\infty} \frac{E_k}{\mu_g} = \frac{1}{2}, \tag{2.53}$$

$$\lim_{\beta_1\to\infty} \frac{E_{\mathrm{int},k}}{E_k} = 1, \qquad \lim_{\beta_1\to\infty} \frac{E_{\mathrm{kin},k}}{E_k} = 0, \qquad k \in \mathbb{N}. \tag{2.54}$$

Again, to verify the results (2.46), (2.48)–(2.54) numerically, we compute and list the errors between the numerically computed first and fifth excited states and their matched asymptotic approximations in Tables 2.2&2.3 . Table 2.4 lists the energies and chemical potentials of the ground state and the first five excited states for different β_1. Furthermore, Figure 2.1(b)&(c) show the numerical solutions of the first and the fifth excited states for different β_1.

From Tables 2.2–2.4 and Figure 2.1(b)&(c), we draw the following conclusions for the excited states:

(1) Conclusions (1) and (2) for the ground state in the previous section are still valid for the excited states.

(2) Boundary layers at $x = 0$ and $x = 1$, and interior layers at $x = j/(k+1)$ $(j = 1, \cdots, k)$ are observed in the kth excited state when $\beta_1 \gg 1$. The width of the boundary layers is about $2/\sqrt{\beta_1}$ and that of the interior layers is about $4/\sqrt{\beta_1}$.

(3) Conclusions (2.52)–(2.54) are confirmed by our numerical results. In fact, (2.52) is valid for all $\beta_1 \geq 0$.

$1/\beta_1$	1/25	1/50	1/100	1/400	1/1600	1/6400
$\max\lvert\phi_1-\phi_1^{\text{MA}}\rvert$	6.44E-3	7.12E-4	3.54E-5	– –	– –	– –
$\lVert\phi_1-\phi_1^{\text{MA}}\rVert_{L^2}$	5.28E-3	6.02E-4	2.99E-5	– –	– –	– –
$\lvert E_{\text{kin},1}-E_{\text{kin},1}^{\text{MA}}\rvert$	5.2073	3.7918	2.5854	1.1783	0.5597	0.2700
Rate		0.4577	0.5525	0.5668	0.5370	0.5258
$\lvert E_{\text{int},1}-E_{\text{int},1}^{\text{MA}}\rvert$	2.3788	1.8432	1.2874	0.5894	0.2804	0.1367
Rate		0.3680	0.5178	0.5636	0.5359	0.5182
$\lvert E_1-E_1^{\text{MA}}\rvert$	2.8285	1.9487	1.2981	0.5890	0.2794	0.1333
Rate		0.5375	0.5861	0.5700	0.5380	0.5338
$\lvert\mu_1-\mu_1^{\text{MA}}\rvert$	0.4496	0.1055	0.0106	0.0003	– –	– –
E_1/μ_1	0.6854	0.6241	0.5813	0.5368	0.5175	0.5085
$E_{\text{int},1}/E_1$	0.4591	0.6042	0.7204	0.8628	0.9323	0.9664
$E_{\text{kin},1}/E_1$	0.5409	0.3958	0.2796	0.1372	0.0677	0.0336

Table 2.2: Convergence study of the matched asymptotic approximation for the BEC first excited state in 1D box potential when $\beta_1 \gg 1$.

$1/\beta_1$	1/50	1/100	1/400	1/1600	1/6400	1/12800
$\max\lvert\phi_5-\phi_5^{\text{MA}}\rvert$	0.1451	0.0437	0.0011	– –	– –	– –
$\lVert\phi_5-\phi_5^{\text{MA}}\rVert_{L^2}$	0.1072	0.0337	0.0009	– –	– –	– –
$\lvert E_{\text{kin},5}-E_{\text{kin},5}^{\text{MA}}\rvert$	68.955	60.445	36.230	16.711	7.7560	5.3607
Rate		0.1900	0.3692	0.5582	0.5537	0.5329
$\lvert E_{\text{int},5}-E_{\text{int},5}^{\text{MA}}\rvert$	25.409	24.679	17.477	8.3534	3.8800	2.6840
Rate		0.0421	0.2489	0.5325	0.5532	0.5317
$\lvert E_5-E_5^{\text{MA}}\rvert$	43.546	35.766	18.754	8.3580	3.8760	2.6766
Rate		0.2840	0.4657	0.5830	0.5543	0.5342
$\lvert\mu_5-\mu_5^{\text{MA}}\rvert$	18.137	11.087	1.2770	0.0046	0.0040	– –
E_5/μ_5	0.8541	0.7772	0.6325	0.5581	0.5269	0.5186
$E_{\text{int},5}/E_5$	0.1708	0.2867	0.5811	0.7919	0.8977	0.9281
$E_{\text{kin},5}/E_5$	0.8292	0.7133	0.4189	0.2081	0.1023	0.0719

Table 2.3: Convergence study of the matched asymptotic approximation for the BEC fifth excited state in 1D box potential when $\beta_1 \gg 1$.

2.2.1.5 Extension to high dimensions

The matched asymptotic approximation for the 1D ground state can be extended to d dimensions ($d>1$). Similar to the 1D case, we can find the approximation for the ground state in d dimensions with $\boldsymbol{x}=(x_1,\cdots,x_d)^T$ as

$$\begin{aligned}\phi_g(\boldsymbol{x}) &\approx \phi_g^{\text{MA}}(\boldsymbol{x}) \\ &= \sqrt{\frac{\mu_g^{\text{MA}}}{\beta_d}}\prod_{j=1}^{d}\left[\tanh\left(\sqrt{\mu_g^{\text{MA}}}x_j\right)+\tanh\left(\sqrt{\mu_g^{\text{MA}}}(1-x_j)\right)-\tanh\left(\sqrt{\mu_g^{\text{MA}}}\right)\right].\end{aligned} \tag{2.55}$$

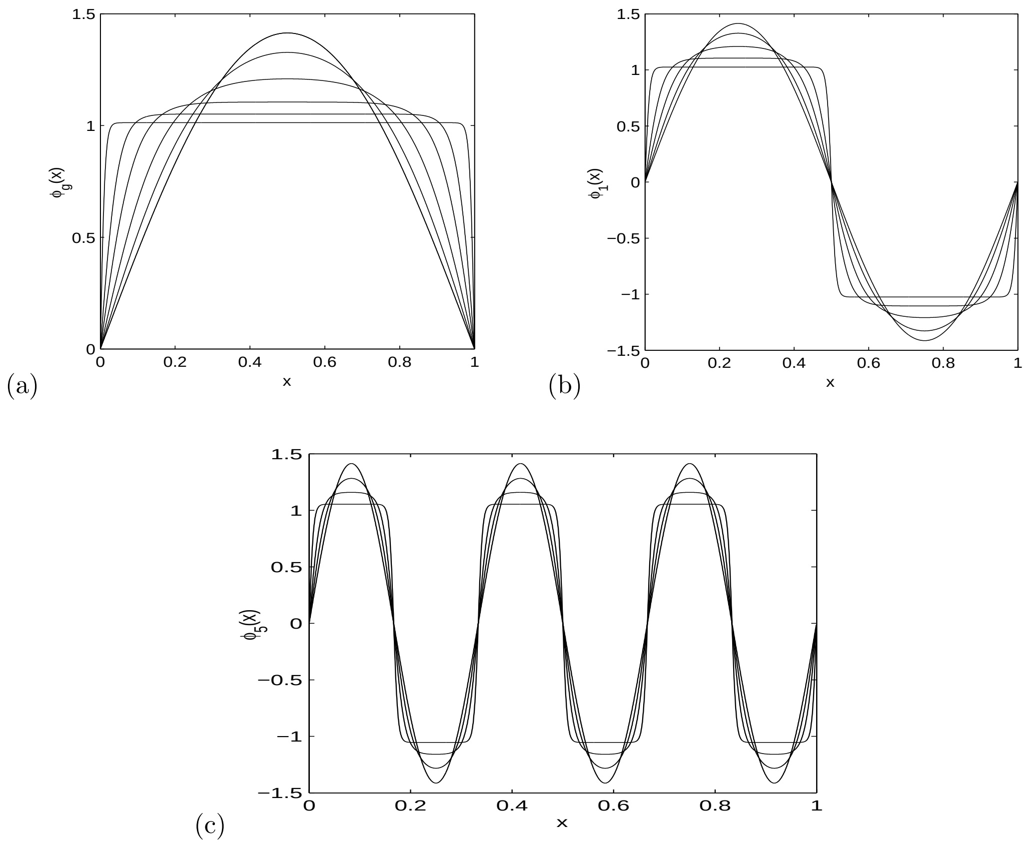

Figure 2.1: Ground state and excited states of BEC in 1D box potential for increasing β_1 (in the order of decreasing peak). (a) Ground state for $\beta_1 = 0, 6.25, 25, 100, 400, 6400$; (b) first excited state for $\beta_1 = 0, 25, 100, 400, 6400$; (c) fifth excited state for $\beta_1 = 0, 400, 1600, 12800$.

β_1	0	25	100	400	1600	6400	25600
E_g	4.9348	21.623	65.547	228.77	855.38	3308.7	13015
E_1	19.739	37.689	86.493	262.19	915.08	3421.5	13235
E_2	44.413	62.765	114.45	300.98	979.42	3538.7	13458
E_3	78.956	97.473	150.76	345.97	1048.8	3660.3	13686
E_4	123.37	141.97	196.17	397.99	1123.5	3786.6	13917
E_5	177.65	196.30	251.06	457.80	1203.9	3917.7	14153
μ_g	4.9348	37.201	122.10	442.05	1682.0	6562.0	25922
μ_1	19.739	54.990	148.80	488.40	1768.2	6728.1	26248
μ_2	44.413	80.758	180.96	539.34	1858.7	6898.3	26578
μ_3	78.956	151.77	219.96	595.21	1953.6	7072.8	26912
μ_4	123.37	160.42	267.06	656.48	2053.1	7251.6	27251
μ_5	177.65	214.83	323.03	723.84	2157.4	7434.7	27593

Table 2.4: Energies and chemical potentials for the ground state and the first five excited states of BEC in 1D box potential.

Substituting (2.55) into (2.20), we obtain

$$1 = \int_{(0,1)^d} |\phi_g^{\mathrm{MA}}(\boldsymbol{x})|^2 d\boldsymbol{x} \approx \frac{\mu_g^{\mathrm{MA}}}{\beta_d}\left(1 - \frac{2}{\sqrt{\mu_g^{\mathrm{MA}}}}\right)^d. \tag{2.56}$$

Solving (2.56) yields an approximation for the chemical potential when $\beta_d \gg 1$, i.e.

$$\mu_g \approx \mu_g^{\mathrm{MA}} = \beta_d + 2d\sqrt{\beta_d + d(2-d)} + 2d, \qquad d > 1. \tag{2.57}$$

Similarly, the approximations for different energies of the ground state are obtained as follows:

$$E_{\mathrm{kin},g} \approx E_{\mathrm{kin},g}^{\mathrm{MA}} = \frac{2d}{3}\sqrt{\beta_d + d(2-d)} + \frac{2d}{3}(d+2), \tag{2.58}$$

$$E_{\mathrm{int},g} \approx E_{\mathrm{int},g}^{\mathrm{MA}} = \frac{\beta_d}{2} + \frac{2d}{3}\sqrt{\beta_d + d(2-d)} + \frac{1}{3}d(1-d), \qquad d > 1, \tag{2.59}$$

$$E_g \approx E_g^{\mathrm{MA}} = \frac{\beta_d}{2} + \frac{4d}{3}\sqrt{\beta_d + d(2-d)} + \frac{1}{3}d(d+5). \tag{2.60}$$

2.2.2 Non-uniform potential

In this section, we will find the energy and chemical potential asymptotics up to $o(1)$ in terms of β_d for a BEC confined within a non-uniform external potential, i.e. $V_d(\boldsymbol{x}) \neq 0$ and $\Omega = \mathbb{R}^d$ in (2.19) [17]. When $\beta_d \gg 1$, we can ignore the kinetic energy term in the GPE (2.19) and derive the Thomas-Fermi (TF) approximation:

$$\mu_g^{\mathrm{TF}}\ \phi_g^{\mathrm{TF}}(\boldsymbol{x}) = V_d(\boldsymbol{x})\phi_g^{\mathrm{TF}}(\boldsymbol{x}) + \beta_d|\phi_g^{\mathrm{TF}}(\boldsymbol{x})|^2\phi_g^{\mathrm{TF}}(\boldsymbol{x}), \qquad \boldsymbol{x} \in \mathbb{R}^d. \tag{2.61}$$

Solving (2.61), we obtain the TF approximation for the ground state:

$$\phi_g^{\mathrm{TF}}(\boldsymbol{x}) = \begin{cases} \sqrt{\left(\mu_g^{\mathrm{TF}} - V_d(\boldsymbol{x})\right)/\beta_d}, & V_d(\boldsymbol{x}) \leq \mu_g^{\mathrm{TF}}, \\ 0, & \text{otherwise,} \end{cases} \tag{2.62}$$

where μ_g^{TF} is determined from the normalization condition

$$\|\phi_g^{\mathrm{TF}}\|^2 := \int_{\mathbb{R}^d} |\phi_g^{\mathrm{TF}}(\boldsymbol{x})|^2\ d\boldsymbol{x} = 1. \tag{2.63}$$

Due to the fact that $\phi_g^{\mathrm{TF}}(\boldsymbol{x})$ is not differentiable at $V_d(\boldsymbol{x}) = \mu_g^{\mathrm{TF}}$, $E(\phi_g^{\mathrm{TF}}) = \infty$ and $E_{\mathrm{kin}}(\phi_g^{\mathrm{TF}}) = \infty$. Therefore, one cannot use the definitions (2.15) and (2.17) to define the total energy and kinetic energy of the TF approximation (2.62). Noticing (2.17) and (2.21), as proposed in [12, 18, 21], we use the following way to calculate the total energy and the kinetic energy:

$$E_g^{\rm TF} \approx E_g = E(\phi_g) = \mu(\phi_g) - E_{\rm int}(\phi_g) \approx \mu_g^{\rm TF} - E_{{\rm int},g}^{\rm TF}\ , \tag{2.64}$$

$$E_{{\rm kin},g}^{\rm TF} \approx E_{{\rm kin},g} = E(\phi_g) - E_{\rm int}(\phi_g) - E_{\rm pot}(\phi_g) \approx E_g^{\rm TF} - E_{{\rm int},g}^{\rm TF} - E_{{\rm pot},g}^{\rm TF}\ , \tag{2.65}$$

where

$$E_{{\rm int},g}^{\rm TF} = E_{\rm int}(\phi_g^{\rm TF}), \qquad E_{{\rm pot},g}^{\rm TF} = E_{\rm pot}(\phi_g^{\rm TF}).$$

2.2.2.1 Harmonic oscillator potential

For a 1D BEC in a harmonic oscillator potential, we take $d = 1$ and $V_1(x) = \gamma_x^2 x^2/2$ with $\gamma_x > 0$ in (2.62). Substituting (2.62) into (2.63), we obtain

$$1 = \int_{-\infty}^{\infty} |\phi_g^{\rm TF}|^2\, dx = \frac{2}{3}\frac{\left(2\mu_g^{TF}\right)^{3/2}}{\beta_1\gamma_x}. \tag{2.66}$$

Solving (2.66) yields the chemical potential asymptotic when $\beta_1 \gg 1$,

$$\mu_g \approx \mu_g^{\rm TF} = \frac{1}{2}\left(\frac{3\beta_1\gamma_x}{2}\right)^{2/3}. \tag{2.67}$$

Substituting (2.62) in this case into (2.16), we obtain the Thomas-Fermi energies

$$E_{{\rm int},g} \approx E_{{\rm int},g}^{\rm TF} = \frac{1}{5}\left(\frac{3\beta\gamma_x}{2}\right)^{2/3}, \qquad E_{{\rm pot},g} \approx E_{\rm pot,g}^{\rm TF} = \frac{1}{10}\left(\frac{3\beta\gamma_x}{2}\right)^{2/3}, \tag{2.68}$$

$$E_g \approx E_g^{\rm TF} = \frac{3}{10}\left(\frac{3\beta\gamma_x}{2}\right)^{2/3}, \qquad E_{{\rm kin},g} \approx E_{{\rm kin},g}^{\rm TF} = 0. \tag{2.69}$$

From (2.67)–(2.69), it can be easily found that

$$\lim_{\beta_1\to\infty}\frac{E_g}{\mu_g} = \frac{3}{5}, \qquad \lim_{\beta_1\to\infty}\frac{E_{{\rm int},g}}{E_g} = \frac{2}{3}, \qquad \lim_{\beta_1\to\infty}\frac{E_{{\rm pot},g}}{E_g} = \frac{1}{3}. \tag{2.70}$$

To verify the TF approximation (2.62) in this case and the TF energies (2.67)–(2.70) , we compute and list the errors between the numerically calculated ground state and its TF approximation in Table 2.5. In Table 2.6, we list the energies and chemical potentials of the ground state and the first excited state. Furthermore, Figure 2.2 shows the ground state and the first excited state for different β_1.

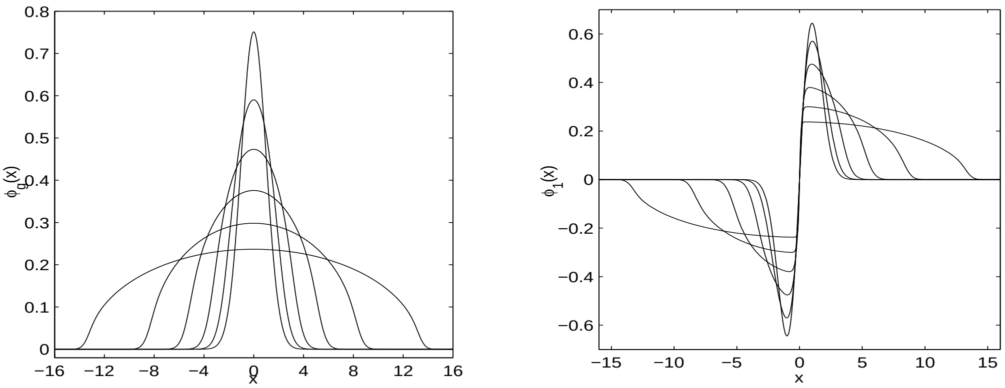

Figure 2.2: Ground state (left) and first excited state (right) of BEC in 1D harmonic oscillator potential $V_1(x) = x^2/2$ for $\beta_1 = 0, 6.25, 25, 100, 400, 1600$ (in the order of decreasing peaks).

$1/\beta_1$	1/100	1/200	1/400	1/800	1/1600	1/6400
$\max\vert\phi_g - \phi_g^{\rm TF}\vert$	0.0788	0.0605	0.0464	0.0355	0.0272	0.0159
Rate		0.3807	0.3836	0.3840	0.3852	0.3872
$\Vert\phi_g - \phi_g^{\rm TF}\Vert_{L^2}$	0.0571	0.04230	0.0312	0.0230	0.0170	0.0092
Rate		0.4350	0.4371	0.4389	0.4404	0.4427
$\vert E_{{\rm pot},g} - E_{{\rm pot},g}^{\rm TF}\vert$	0.0246	0.0171	0.0118	0.0080	0.0054	0.0023
Rate		0.5238	0.5383	0.5528	0.5687	0.6196
$\vert E_{{\rm int},g} - E_{{\rm int},g}^{\rm TF}\vert$	0.0204	0.0144	0.0101	0.0070	0.0047	0.0021
Rate		0.4980	0.5167	0.5348	0.5531	0.6051
$E_{{\rm kin},g} - 0$	0.0350	0.0245	0.0170	0.0117	0.0080	0.0037
Rate		0.5134	0.5267	0.5381	0.5478	0.5599
$\vert E_g - E_g^{\rm TF}\vert$	0.0392	0.0272	0.0187	0.0128	0.0087	0.0039
Rate		0.5280	0.5394	0.5492	0.5582	0.5725
$\vert\mu_g - \mu_g^{\rm TF}\vert$	0.0188	0.0128	0.0086	0.0058	0.0039	0.0019
Rate		0.5613	0.5651	0.5659	0.5638	0.5329
E_g/μ_g	0.6020	0.6009	0.6004	0.6002	0.6001	0.6000
$E_{{\rm int},g}/E_g$	0.6612	0.6643	0.6656	0.6662	0.6665	0.6666
$E_{{\rm pot},g}/E_g$	0.3347	0.3339	0.3336	0.3334	0.3334	0.3333

Table 2.5: Convergence study for the TF approximation of BEC ground state in 1D harmonic oscillator potential $V_1(x) = x^2/2$.

β_1	0	25	100	400	1600	6400	25600
E_g	0.5000	3.4402	8.5085	21.360	55.786	135.51	341.46
E_1	1.5000	4.2115	9.2419	22.078	54.497	136.22	342.17
μ_g	0.5000	5.6421	14.134	35.578	89.632	225.85	569.10
μ_1	1.5000	6.3732	14.850	36.288	90.340	226.56	569.80

Table 2.6: Energies and chemical potentials of the ground state and the first excited state of a BEC in 1D harmonic oscillator potential $V_1(x) = x^2/2$.

From Tables 2.5&2.6 and Figure 2.2, we draw the following conclusions:

(1) The TF approximation converges to the ground state, when $\beta_1 \to \infty$, with convergence rate $\theta_1 = 2/5$, i.e.

$$\max|\phi_g - \phi_g^{\rm TF}| = O\left(\frac{\ln\beta_1}{\beta_1^{\theta_1}}\right), \qquad \|\phi_g - \phi_g^{\rm TF}\|_{L^2} = O\left(\frac{\ln\beta_1}{\beta_1^{\theta_1}}\right).$$

(2) The TF approximation (2.62) in a harmonic oscillator potential and (2.67)–(2.70) are verified. Furthermore, the numerical results suggest a convergence rate of $\theta_2 = 2/3$ for the energies and chemical potential in the following way:

$$\begin{aligned} &E_{{\rm kin},g} = O\left(\frac{\ln\beta_1}{\beta_1^{\theta_2}}\right),\ E_{{\rm int},g} = E_{{\rm int},g}^{\rm TF} + O\left(\frac{\ln\beta_1}{\beta_1^{\theta_2}}\right),\ E_{{\rm pot},g} = E_{{\rm pot},g}^{\rm TF} + O\left(\frac{\ln\beta_1}{\beta_1^{\theta_2}}\right), \\ &E_g = E_g^{\rm TF} + O\left(\frac{\beta_1}{\beta_1^{\theta_2}}\right), \quad \mu_g = \mu_g^{\rm TF} + O\left(\frac{\beta_1}{\beta_1^{\theta_2}}\right), \qquad \beta_1 \gg 1. \end{aligned}$$

(3) Interior layer is observed at $x = 0$ in the first excited state when $\beta_1 \gg 1$ and the width of the layer is $O(1/\beta_1^{1/3})$.

(4) The energies and chemical potentials of the ground and the first excited states are in the same order for any $\beta_1 \geq 0$, i.e.

$$E(\phi_g) < E(\phi_1) \quad \Longrightarrow \quad \mu(\phi_g) < \mu(\phi_1).$$

2.2.2.2 Double well potential

While considering a 1D BEC in a double well potential, we take $d = 1$ and $V_1(x) = \gamma_x^4(x^2 - a^2)^2/2$ with $\gamma_x > 0$ and $a \geq 0$, in (2.62). Substituting (2.62) into (2.63) yields

$$1 = \int_{-\infty}^{\infty} |\phi_g^{\rm TF}(x)|^2\, dx = \frac{4}{15\beta_1\gamma_x}\left(6\mu_g^{\rm TF} + a^2\gamma_x^2\sqrt{2\mu_g^{\rm TF}} - 2a^4\gamma_x^4\right)\sqrt{\sqrt{2\mu_g^{\rm TF}} + a^2\gamma_x^2}. \tag{2.71}$$

Solving (2.71), we get the TF approximation for the chemical potential,

$$\mu_g \approx \mu_g^{\rm TF} = \frac{1}{8}(50\beta_1^2\gamma_x^2)^{2/5} - \frac{a^2\gamma_x^2}{6}(50\beta_1^2\gamma_x^2)^{1/5} + \frac{7a^4\gamma_x^4}{18}. \tag{2.72}$$

Substituting (2.62) in this case into (2.16) gives the Thomas-Fermi energies

$$E_{\text{int},g} \approx E_{\text{int},g}^{\text{TF}} = \frac{1}{18}\left(50\beta_1^2\gamma_x^2\right)^{2/5} - \frac{a^2\gamma_x^2}{21}\left(50\beta_1^2\gamma_x^2\right)^{1/5}, \tag{2.73}$$

$$E_{\text{pot},g} \approx E_{\text{pot},g}^{\text{TF}} = \frac{1}{72}\left(50\beta_1^2\gamma_x^2\right)^{2/5} - \frac{a^2\gamma_x^2}{14}\left(50\beta_1^2\gamma_x^2\right)^{1/5} + \frac{7a^4\gamma_x^4}{18}, \tag{2.74}$$

$$E_g \approx E_g^{\text{TF}} = \frac{5}{72}\left(50\beta_1^2\gamma_x^2\right)^{2/5} - \frac{5}{42}a^2\gamma_x^2\left(50\beta_1^2\gamma_x^2\right)^{1/5} + \frac{7a^4\gamma_x^4}{18}, \tag{2.75}$$

$$E_{\text{kin},g} \approx E_{\text{kin},g}^{\text{TF}} = 0. \tag{2.76}$$

From (2.72)–(2.75), we obtain

$$\lim_{\beta_1\to\infty}\frac{E_g}{\mu_g} = \frac{5}{9}, \qquad \lim_{\beta_1\to\infty}\frac{E_{\text{int},g}}{E_g} = \frac{4}{5}, \qquad \lim_{\beta_1\to\infty}\frac{E_{\text{pot},g}}{E_g} = \frac{1}{5}. \tag{2.77}$$

To verify the TF approximation (2.62) in the double well and the TF energies (2.72)–(2.77), we compute and list the errors between the numerically computed ground state and its TF approximation in Table 2.7. Table 2.8 lists the energies and chemical potentials of the ground and the first excited states, for the case of $d = 1$ and $V_1(x) = (x^2 - 3^2)^2/2$ in (2.19). Furthermore, Figure 2.3 shows the ground state and the first excited state for different β_1.

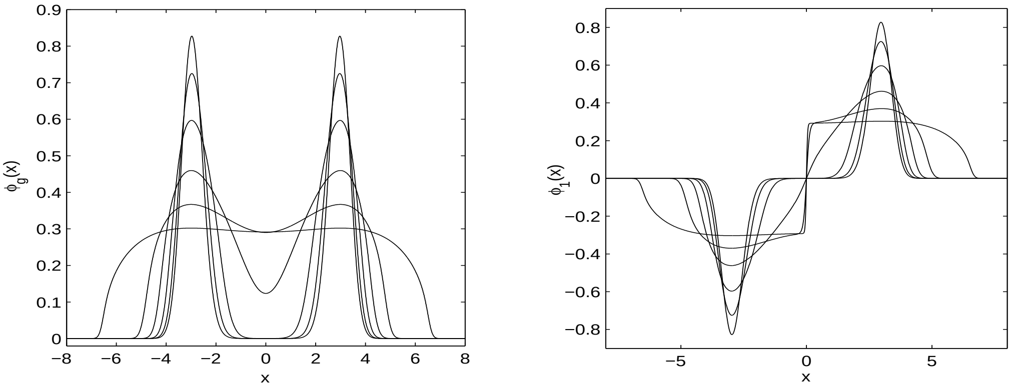

Figure 2.3: Ground state (left) and first excited state (right) of BEC in type I double well potential $V_1(x) = (x^2 - 3^2)/2$ for $\beta_1 = 0, 12.5, 50, 200, 800, 6400$ (in the order of decreasing peaks).

From Tables 2.7&2.8 and Figure 2.3, conclusions (1)–(4) in section 2.2.2.1 are still valid except that θ_1, θ_2 are to be replaced by $\theta_1 = 2/5$, $\theta_2 = 2/5$ and the width of the interior layers is $O(1/\beta_1^{3/10})$.

[Remark] In physics literature [33, 67], another type of double well potential, i.e. $d = 1$ and $V_1(x) = \gamma_x^2(|x| - a)^2/2$ with $\gamma_x > 0$ and $a \geq 0$ is also used. In this case, the following TF approxi-

$1/\beta_1$	1/100	1/400	1/1600	1/6400	1/25600	1/51200
$\max\lvert\phi_g - \phi_g^{\rm TF}\rvert$	0.1260	0.0915	0.0634	0.0429	0.0286	0.0233
Rate		0.2312	0.2638	0.2824	0.2921	0.2950
$\lVert\phi_g - \phi_g^{\rm TF}\rVert_{L^2}$	0.2238	0.0495	0.0254	0.0149	0.0087	0.0066
Rate		1.0888	0.4806	0.3865	0.3892	0.3958
$\lvert E_{{\rm pot},g} - E_{{\rm pot},g}^{\rm TF}\rvert$	18.824	8.7812	4.0019	2.0167	1.0758	0.7963
Rate		0.5500	0.5669	0.4943	0.4533	0.4340
$\lvert E_{{\rm int},g} - E_{{\rm int},g}^{\rm TF}\rvert$	6.0436	3.1554	1.3089	0.6176	0.3157	0.2303
Rate		0.4688	0.6347	0.5418	0.4841	0.4550
$E_{{\rm kin},g} - 0$	0.3982	0.1460	0.0854	0.0565	0.0376	0.0306
Rate		0.7238	0.3868	0.2980	0.2938	0.2972
$\lvert E_g - E_g^{\rm TF}\rvert$	12.382	5.4797	2.6076	1.3426	0.7225	0.5355
Rate		0.5880	0.5357	0.4788	0.4470	0.4321
$\lvert\mu_g - \mu_g^{\rm TF}\rvert$	6.3386	2.3244	1.2986	0.7249	0.4067	0.3051
Rate		0.7237	0.4180	0.4206	0.4169	0.4147
E_g/μ_g	0.6212	0.6182	0.5671	0.5482	0.5465	0.5476
$E_{{\rm int},g}/E_g$	0.6099	0.6175	0.7632	0.8240	0.8297	0.8263
$E_{{\rm pot},g}/E_g$	0.3674	0.3789	0.2359	0.1758	0.1703	0.1737

Table 2.7: Convergence study of the TF approximation of BEC ground state in type I double well potential $V_1(x) = (x^2 - 3^2)^2/2$.

β_1	0	25	100	400	1600	3200	25600
E_g	2.9716	7.8639	17.555	40.357	105.56	320.41	1011.3
E_1	2.9716	7.8639	17.555	40.790	107.05	323.06	1015.3
μ_g	2.9716	11.990	28.261	65.277	186.14	584.43	1850.4
μ_1	2.9716	11.990	28.261	66.396	188.42	587.99	1855.5

Table 2.8: Energies and chemical potentials of the ground and the first excited states of a BEC in type I double well potential $V_1(x) = (x^2 - 3^2)^2/2$.

mations are obtained:

$$\mu_g \approx \mu_g^{\rm TF} = \frac{1}{2}\left(\frac{3\beta_1\gamma_x}{2}\right)^{2/3} - \frac{a\gamma_x}{2}\left(\frac{3\beta_1\gamma_x}{2}\right)^{1/3} + \frac{3}{8}a^2\gamma_x^2, \tag{2.78}$$

$$E_{{\rm int},g} \approx E_{{\rm int},g}^{\rm TF} = \frac{1}{5}\left(\frac{3\beta_1\gamma_x}{2}\right)^{2/3} - \frac{a\gamma_x}{8}\left(\frac{3\beta_1\gamma_x}{2}\right)^{1/3}, \tag{2.79}$$

$$E_{{\rm pot},g} \approx E_{{\rm pot},g}^{\rm TF} = \frac{1}{10}\left(\frac{3\beta_1\gamma_x}{2}\right)^{2/3} - \frac{a\gamma_x}{4}\left(\frac{3\beta_1\gamma_x}{2}\right)^{1/3} + \frac{3}{8}a^2\gamma_x^2, \tag{2.80}$$

$$E_g \approx E_g^{\rm TF} = \frac{3}{10}\left(\frac{3\beta_1\gamma_x}{2}\right)^{2/3} - \frac{3a\gamma_x}{8}\left(\frac{3\beta_1\gamma_x}{2}\right)^{1/3} + \frac{3}{8}a^2\gamma_x^2, \tag{2.81}$$

$$E_{{\rm kin},g} \approx E_{{\rm kin},g}^{\rm TF} = 0, \tag{2.82}$$

$$\lim_{\beta_1\to\infty}\frac{E_g}{\mu_g} = \frac{3}{5}, \qquad \lim_{\beta_1\to\infty}\frac{E_{{\rm int},g}}{E_g} = \frac{2}{3}, \qquad \lim_{\beta_1\to\infty}\frac{E_{{\rm pot},g}}{E_g} = \frac{1}{3}. \tag{2.83}$$

2.2.2.3 Optical lattice potential

For a 1D BEC in a harmonic plus optical lattice potential, we take $d = 1$ and $V_1(x) = \gamma_x^2 x^2/2 + k_x \sin^2(q_x x)$ in (2.62). Substituting (2.62) into (2.63) yields

$$1 = \int_{-\infty}^{\infty} |\phi_g^{\mathrm{TF}}(x)|^2 \, dx \approx \frac{1}{3\beta_1\gamma_x}\left(2\sqrt{(2\mu_g^{\mathrm{TF}})^3} - k_x\sqrt{2\mu_g^{\mathrm{TF}}}\right). \tag{2.84}$$

Solving (2.84), we get

$$\mu_g \approx \mu_g^{\mathrm{TF}} = \frac{1}{2}\left(\frac{3\beta_1\gamma_x}{2}\right)^{2/3} + \frac{k_x}{2}. \tag{2.85}$$

Substituting (2.62) in this case into (2.16) gives

$$E_{\mathrm{int},g} \approx E_{\mathrm{int},g}^{\mathrm{TF}} = \frac{1}{5}\left(\frac{3\beta_1\gamma_x}{2}\right)^{2/3}, \quad E_{\mathrm{pot},g} \approx E_{\mathrm{pot},g}^{\mathrm{TF}} = \frac{1}{10}\left(\frac{3\beta_1\gamma_x}{2}\right)^{2/3} + \frac{k_x}{2}, \tag{2.86}$$

$$E_g \approx E_g^{\mathrm{TF}} = \frac{3}{10}\left(\frac{3\beta_1\gamma_x}{2}\right)^{2/3} + \frac{k_x}{2}, \quad E_{\mathrm{kin},g} \approx E_{\mathrm{kin},g}^{\mathrm{TF}} = 0. \tag{2.87}$$

From (2.85)–(2.87), we obtain

$$\lim_{\beta_1\to\infty}\frac{E_g}{\mu_g} = \frac{3}{5}, \qquad \lim_{\beta_1\to\infty}\frac{E_{\mathrm{int},g}}{E_g} = \frac{2}{3}, \qquad \lim_{\beta_1\to\infty}\frac{E_{\mathrm{pot},g}}{E_g} = \frac{1}{3}. \tag{2.88}$$

To verify the approximation (2.62) in this case and the TF energies (2.85)–(2.88), we compute and list the errors between the numerically computed ground state and its TF approximation in Table 2.9. In Table 2.10, we list the energies and chemical potentials of the ground and the first excited states for $V_1(x) = x^2/2 + 25\sin^2(\pi x/4)$. Figure 2.4 shows the ground state and the first excited state for different β_1.

From Tables 2.9&2.10 and Figure 2.4, conclusions (1)–(4) in section 2.2.2.1 are valid except that θ_1, θ_2 are to be replaced by $\theta_1 = 2/5$, $\theta_2 = 2/3$ and the width of the interior layers is $O(1/\beta_1^{1/3})$.

2.2.2.4 Extension to general case

For a BEC in a general d-dimensional potential, $V_d(\boldsymbol{x}) = V_0(\boldsymbol{x}) + W(\boldsymbol{x})$ satisfying

$$V_0(\boldsymbol{x}) = \frac{1}{2}(\gamma_1^\alpha|x_1|^\alpha + \cdots + \gamma_d^\alpha|x_d|^\alpha), \qquad \lim_{|\boldsymbol{x}|\to\infty}\frac{W(\boldsymbol{x})}{V_0(\boldsymbol{x})} = 0, \tag{2.89}$$

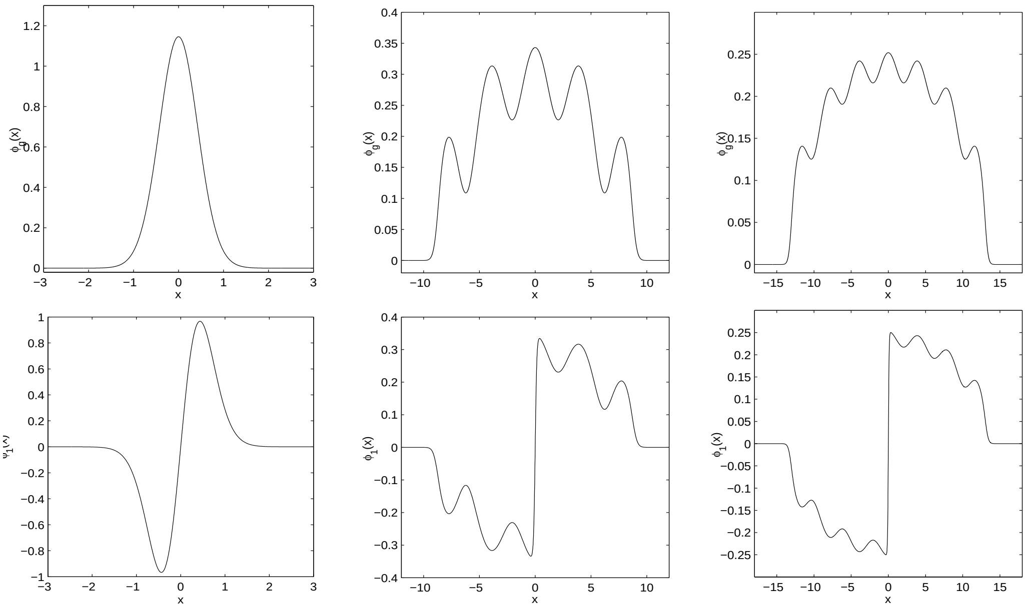

Figure 2.4: Ground state (upper row) and first excited state (lower row) of a BEC in optical lattice potential $V_1(x) = x^2/2 + 25\sin^2(\pi x/4)$ for $\beta_1 = 0$ (left column), $\beta_1 = 400$ (middle column) and $\beta_1 = 1600$ (right column).

$1/\beta_1$	1/100	1/400	1/1600	1/3200	1/25600
$\max\lvert\phi_g - \phi_g^{\mathrm{TF}}\rvert$	0.3963	0.1544	0.0699	0.0366	0.0190
Rate		0.6800	0.5717	0.9334	0.3647
$\lVert\phi_g - \phi_g^{\mathrm{TF}}\rVert_{L^2}$	0.8257	0.3471	0.1569	0.0952	0.0313
Rate		0.6251	0.5728	0.7208	0.5305
$\lvert E_{\mathrm{pot},g} - E_{\mathrm{pot},g}^{\mathrm{TF}}\rvert$	5.8815	2.2310	0.7943	0.3403	0.0857
Rate		1.1282	0.3160	1.2229	0.5203
$\lvert E_{\mathrm{int},g} - E_{\mathrm{int},g}^{\mathrm{TF}}\rvert$	1.8585	0.6681	0.1102	0.0638	0.0282
Rate		0.7380	1.3000	0.7885	0.8623
$E_{\mathrm{kin},g} - 0$	0.2928	0.0727	0.0193	0.0103	0.0022
Rate		1.0049	0.9567	0.9060	0.7357
$\lvert E_g - E_g^{\mathrm{TF}}\rvert$	3.7301	1.4902	0.6648	0.3936	0.1117
Rate		0.6619	0.5823	0.7562	0.6188
$\lvert\mu_g - \mu_g^{\mathrm{TF}}\rvert$	1.8716	0.8222	0.5547	0.4571	0.1400
Rate		0.6340	0.5934	0.5678	0.1793
E_g/μ_g	0.6967	0.6847	0.6460	0.6316	0.6086
$E_{\mathrm{int},g}/E_g$	0.4353	0.4604	0.5481	0.5832	0.6433
$E_{\mathrm{pot},g}/E_g$	0.5477	0.5373	0.4516	0.4167	0.3567

Table 2.9: Convergence study of the TF approximation of BEC ground state in optical lattice potential $V_1(x) = x^2/2 + 25\sin^2(\pi x/4)$.

with $\boldsymbol{x} = (x_1, \cdots, x_d)^T$, $\alpha > 0$, $\gamma_j > 0$, $1 \le j \le d$, substituting the TF approximation (2.62) into normalization condition (2.63) gives

$$1 = \int_{\mathbb{R}^d} |\phi_g^{\mathrm{TF}}(\boldsymbol{x})|^2 d\boldsymbol{x} \approx \frac{(2\mu_g^{\mathrm{TF}})^{(\alpha+d)/\alpha}}{2\beta_d \prod_{j=1}^{d} \gamma_{x_j}}\, C_{\alpha,d}, \tag{2.90}$$

β_1	0	25	100	400	1600	6400	25600
E_g	2.7447	9.7896	17.239	32.351	65.612	147.75	353.85
E_1	8.0708	12.382	18.884	33.438	66.468	148.51	354.58
μ_g	2.7447	13.595	24.744	47.247	101.57	237.99	581.46
μ_1	8.0708	15.192	25.868	48.041	102.34	238.72	582.18

Table 2.10: Energies and chemical potentials of the ground and the first excited states of a BEC in optical lattice potential $V_1(x) = x^2/2 + 25\sin^2(\pi x/4)$.

where $C_{\alpha,d}$ is given by

$$C_{\alpha,d} = \int_{\sum_{j=1}^{d}|x_j|^\alpha \le 1} \left(1 - 2\sum_{j=1}^{d}|x_j|^\alpha\right) d\boldsymbol{x}. \tag{2.91}$$

Solving (2.90) yields

$$\mu_g^{\mathrm{TF}} = \frac{1}{2}\left(\frac{2\beta_d \prod_{j=1}^{d}\gamma_{x_j}}{C_{\alpha,d}}\right)^{\alpha/(\alpha+d)}. \tag{2.92}$$

Substituting (2.62) into (2.16), we get the Thomas-Fermi energies as

$$E_{\mathrm{int},g} \approx E_{\mathrm{int},g}^{\mathrm{TF}} = \frac{D_{\alpha,d}}{4C_{\alpha,d}}\left(\frac{2\beta_d \prod_{j=1}^{d}\gamma_{x_j}}{C_{\alpha,d}}\right)^{\alpha/(\alpha+d)}, \tag{2.93}$$

$$E_{\mathrm{pot},g} \approx E_{\mathrm{pot},g}^{\mathrm{TF}} = \frac{C_{\alpha,d} - D_{\alpha,d}}{2C_{\alpha,d}}\left(\frac{2\beta_d \prod_{j=1}^{d}\gamma_{x_j}}{C_{\alpha,d}}\right)^{\alpha/(\alpha+d)}, \tag{2.94}$$

$$E_g \approx E_g^{\mathrm{TF}} = \frac{G_{\alpha,d}}{4C_{\alpha,d}}\left(\frac{2\beta_d \prod_{j=1}^{d}\gamma_{x_j}}{C_{\alpha,d}}\right)^{\alpha/(\alpha+d)}, \quad G_{\alpha,d} = 2C_{\alpha,d} - D_{\alpha,d}, \tag{2.95}$$

where $D_{\alpha,d}$ is given by

$$D_{\alpha,d} = \int_{\sum_{j=1}^{d}|x_j|^\alpha \le 1} \left(1 - 2\sum_{j=1}^{d}|x_j|^\alpha\right)^2 d\boldsymbol{x}. \tag{2.96}$$

From (2.92)–(2.95), we obtain

$$\lim_{\beta_d\to\infty}\frac{E_g}{\mu_g} = \frac{G_{\alpha,d}}{2C_{\alpha,d}}, \quad \lim_{\beta_d\to\infty}\frac{E_{\mathrm{int},g}}{E_g} = \frac{D_{\alpha,d}}{G_{\alpha,d}}, \quad \lim_{\beta_d\to\infty}\frac{E_{\mathrm{pot},g}}{E_g} = \frac{2(C_{\alpha,d} - D_{\alpha,d})}{G_{\alpha,d}}. \tag{2.97}$$

2.3 Condensate Ground State with Attractive Interaction in One Dimension

Various studies have been carried out to investigate the ground state of Bose-Einstein condensate, in particular the condensate with repulsive interaction, whose ground state is unique and is symmetric in a symmetric trapping potential [76]. As discussed in section 2.2, the ground state of a weakly interacting condensate may be approximated by non-interacting BEC ground state, while the ground state of a strongly repulsively interacting condensate can be obtained asymptotically through the Thomas-Fermi approximation. For condensate in which particles interact attractively, the ground state may not be unique, depending on the type of the confining potential. In spite of the symmetry of the external trapping potential, the symmetry of the stationary states may be broken when the interaction becomes large.

There are two types of trapping potentials allow the analytical solution of the GPE (2.19) under attractive interaction ($\beta < 0$) to be studied up to date: uniform potential subject to periodic boundary conditions and double square well potential subject to zero boundary conditions. Condensate in a ring shape uniform potential can be described by a 1D GPE,

$$\mu\phi(\theta) = -\frac{1}{2}\frac{d^2}{d\theta^2}\phi(\theta) + \beta|\phi(\theta)|^2\phi(\theta), \quad 0 \le \theta < 2\pi, \tag{2.98}$$

with

$$\int_0^{2\pi} |\phi(\theta)|^2 \, d\theta = 1. \tag{2.99}$$

The condensate is uniformly distributed for both non-interacting case ($\beta = 0$) and repulsively interacting case ($\beta > 0$). For attractively interacting condensate, the translational symmetry is spontaneously broken when $\beta < -2\pi$ and the lowest energy stationary state is a bright soliton [71, 73]. The ground state can be expressed in terms of the Jacobian elliptic functions [71]. For attractive BEC in a 1D double square well, Mahmud et al. [79] have studied the analytical solutions through the Jacobi elliptic functions and Zin et al. [121] have derived the exact condition for the critical value β_c at which the symmetry breaking state starts emerging as the ground state. An approximate formula for β_c was also derived from a simple variational method, for the case of deep double square well [121].

In this section, we will study the ground state of attractively interacting condensates in another two generally used double well potentials and investigates the effect of the interplay between the interparticle interaction and the depth of the double well on the symmetry of the condensate ground state. For clarity, the negative sign of the interaction parameter β, which corresponds to the attractive interaction will be included in the GPE in this section. Furthermore, for simplicity, only 1D Bose-condensed system will be studied. The GPE (2.19) is therefore modified into

$$\mu\,\phi(x) = -\frac{1}{2}\frac{d^2}{dx^2}\phi(x) + V(x)\,\phi(x) - \beta|\phi(x)|^2\phi(x), \quad x \in \mathbb{R}, \tag{2.100}$$

for a 1D BEC. Here, the wavefunction is normalized to 1 and $\beta > 0$ denotes the attractive interaction. The total energy per particle is

$$\begin{aligned} E(\phi) &= E_{\text{kin}}(\phi) + E_{\text{pot}}(\phi) + E_{\text{int}}(\phi) \\ &= \int_{\mathbb{R}} \frac{1}{2}|\frac{d\phi}{dx}|^2 + V|\phi|^2 - \frac{\beta}{2}|\phi|^4\,dx, \end{aligned} \tag{2.101}$$

where E_{kin}, E_{pot} and E_{int} denote the kinetic energy, potential energy, and interaction energy, respectively. The chemical potential, μ, is given by

$$\begin{aligned} \mu(\phi) &= \int_{\mathbb{R}} \frac{1}{2}|\frac{d\phi}{dx}|^2 + V|\phi|^2 - \beta|\phi|^4\,dx \\ &= E - \int_{\mathbb{R}} \frac{\beta}{2}|\phi|^4\,dx. \end{aligned} \tag{2.102}$$

2.3.1 Harmonic oscillator potential

We first study the attractively interacting condensate in a 1D harmonic oscillator potential

$$V(x) = \frac{1}{2}\gamma^2 x^2. \tag{2.103}$$

For non-interacting particles, the ground state is a Gaussian wave packet. For interacting particles, we assume that the ground state takes a similar kind of Gaussian profile,

$$f(x) = \frac{1}{\sqrt{\sigma\sqrt{\pi}}}\exp\left(-\frac{x^2}{2\sigma^2}\right), \tag{2.104}$$

whose L_2 norm is 1 and σ is the condensate width. The energy of the trial wavefunction (2.104) is

$$E = \frac{1}{4\sigma^2} + \frac{\gamma^2\sigma^2}{4} - \frac{\beta}{2\sqrt{2\pi}\sigma}. \tag{2.105}$$

It can be observed that the minimizer of the energy (2.105) always exists. Using the variational approach, σ that minimizes the energy is found to satisfy

$$\sigma^4 + \frac{1}{\gamma^2}\left(\frac{\beta}{\sqrt{2\pi}}\sigma - 1\right) = 0. \tag{2.106}$$

In fact, a Gaussian ansatz with variational method has been applied in several articles to study the stationary states as well as the dynamical stability of attractively interacting BEC in a 3D harmonic oscillator potential [92, 93, 101, 106]. In the experiment conducted for the attractively interacting BEC, the condensate is found to collapse when the number of particles is larger than a critical value [27]. The Gaussian ansatz applied to the GPE provided an approximation to this critical value [93, 101]. Inelastic collision and three-body collisions which are not included in the GPE also contribute to the collapse. The collapse of the BEC, however, does not appear in one dimension under the Gaussian ansatz, since the ground state of (2.105) always exists.

Two regimes are considered under the Gaussian ansatz (2.104):

(i) **Non-interacting regime**: When $\beta = 0$, the solution of (2.106) is the exact solution of a linear Schrödinger equation with a harmonic oscillator potential, i.e.

$$\sigma = \frac{1}{\sqrt{\gamma}}, \quad E = \frac{\gamma}{2}. \tag{2.107}$$

(ii)**Weakly interacting regime**: When $\beta \sim 1$, the solution of (2.106) may be approximated by σ of non-interacting system and we have

$$\sigma \sim \frac{1}{\sqrt{\gamma}}, \quad E \sim \frac{\gamma}{2} - \frac{\beta}{2}\sqrt{\frac{\gamma}{2\pi}}. \tag{2.108}$$

Other than case (i) and case (ii), another regime that is the strongly attractively interacting regime ($\beta \gg 1$) should be considered. In this regime, the potential energy is relatively smaller than the kinetic energy and the interacting energy. It can be neglected near the center of the trap which is occupied by a large fraction of condensate. By introducing two new variables $X = \sqrt{-\mu}x$ and

$\Phi = \sqrt{\frac{-\mu}{\beta}}\phi$ and ignoring the trapping potential, the GPE (2.100) is reduced to

$$-\frac{1}{2}\Phi_{XX}(X) - |\Phi(X)|^2\Phi(X) + \Phi(X) = 0, \quad X \in \mathbb{R}, \tag{2.109}$$

The solution of the equation above is

$$\Phi(X) = \sqrt{2}\,\mathrm{sech}(\sqrt{2}X), \tag{2.110}$$

and the solution of the GPE (2.100) is a bright soliton

$$\phi(x) = \sqrt{\frac{-2\mu}{\beta}}\,\mathrm{sech}\left(\sqrt{-2\mu}x\right), \tag{2.111}$$

where the chemical potential μ, as determined from the normalization of the wavefunction, and the energy are

$$\mu = -\frac{\beta^2}{8}, \quad E = -\frac{\beta^2}{24}. \tag{2.112}$$

Table 2.11 displays the energy approximations of the condensate ground state with different interacting strength as well as the numerical solution of the GPE. For $\beta < 5.0$, the Gaussian ansatz (2.104) works well in approximating the ground state. For $\beta > 5.0$, the interaction is strong enough such that the trapping potential plays less significant role and that the ground state is a sech soliton.

2.3.2 Symmetry breaking state of weakly interacting condensate in double well potential

A class of widely studied trapping potential other than the harmonic oscillator trap is the double well potential. We consider double well potentials of type I,

$$V(x) = \frac{1}{2}\gamma^4\left(x^2 - a^2\right)^2, \tag{2.113}$$

and of type II,

$$V(x) = \frac{1}{2}\gamma^2\left(|x| - a\right)^2, \tag{2.114}$$

β	E_{num}	E_{var}	$E_{\beta\sim 1}$	E_{sech}
0	0.5000	0.5000	-	-
0.1	0.4799	0.4800	0.4801	-
0.2	0.4597	0.4597	0.4601	-
0.5	0.3974	0.3976	0.4003	-
1.0	0.2882	0.2875	0.3005	-
2.0	0.0458	0.0515	0.1011	0.1667
5.0	-0.9801	-0.9353	-0.4974	-1.0417
10.0	-4.1503	-3.9632	-1.4947	-4.1667
20.0	-16.6626	-15.9116	-	-16.6667
50.0	-104.1600	-99.4712	-	-104.1667
100.0	-416.6665	-397.8872	-	-416.6667

Table 2.11: Energies of an attractively interacting BEC in harmonic potential $V(x) = \frac{1}{2}x^2$. (E_{num}: numerical solution from the GPE (2.100); E_{var}: numerical solution from variational method (2.106); $E_{\beta\sim 1}$: weakly interacting energy approximation as in (2.108); E_{sech}: strongly interacting energy approximation as in (2.112)).

where $\gamma > 0$ measures the height of the well and $\pm a$ are the centers of the double well, both assumed to be $O(1)$. For the dynamics of attractively interacting condensate in the double well (2.113), it is known that they exhibit the self-trapping property, in spite of the symmetry of the trap [4, 82, 113]. In their stationary states, a similar property, the existence of symmetry breaking states, is observed in the solutions of the GPE [45]. In order to investigate the energy ranking of a positive symmetric state and a positive symmetry breaking state, we consider two regimes characterized by different strength of interaction, and carry out some analytical studies to these low-lying energy states. Condensates in non-interacting and weakly interacting regime will be studied in this section, while those in strongly interacting regime will be studied in the next section.

For a system of non-interacting atoms or weakly interacting atoms, the following normalized trial wavefunction is taken to approximate the positive stationary solution of the GPE (2.100),

$$\phi_{\text{trial}}(x) = Cf(x+\kappa) + Df(x-\kappa), \tag{2.115}$$

where f is the Gaussian function defined in (2.104) and coefficients C and D satisfy

$$C^2 + D^2 + 2CDe^{-\frac{\kappa^2}{\sigma^2}} = 1. \tag{2.116}$$

Such approximation is justified by the fact that the potential near $x = \pm a$ can be approximated by a harmonic potential with frequency $2\gamma^2 a$ for type I double well and by a harmonic potential with frequency γ for type II double well.

2.3.2.1 Type I double well potential

The energy functionals of the trial wavefunction (2.115) in type I double well (2.113) are

$$E_{\text{kin}} = \frac{1}{4\sigma^2}\left[1 - 4CDe^{-\frac{\kappa^2}{\sigma^2}}\left(\frac{\kappa^2}{\sigma^2}\right)\right], \tag{2.117}$$

$$E_{\text{pot}} = \frac{1}{2}\gamma^4\left[a^4 - a^2\sigma^2 + \frac{3}{4}\sigma^4 + (C^2+D^2)\left((3\sigma^2 - 2a^2)\kappa^2 + \kappa^4\right)\right], \tag{2.118}$$

$$E_{\text{int}} = -\frac{\beta}{2\sqrt{2\pi}\sigma}\left[C^4 + D^4 + 6C^2D^2e^{-\frac{2\kappa^2}{\sigma^2}} + 4CD(C^2+D^2)e^{-\frac{3\kappa^2}{2\sigma^2}}\right]. \tag{2.119}$$

We consider the case when the two Gaussian profiles are well separated, i.e. $a \gg \sigma$, or equivalently $\kappa \gg \sigma$, since the condensate is expected to localize around $\pm a$ where the trapping potential is minimum. By neglecting the term $e^{-\frac{\kappa^2}{\sigma^2}}$, the total energy can be estimated by

$$E \sim \frac{1}{4\sigma^2} + \frac{1}{2}\gamma^4\left[a^4 - a^2\sigma^2 + \frac{3}{4}\sigma^4 + (3\sigma^2 - 2a^2)\kappa^2 + \kappa^4\right] - \frac{\beta}{2\sqrt{2\pi}\sigma}(C^4 + D^4), \tag{2.120}$$

where C and D satisfy the normalization condition

$$C^2 + D^2 \sim 1. \tag{2.121}$$

Minimizing the energy with respect to κ and σ yields the following set of equations:

$$\kappa = \sqrt{a^2 - \frac{3}{2}\sigma^2}, \tag{2.122}$$

$$\sigma^6 - \frac{2}{3}a^2\sigma^4 - \frac{\beta}{6\sqrt{2\pi}\gamma^4}(C^4 + D^4)\sigma + \frac{1}{6\gamma^4} = 0. \tag{2.123}$$

Minimizing the energy again with respect to C, two sets of solutions are obtained:

(i) **Symmetric state 1**:

$$C = \frac{1}{\sqrt{2}}, \quad D = \frac{1}{\sqrt{2}}, \quad \phi_{s1} = \frac{1}{\sqrt{2\sigma_{s1}\sqrt{\pi}}}\left[\exp\left(-\frac{(x+\kappa)^2}{2\sigma_{s1}^2}\right) + \exp\left(-\frac{(x-\kappa)^2}{2\sigma_{s1}^2}\right)\right]. \tag{2.124}$$

(ii) **Symmetry breaking state**:

$$C = 0, \quad D = 1, \quad \phi_{sb} = \frac{1}{\sqrt{\sigma_{sb}\sqrt{\pi}}}\exp\left(-\frac{(x-\kappa)^2}{2\sigma_{sb}^2}\right). \tag{2.125}$$

The symmetry breaking state has an energy degeneracy of two, in such a way that the condensate can either stay in the left well or in the right well. The two states have condensate width satisfying

(i) **Symmetric state 1**:

$$\sigma_{s1}^6 - \frac{2}{3}a^2\sigma_{s1}^4 - \frac{\beta}{12\sqrt{2\pi}\gamma^4}\sigma_{s1} + \frac{1}{6\gamma^4} = 0. \tag{2.126}$$

(ii) **Symmetry breaking state**:

$$\sigma_{sb}^6 - \frac{2}{3}a^2\sigma_{sb}^4 - \frac{\beta}{6\sqrt{2\pi}\gamma^4}\sigma_{sb} + \frac{1}{6\gamma^4} = 0. \tag{2.127}$$

In the weakly interacting regime, the solutions of (2.126)–(2.127) may be approximated with the condensate width with $\beta = 0$, i.e. both states have the same width $\sigma_{s1} = \sigma_{sb} = \sigma$, given by

$$\sigma = \sqrt{-\frac{1}{2}(s+t) + \frac{2}{9}a^2 - \frac{\sqrt{3}i}{2}(s-t)}, \tag{2.128}$$

where

$$\begin{aligned} s &= \frac{1}{3\sqrt[3]{2}}\sqrt[3]{\left(-\frac{9}{2\gamma^4} + \frac{16}{27}a^6\right) + \sqrt{\left(\frac{9}{2\gamma^4}\right)^2 - \frac{16}{3\gamma^4}a^6}}, \\ t &= \frac{1}{3\sqrt[3]{2}}\sqrt[3]{\left(-\frac{9}{2\gamma^4} + \frac{16}{27}a^6\right) - \sqrt{\left(\frac{9}{2\gamma^4}\right)^2 - \frac{16}{3\gamma^4}a^6}}. \end{aligned}$$

The energies of the two states, by taking the coupling term into account, are

(i) **Symmetric state 1**:

$$E_{s1} = \frac{1}{4\sigma^2}\left[1 - 2e^{-\frac{\kappa^2}{\sigma^2}}\left(\frac{\kappa^2}{\sigma^2}\right)\right] + \gamma^4\left[a^2\sigma^2 - \frac{3}{4}\sigma^4\right] - \frac{\beta}{2\sqrt{2\pi}\sigma}\left[\frac{1}{2} + \frac{3}{2}e^{-\frac{2\kappa^2}{\sigma^2}} + 2e^{-\frac{3\kappa^2}{2\sigma^2}}\right]. \tag{2.129}$$

(ii) **Symmetry breaking state**:

$$E_{sb} = \frac{1}{4\sigma^2} + \gamma^4\left[a^2\sigma^2 - \frac{3}{4}\sigma^4\right] - \frac{\beta}{2\sqrt{2\pi}\sigma}. \tag{2.130}$$

If the coupling term in (2.129)–(2.130) is ignored, then $E_{s1} - E_{sb} = \frac{\beta}{4\sqrt{2\pi}\sigma}$. For a non-interacting condensate, symmetric state 1 and the symmetry breaking state have the same energy and the symmetry breaking state is the ground state for any $\beta > 0$. This is valid when $\gamma = \infty$ or $a = \infty$, i.e. when there is totally no overlap between the two Gaussian profiles. By taking the coupling term into account, the energy difference between symmetric state 1 and the symmetry breaking state is

$$E_{s1} - E_{sb} = -\frac{1}{2}\frac{\kappa^2}{\sigma^4}e^{-\frac{\kappa^2}{\sigma^2}} + \frac{\beta}{2\sqrt{2\pi}\sigma}\left[\frac{1}{2} - \frac{3}{2}e^{-\frac{2\kappa^2}{\sigma^2}} - 2e^{-\frac{3\kappa^2}{2\sigma^2}}\right]. \tag{2.131}$$

For non-interacting particles, symmetric state 1 is the ground state. The energy of the symmetry breaking state becomes smaller than the energy of symmetric state 1 when the interaction becomes larger in such a way that the increment in the kinetic energy and potential energy when all particles stay in single well is compensated by the decrement in their interacting energy. This takes place at the critical value

$$\beta_c = \frac{2\sqrt{2\pi}e^{-\frac{\kappa^2}{\sigma^2}}}{1 - 3e^{-\frac{2\kappa^2}{\sigma^2}} - 4e^{-\frac{3\kappa^2}{2\sigma^2}}}\left(\frac{\kappa^2}{\sigma^3}\right). \tag{2.132}$$

The energies of the two states are ranked according to

$$\begin{aligned} E_{s1} &< E_{sb}, \qquad && \beta < \beta_c, \\ E_{sb} &\leq E_{s1}, \qquad && \beta \geq \beta_c. \end{aligned}$$

Minimizing the total energy (2.120) with respect to σ and κ will give another set of solutions other than (2.122)–(2.123), i.e.

$$\kappa = 0, \tag{2.133}$$

$$\sigma^6 - \frac{2}{3}a^2\sigma^4 + \frac{\beta}{3\sqrt{2\pi}\gamma^4}\sigma - \frac{1}{3\gamma^4} = 0. \tag{2.134}$$

This is a symmetric state (symmetric state 2) located at the trap center with a potential barrier specified by γ. The potential barrier is poorly approximated by a harmonic potential and therefore the Gaussian ansatz fails. In the weakly interacting regime, the potential energy plays a significant role in the total energy and thus symmetric state 2, where large number of particles stays at the trap center, has relatively high potential energy, and higher total energy than the other two states.

2.3.2.2 Type II double well potential

The energy functionals of the trial wavefunction (2.115) in type II double well potential (2.114) are

$$E_{\text{kin}} = \frac{1}{4\sigma^2}\left[1 - 4CDe^{-\frac{\kappa^2}{\sigma^2}}\left(\frac{\kappa^2}{\sigma^2}\right)\right], \tag{2.135}$$

$$E_{\text{pot}} = \frac{1}{4}\gamma^2\left[2a^2 - \frac{4a\sigma}{\sqrt{\pi}} + \sigma^2 + (C^2+D^2)\left(2\kappa^2 + \frac{4a\sigma}{\sqrt{\pi}}(1-e^{-\frac{\kappa^2}{\sigma^2}}) - 4\kappa a\text{Erf}\left(\frac{\kappa}{\sigma}\right)\right)\right] \tag{2.136}$$

$$E_{\text{int}} = -\frac{\beta}{2\sqrt{2\pi}\sigma}\left[C^4 + D^4 + 6C^2D^2e^{-\frac{2\kappa^2}{\sigma^2}} + 4CD(C^2+D^2)e^{-\frac{3\kappa^2}{2\sigma^2}}\right]. \tag{2.137}$$

We again consider the case when the two Gaussian profiles are well separated, i.e. $a \gg \sigma$, or equivalently $\kappa \gg \sigma$. By neglecting the term $e^{-\frac{\kappa^2}{\sigma^2}}$, the total energy can be estimated by

$$E \sim \frac{1}{4\sigma^2} + \frac{1}{4}\gamma^2\left[2\kappa^2 + 2a^2 + \sigma^2 - 4\kappa a\text{Erf}\left(\frac{\kappa}{\sigma}\right)\right] - \frac{\beta}{2\sqrt{2\pi}\sigma}(C^4+D^4), \tag{2.138}$$

where C and D satisfy the normalization condition (2.121). Minimizing the energy (2.138) with respect to κ and σ, by neglecting the term $e^{-\frac{\kappa^2}{\sigma^2}}$ and approximating $\text{Erf}(\kappa/\sigma) \sim 1$ when $\kappa \gg \sigma$, the two parameters are found to satisfy the following set of equations:

$$\kappa = a, \tag{2.139}$$

$$\sigma^4 + \frac{\beta}{\sqrt{2\pi}\gamma^2}(C^4+D^4)\sigma - \frac{1}{\gamma^2} = 0. \tag{2.140}$$

Minimizing the energy again with respect to C yields two sets of solutions:

(i) **Symmetric state 1**:

$$C = \frac{1}{\sqrt{2}}, \quad D = \frac{1}{\sqrt{2}}, \quad \phi_{s1} = \frac{1}{\sqrt{2\sigma_{s1}\sqrt{\pi}}}\left[\exp\left(-\frac{(x+a)^2}{2\sigma_{s1}^2}\right) + \exp\left(-\frac{(x-a)^2}{2\sigma_{s1}^2}\right)\right]. \tag{2.141}$$

(ii) **Symmetry breaking state**:

$$C = 0, \quad D = 1, \quad \phi_{sb} = \frac{1}{\sqrt{\sigma_{sb}\sqrt{\pi}}}\exp\left(-\frac{(x-a)^2}{2\sigma_{sb}^2}\right). \tag{2.142}$$

Similarly to type I double well, the symmetry breaking state has an energy degeneracy of two. The two states have condensate width satisfying

(i) **Symmetric state 1**:

$$\sigma_{s1}^4 + \frac{\beta}{2\sqrt{2\pi}\gamma^2}\sigma_{s1} - \frac{1}{\gamma^2} = 0. \tag{2.143}$$

(ii) **Symmetry breaking state**:

$$\sigma_{sb}^4 + \frac{\beta}{\sqrt{2\pi}\gamma^2}\sigma_{sb} - \frac{1}{\gamma^2} = 0. \tag{2.144}$$

In the weakly interacting regime, the solutions may be approximated with the condensate width with $\beta = 0$, i.e. both states have the same width $\sigma_{s1} = \sigma_{sb} = \sigma$, given by

$$\sigma = \frac{1}{\sqrt{\gamma}}. \tag{2.145}$$

The energies of the two states, by taking the coupling term into account, are

(i) **Symmetric state 1**:

$$\begin{aligned} E_{s1} &= \frac{\gamma}{2}\left[1 - \gamma a^2 e^{-\gamma a^2}\right] + \gamma^2\left[a^2\left(1 - \mathrm{Erf}\left(\sqrt{\gamma}a\right)\right) - \frac{a}{\sqrt{\gamma\pi}}e^{-\gamma a^2}\right] \\ &\quad - \frac{\beta}{2}\sqrt{\frac{\gamma}{2\pi}}\left[\frac{1}{2} + \frac{3}{2}e^{-2\gamma a^2} + 2e^{-\frac{3}{2}\gamma a^2}\right]. \end{aligned} \tag{2.146}$$

(ii) **Symmetry breaking state**:

$$E_{sb} = \frac{\gamma}{2} + \gamma^2\left[a^2\left(1 - \mathrm{Erf}\left(\sqrt{\gamma}a\right)\right) - \frac{a}{\sqrt{\gamma\pi}}e^{-\gamma a^2}\right] - \frac{\beta}{2}\sqrt{\frac{\gamma}{2\pi}}. \tag{2.147}$$

If the coupling term in (2.146)–(2.147) is ignored, then $E_{s1} - E_{sb} = \frac{\beta}{4\sqrt{2\pi}\sigma}$. Similarly to type I double well potential, symmetric state 1 and the symmetry breaking state have the same energy for non-interacting condensate and the symmetry breaking state is the ground state for any $\beta > 0$. By taking the coupling term into account, the energy difference between symmetric state 1 and the symmetry breaking state is

$$E_{s1} - E_{sb} = -\frac{1}{2}\gamma^2 a^2 e^{-\gamma a^2} + \frac{\beta}{2}\sqrt{\frac{\gamma}{2\pi}}\left[\frac{1}{2} - \frac{3}{2}e^{-2\gamma a^2} - 2e^{-\frac{3}{2}\gamma a^2}\right]. \tag{2.148}$$

For non-interacting particles, symmetric state 1 is the ground state. The critical interaction at which the energy of the symmetry breaking state becomes smaller than the energy of symmetric state 1 is

$$\beta_c = \frac{2\sqrt{2\pi}e^{-\gamma a^2}}{1-3e^{-2\gamma a^2}-4e^{-\frac{3}{2}\gamma a^2}}\left(\gamma^{\frac{3}{2}}a^2\right). \tag{2.149}$$

Minimizing the total energy (2.138) with respect to σ and κ will yield another set of solutions other than (2.139)–(2.140), i.e.

$$\kappa = 0, \tag{2.150}$$

$$\sigma^4 + \frac{\beta}{\sqrt{2\pi}\gamma^2}\sigma - \frac{1}{\gamma^2} = 0. \tag{2.151}$$

This is a symmetric state (symmetric state 2) located at the trap center. By the same argument stated in the case of type I double well, this state has high energy and will not be considered in the weakly interacting regime.

2.3.3 Strongly interacting condensate in double well potential

For a strongly attractively interacting BEC, asymptotic approximation can be performed by neglecting the potential energy term in the GPE (2.100). In this regime, the interaction energy and the kinetic energy are so large that the potential barrier plays a negligible role at where the atoms are located. The solution of such approximation is a bright soliton, as shown in (2.109)–(2.111). As an extension of the results obtained in the weakly interacting regime, we consider two possibilities for the positive stationary states: single bright soliton solution and two bright solitons solution. The two-soliton solution (symmetry state 1) together with its energy and chemical potential approximations is

$$\phi_1(x) = \frac{\sqrt{\beta}}{4}\left[\text{ sech}\left(\frac{\beta}{4}(x+\kappa)\right) + \text{ sech}\left(\frac{\beta}{4}(x-\kappa)\right)\right], \quad E_1 \sim -\frac{\beta^2}{96}, \quad \mu_1 \sim -\frac{\beta^2}{32}, \tag{2.152}$$

while the one-soliton solution (symmetry breaking state and symmetry state 2), together with its energy and chemical potential approximations is

$$\phi_2(x) = \frac{\sqrt{\beta}}{2}\text{ sech}\left(\frac{\beta}{2}(x-\kappa)\right), \quad E_2 \sim -\frac{\beta^2}{24}, \quad \mu_2 \sim -\frac{\beta^2}{8}. \tag{2.153}$$

The location of the peak(s), κ, can be determined by minimizing the energy functional (2.101).

2.3.3.1 Type I double well potential

Minimizing the energy functional (2.101) with respect to κ in the soliton solutions (2.152) and (2.153), κ and the total energy of the three states in type I double well (2.113), with potential energy included, are found to be

(i) **Symmetric state 1**:

$$\kappa_{s1} = \sqrt{a^2 - \left(\frac{2\pi}{\beta}\right)^2}, \tag{2.154}$$

$$E_{s1} = -\frac{\beta^2}{96} + \gamma^4 \left[\frac{8\pi^2 a^2}{3\beta^2} - \frac{64\pi^4}{15\beta^4}\right]. \tag{2.155}$$

(ii) **Symmetry breaking state**:

$$\kappa_{sb} = \sqrt{a^2 - \left(\frac{\pi}{\beta}\right)^2}, \tag{2.156}$$

$$E_{sb} = -\frac{\beta^2}{24} + \gamma^4 \left[\frac{2\pi^2 a^2}{3\beta^2} - \frac{4\pi^4}{15\beta^4}\right]. \tag{2.157}$$

(iii) **Symmetric state 2**:

$$\kappa_{s2} = 0, \tag{2.158}$$

$$E_{s2} = -\frac{\beta^2}{24} + \gamma^4 \left[\frac{a^4}{2} - \frac{\pi^2 a^2}{3\beta^2} + \frac{7\pi^4}{30\beta^4}\right]. \tag{2.159}$$

The energy differences between the three stationary states are

$$E_{s1} - E_{sb} = \frac{\beta^2}{32} + \frac{\pi^2\gamma^4}{\beta^2}\left[2a^2 - \frac{4\pi^2}{\beta^2}\right], \tag{2.160}$$

$$E_{s2} - E_{sb} = \frac{\gamma^4 a^4}{2} - \frac{\pi^2\gamma^4}{\beta^2}\left[a^2 - \frac{\pi^2}{2\beta^2}\right], \tag{2.161}$$

$$E_{s1} - E_{s2} = \frac{\beta^2}{32} - \frac{\gamma^4 a^4}{2} + \frac{\pi^2\gamma^4}{\beta^2}\left[3a^2 - \frac{9\pi^2}{2\beta^2}\right]. \tag{2.162}$$

In this regime, terms with $\frac{1}{\beta^4}$ may be safely neglected and the energies are ranked according to

$$E_{sb} < E_{s1} < E_{s2}, \qquad \beta < \beta_{c2},$$

$$E_{sb} < E_{s2} \leq E_{s1}, \qquad \beta \geq \beta_{c2},$$

where

$$\beta_{c2} = 2\sqrt{2}\sqrt{\gamma^4 a^4 + \gamma a\sqrt{\gamma^4 a^6 - \frac{3\pi^2}{2}}} \tag{2.163}$$

is the critical value for which symmetric state 2 possesses the same energy as symmetric state 1. This happens when the interparticle interaction is so strong that the interaction energy, which value is negative, is dominant in spite of the high potential energy acquired by the particles at the trap center, which results in a lower total energy than symmetric state 1. Symmetric state 2 has higher energy than the symmetric breaking state when $\beta > \sqrt{2}\pi/a$, which is $O(1)$, and thus in the strongly interacting regime ($\beta \gg 1$), the symmetry breaking state is always the ground state.

2.3.3.2 Type II double well potential

The energies of the sech soliton solutions (2.152) and (2.153) in type II double well (2.114), with potential energy included, are

$$E_1 = -\frac{\beta^2}{96} + \frac{\gamma^2}{6\beta^2}\left[4\pi^2 + 3\beta^2(\kappa - a)^2 - 24\beta a \ln\left(1 + e^{-\beta\kappa/2}\right)\right], \tag{2.164}$$

$$E_2 = -\frac{\beta^2}{24} + \frac{\gamma^2}{6\beta^2}\left[\pi^2 + 3\beta^2(\kappa - a)^2 - 12\beta a \ln\left(1 + e^{-\beta\kappa}\right)\right]. \tag{2.165}$$

Energy minimization with respect to κ yields

(i) **Symmetric state 1**:

$$\kappa_{s1} \approx a, \tag{2.166}$$

$$E_{s1} = -\frac{\beta^2}{96} + \gamma^2\left[\frac{2\pi^2}{3\beta^2} - \frac{4a}{\beta}\ln\left(1 + e^{-\beta a/2}\right)\right]. \tag{2.167}$$

(ii) **Symmetry breaking state**:

$$\kappa_{sb} \approx a, \tag{2.168}$$

$$E_{sb} = -\frac{\beta^2}{24} + \gamma^2\left[\frac{\pi^2}{6\beta^2} - \frac{2a}{\beta}\ln\left(1 + e^{-\beta a}\right)\right]. \tag{2.169}$$

(iii) **Symmetric state 2**:

$$\kappa_{s2} = 0, \tag{2.170}$$

$$E_{s2} = -\frac{\beta^2}{24} + \gamma^2 \left[\frac{\pi^2}{6\beta^2} + \frac{1}{2}a^2 \right]. \tag{2.171}$$

The energy differences between the three stationary states are

$$E_{s1} - E_{sb} = \frac{\beta^2}{32} + \gamma^2 \left[\frac{\pi^2}{2\beta^2} + \frac{2a}{\beta} \ln\left(1 + e^{-\beta a}\right) - \frac{4a}{\beta} \ln\left(1 + e^{-\beta a/2}\right) \right], \tag{2.172}$$

$$E_{s2} - E_{sb} = \gamma^2 \left[\frac{1}{2}a^2 + \frac{2a}{\beta} \ln\left(1 + e^{-\beta a}\right) \right], \tag{2.173}$$

$$E_{s1} - E_{s2} = \frac{\beta^2}{32} + \gamma^2 \left[\frac{\pi^2}{2\beta^2} - \frac{1}{2}a^2 - \frac{4a}{\beta} \ln\left(1 + e^{-\beta a/2}\right) \right]. \tag{2.174}$$

When $\beta \gg 1$ and $a \sim O(1)$, the terms with $e^{-\beta a}$ and $e^{-\beta a/2}$ may be neglected and the energies are ranked according to

$$E_{sb} < E_{s1} < E_{s2}, \qquad \beta < \beta_{c2},$$

$$E_{sb} < E_{s2} \leq E_{s1}, \qquad \beta \geq \beta_{c2},$$

where the critical interaction strength at which the energy of symmetric state 2 becomes smaller than the energy of symmetric state 1 is approximated by

$$\beta_{c2} = 2\sqrt{2\gamma^2 a^2 + \gamma\sqrt{4\gamma^2 a^4 - \pi^2}}. \tag{2.175}$$

2.3.4 Numerical results

2.3.4.1 Type I double well potential

Figure 2.5 depicts symmetric state 1 and the symmetry breaking state obtained through numerically solving the GPE (2.100) as well as the approximation via the variational method, by finding the condensate width in (2.126) and (2.127) numerically. Figure 2.6 shows symmetric states 1&2 and the symmetry breaking state, for both numerical solutions and approximated sech soliton solutions.

Tables 2.12&2.13 show the energies obtained through the variational method as well as the energies obtained from the numerical solutions of the GPE, with respect to several values of β. The

β	E_{num}	κ_{var}	E_{var}	$E_{\beta\sim 1}$	κ_{sech}	E_{sech}
0	4.1136	0.9023	4.2283	-	-	-
	4.1270	0.9023	4.2655	-	-	-
0.1	4.0872	0.9027	4.2008	4.2000	-	-
	4.0878	0.9031	4.2087	4.2088	-	-
0.2	4.0607	0.9031	4.1732	4.1717	-	-
	4.0500	0.9039	4.1517	4.1522	-	-
0.5	3.9806	0.9043	4.0901	4.0866	-	-
	3.8932	0.9063	3.9793	3.9822	-	-
1.0	3.8457	0.9063	3.9501	3.9449	-	-
	3.6125	0.9103	3.6873	3.6988	-	-
2.0	3.5698	0.9103	3.6647	3.6615	-	-
	3.0228	0.9180	3.0844	3.1322	-	-
5.0	2.6904	0.9217	2.7641	2.8114	-	-
	1.0432	0.9389	1.1025	1.4322	-	-
7.5	1.8971	0.9306	1.9594	2.1029	-	-
	-0.8917	0.9537	-0.7949	0.0155	-	-
10.0	1.0351	0.9389	1.1015	1.3944	0.7780	3.3909
	-3.1471	0.9655	-2.9780	-1.4012	0.9494	-2.9027
	5.0199	-	-	-	0	5.2208
15.0	-0.8840	0.9537	-0.7950	-0.0226	0.9080	-0.1685
	-8.8367	0.9809	-8.4332	-4.2345	0.9778	-8.8004
	0.3306	-	-	-	0	0.3415
20.0	-3.1148	-	-	-	0.9494	2.9027
	-16.3484	-	-	-	0.9876	-16.3409
	-6.8302	-	-	-	0	-6.8283
35.0	-12.3414	-	-	-	0.9838	-12.3363
	-50.9349	-	-	-	0.9960	-50.9346
	-41.0951	-	-	-	0	-41.0951
50.0	-25.8313	-	-	-	0.9921	-25.8324
	-104.1141	-	-	-	0.9980	-104.1141
	-94.1929	-	-	-	0	-94.1929

Table 2.12: Comparison between the energies for BEC in type I double well $V(x) = 10(x^2-1)^2$. Row 1: symmetric state 1; row 2: symmetry breaking state; row 3: symmetric state 2; E_{num}: numerical solution of the GPE; E_{var}: numerical solution from variational method (2.126)&(2.127); $E_{\beta\sim 1}$: weakly interacting energy approximation (2.129)–(2.130); E_{sech}: strongly interacting energy approximation (2.154)–(2.159).

β	E_{num}	κ_{var}	E_{var}	$E_{\beta\sim 1}$	κ_{sech}	E_{sech}
0	8.8808	1.9787	8.8969	-	-	-
	8.8808	1.9787	8.8969	-	-	-
0.1	8.8389	1.9787	8.8549	-	-	-
	8.7969	1.9788	8.8129	8.8130	-	-
0.2	8.7969	1.9788	8.8129	8.8130	-	-
	8.7129	1.9789	8.7287	8.7291	-	-
0.5	8.6707	1.9790	8.6865	8.6871	-	-
	8.4593	1.9792	8.4748	8.4773	-	-
1.0	8.4593	1.9792	8.4748	8.4773	-	-
	8.0321	1.9797	8.0474	8.0577	-	-
2.0	8.0321	1.9797	8.0474	8.0577	-	-
	7.1592	1.9807	7.1764	7.2186	-	-
5.0	6.7132	1.9813	6.7322	6.7990	-	-
	4.3762	1.9838	4.4165	4.7011	-	-
10.0	4.3762	1.9838	4.4165	4.7011	-	-
	-0.9528	1.9884	-0.7993	0.5053	-	-
15.0	1.8346	1.9862	1.9185	2.6032	1.9556	6.8499
	-7.4471	1.9922	-7.0695	-3.6904	1.9890	-7.0458
	149.2266	-	-	-	0	149.4642
20.0	-0.9478	1.9884	-0.7993	0.5053	1.9752	1.0452
	-15.4539	1.9948	-14.7432	-7.8862	1.9938	-15.3540
	142.6403	-	-	-	0	142.6782
35.0	-11.2265	-	-	-	1.9919	-11.0472
	-50.6167	-	-	-	1.9980	-50.6123
	108.7427	-	-	-	0	108.7438
50.0	-25.2253	-	-	-	1.9960	-25.2008
	-103.9567	-	-	-	1.9990	-103.9562
	55.7280	-	-	-	0	55.7281
75.0	-58.2217	-	-	-	1.9982	-58.2197
	-234.2815	-	-	-	1.9996	-234.2814
	-74.4217	-	-	-	0	-74.4218
100.0	-103.9565	-	-	-	1.9990	-103.9562
	-416.6140	-	-	-	1.9998	-416.6140
	-256.6930	-	-	-	0	-256.6930

Table 2.13: Comparison between the energies for BEC in type I double well $V(x) = 10(x^2-4)^2$. Row 1: symmetric state 1; row 2: symmetry breaking state; row 3: symmetric state 2; E_{num}: numerical solution of the GPE; E_{var}: numerical solution from variational method (2.126)&(2.127); $E_{\beta\sim 1}$: weakly interacting energy approximation (2.129)–(2.130); E_{sech}: strongly interacting energy approximation (2.154)–(2.159).

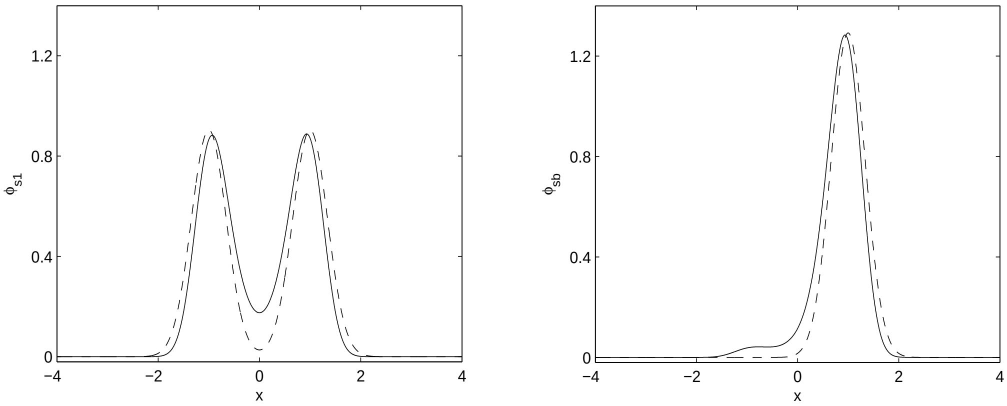

Figure 2.5: Symmetric state 1 (left) and symmetry breaking state (right) of an attractively interacting BEC in type I double well $V(x) = 10(x^2 - 1)^2$, with interaction $\beta = 1.0$. Solid line: numerical solution from solving the GPE; dashed line: approximated solution with the Gaussian ansatz.

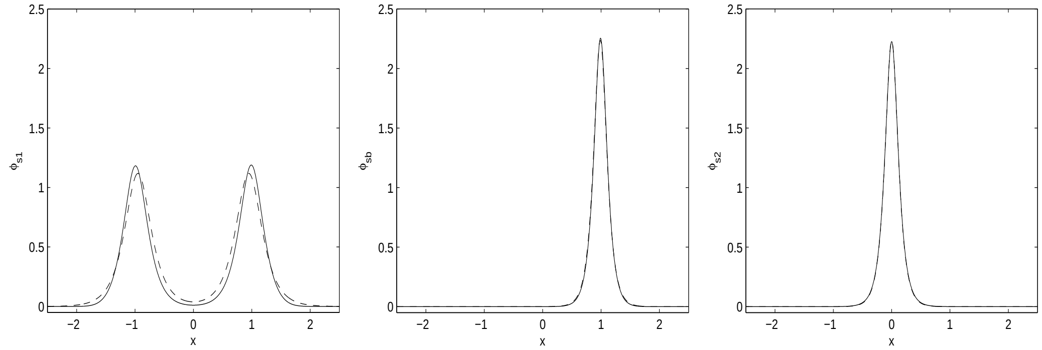

Figure 2.6: Symmetric state 1 (left), symmetry breaking state (middle), and symmetric state 2 (right) of an attractively interacting BEC in type I double well $V(x) = 10(x^2 - 1)^2$, with interaction $\beta = 20.0$. Solid line: numerical solution from solving the GPE; dashed line: approximated solution with sech soliton(s).

Gaussian ansatz is shown to work quite well for small β, in particular for double well potential with large γ or large a. In the case of small γ or small a, the difference between the computed energy and the variational energy is greater due to the neglected overlapping term. The numerically calculated energies and chemical potentials of the three states in double well $V(x) = 10(x^2 - 1)^2$, as functions of the interaction strength, are also plotted in Figure 2.7. It can be seen from Figure 2.7(b) that both critical interaction parameters, β_c and β_{c2}, for the chemical potential are smaller than those for the energy. Therefore, if one uses the smallest eigenvalue of the nonlinear eigenvalue problem (2.100) to define the ground state, the ground state could be different from the one defined with the lowest energy. This is in contrast to the repulsively interacting BEC whose ground state is the same under the two definitions.

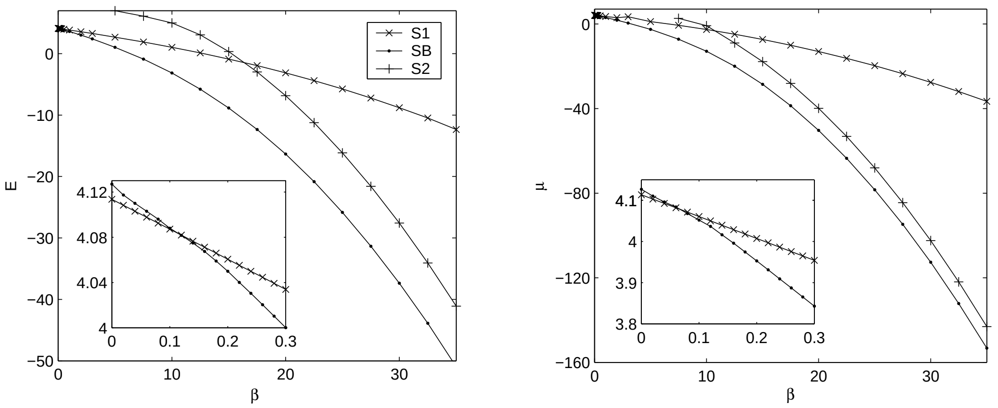

Figure 2.7: Energy (left) and chemical potential (right) of BEC in type I double well $V(x) = 10(x^2 - 1)^2$ (S1: symmetric state 1; SB: symmetry breaking state; S2: symmetric state 2). The inset shows a zoom for small β, in the vicinity of β_c.

Figures 2.8&2.9 show the dependence of the critical interaction parameters β_c and β_{c2} on the double well parameters γ and a, respectively. For large γ or large a cases, the predicted critical values are quite close to those obtained through numerical simulation.

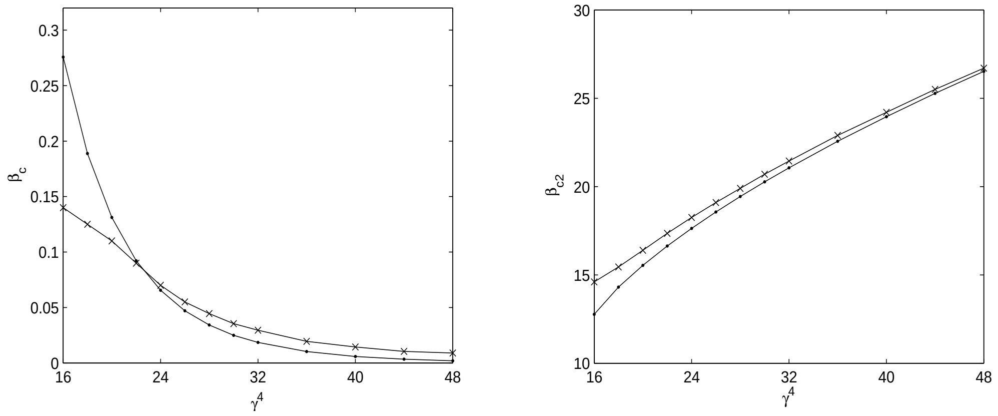

Figure 2.8: Dependence of β_c (left) and β_{c2} (right) on γ^4, for type I double well potential $V(x) = \frac{1}{2}\gamma^4 \left(x^2 - 1\right)^2$. Solid dot line: analytical result; solid cross line: numerical result.

2.3.4.2 Type II double well potential

Figure 2.10 depicts symmetric state 1 and the symmetry breaking state obtained through numerically solving the GPE (2.100) as well as the approximation via the variational method, by finding the condensate width in (2.143) and (2.144) numerically. Figure 2.11 shows symmetric states 1&2 and the symmetry breaking state, for both numerical solutions and approximated sech soliton solutions. Tables 2.14&2.15 show the energies obtained through the variational method as well as

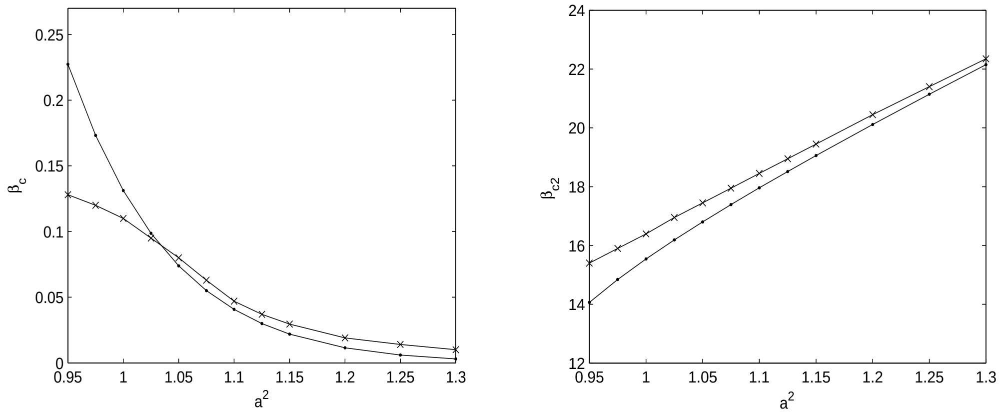

Figure 2.9: Dependence of β_c (left) and β_{c2} (right) on a^2, for type I double well potential $V(x) = 10\left(x^2 - a^2\right)^2$. Solid dot line: analytical result; solid cross line: numerical result.

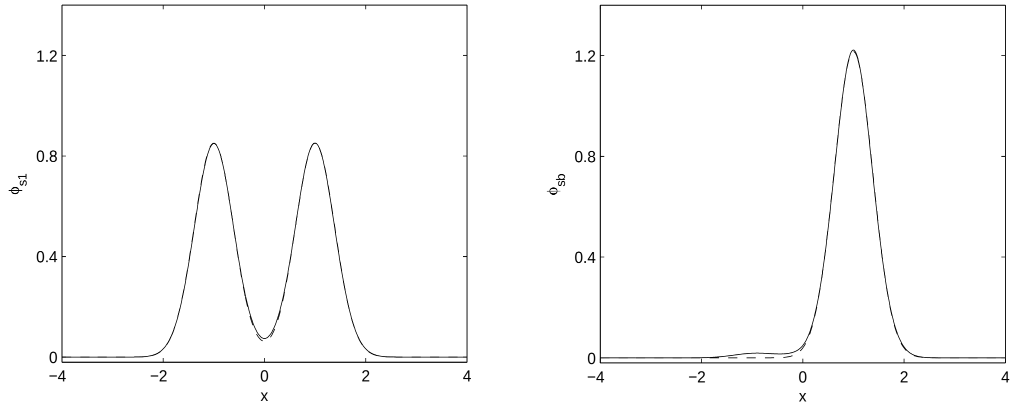

Figure 2.10: Symmetric state 1 (left) and symmetry breaking state (right) of an attractively interacting BEC in type II double well $V(x) = 20(|x| - 1)^2$, with $\beta = 1.0$. Solid line: numerical solution from solving the GPE; dashed line: approximated solution with the Gaussian ansatz.

the energies obtained from the numerical solutions of the GPE, with respect to several values of β. Similarly to type I double well, the Gaussian ansatz is shown to work quite well here for small β, in particular for the double well potential with large γ or large a. The numerically calculated energies and chemical potentials of the three states in double well $V(x) = 20(|x| - 1)^2$, as function of the interaction strength, are plotted in Figure 2.12. Similarly to type I double well, the critical interaction parameters for the energy and those for the chemical potential are different. Thus in this case, the ground state defined by the lowest energy and by the smallest nonlinear eigenvalue could be different.

The dependencies of the critical interaction β_c and β_{c2} on the double well parameters γ and a are shown in Figures 2.13&2.14 respectively. Compared to type I double well, the Gaussian ansatz

β	E_{num}	E_{var}	$E_{\beta\sim1}$	E_{sech}
0	3.1443	3.1254	-	-
	3.1581	3.1612	-	-
0.1	3.1194	3.1009	3.1003	-
	3.1078	3.1110	3.1111	-
0.2	3.0945	3.0764	3.0752	-
	3.0587	3.0606	3.0609	-
0.5	3.0194	3.0025	2.9999	-
	2.9068	2.9082	2.9104	-
1.0	2.8930	2.8782	2.8745	-
	2.6478	2.6497	2.6595	-
2.0	2.6356	2.6251	2.6236	-
	2.1100	2.1155	2.1579	-
5.0	1.8229	1.8272	1.8709	-
	0.3088	0.3450	0.6530	-
10.0	0.3059	0.3432	0.6164	1.4828
	-3.5928	-3.4209	-1.8552	-3.5091
15.0	-1.4728	-1.3835	-0.6381	-1.1799
	-9.0927	-8.6812	-4.3634	-9.0826
20.0	-3.5806	-3.4209	-1.8926	-3.5091
	-16.5041	-15.7599	-6.8716	-16.5022
	0.6174	-	-	3.4978
30.0	-9.0903	-	-	-9.0826
	-37.4270	-	-	-37.4269
	-19.2950	-	-	-17.4269
40.0	-16.4693	-	-	-16.5022
	-66.6256	-	-	-66.6255
	-48.0169	-	-	-46.6255
50.0	-25.9348	-	-	-25.9364
	-104.1404	-	-	-104.1403
	-85.2501	-	-	-84.1403

Table 2.14: Comparison between the energies for BEC in type II double well $V(x) = 20(|x|-1)^2$. Row 1: symmetric state 1; row 2: symmetry breaking state; row 3: symmetric state 2; E_{num}: numerical solution of the GPE; E_{var}: numerical solution from variational method (2.143)&(2.144); $E_{\beta\sim1}$: weakly interacting energy approximation (2.146)–(2.147); E_{sech}: strongly interacting energy approximation (2.166)–(2.171).

β	E_{num}	E_{var}	$E_{\beta\sim 1}$	E_{sech}
0	3.1623	3.1623	-	-
	3.1623	3.1623	-	-
0.1	3.1372	3.1372	3.1372	-
	3.1120	3.1120	3.1121	-
0.2	3.1120	3.1120	3.1121	-
	3.0615	3.0615	3.0619	-
0.5	3.0362	3.0362	3.0369	-
	2.9086	2.9089	2.9115	-
1.0	2.9086	2.9089	2.9115	-
	2.6491	2.6503	2.6606	-
2.0	2.6491	2.6503	2.6606	-
	2.1109	2.1158	2.1590	-
5.0	1.8313	1.8392	1.9082	-
	0.3090	0.3450	0.6541	-
10.0	0.3090	0.3450	0.6541	-1.5888
	-3.5928	-3.4209	-1.8542	-3.5087
15.0	-1.4730	-1.3834	-0.6000	-1.1740
	-9.0927	-8.6812	-4.3624	-9.0826
20.0	-3.5928	-3.4209	-1.8542	-3.5087
	-16.5041	-15.7599	-6.8706	-16.5022
30.0	-9.0927	-	-	-9.0826
	-37.4271	-	-	-37.4269
	38.7813	-	-	42.5731
40.0	-16.4940	-	-	-16.5022
	-66.6256	-	-	-66.6255
	10.5756	-	-	13.3745
50.0	-25.9334	-	-	-25.9364
	-104.1404	-	-	-104.1403
	-26.3664	-	-	-24.1403

Table 2.15: Comparison between the energies for BEC in type II double well $V(x) = 20(|x|-2)^2$. Row 1: symmetric state 1; row 2: symmetry breaking state; row 3: symmetric state 2; E_{num}: numerical solution of the GPE; E_{var}: numerical solution from variational method (2.143)&(2.144); $E_{\beta\sim 1}$: weakly interacting energy approximation (2.146)–(2.147); E_{sech}: strongly interacting energy approximation (2.166)–(2.171).

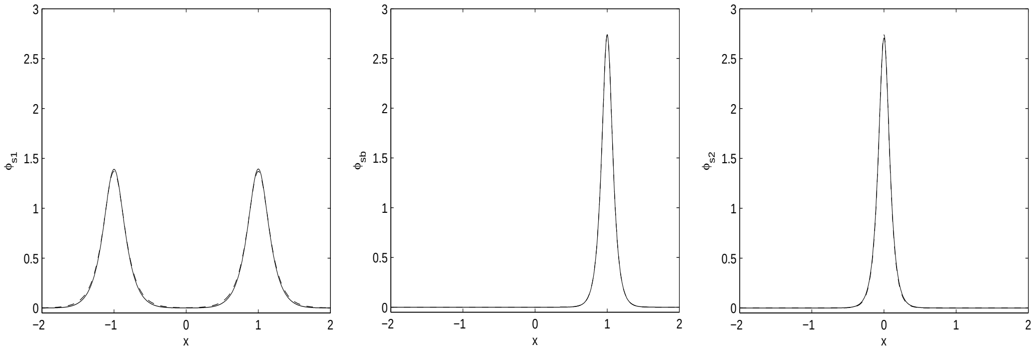

Figure 2.11: Symmetric state 1 (left), symmetry breaking state (middle), and symmetric state 2 (right) of an attractively interacting BEC in type II double well $V(x) = 20(|x| - 1)^2$, with $\beta = 30.0$. Solid line: numerical solution from solving the GPE; dashed line: approximated solution with sech soliton(s).

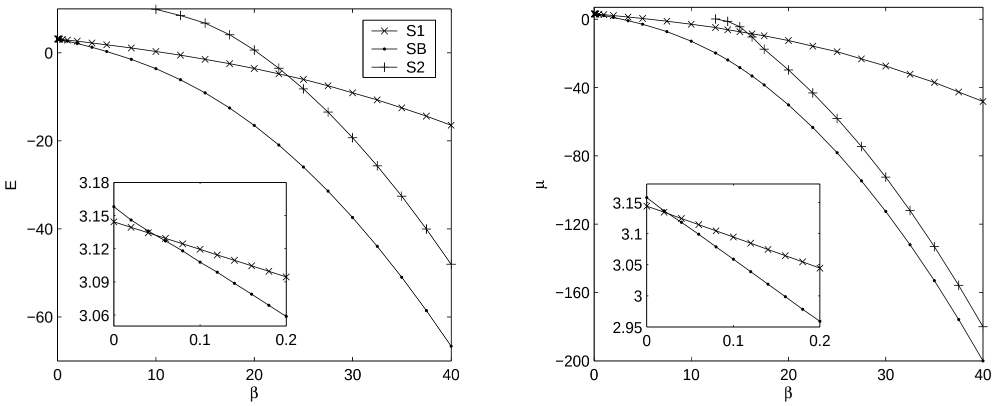

Figure 2.12: Energy (right) and chemical potential (left) of BEC in type II double well $V(x) = 20(|x|-1)^2$ (S1: symmetric state 1; SB: symmetry breaking state; S2: symmetric state 2). The inset shows a zoom for small β, in the vicinity of β_c.

and sech soliton approximation both give better approximation to the wavefunction, however, both are less accurate in predicting the critical values, which are obtained through neglecting the terms $e^{-\beta a}$ and $e^{-\beta a/2}$ in the energy differences (2.172)–(2.174).

2.4 Discussion

We studied analytically the ground state of a Bose-Einstein condensate (BEC) in a trapping potential for both repulsively interacting particles ($\beta_d > 0$) and attractively interacting particles ($\beta_d < 0$). For a condensate with repulsive interaction, we presented asymptotic approximations up to $o(1)$ in terms of the interacting parameter, β_d, for the energy and chemical potential of the ground state of BEC

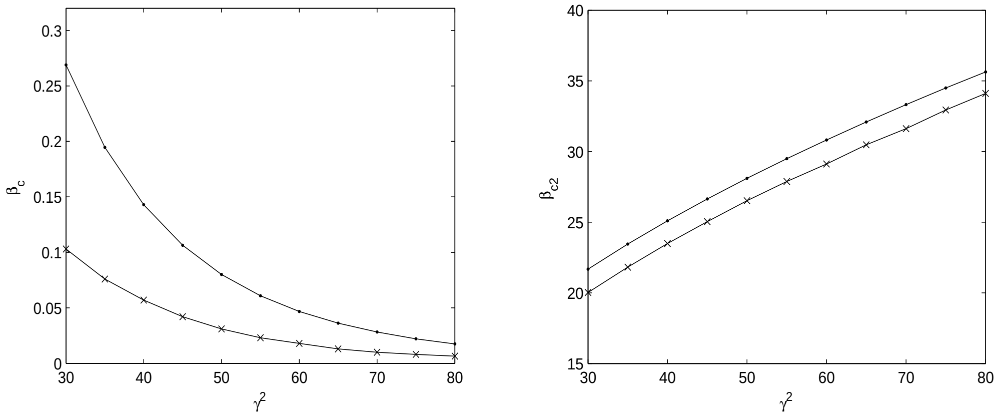

Figure 2.13: Dependence of β_c (left) and β_{c2} (right) on γ^2, for type II double well potential $V(x) = \frac{1}{2}\gamma^2\left(|x| - 1\right)^2$. Solid dot line: analytical result; solid cross line: numerical result.

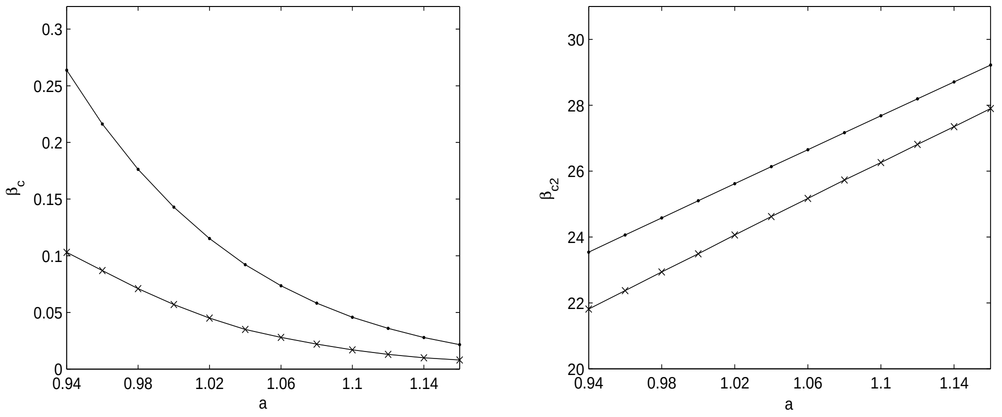

Figure 2.14: Dependence of β_c (left) and β_{c2} (right) on a, for type II double well potential $V(x) = 20\left(|x| - a\right)^2$. Solid dot line: analytical result; solid cross line: numerical result.

in the semiclassical regime with several typical trapping potentials. For a uniform box potential, the approximations were obtained by a matched asymptotic method; while for non-uniform potentials, e.g. harmonic oscillator, double well and optical lattice potentials, the approximations were derived from the Thomas-Fermi approximation. These asymptotic approximations were verified by our extensive numerical results.

Furthermore, based on the asymptotic and numerical studies for the time-independent Gross-Pitaevskii equation (GPE) with $\beta_d \geq 0$ in bounded Ω (or in unbounded Ω with $\lim_{|\boldsymbol{x}|\to\infty} V_d(\boldsymbol{x}) = \infty$), we draw the following conjectures:

(i) The GPE admits infinitely many eigenfunctions which are linearly independent.

(ii) If all the eigenfunctions are ranked according to their energies, ϕ_g, ϕ_1, $\cdots$, then the corresponding eigenvalues (or chemical potentials) are in the increasing order, i.e.

$$E(\phi_g) \le E(\phi_1) \le E(\phi_2) \le \cdots \quad \Longrightarrow \quad \mu(\phi_g) \le \mu(\phi_1) \le \mu(\phi_2) \le \cdots .$$

(iii) When $\beta_d \to \infty$, the ratios between energy and chemical potential are constants, i.e.

$$\lim_{\beta_d \to \infty} \frac{E(\phi_g)}{\mu(\phi_g)} = \text{const}, \qquad \lim_{\beta_d \to \infty} \frac{E(\phi_k)}{E(\phi_g)} = 1, \quad \lim_{\beta_d \to \infty} \frac{\mu(\phi_k)}{\mu(\phi_g)} = 1, \quad k \in \mathbb{N}.$$

(iv) When Ω is bounded, in the semiclassical regime, i.e. $\beta_d \gg 1$, boundary layers with width $O(1/\sqrt{\beta_d})$ are observed at $\partial\Omega$ in both the ground and the excited states, and interior layers with width $O(1/\sqrt{\beta_d})$ are observed in the excited states. When $\Omega = \mathbb{R}^d$ and $V(\boldsymbol{x})$ is chosen as (2.89), interior layers with width $O(1/\beta_d^{(2+\alpha)/4(\alpha+d)})$ are observed in the excited states.

For a condensate with attractive interaction, two regimes are identified: the weakly interacting regime ($\beta_d < 0, |\beta_d| \sim 1$) and the strongly interacting regime ($\beta_d < 0, |\beta_d| \gg 1$). Gaussian approximation was applied to the weakly interacting regime, for harmonic potential and two types of double well potentials. The approximations of the positive stationary states in a double well potential, in particular the symmetric state in which the condensate particles stay symmetrically in two wells (symmetric state 1) and the symmetry breaking state in which the condensate occupies only one well, were verified by the numerical results. For non-interacting particles, symmetric state 1 is always the ground state. For interacting particles, symmetry breaking state has a chance to possess energy lower than the energy of symmetric state 1. A critical value β_c at which the ground state becomes non-unique, was predicted. For interaction $|\beta_d| > |\beta_c|$, the symmetry breaking state emerges as the ground state. Due to the existence of symmetry breaking state in a double well potential, if all stationary states are ranked according to their energies, the corresponding chemical potentials might not be in the increasing order.

In the case of a strongly attractively interacting condensate in a non-uniform potential satisfying $\lim_{|\boldsymbol{x}| \to \infty} V_d(\boldsymbol{x}) = \infty$, asymptotic approximation was derived from the GPE by neglecting the trapping potential term, and the stationary states of the condensate are found in the form of sech solitons. Three bright soliton states were identified for double well potentials: symmetric state 1, symmetry breaking state, and symmetric state 2 in which the particles stay around the center of the trap which is a local maximum of the double well potential. The symmetry breaking state was found to remain as the ground state in this regime and the soliton approximation were verified by the extensive numerical results.

Chapter 3

Numerical Study of Single Component BEC Ground State

One of the fundamental problems in the numerical simulation of BEC is to find its ground state so as to compare the numerical results with theoretical studies or with experimental observations, as well as to prepare the initial data for studying the dynamics of BEC. An efficient and accurate numerical method is one of the key issues in order to compute effectively the ground state of BEC, especially in the strongly repulsive interaction regime and in optical lattice potential. There has been a series of recent studies for developing numerical methods to compute the BEC ground state. For example, Bao and Du [12] presented a continuous normalized gradient flow with diminishing energy and discretized it with a backward Euler finite difference (BEFD) and time-splitting sine-pseudospectral method (TSSP) for computing the ground state and the first excited state of the condensate. This idea was extended to multi-component BEC [10] and rotating BEC [20]. Bao and Tang [18] proposed a method by directly minimizing the energy functional via finite element approximation to obtain the ground and the excited states. Edwards and Burnett [57] presented a Runge-Kutta type method and used it to solve for one-dimensional ground state and three-dimensional ground state with spherical symmetry. Adhikari [1] used this approach to get the ground state solution of the GPE in two dimesions with radial symmetry. Ruprecht et al. [97] used the Crank-Nicolson finite difference method to solve for the BEC ground state. Chang et al. [38, 39] proposed a Gauss-Seidel-type method to compute the stationary states of a multi-component BEC. Other approaches include an explicit imaginary-time algorithm used by Cerimele et al. [37] and Chiofalo et al. [40], a direct inversion in the iterated subspace (DIIS) used by Schneider et al. [99], and a simple analytical type method proposed by Dodd [54]. These numerical methods were applied to compute the ground state of BEC with different trapping potentials.

For a BEC in an optical lattice or in a rotational frame, due to the oscillatory nature of the trapping potential or the appearance of quantized vortices, the stationary states are smooth but exhibit multiscale structures. Therefore the resolution in space of a numerical method is essential for an efficient computation, especially in three-dimensional case. In this case, the numerical methods proposed in the literature have some drawbacks: (i) TSSP is explicit, conditionally stable and of spectral accuracy in space [12]. It is energy diminishing when the time step satisfies a constraint. However, due to the time-splitting error which does not vanish at steady state, the time step must be chosen to be very small so as to get the ground state solution in high accuracy. Therefore, the total computational time is large due to the small time step. (ii) BEFD is implicit, unconditionally stable and energy diminishing for any time step, thus large time step can be chosen in practical computation. Yet, it is only of second order accuracy in space. When high accuracy is required or when the solution exhibits multiscale structures, a large number of grid points must be taken so as to get a reasonable solution. Hence, the memory requirement is a big burden in this case. (iii) Other finite difference or finite element methods are usually of low order accuracy in space and in many cases they have a severe constraint for time step due to the stability or energy diminishing requirement [12]. In this chapter, we develop new numerical methods which enjoy the advantages of both TSSP and BEFD, i.e. they are spectrally accurate in space and are efficient in terms of computational time. The key features of the numerical methods are based on: (i) the application of sine-pseudospectral discretization for spatial derivatives such that it is spectrally accurate; (ii) the adoption of the backward Euler scheme (BESP) or the backward/forward Euler scheme (BFSP) for linear/nonlinear terms in temporal derivatives in such a way that the numerical schemes have good energy diminishing property; (iii) the introduction of a stabilization term with constant coefficient in BESP to accelerate the convergence rate of the iterative method for solving a linear system or in BFSP to increase the upper bound of time step constraint; and (iv) the utilization of the fast sine transform (FST) as a preconditioner for solving a linear system efficiently [11].

3.1 Numerical Methods

In this section, we will first review the normalized gradient flow (NGF) [12] for computing the solution of the minimization problem (2.22) and its energy diminishing property, followed by showing how to choose the initial data to compute the ground and the first excited states of a BEC with the NGF. Two numerical schemes will be proposed, the backward Euler sine-pseudospectral method (BESP) and the backward-forward Euler sine-pseudospectral method (BFSP) [11], to fully discretize the NGF. We will then discuss how to choose the optimal stabilization parameter in the numerical schemes to improve the computational efficiency.

3.1.1 Normalized gradient flow (NGF)

Consider a time step $k = \Delta t > 0$ and set $t_n = n\Delta t$ for $n = 0, 1, 2, \cdots$. Applying the steepest decent method to the energy functional $E(\phi)$ (2.15) without constraint (2.14), and then projecting the solution back to a unit sphere at the end of each time interval $[t_n, t_{n+1}]$ to satisfy the constraint (2.14), we obtain the following normalized gradient flow (NGF) [3, 12, 37, 40],

$$\begin{aligned} \frac{\partial}{\partial t}\phi(\boldsymbol{x},t) &= -\frac{1}{2}\frac{\delta E(\phi)}{\delta\phi} \\ &= \left(\frac{1}{2}\nabla^2 - V(\boldsymbol{x}) - \beta|\phi|^2\right)\phi(\boldsymbol{x},t), \quad \boldsymbol{x}\in\mathbb{R}^d,\ t_n \le t < t_{n+1},\ n\ge 0, \end{aligned} \tag{3.1}$$

$$\phi(\boldsymbol{x},t_{n+1}) := \phi(\boldsymbol{x},t_{n+1}^+) = \frac{\phi(\boldsymbol{x},t_{n+1}^-)}{\|\phi(\cdot,t_{n+1}^-)\|_{L_2}}, \qquad \boldsymbol{x}\in\mathbb{R}^d,\ n\ge 0, \tag{3.2}$$

$$\phi(\boldsymbol{x},0) = \phi_0(\boldsymbol{x}), \quad \boldsymbol{x}\in\mathbb{R}^d \qquad \text{with} \quad \|\phi_0\| = 1; \tag{3.3}$$

where $\phi(\boldsymbol{x},t_n^\pm) = \lim_{t\to t_n^\pm}\phi(\boldsymbol{x},t)$. The gradient flow (3.1) can also be obtained from the GPE (2.11) by changing the time t to imaginary time $\tau = it$ and this method is known as the imaginary time method in physics literature [3, 40].

When $\beta = 0$ and $V(\boldsymbol{x}) \ge 0$ for all $\boldsymbol{x}\in\mathbb{R}^d$, it was proved that the NFG (3.1)–(3.3) is energy diminishing for any time step $\Delta t > 0$ and for any initial data ϕ_0 [12], i.e.

$$E(\phi(\cdot,t_{n+1})) \le E(\phi(\cdot,t_n)) \le \cdots \le E(\phi(\cdot,t_0)) = E(\phi_0), \quad n = 0,1,2,\cdots,$$

which provides a rigorous mathematical justification for the algorithm to compute the ground state in the linear case. When $\beta > 0$, a similar argument is no longer valid. However, letting $\Delta t \to 0$ in the NGF(3.1)–(3.3) yields the following continuous normalized gradient flow (CNGF) [12]:

$$\frac{\partial}{\partial t}\phi(\boldsymbol{x},t) = \left(\frac{1}{2}\nabla^2 - V(\boldsymbol{x}) - \beta\,|\phi|^2 + \frac{\mu(\phi(\cdot,t))}{\|\phi(\cdot,t)\|^2}\right)\phi(\boldsymbol{x},t), \quad \boldsymbol{x}\in\mathbb{R}^d,\ t\geq 0, \tag{3.4}$$

$$\phi(\boldsymbol{x},0) = \phi_0(\boldsymbol{x}), \quad \boldsymbol{x}\in\mathbb{R}^d \qquad \text{with} \qquad \|\phi_0\| = 1. \tag{3.5}$$

This CNGF is normalization conserved and is energy diminishing provided that $\beta \geq 0$ and $V(\boldsymbol{x}) \geq 0$ for all $\boldsymbol{x} \in \mathbb{R}^d$ [12], i.e.

$$\|\phi(\cdot,t)\|^2 \equiv \|\phi_0\|^2 = 1, \quad \frac{d}{dt}E(\phi(\cdot,t)) = -2\|\phi_t(\cdot,t)\|^2 \leq 0, \qquad t \geq 0,$$

which in turn implies that

$$E(\phi(\cdot,t_2)) \leq E(\phi(\cdot,t_1)), \qquad 0 \leq t_1 \leq t_2 < \infty.$$

This provides a mathematical justification for the algorithm to compute the ground state in the nonlinear case at least when the time step Δt is small.

Due to uniqueness of the positive ground state of a non-rotating repulsively interacting BEC [76], the ground state $\phi_g(\boldsymbol{x})$ and its corresponding chemical potential μ_g can be obtained from the steady state solution of the NGF (3.1)–(3.3) or the CNGF (3.4)–(3.5), provided that the initial data $\phi_0(\boldsymbol{x})$ is chosen as a positive function, i.e. $\phi_0(\boldsymbol{x}) \geq 0$ for $\boldsymbol{x} \in \mathbb{R}^d$. Furthermore, when $V(\boldsymbol{x})$ is an even function, the NGF (3.1)–(3.3) can also be applied to compute the first excited state of the BEC when the initial data $\phi_0(\boldsymbol{x})$ is chosen to be an odd function [12]. In this case, the first excited state is a metastable steady state of the gradient flow, corresponding to a local minimum in the energy functional (2.15). In order to compute the ground and the first excited states of the BEC efficiently and accurately, we will discuss how to choose proper initial data $\phi_0(\boldsymbol{x})$ for different parameter regimes and propose two numerical schemes: the backward Euler sine-pseudospectral method (BESP) and the backward-forward Euler sine-pseudospectral method (BFSP), to discretize the NGF (3.1)–(3.3) in the next two sections.

The choice of proper initial data for the gradient flow is crucial to save the computational cost for computing the ground state. Without loss of generality, we assume that the trapping potential $V(\boldsymbol{x})$ in (2.11) satisfies

$$V(\boldsymbol{x}) = V_0(\boldsymbol{x}) + W(\boldsymbol{x}),\ V_0(\boldsymbol{x}) = \frac{1}{2}\left(\gamma_1^2 x_1^2 + \cdots + \gamma_d^2 x_d^2\right), \lim_{|\boldsymbol{x}|\to+\infty}\frac{W(\boldsymbol{x})}{V_0(\boldsymbol{x})} = 0, \tag{3.6}$$

where $\boldsymbol{x} = (x_1, \cdots, x_d)^T \in \mathbb{R}^d$ and $\gamma_j > 0$ for $1 \le j \le d$. In this case, when $|\beta|$ is not large, e.g. $|\beta| < 10$, a possible choice of the initial data is the ground state of the GPE (2.19) with $\beta = 0$ and $V(\boldsymbol{x}) = V_0(\boldsymbol{x})$ [13, 18, 94], i.e.

$$\phi_0(\boldsymbol{x}) = \frac{\left(\prod_{j=1}^d \gamma_j\right)^{1/4}}{\pi^{d/4}} \exp\left[-\left(\gamma_1 x_1^2 + \cdots + \gamma_d x_d^2\right)\right], \qquad \boldsymbol{x} \in \mathbb{R}^d. \tag{3.7}$$

On the other hand, when $|\beta|$ is not small, e.g. $|\beta| \ge 10$, a possible choice of the initial data is the Thomas-Fermi approximation [13]:

$$\phi_0(\boldsymbol{x}) = \frac{\phi_g^{\mathrm{TF}}(\boldsymbol{x})}{\|\phi_g^{\mathrm{TF}}\|}, \quad \phi_g^{\mathrm{TF}}(\boldsymbol{x}) = \begin{cases} \sqrt{\frac{\mu_g^{\mathrm{TF}} - V(\boldsymbol{x})}{\beta}}, & V_0(\boldsymbol{x}) < \mu_g^{\mathrm{TF}}, \\ 0, & \text{otherwise}, \end{cases} \qquad \boldsymbol{x} \in \mathbb{R}^d, \tag{3.8}$$

where

$$\mu_g^{\mathrm{TF}} = \frac{1}{2} \begin{cases} (3\beta\gamma_1)^{2/3}, & d = 1, \\ (4\beta\gamma_1\gamma_2)^{1/2}, & d = 2, \\ (15\beta\gamma_1\gamma_2\gamma_3/4\pi)^{2/5}, & d = 3. \end{cases}$$

3.1.2 Backward Euler sine-pseudospectral method (BESP)

As the trapping potential $V(\boldsymbol{x})$ given by (3.6) is infinity at far-field, the solution $\phi(\boldsymbol{x}, t)$ of (3.1)–(3.3) decays to zero exponentially fast when $|\boldsymbol{x}| \to \infty$. Therefore, in practical computation, the problem (3.1)–(3.3) can be truncated into a bounded computational domain with homogeneous Dirichlet boundary conditions:

$$\frac{\partial}{\partial t}\phi(\boldsymbol{x}, t) = \left(\frac{1}{2}\nabla^2 - V(\boldsymbol{x}) - \beta|\phi|^2\right)\phi(\boldsymbol{x}, t), \quad \boldsymbol{x} \in \Omega,\ t_n \le t < t_{n+1},\ n \ge 0, \tag{3.9}$$

$$\phi(\boldsymbol{x}, t_{n+1}) = \frac{\phi(\boldsymbol{x}, t_{n+1}^-)}{\|\phi(\cdot, t_{n+1}^-)\|}, \qquad \boldsymbol{x} \in \Omega,\ n \ge 0, \tag{3.10}$$

$$\phi(\boldsymbol{x}, t) = 0, \qquad \boldsymbol{x} \in \Gamma = \partial\Omega, \quad t > 0, \tag{3.11}$$

$$\phi(\boldsymbol{x}, 0) = \phi_0(\boldsymbol{x}), \quad \boldsymbol{x} \in \Omega \qquad \text{with} \quad \|\phi_0\|^2 := \int_\Omega |\phi_0(\boldsymbol{x})|^2\, d\boldsymbol{x} = 1. \tag{3.12}$$

We choose Ω as an interval (a, b) in 1D, a rectangle $(a, b) \times (c, d)$ in 2D, and a box $(a, b) \times (c, d) \times (e, f)$ in 3D, with $|a - b|$, $|c - d|$, and $|e - f|$ sufficiently large.

For simplicity of notation, we shall introduce the method in 1D, i.e. $d = 1$ in (3.9)–(3.12). Generalization to $d > 1$ is straightforward for tensor product grids and the results remain valid without modifications. For 1D, we choose the spatial mesh size $h = \Delta x > 0$ with $h = (b-a)/M$ where M is an even positive integer, and let the grid points be

$$x_j := a + j\ h, \qquad j = 0, 1, \cdots, M.$$

We let ϕ_j^n be the approximation of $\phi(x_j, t_n)$ and ϕ^n be the solution vector with component ϕ_j^n.

In order to discretize the gradient flow (3.9) with $d = 1$, we use the backward Euler method for time discretization and sine-pseudospectral method for spatial derivatives (BESP). Thus discretization of (3.9)–(3.12) reads

$$\frac{\phi_j^* - \phi_j^n}{\Delta t} = \frac{1}{2}\ D_{xx}^s \phi^*|_{x=x_j} - V(x_j)\phi_j^* - \beta|\phi_j^n|^2\phi_j^*, \quad j = 1, 2, \cdots, M-1, \tag{3.13}$$

$$\phi_0^* = \phi_M^* = 0, \qquad \phi_j^0 = \phi_0(x_j), \quad j = 0, 1, \cdots, M, \tag{3.14}$$

$$\phi_j^{n+1} = \frac{\phi_j^*}{\|\phi^*\|}, \qquad j = 0, 1, \cdots, M, \quad n = 0, 1, \cdots ; \tag{3.15}$$

where the norm is calculated as $\|\phi^*\|^2 = h\sum_{j=1}^{M-1}|\phi_j^*|^2$. Here D_{xx}^s, a spectral differential operator approximation of $\frac{\partial^2}{\partial x^2}$, is defined as

$$D_{xx}^s U|_{x=x_j} = -\frac{2}{M}\sum_{l=1}^{M-1}\ \mu_l^2 (\hat{U})_l\ \sin(\mu_l(x_j - a)), \qquad j = 1, 2, \cdots, M-1, \tag{3.16}$$

where $(\hat{U})_l$ $(l = 1, 2, \cdots, M-1)$, the sine transform coefficients of the vector $U = (U_0, U_1, \cdots, U_M)^T$ satisfying $U_0 = U_M = 0$, are defined as

$$\mu_l = \frac{\pi l}{b-a}, \qquad (\hat{U})_l = \sum_{j=1}^{M-1} U_j\ \sin(\mu_l(x_j - a)), \quad l = 1, 2, \cdots, M-1. \tag{3.17}$$

In discretization (3.13), a linear system has to be solved at every time step. We present here an efficient way to solve it iteratively by introducing a stabilization term with constant coefficient, and by using discrete sine transform:

$$\frac{\phi_j^{*,m+1} - \phi_j^n}{\Delta t} = \frac{1}{2}\ D_{xx}^s \phi^{*,m+1}\big|_{x=x_j} - \alpha\phi_j^{*,m+1} + \left(\alpha - V(x_j) - \beta|\phi_j^n|^2\right)\phi_j^{*,m},\ m \geq 0, \tag{3.18}$$

$$\phi_j^{*,0} = \phi_j^n, \qquad j = 0, 1, \cdots, M; \tag{3.19}$$

where $\alpha \geq 0$, called stabilization parameter, is to be determined. Taking discrete sine transform at both sides of (3.18) yields

$$\frac{(\widehat{\phi^{*,m+1}})_l - (\widehat{\phi^n})_l}{\Delta t} = -\left(\alpha + \frac{1}{2}\mu_l^2\right)(\widehat{\phi^{*,m+1}})_l + (\widehat{G^m})_l, \qquad l = 1, 2, \cdots, M-1, \tag{3.20}$$

where $(\widehat{G^m})_l$ are the sine transform coefficients of vector $G^m = (G_0^m, G_1^m, \cdots, G_M^m)^T$ which is defined as

$$G_j^m = \left(\alpha - V(x_j) - \beta|\phi_j^n|^2\right)\phi_j^{*,m}, \qquad j = 0, 1, \cdots, M. \tag{3.21}$$

Solving (3.20), we get

$$(\widehat{\phi^{*,m+1}})_l = \frac{2}{2 + \Delta t(2\alpha + \mu_l^2)}\left[(\widehat{\phi^n})_l + \Delta t\ (\widehat{G^m})_l\right], \qquad l = 1, 2, \cdots, M-1. \tag{3.22}$$

Taking the inverse discrete sine transform of (3.22) gives the solution of (3.18) immediately.

In order to find the optimal stabilization parameter α in (3.18) such that the iterative method (3.18) for solving (3.13) converges as fast as possible, we write (3.18) in matrix form

$$A\phi^{*,m+1} = B\phi^{*,m} + C, \qquad m = 0, 1, \cdots, \tag{3.23}$$

where

$$A = (1 + \alpha\Delta t)I - \frac{\Delta t}{2}D_{xx}^s, \qquad C = \left(\phi_1^n, \cdots, \phi_{M-1}^n\right)^{\mathrm{T}}, \tag{3.24}$$

$$B = \Delta t\ \mathrm{diag}\left(\alpha - V(x_1) - \beta|\phi_1^n|^2, \cdots, \alpha - V(x_{M-1}) - \beta|\phi_{M-1}^n|^2\right), \tag{3.25}$$

and I is the $(M-1)\times(M-1)$ identity matrix. Since A is a positive definite matrix, by the standard theory of iterative methods for a linear system [62], a sufficient and necessary condition for the convergence of the iterative method is

$$\rho\left(A^{-1}B\right) < 1. \tag{3.26}$$

Substituting (3.24) and (3.25) into condition (3.26), we obtain

$$\begin{aligned}\rho\left(A^{-1}B\right) &\leq \|A^{-1}B\|_2 \leq \|A^{-1}\|_2\|B\|_2 = \frac{\Delta t\ \max_{1\leq j\leq M-1}\left|\alpha - V(x_j) - \beta|\phi_j^n|^2\right|}{1 + \alpha\Delta t + \frac{\Delta t}{2}\min_{1\leq l\leq M-1}\mu_l^2} \\ &= \frac{\Delta t\max\{|\alpha - b_{\max}|, |\alpha - b_{\min}|\}}{1 + \alpha\Delta t + \frac{\pi^2\Delta t}{2(b-a)^2}},\end{aligned} \tag{3.27}$$

where

$$b_{\max} = \max_{1\le j\le M-1} \left(V(x_j) + \beta|\phi_j^n|^2\right), \qquad b_{\min} = \min_{1\le j\le M-1} \left(V(x_j) + \beta|\phi_j^n|^2\right).$$

Therefore, if we take the stabilization parameter α as

$$\alpha_{\text{opt}} = \frac{1}{2}\left(b_{\max} + b_{\min}\right), \tag{3.28}$$

we get

$$\begin{aligned} \rho\left(A^{-1}B\right) &\le \frac{\Delta t \max\{|\alpha_{\text{opt}} - b_{\max}|, |\alpha_{\text{opt}} - b_{\min}|\}}{1 + \alpha_{\text{opt}}\Delta t + \frac{\pi^2\Delta t}{2(b-a)^2}} \\ &\le \frac{\Delta t\left(b_{\min} + b_{\max}\right)}{2 + \Delta t\left(b_{\min} + b_{\max}\right) + \frac{\pi^2\Delta t}{(b-a)^2}} < 1, \end{aligned}$$

which guarantees the convergence of the iterative method (3.18) and the convergent rate is optimal as given by

$$R\left(A^{-1}B\right) := -\ln\rho\left(A^{-1}B\right) \ge \ln\frac{2 + \Delta t\left(b_{\min} + b_{\max}\right) + \frac{\pi^2\Delta t}{(b-a)^2}}{\Delta t\left(b_{\min} + b_{\max}\right)}. \tag{3.29}$$

3.1.3 Backward-forward Euler sine-pseudospectral method (BFSP)

Since ϕ^{n+1} in (3.15), i.e. ϕ^* in (3.13), is just an intermediate approximation of the ground state solution, it is not required to solve the linear system (3.13) for ϕ^* very accurately. Specifically, if we only iterate (3.18) for one step, the algorithm is significantly simplified. This is equivalent to using the sine-pseudospectral method for the spatial derivatives and the backward/forward Euler scheme for linear/nonlinear terms in the time derivatives (BFSP) for discretizing the gradient flow (3.9) with $d = 1$. Thus discretization of (3.9)–(3.12) reads

$$\frac{\phi_j^* - \phi_j^n}{\Delta t} = \frac{1}{2}\, D_{xx}^s\phi^*|_{x=x_j} - \alpha\phi_j^* + \left(\alpha - V(x_j) - \beta|\phi_j^n|^2\right)\phi_j^n, \quad j = 1, 2, \cdots, M-1, \tag{3.30}$$

$$\phi_0^* = \phi_M^* = 0, \qquad \phi_j^0 = \phi_0(x_j), \quad j = 0, 1, \cdots, M, \tag{3.31}$$

$$\phi_j^{n+1} = \frac{\phi_j^*}{\|\phi^*\|}, \qquad j = 0, 1, \cdots, M, \quad n = 0, 1, \cdots\ ; \tag{3.32}$$

where $\alpha \ge 0$ is the stabilization parameter. This discretization is implicit, but it can be solved directly via the fast sine transform. Therefore this numerical scheme is extremely efficient in practical computation. In fact, the memory requirement is $O(M)$ and computational cost per time step is $O(M\ln(M))$. Of course, there is a constraint for the time step such that the flow is energy diminishing. By Remark 2.13 in [12], the constraint for the time step Δt is

$$\Delta t < \frac{1}{\left|\alpha - V(x_j) - \beta|\phi_j^n|^2\right|} = \frac{1}{\max\{|\alpha - b_{\min}|,\ |\alpha - b_{\max}|\}}. \tag{3.33}$$

If we take $\alpha = \alpha_{\text{opt}} = \frac{b_{\max}+b_{\min}}{2}$, then the bound in the constraint for Δt is optimal. In this case, it reads

$$\Delta t < \frac{2}{b_{\min} + b_{\max}}. \tag{3.34}$$

3.1.4 Other discretization schemes

For comparison purposes, we review alternative discretization schemes for discretizing the gradient flow (3.9)–(3.12), which are currently used in the literature. One of them is the forward Euler sine-pseudospectral (FESP) scheme:

$$\frac{\phi_j^* - \phi_j^n}{\Delta t} = \frac{1}{2}\, D_{xx}^s \phi^n|_{x=x_j} - V(x_j)\phi_j^n - \beta|\phi_j^n|^2\phi_j^n, \quad j = 1, 2, \cdots, M-1. \tag{3.35}$$

The constraint for the time step Δt is

$$\Delta t < \frac{2}{2b_{\max} + \mu_{M-1}^2} = \frac{2}{2b_{\max} + (M-1)^2\pi^2/(b-a)^2} < \frac{2h^2}{\pi^2 + 2h^2 b_{\max}}. \tag{3.36}$$

Another scheme is the backward Euler finite difference (BEFD) method proposed in [12], which is unconditionally stable,

$$\frac{\phi_j^* - \phi_j^n}{\Delta t} = \frac{\phi_{j-1}^* - 2\phi_j^* + \phi_{j+1}^*}{2h^2} - V(x_j)\phi_j^n - \beta|\phi_j^n|^2\phi_j^n, \quad j = 1, 2, \cdots, M-1. \tag{3.37}$$

This discretization is second order accurate in space as demonstrated in [12].

3.2 Numerical results

In this section, we will demonstrate the spectral accuracy in space of the numerical methods BESP (3.13)–(3.15) and BFSP (3.30)–(3.32) for computing the ground and the first excited states of BEC. Numerical comparison between BESP and BFSP as well as with other existing numerical methods e.g. FESP and BEFD, will be performed in terms of spatial accuracy and computational time. The methods will then be applied to compute the ground and the first excited states of BEC in 1D, 2D and 3D for different trapping potentials, in particular the optical lattice potential.

3.2.1 Comparison of spatial accuracy and results in 1D

Example 3.2.1. We take $d = 1$ in (2.11) and study two kinds of trapping potentials

Case I. Harmonic oscillator potential $V(x) = \frac{x^2}{2}$ and $\beta = 400$;

Case II. Optical lattice potential $V(x) = \frac{x^2}{2} + 25\sin^2\left(\frac{\pi x}{4}\right)$ and $\beta = 250$.

The initial data (3.12) is chosen as (3.8) for computing the ground state, and as $\phi_0(x) = \frac{\sqrt{2}x}{\pi^{1/4}}e^{-x^2/2}$ for computing the first excited state. We solve the problem with BESP for $x \in [-16, 16]$, i.e. $a = -16$ and $b = 16$, and take the time step $\Delta t = 0.05$ for computing the ground state, and time step $\Delta t = 0.001$ for computing the first excited state. In this example and in the next two examples, the reason for smaller time step chosen in the computation of the first excited state is to suppress the round-off error in the fast sine transform (FST) and the inverse fast sine transform (IFST), such that the numerical solution is an odd function. The termination condition for solving the linear system is $\max_{1\le j\le M-1} |\phi_j^{*,m+1} - \phi_j^{*,m}| < 10^{-13}$, and the steady state solution of BESP is reached when $\max_{1\le j\le M-1}\ |\phi_j^{n+1} - \phi_j^{n}| < 10^{-12}$. We let ϕ_g and ϕ_1 be the ‘exact’ ground state and the ’exact’ first excited state which are obtained numerically by applying BESP with a very fine mesh $h = \frac{1}{32}$ and $h = \frac{1}{128}$, respectively. Their energies and chemical potentials are denoted as $E_g := E(\phi_g)$, $E_1 := E(\phi_1)$, and $\mu_g := \mu(\phi_g)$, $\mu_1 := \mu(\phi_1)$. We let $\phi_{g,h}^{\rm SP}$ and $\phi_{1,h}^{\rm SP}$ be the computed ground state and first excited state obtained by applying BESP with mesh size h. Similarly, $\phi_{g,h}^{\rm FD}$ and $\phi_{1,h}^{\rm FD}$ are obtained by applying BEFD in a similar way. Tables 3.1&3.2 list the errors for Case I, and Tables 3.3&3.4 list the errors for Case II. We also compute the energies and chemical potentials of the ground state and the first excited state based on our ‘exact’ solutions ϕ_g and ϕ_1. For Case I, we get $E_g := E(\phi_g) = 21.3601$ and $\mu_g := \mu(\phi_g) = 35.5775$ for the ground state, and $E_1 := E(\phi_1) = 22.0777$ and $\mu_1 := \mu(\phi_1) = 36.2881$ for the first excited state. Similarly, for Case II, we have $E_g = 26.0838$, $\mu_g = 38.0692$, $E_1 = 27.3408$ and $\mu_1 = 38.9195$. Figure 3.1 plots ϕ_g and ϕ_1 as well as their corresponding trapping potentials for Cases I&II.

mesh size	$h=1$	$h=1/2$	$h=1/4$	$h=1/8$
$\max\lvert\phi_g-\phi_{g,h}^{\mathrm{SP}}\rvert$	1.310E-3	7.037E-5	1.954E-8	<E-12
$\lVert\phi_g-\phi_{g,h}^{\mathrm{SP}}\rVert$	1.975E-3	7.425E-5	2.325E-8	<E-12
$\lvert E_g-E(\phi_{g,h}^{\mathrm{SP}})\rvert$	5.688E-5	2.642E-6	9E-12	<E-12
$\lvert\mu_g-\mu(\phi_{g,h}^{\mathrm{SP}})\rvert$	1.661E-2	8.705E-5	9.44E-10	4E-12
$\max\lvert\phi_g-\phi_{g,h}^{\mathrm{FD}}\rvert$	2.063E-3	1.241E-3	2.890E-4	7.542E-5
$\lVert\phi_g-\phi_{g,h}^{\mathrm{FD}}\rVert$	3.825E-3	1.439E-3	3.130E-4	7.705E-5
$\lvert E_g-E(\phi_{g,h}^{\mathrm{FD}})\rvert$	2.726E-3	9.650E-4	2.540E-4	6.439E-5
$\lvert\mu_g-\mu(\phi_{g,h}^{\mathrm{FD}})\rvert$	2.395E-2	6.040E-4	2.240E-4	5.694E-5

Table 3.1: Spatial resolution of BESP and BEFD for the ground state of Case I in Example 3.2.1.

Mesh size	$h=1/4$	$h=1/8$	$h=1/16$	$h=1/32$
$\max\lvert\phi_1-\phi_{1,h}^{\mathrm{SP}}\rvert$	2.064E-1	6.190E-4	2.099E-7	<E-12
$\lVert\phi_1-\phi_{1,h}^{\mathrm{SP}}\rVert$	1.093E-1	3.200E-4	1.403E-7	<E-12
$\lvert E_1-E(\phi_{1,h}^{\mathrm{SP}})\rvert$	5.259E-2	3.510E-4	5.550E-9	<E-12
$\lvert\mu_1-\mu(\phi_{1,h}^{\mathrm{SP}})\rvert$	1.216E-1	1.509E-3	4.762E-8	<E-12
$\max\lvert\phi_1-\phi_{1,h}^{\mathrm{FD}}\rvert$	2.348E-1	8.432E-3	2.267E-3	6.040E-4
$\lVert\phi_1-\phi_{1,h}^{\mathrm{FD}}\rVert$	1.197E-1	4.298E-3	1.215E-3	2.950E-4
$\lvert E_1-E(\phi_{1,h}^{\mathrm{FD}})\rvert$	3.154E-1	5.212E-2	1.382E-2	3.449E-3
$\lvert\mu_1-\mu(\phi_{1,h}^{\mathrm{FD}})\rvert$	4.216E-1	5.884E-2	1.609E-2	3.999E-3

Table 3.2: Spatial resolution of BESP and BEFD for the first excited state of Case I in Example 3.2.1.

Mesh size	$h=1$	$h=1/2$	$h=1/4$	$h=1/8$
$\max\lvert\phi_g-\phi_{g,h}^{\mathrm{SP}}\rvert$	7.982E-3	1.212E-3	2.219E-6	1.9E-11
$\lVert\phi_g-\phi_{g,h}^{\mathrm{SP}}\rVert$	1.304E-2	1.313E-3	2.431E-6	2.8E-11
$\lvert E_g-E(\phi_{g,h}^{\mathrm{SP}})\rvert$	4.222E-4	1.957E-4	4.994E-8	<E-12
$\lvert\mu_g-\mu(\phi_{g,h}^{\mathrm{SP}})\rvert$	9.761E-2	4.114E-3	5.605E-7	<E-12
$\max\lvert\phi_g-\phi_{g,h}^{\mathrm{FD}}\rvert$	1.019E-2	5.815E-3	1.001E-3	2.541E-4
$\lVert\phi_g-\phi_{g,h}^{\mathrm{FD}}\rVert$	1.967E-2	7.051E-3	1.390E-3	3.387E-4
$\lvert E_g-E(\phi_{g,h}^{\mathrm{FD}})\rvert$	7.852E-2	2.961E-2	7.940E-3	2.027E-3
$\lvert\mu_g-\mu(\phi_{g,h}^{\mathrm{FD}})\rvert$	1.786E-1	1.716E-2	6.730E-3	1.728E-3

Table 3.3: Spatial resolution of BESP and BEFD for the ground state of Case II in Example 3.2.1.

Mesh size	$h=1/4$	$h=1/8$	$h=1/16$	$h=1/32$
$\max\lvert\phi_1-\phi_{1,h}^{\rm SP}\rvert$	2.793E-1	1.010E-3	4.240E-7	2E-12
$\lVert\phi_1-\phi_{1,h}^{\rm SP}\rVert$	1.477E-1	5.241E-4	2.784E-7	2E-12
$\lvert E_1-E(\phi_{1,h}^{\rm SP})\rvert$	1.145E-1	8.337E-4	1.943E-8	<E-12
$\lvert\mu_1-\mu(\phi_{1,h}^{\rm SP})\rvert$	1.593E-1	2.357E-3	1.097E-7	5E-12
$\max\lvert\phi_1-\phi_{1,h}^{\rm FD}\rvert$	3.134E-1	1.124E-2	3.231E-3	8.450E-4
$\lVert\phi_1-\phi_{1,h}^{\rm FD}\rVert$	1.599E-1	5.779E-3	1.701E-3	4.122E-4
$\lvert E_1-E(\phi_{1,h}^{\rm FD})\rvert$	6.011E-1	1.002E-1	2.688E-2	6.707E-3
$\lvert\mu_1-\mu(\phi_{1,h}^{\rm FD})\rvert$	6.315E-1	9.887E-2	2.742E-2	6.827E-3

Table 3.4: Spatial resolution of BESP and BEFD for the first excited state of Case II in Example 3.2.1.

From Tables 3.1–3.4 and additional numerical experiments not presented here, it can be observed that BESP, BFSP and FESP are spectrally accurate in spatial discretization; where BEFD is only second-order accurate. The error in the ground and the first excited states is only due to the spatial discretization. We have also found how fine the mesh size h should be for BEFD so as to achieve very high accuracy. For Case I, we have $\max|\phi_g-\phi_{g,h}^{\rm FD}| = 1.4\times10^{-11}$ and $|E_g-E(\phi_{g,h}^{\rm FD})| = 8\times10^{-12}$ for the mesh size $h = 1/32768$; and $\max|\phi_1-\phi_{1,h}^{\rm FD}| = 2.68\times10^{-10}$ and $|E_1-E(\phi_{1,h}^{\rm FD})| = 8.30\times10^{-10}$ for the mesh size $h = 1/65536$. Similarly, for Case II, we have $\max|\phi_g-\phi_{g,h}^{\rm FD}| = 2.3\times10^{-11}$ and $|E_g-E(\phi_{g,h}^{\rm FD})| = 1.23\times10^{-10}$ for the mesh size $h = 1/32768$. When an optical lattice potential is applied, multiscale structures are observed in both ground and first excited states (cf. Figure 3.1(b)). Therefore, when high accuracy is required or when the solution exhibits multiscale or oscillatory structure, BESP and BFSP are much better than BEFD in a way that they need much less grid points. Thus they can save plenty of memory and computational time, especially in 2D and 3D simulations.

3.2.2 Comparison of computational time and results in 2D

Example 3.2.2. We consider a BEC in 2D harmonic plus optical lattice potential, $V(x,y) = \frac{1}{2}(x^2+y^2)+\kappa\left[\sin^2\left(\frac{\pi x}{4}\right)+\sin^2\left(\frac{\pi y}{4}\right)\right]$ in the GPE. The initial data (3.12) is chosen as (3.8) for computing the ground state ϕ_g, as $\phi_0(x,y)=\frac{\sqrt{2}x}{\pi^{1/2}}e^{-(x^2+y^2)/2}$ for the first excited state in x-direction ϕ_{10}, as $\phi_0(x,y)=\frac{\sqrt{2}y}{\pi^{1/2}}e^{-(x^2+y^2)/2}$ for the first excited state in y-direction ϕ_{01}, and as $\phi_0(x,y)=\frac{2xy}{\pi^{1/2}}e^{-(x^2+y^2)/2}$ for the first excited state in both x- and y-directions ϕ_{11}. The problem is solved in $\Omega=[-16,16]^2$ with the mesh size $h=\frac{1}{16}$. For comparison of different methods and different time steps, the termination condition for steady state solution is uniformly chosen as $\max_{j,k}\ \frac{|\phi_{jk}^{n+1}-\phi_{jk}^{n}|}{\Delta t} <$

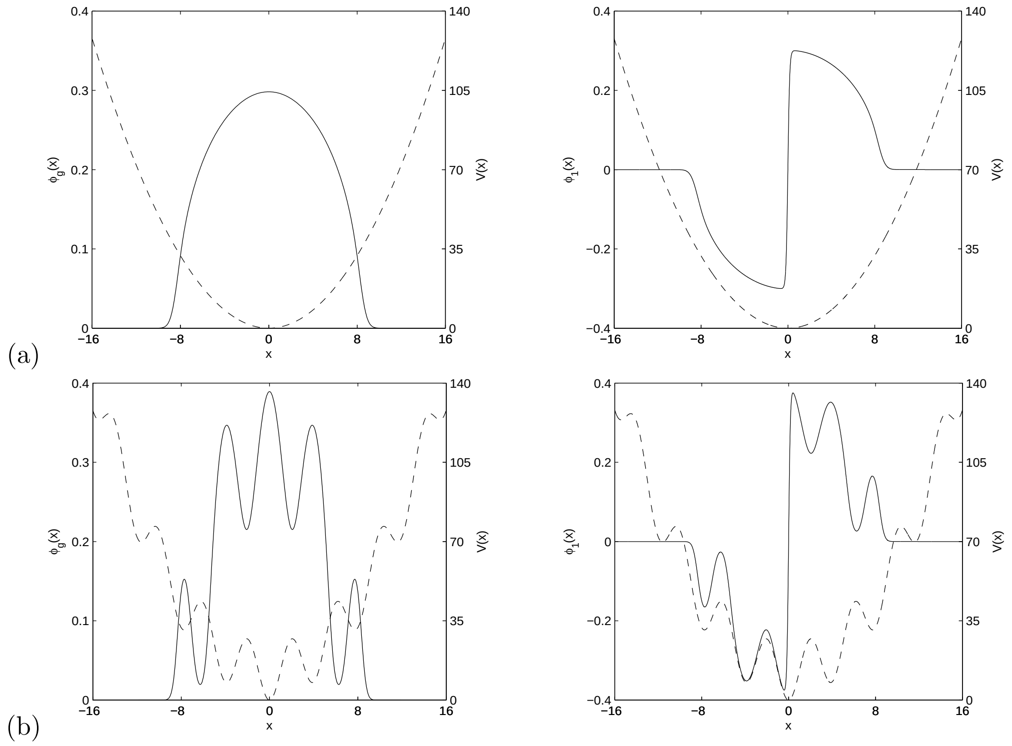

Figure 3.1: Ground state ϕ_g (left column, solid lines) and first excited state ϕ_1 (right column, solid lines) as well as trapping potentials (dashed lines) in Example 3.2.1 for (a) Case I; (b) Case II.

10^{-6}. Tables 3.5&3.6 show the computational time taken to get the ground state by using different methods and different time steps with $\kappa = 100$ for $\beta = 100$ and $\beta = 1000$ respectively. Also, Figure 3.2 visualizes the ground and the first excited states for $\beta = 500$ and $\kappa = 50$ by using BESP with the time step $\Delta t = 0.1$ and $\Delta t = 0.001$, respectively. Their energies and chemical potentials are also computed: $E_g = 32.2079$, $\mu_g = 41.7854$; $E_{10} := E(\phi_{10}) = E_{01} := E(\phi_{01}) = 34.6044$, $\mu_{10} := \mu(\phi_{10}) = \mu_{01} := \mu(\phi_{01}) = 43.8228$; and $E_{11} := E(\phi_{11}) = 37.0849$, $\mu_{11} := \mu(\phi_{11}) = 46.1402$.

From Tables 3.5–3.6 and Figure 3.2, following observations are made:

(i) BESP and BEFD are implicit methods. Energy diminishing is observed for both linear and nonlinear cases under any time step $\Delta t > 0$; FESP is explicit and BFSP is implicit but it can be implemented explicitly. For these two methods, energy diminishing is observed only when the time step Δt satisfies a constraint.

(ii) For BESP, the computational time is almost constant in the example for different β and different time step $0.001 \leq \Delta t \leq 0.5$. Thus it is not important how the time step is chosen. One can always choose $\Delta t = 0.5$ or $\Delta t = 0.1$ in practical computation. For FESP, only very small time step

Numerical scheme	Δt	Computational time	E_g	μ_g
BESP	0.5	597.6s	26.92580539	33.292591
	0.25	622.6s	26.92580539	33.292586
	0.1	637.3s	26.92580539	33.292585
	0.05	661.8s	26.92580539	33.292584
	0.01	805.9s	26.92580539	33.292584
	0.0025	1290s	26.92580539	33.292584
BFSP	0.1	52.1s	26.9357459	33.410725
	0.05	56.4s	26.9348784	33.405024
	0.025	63.7s	26.9334524	33.395124
	0.01	84.9s	26.9307326	33.373672
	0.005	117.2s	26.9285960	33.352679
	0.001	372.3s	26.9261198	33.312119
FESP	0.001	—	—	—
	0.0005	643.9s	26.92580539	33.29258356
	0.00025	1304s	26.92580539	33.29258357
	0.0001	3295s	26.92580539	33.29258357

Table 3.5: Computational times for computing the ground state in Example 3.2.2 by using different numerical schemes for $\beta = 100$.

Numerical scheme	Δt	Computational time	E_g	μ_g
BESP	0.5	593.9s	51.22028604	66.249024
	0.25	608.1s	51.22028604	66.249017
	0.1	620.6s	51.22028604	66.249013
	0.05	635.7s	51.22028604	66.249011
	0.01	743.3s	51.22028604	66.249010
	0.0025	1144s	51.22028604	66.249010
BFSP	0.025	—	—	—
	0.01	79.9s	51.2283083	66.376381
	0.005	106.1s	51.2248581	66.344476
	0.0025	165.8s	51.2223469	66.312619
	0.001	345.3s	51.2208091	66.280800
	0.0005	648.6s	51.2204428	66.266346
	0.00025	1251s	51.2203292	66.258089
FESP	0.001	—	—	—
	0.0005	606.8s	51.22028604	66.2490096
	0.00025	1306s	51.22028604	66.2490096
	0.0001	3331s	51.22028604	66.2490094

Table 3.6: Computational times for computing the ground state in Example 3.2.2 by using different numerical schemes for $\beta = 1000$.

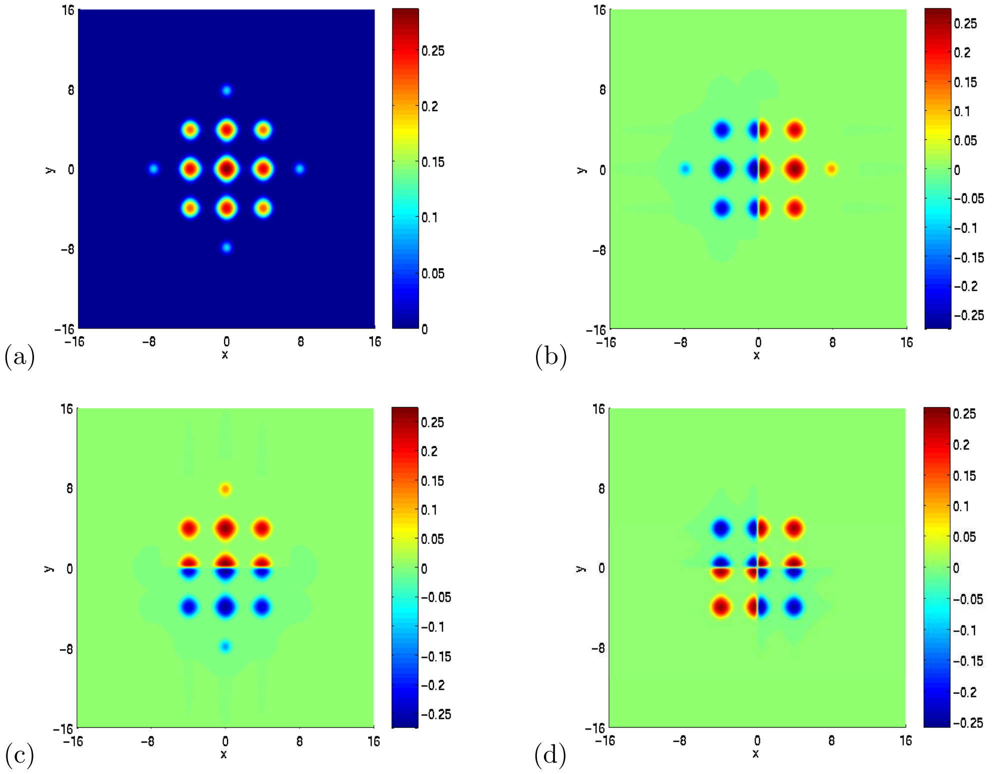

Figure 3.2: Top views of the (a) ground state ϕ_g; (b) first excited state in x-direction ϕ_{10}; (c) first excited state in y-direction ϕ_{01}; (d) first excited state in both x- and y-directions ϕ_{11}, of BEC in Example 3.2.2 for $\beta = 500$.

is allowed. When the time step is decreased by half, the computational time is doubled. For BFSP, a larger time step is allowed. The introduction of the stabilization term allows a larger time step to be chosen in the computation. When the time step is chosen near to the largest allowable time step, the computational time is much smaller than that in BESP. Furthermore, the growth rate of computational time with respect to time step size for BFSP is faster than that for BESP.

(iii) From the numerical values of the energy and chemical potential calculated, BESP performs better than BFSP in terms of accuracy. For BESP, the energy and chemical potential are almost independent of the time step chosen, while for BFSP, better results are obtained when smaller time step is used.

(iv) Interior layers are observed in the excited states when β is large (cf. Figure 3.2). Multiscale structures are observed in both ground and first excited states. Furthermore,

$$E(\phi_g) < E(\phi_{10}) = E(\phi_{01}) < E(\phi_{11}), \;\; \mu(\phi_g) < \mu(\phi_{10}) = \mu(\phi_{01}) < \mu(\phi_{11}), \quad \beta \geq 0,$$

$$\lim_{\beta\to\infty} \frac{E(\phi_{10})}{E(\phi_g)} = \frac{E(\phi_{11})}{E(\phi_g)} = 1, \qquad \lim_{\beta\to\infty} \frac{\mu(\phi_{10})}{\mu(\phi_g)} = \frac{\mu(\phi_{11})}{\mu(\phi_g)} = 1.$$

The relations $\phi_{10}(x,y) = \phi_{01}(y,x)$, $E(\phi_{10}) = E(\phi_{01})$ and $\mu(\phi_{10}) = \mu(\phi_{01})$ are due to the symmetry of the trapping potential, i.e. $V(x,y) = V(y,x)$.

3.2.3 Results in 3D

Example 3.2.3. The ground state and the first excited state of a BEC in a 3D harmonic plus optical lattice potential are computed, i.e. we take $d = 3$ and $V(x,y,z) = \frac{1}{2}(x^2+y^2+z^2) + 50\left[\sin^2\left(\frac{\pi x}{4}\right) + \sin^2\left(\frac{\pi y}{4}\right) + \sin^2\left(\frac{\pi z}{4}\right)\right]$. The initial data (3.12) is chosen as (3.8) for computing the ground state ϕ_g, as $\phi_0(x,y,z) = \frac{\sqrt{2}x}{\pi^{3/4}} e^{-(x^2+y^2+z^2)/2}$ for the first excited state in x-direction ϕ_{100}, as $\phi_0(x,y,z) = \frac{2xy}{\pi^{3/4}} e^{-(x^2+y^2+z^2)/2}$ for the first excited state in x- and y-directions ϕ_{110}, and as $\phi_0(x,y,z) = \frac{2^{3/2}xyz}{\pi^{3/4}} e^{-(x^2+y^2+z^2)/2}$ for the first excited state in x-, y- and z-directions ϕ_{111}. The problem is solved in $\Omega = [-8,8]^3$ by using BESP with mesh size $h = \frac{1}{8}$. The time step is chosen to be $\Delta t = 0.1$ for the computation of the ground state and $\Delta t = 0.001$ for the computation of the excited states. Figure 3.3 plots the isosurfaces of the ground state for $\beta = 100$, 800 and 6400. Figure 3.4 shows the isosurfaces of the excited states for $\beta = 100$. Table 3.7 lists the energies and chemical potentials of the ground state and the excited states for different β. BFSP gives similar results when $\Delta t = 0.01$ in the computation of the ground state and $\Delta t = 0.001$ in the computation of the excited states.

From Table 3.7, Figures 3.3–3.4 and additional experiments not presented here, the following observations are made:

(i) The BESP and BFSP are capable of computing the ground and the first excited states of BEC in 3D when the solutions exhibit multiscale structures.

(ii) Interior layers are observed in the excited state when β is large (cf. Figure 3.4). Multiscale structures are observed in both ground and first excited states for a condensate trapped in an optical lattice potential. Furthermore, we also observed numerically

$$E(\phi_g) < E(\phi_{100}) = E(\phi_{010}) = E(\phi_{001}) < E(\phi_{110}) = E(\phi_{101}) = E(\phi_{011}) < E(\phi_{111}),$$

$$\mu(\phi_g) < \mu(\phi_{100}) = \mu(\phi_{010}) = \mu(\phi_{001}) < \mu(\phi_{110}) = \mu(\phi_{101}) = \mu(\phi_{011}) < \mu(\phi_{11}), \quad \beta \geq 0,$$

$$\lim_{\beta\to\infty} \frac{E(\phi_{100})}{E(\phi_g)} = \frac{E(\phi_{110})}{E(\phi_g)} = \frac{E(\phi_{111})}{E(\phi_g)} = \lim_{\beta\to\infty} \frac{\mu(\phi_{100})}{\mu(\phi_g)} = \frac{\mu(\phi_{110})}{\mu(\phi_g)} = \frac{\mu(\phi_{111})}{\mu(\phi_g)} = 1.$$

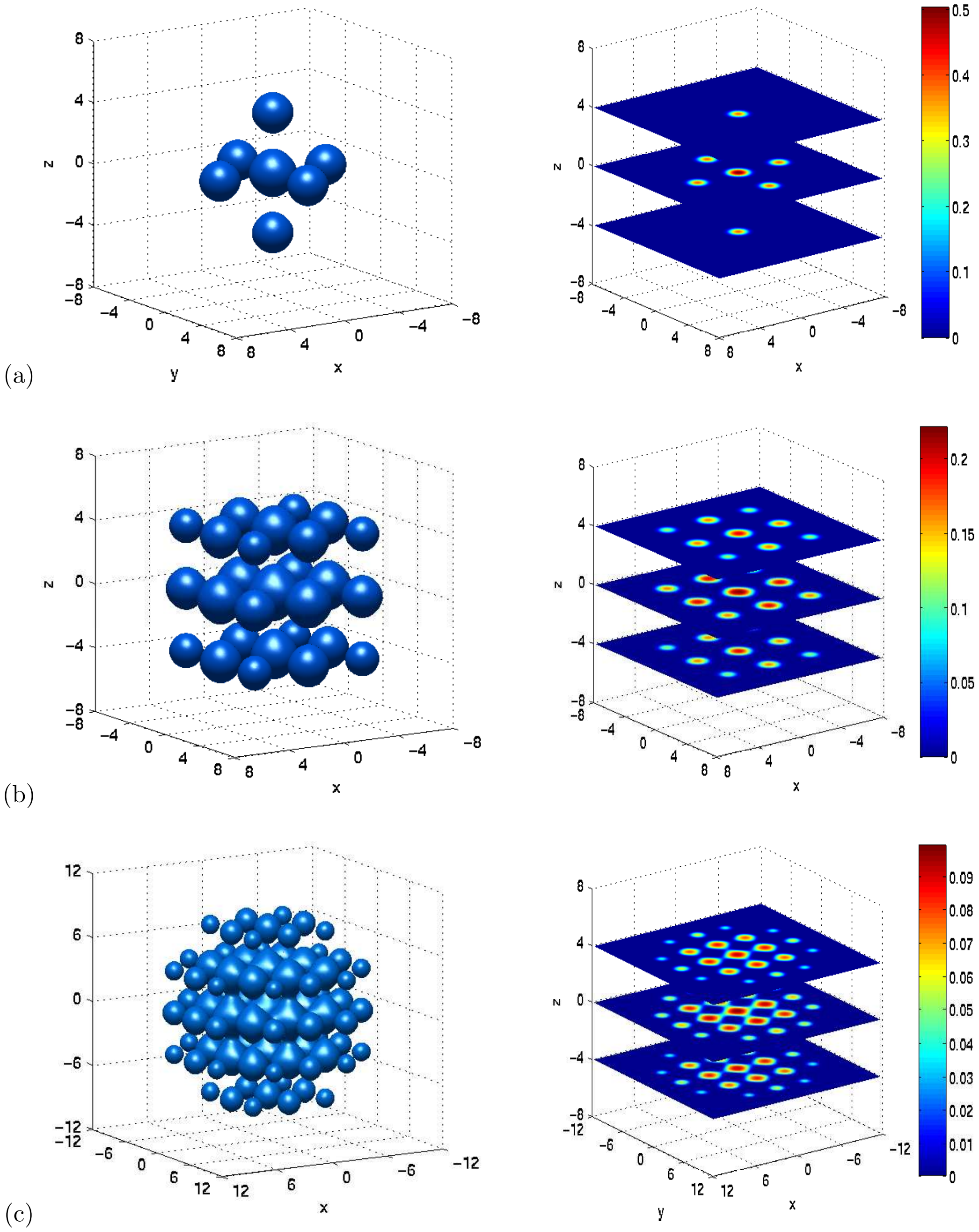

Figure 3.3: Isosurfaces (left column) and their corresponding slice views (right column) of BEC ground state in Example 3.2.3 for (a) $\beta = 100$; (b) $\beta = 800$; (c) $\beta = 6400$.

The relations $E(\phi_{100}) = E(\phi_{010})$ and $\mu(\phi_{100}) = \mu(\phi_{010})$ are due to the symmetry of the trapping potential, $V(x, y, z) = V(y, x, z)$.

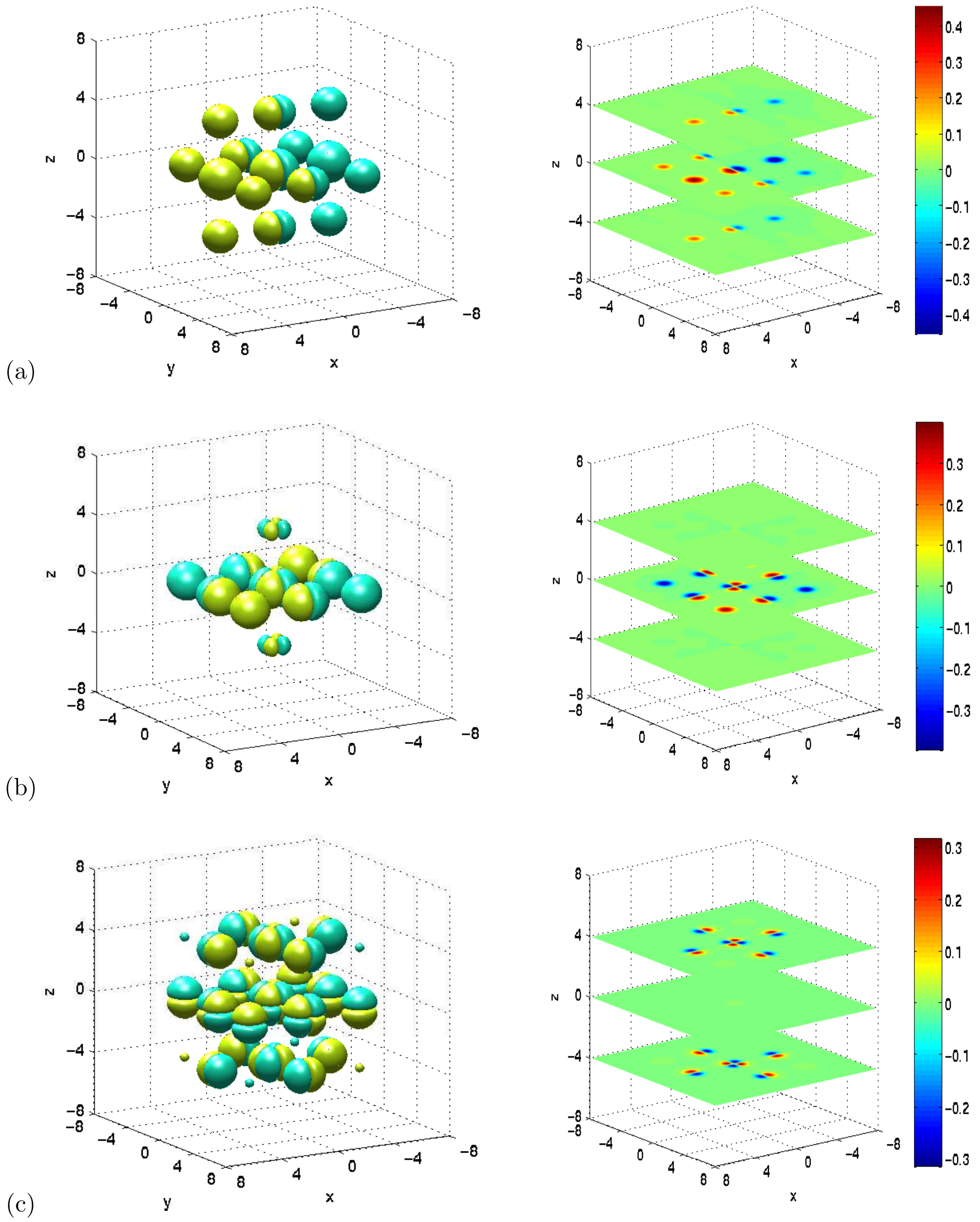

Figure 3.4: Isosurfaces (left column) and their corresponding slice views (right column) of BEC excited states in Example 3.2.3 for $\beta = 100$. (a) First excited state in x-direction ϕ_{100}; (b) first excited state in x- and y-directions ϕ_{110}; (c) first excited state in x-, y- and z-directions ϕ_{111}.

3.3 Discussion

We have presented two efficient and spectrally accurate numerical methods for computing the ground and the first excited states in BEC. The methods are based on the application of the

β	E_g μ_g	$E(\phi_{100})$ $\mu(\phi_{100})$	$E(\phi_{110})$ $\mu(\phi_{110})$	$E(\phi_{111})$ $\mu(\phi_{111})$
0	11.6439	19.2450	26.8462	34.4473
	11.6439	19.2450	26.8462	34.4473
10	15.9852	21.0720	27.8833	35.1742
	19.1506	22.5140	28.6755	35.7086
25	18.6574	22.9316	28.9665	35.7780
	21.3997	25.6428	30.6305	36.8161
100	23.2356	27.1939	31.2498	36.7368
	27.4757	30.4217	34.3400	38.4113
200	26.1956	29.7009	33.7883	38.2237
	30.6831	33.8039	38.0816	40.9526
800	33.8023	36.7106	39.6478	42.6474
	40.4476	42.9200	45.3623	47.8224
3200	45.2035	47.4672	50.3045	52.7426
	54.9862	56.8902	60.2456	62.3855
6400	52.4955	54.8717	58.0720	60.3200
	63.7149	66.3303	70.5760	72.5372

Table 3.7: Energies and chemical potentials of the ground and the excited states in Example 3.2.3 for different β.

sine-pseudospectral discretization for spatial derivatives and the backward Euler (BESP) or the backward/forward Euler (BFSP) discretization for linear/nonlinear terms for time derivatives in a normalized gradient flow. Both discretization schemes are demonstrated to be spectrally accurate in the computation of the ground and the first excited states of BEC. Furthermore, BESP is energy diminishing for any time step $\Delta t > 0$, while BFSP has a constraint on the time step Δt. Therefore larger mesh size and larger time step can be chosen in practical computation when high accuracy is required. Thus, the computational memory and computational time can be saved significantly, especially in 2D and 3D simulations.

Based on our extensive comparison of numerical results in terms of accuracy and computational time, we make the following suggestions on how to choose a suitable numerical method:

(i) If high accuracy is crucial in computing the BEC ground state, e.g. in an optical lattice potential or in a rotational frame, we always recommend to use BESP or BFSP. If one would like to avoid the difficulty on how to choose the time step, BESP with time step $\Delta t = 0.5$ or $\Delta t = 0.1$ is a good choice. Of course, if one can find the largest allowable time step for BFSP, then BFSP is a better choice since it needs much less computational time.

(ii) For computing the first excited state of BEC, in order to suppress the round-off error in the

FST and IFST in such a way that the numerical solution is an odd function, a small time step is required. Therefore, BFSP is recommended for computation.

(iii) We also propose here a combined method of BESP and BFSP, which gives high efficiency of BFSP and high resolution of BESP: first apply BFSP for the gradient flow evolution to reach a steady state solution, followed by applying BESP at a later stage to refine the solution. This scheme gives as highly accurate solution as BESP does, but with much less computational time as compared to applying only BESP.

Furthermore, an observation from our numerical simulation for BEC in a 1D box potential, which was performed for the asymptotic approximation in Chapter 2 but not presented in this chapter, is that the normalized gradient flow (NGF) and its BESP/BFSP discretization can be applied to compute the ground state and all the excited states in a box potential provided appropriate initial data is chosen. To compute the ground state, one can choose the initial data as $\phi_0(x) = \sqrt{2}\sin(\pi x)$. To compute the kth excited state, one can choose the initial data as $\phi_0(x) = \sqrt{2}\sin((k+1)\pi x)$. The reason that the algorithm can be used to compute any excited state is due to the fact that the roots of any fixed kth excited state are independent of the interaction parameter. Extension of this observation to high dimension is straightforward by tensor product.

Chapter 4

Spin-1 BEC Ground State

In earlier BEC experiments, atoms were confined in magnetic trap, in which the spin degree of freedom is frozen. The particles are described by the Gross-Pitaevskii equation (GPE) within the mean field approximation, which is a scalar model. In recent years, experimental achievement in creating spin-1 and spin-2 condensates [22, 63, 81, 103, 105] allows us to study various quantum phenomena that are generally absent in a single component condensate. The spinor condensate is achieved experimentally when an optical trap, instead of a magnetic trap, is used to provide equal confinement for all hyperfine states.

The theoretical formulation was first carried out by Ho [66], Ohmi and Machida [90], and Stamper-Kurn and Ketterle [104] for spin-1 condensate, and Ciobanu et al. [42], and Ueda and Kaoshi [110] for spin-2 condensate. In the effort of exploring the rich properties of spinor dynamics, various theoretical studies e.g. the coreless vortices [83], the quantum tunneling phenomena in double well potential [88], the interactions of soliton solutions [109], the effect of finite temperature in the context of Bogoliubov-de Gennes framework [85], etc, have been carried out to date by several authors.

In this chapter, we will study the ground state of spin-1 BEC by proposing an efficient numerical method to solve the coupled Gross-Pitaevskii equations (CGPEs) describing the condensate, by extending the normalized gradient flow (NGF) method applied in Chapter 3 [15]. The method will then be extended to spin-1 BEC in the presence of a uniform external magnetic field [16].

4.1 The Coupled Gross-Pitaevskii Equations (CGPEs)

In contrast to single component condensate, a spin-F ($F \in \mathbb{N}$) condensate is described by a generalized coupled GPEs which consist of $2F+1$ equations, each governing one of the $2F+1$ hyperfine states ($m_F = -F, -F+1, ..., F-1, F$) within the mean field approximation. For a spin-1 condensate, at temperature much lower than the critical temperature T_c, the three-component wavefunction $\Psi(\boldsymbol{x},t) = (\psi_1(\boldsymbol{x},t), \psi_0(\boldsymbol{x},t), \psi_{-1}(\boldsymbol{x},t))^T$ is well described by the following coupled Gross-Pitavskii equations (CGPEs) [44, 104, 115, 118, 119],

$$\begin{aligned}
i\hbar\frac{\partial}{\partial t}\psi_1(\boldsymbol{x},t) &= \left[-\frac{\hbar^2}{2m}\nabla^2 + V(\boldsymbol{x}) + (c_0+c_2)\left(|\psi_1|^2+|\psi_0|^2\right) + (c_0-c_2)|\psi_{-1}|^2\right]\psi_1 \\
&\quad + c_2\,\bar{\psi}_{-1}\,\psi_0^2, \qquad (4.1)\\
i\hbar\frac{\partial}{\partial t}\psi_0(\boldsymbol{x},t) &= \left[-\frac{\hbar^2}{2m}\nabla^2 + V(\boldsymbol{x}) + (c_0+c_2)\left(|\psi_1|^2+|\psi_{-1}|^2\right) + c_0|\psi_0|^2\right]\psi_0 \\
&\quad + 2c_2\,\psi_{-1}\,\bar{\psi}_0\,\psi_1, \qquad (4.2)\\
i\hbar\frac{\partial}{\partial t}\psi_{-1}(\boldsymbol{x},t) &= \left[-\frac{\hbar^2}{2m}\nabla^2 + V(\boldsymbol{x}) + (c_0+c_2)\left(|\psi_{-1}|^2+|\psi_0|^2\right) + (c_0-c_2)|\psi_1|^2\right]\psi_{-1} \\
&\quad + c_2\,\psi_0^2\,\bar{\psi}_1. \qquad (4.3)
\end{aligned}$$

Here $\bar{f}$ and $\mathrm{Re}(f)$ denote the conjugate and real part of the function f. There are two atomic collision terms, $c_0 = \frac{4\pi\hbar^2}{3m}(a_0+2a_2)$ and $c_2 = \frac{4\pi\hbar^2}{3m}(a_2-a_0)$, expressed in terms of the s-wave scattering lengths, a_0 and a_2, for scattering channel of total hyperfine spin 0 (anti-parallel spin collision) and spin 2 (parallel spin collision), respectively. The usual mean field interaction, c_0, is positive for repulsive interaction and negative for attractive interaction. The spin-exchange interaction, c_2, is positive for antiferromagnetic interaction and negative for ferromagnetic interaction. The three-component wavefunction is normalized according to

$$\|\Psi\|^2 := \int_{\mathbb{R}^3} |\Psi(\boldsymbol{x},t)|^2\, d\boldsymbol{x} = \int_{\mathbb{R}^3} \sum_{l=-1}^{1} |\psi_l(\boldsymbol{x},t)|^2\, d\boldsymbol{x} = \sum_{l=-1}^{1} \|\psi_l\|^2 = N, \qquad (4.4)$$

where N is the total number of particles in the condensate. The external trapping potential is taken to be a harmonic oscillator potential throughout this chapter, i.e.

$$V(\boldsymbol{x}) = \frac{m}{2}(\omega_x^2x^2 + \omega_y^2y^2 + \omega_z^2z^2), \qquad (4.5)$$

with ω_x, ω_y and ω_z being the trapping frequencies in x-, y- and z-direction, respectively.

By introducing dimensionless variables similar to a single component BEC: $t \to t/\omega_x$, $\boldsymbol{x} \to \boldsymbol{x}\ a_s$

with $a_s = \sqrt{\frac{\hbar}{m\omega_x}}$, $\psi_l \to \sqrt{N}\psi_l/a_s^{3/2}$ $(l=-1,0,1)$, we get the dimensionless CGPEs from (4.1)–(4.3) as [19, 118, 120]:

$$\begin{aligned} i\frac{\partial}{\partial t}\psi_1(\boldsymbol{x},t) &= \left[-\frac{1}{2}\nabla^2 + V(\boldsymbol{x}) + (\beta_n+\beta_s)\left(|\psi_1|^2+|\psi_0|^2\right) + (\beta_n-\beta_s)|\psi_{-1}|^2\right]\psi_1 \\ &\quad +\beta_s\,\bar{\psi}_{-1}\,\psi_0^2, \qquad (4.6)\\ i\frac{\partial}{\partial t}\psi_0(\boldsymbol{x},t) &= \left[-\frac{1}{2}\nabla^2 + V(\boldsymbol{x}) + (\beta_n+\beta_s)\left(|\psi_1|^2+|\psi_{-1}|^2\right) + \beta_n|\psi_0|^2\right]\psi_0 \\ &\quad +2\beta_s\,\psi_{-1}\,\bar{\psi}_0\,\psi_1, \qquad (4.7)\\ i\frac{\partial}{\partial t}\psi_{-1}(\boldsymbol{x},t) &= \left[-\frac{1}{2}\nabla^2 + V(\boldsymbol{x}) + (\beta_n+\beta_s)\left(|\psi_{-1}|^2+|\psi_0|^2\right) + (\beta_n-\beta_s)|\psi_1|^2\right]\psi_{-1} \\ &\quad +\beta_s\,\psi_0^2\,\bar{\psi}_1, \qquad (4.8)\end{aligned}$$

where $\beta_n = \frac{N\,c_0}{a_s^3\hbar\omega_x} = \frac{4\pi N(a_0+2a_2)}{3a_s}$, $\beta_s = \frac{N\,c_2}{a_s^3\hbar\omega_m} = \frac{4\pi N(a_2-a_0)}{3a_s}$ and $V(\boldsymbol{x}) = \frac{1}{2}(x^2 + \gamma_y^2 y^2 + \gamma_z^2 z^2)$ with $\gamma_y = \frac{\omega_y}{\omega_m}$ and $\gamma_z = \frac{\omega_z}{\omega_m}$. Similarly to those in a single component BEC, in a disk-shaped condensation ($\omega_y \approx \omega_x, \omega_z \gg \omega_x$), the 3D CGPEs can be reduced to 2D CGPEs; while in a cigar-shaped condensation ($\omega_y \gg \omega_x, \omega_z \gg \omega_x$) they can be reduced to 1D CGPEs. Thus, we consider here the dimensionless CGPEs in d dimensions ($d=1,2,3$), which take exactly the same form as (4.6)–(4.8), with

$$V(\boldsymbol{x}) = \frac{1}{2}\begin{cases} x^2, & d=1,\\ x^2+\gamma_y^2y^2, & d=2,\\ x^2+\gamma_y^2y^2+\gamma_z^2z^2, & d=3,\end{cases} \qquad (4.9)$$

being the harmonic oscillator trap in d dimensions, and

$$\beta_n = \begin{cases} \frac{2N(a_0+2a_2)}{3a_s}\frac{\sqrt{\omega_y\omega_z}}{\omega_x}, \\ \frac{2\sqrt{2\pi}N(a_0+2a_2)}{3a_s}\sqrt{\frac{\omega_z}{\omega_x}}, \\ \frac{4\pi N(a_0+2a_2)}{3a_s}, \end{cases} \qquad \beta_s = \begin{cases} \frac{2N(a_2-a_0)}{3a_s}\frac{\sqrt{\omega_y\omega_z}}{\omega_x}, & d=1,\\ \frac{2\sqrt{2\pi}N(a_2-a_0)}{3a_s}\sqrt{\frac{\omega_z}{\omega_x}}, & d=2,\\ \frac{4\pi N(a_2-a_0)}{3a_s}, & d=3,\end{cases} \qquad (4.10)$$

being the mean field interaction (spin-independent) and spin-exchange interaction (spin-dependent) in d dimensions. Three important invariants associated with (4.6)–(4.8) are the total mass (or normalization) of the wavefunction,

$$N(\Psi(\cdot,t)) := \|\Psi(\cdot,t)\|^2 := \int_{\mathbb{R}^d}\sum_{l=-1}^{1}|\psi_l(\boldsymbol{x},t)|^2\,d\boldsymbol{x} \equiv N(\Psi(\cdot,0)) = 1, \qquad t\ge 0, \qquad (4.11)$$

the total magnetization (or total spin) (with $-1 \le M \le 1$),

$$M(\Psi(\cdot,t)) := \int_{\mathbb{R}^d} \left[|\psi_1(\boldsymbol{x},t)|^2 - |\psi_{-1}(\boldsymbol{x},t)|^2\right] d\boldsymbol{x} \equiv M(\Psi(\cdot,0)) = M, \qquad t \ge 0, \tag{4.12}$$

and the energy per particle,

$$\begin{aligned} E(\Psi(\cdot,t)) \;=\; & \int_{\mathbb{R}^d} \Bigg\{ \sum_{l=-1}^{1} \left(\frac{1}{2}|\nabla\psi_l|^2 + V(\boldsymbol{x})|\psi_l|^2\right) + (\beta_n - \beta_s)|\psi_1|^2|\psi_{-1}|^2 \\ & + \frac{\beta_n}{2}|\psi_0|^4 + \frac{\beta_n + \beta_s}{2}\left[|\psi_1|^4 + |\psi_{-1}|^4 + 2|\psi_0|^2\left(|\psi_1|^2 + |\psi_{-1}|^2\right)\right] \\ & + \beta_s\left(\bar{\psi}_{-1}\psi_0^2\bar{\psi}_1 + \psi_{-1}\bar{\psi}_0^2\psi_1\right)\Bigg\} \, d\boldsymbol{x} \equiv E(\Psi(\cdot,0)), \qquad t \ge 0. \end{aligned} \tag{4.13}$$

We are interested to find the ground state of the condensate, $\Phi_g(\boldsymbol{x})$, which is obtained from the minimization of the energy functional (4.13) subjected to the conservation of total mass and magnetization:

Find ($\Phi_g \in S$) such that

$$E_g := E\left(\Phi_g\right) = \min_{\Phi \in S} E\left(\Phi\right), \tag{4.14}$$

where the nonconvex set S is defined as

$$S = \left\{ \Phi = (\phi_1, \phi_0, \phi_{-1})^T \mid \|\Phi\| = 1, \; \int_{\mathbb{R}^d} \left[|\phi_1(\boldsymbol{x})|^2 - |\phi_{-1}(\boldsymbol{x})|^2\right] d\boldsymbol{x} = M, \; E(\Phi) < \infty \right\}. \tag{4.15}$$

This is a nonconvex minimization problem. When $\beta_n \ge 0$, $\beta_n \ge |\beta_s|$ and $\lim_{|\boldsymbol{x}|\to\infty} V(\boldsymbol{x}) = \infty$, the existence of a solution of the nonconvex minimization problem (4.14) follows the standard theory [102]. Concerning uniqueness of the ground state, note that $E(\alpha \cdot \Phi_g) = E(\Phi_g)$ for all $\alpha = \left(e^{i\theta_1}, e^{i\theta_0}, e^{i\theta_{-1}}\right)^T$ with $\theta_1 + \theta_{-1} = 2\theta_0$. Therefore additional constraints have to be introduced to ensure the uniqueness.

As derived in [19], by defining the Lagrangian

$$\mathcal{L}(\Phi, \mu, \lambda) := E(\Phi) - \mu\left(\|\phi_1\|^2 + \|\phi_0\|^2 + \|\phi_{-1}\|^2 - 1\right) - \lambda\left(\|\phi_1\|^2 - \|\phi_{-1}\|^2 - M\right), \tag{4.16}$$

we get the Euler-Lagrange equations associated with the minimization problem (4.14):

$$(\mu + \lambda)\,\phi_1(\boldsymbol{x}) \;=\; \left[-\frac{1}{2}\nabla^2 + V(\boldsymbol{x}) + (\beta_n + \beta_s)\left(|\phi_1|^2 + |\phi_0|^2\right) + (\beta_n - \beta_s)|\phi_{-1}|^2\right]\phi_1$$

$$
\begin{aligned}
& +\beta_s\,\bar{\phi}_{-1}\,\phi_0^2 := H_1\,\phi_1, \qquad (4.17)\\
\mu\,\phi_0(\boldsymbol{x}) &= \left[-\frac{1}{2}\nabla^2 + V(\boldsymbol{x}) + (\beta_n+\beta_s)\left(|\phi_1|^2+|\phi_{-1}|^2\right) + \beta_n|\phi_0|^2\right]\phi_0\\
& +2\beta_s\,\phi_{-1}\,\bar{\phi}_0\,\phi_1 := H_0\,\phi_0, \qquad (4.18)\\
(\mu-\lambda)\,\phi_{-1}(\boldsymbol{x}) &= \left[-\frac{1}{2}\nabla^2 + V(\boldsymbol{x}) + (\beta_n+\beta_s)\left(|\phi_{-1}|^2+|\phi_0|^2\right) + (\beta_n-\beta_s)|\phi_1|^2\right]\phi_{-1}\\
& +\beta_s\,\phi_0^2\,\bar{\phi}_1 := H_{-1}\,\phi_{-1}, \qquad (4.19)
\end{aligned}
$$

where μ and λ are the Lagrange multipliers of the CGPEs (4.6)–(4.8). Equations (4.17)–(4.19) form a nonlinear eigenvalue problem under the two constraints

$$
\|\Phi\|^2 := \int_{\mathbb{R}^d} |\Phi(\boldsymbol{x})|^2\,d\boldsymbol{x} = \int_{\mathbb{R}^d} \sum_{l=-1}^{1} |\phi_l(\boldsymbol{x})|^2\,d\boldsymbol{x} := \sum_{l=-1}^{1} \|\phi_l\|^2 = 1, \qquad (4.20)
$$

$$
\|\phi_1\|^2 - \|\phi_{-1}\|^2 := \int_{\mathbb{R}^d} \left[|\phi_1(\boldsymbol{x})|^2 - |\phi_{-1}(\boldsymbol{x})|^2\right] d\boldsymbol{x} = M. \qquad (4.21)
$$

The nonlinear eigenvalue problem can also be obtained from the CGPEs (4.6)–(4.8) by substituting $\psi_l(\boldsymbol{x},t) = e^{-i\mu_l t}\phi_l(\boldsymbol{x})$ $(l = 1, 0, -1)$ with

$$
\mu_1 = \mu+\lambda, \quad \mu_0 = \mu, \quad \mu_{-1} = \mu-\lambda \qquad \Longleftrightarrow \qquad \mu_1+\mu_{-1} = 2\mu_0. \qquad (4.22)
$$

Since ϕ is independent of time, (4.17)–(4.19) are also called the time-independent CGPEs and μ_l is the chemical potential of the l-component. Any eigenfucntion Φ of the nonlinear eigenvalue problem (4.17)–(4.19) under constraints (4.20) and (4.21), whose energy is larger than the energy of the ground state is called the excited state of the condensate.

It is not obvious that the normalized gradient flow for solving the single component BEC ground state could be directly extended to compute the ground state of spin-1 BEC. The difficulty is that we only have two normalization conditions (i.e. the two constraints: conservation of total mass and magnetization) which are insufficient to determine the three projection constants for the three components of the wavefunction used in the normalization step. In the literature, the imaginary time method is applied to compute the ground state of spin-1 BEC through the introduction of a random variable to choose the three projection parameters in the projection step [118, 120]. This is not a determinate and efficient way to compute the ground state of spin-1 BEC due to the choice of the random variable. Bao and Wang [19] have proposed a continuous normalized gradient flow (CNGF) to compute the spin-1 BEC ground state. The CNGF is discretized by the Crank-Nicolson finite difference method with a special treatment of the nonlinear terms and thus the discretization scheme can be proved to be mass and magnetization conserved, and energy diminishing in the discretized level. However, at each time step, a fully nonlinear system must be solved which is tedious from computational point of view since the CNGF consists of integral-differential equations (see details in (4.32)–(4.40)) which involve implicitly the Lagrange multipliers in the normalized gradient flow evolution. The aim of this chapter is to introduce a third normalization condition based on the relation between the chemical potentials of a spin-1 BEC, in addition to the two existing normalization conditions given by the conservation of the total mass and the conservation of total magnetization. Thus the three projection constants used in the normalization step for the normalized gradient flow can be completely determined. This allows us to develop the normalized gradient flow method to compute the ground state of a spin-1 BEC.

4.2 Numerical Method

4.2.1 Normalized gradient flow (NGF) revisited

In order to compute the minimizer of the nonconvex minimization problem (4.14), an efficient technique for dealing with the normalization constraints in (4.15) is proposed based on the following construction: choose a time step size $k = \Delta t > 0$, discretize the time as $t_n = nk$ for $n = 0, 1, 2, \cdots$, and apply the imaginary time method, i.e. through a change of variable $t \to -it$, to form a normalized gradient flow with the following splitting scheme:

$$\begin{aligned}\frac{\partial}{\partial t}\phi_1(\boldsymbol{x},t) &= \left[\frac{1}{2}\nabla^2 - V(\boldsymbol{x}) - (\beta_n+\beta_s)\left(|\phi_1|^2+|\phi_0|^2\right) - (\beta_n-\beta_s)|\phi_{-1}|^2\right]\phi_1 \\ &\quad -\beta_s\,\bar{\phi}_{-1}\,\phi_0^2, \qquad\qquad (4.23)\\ \frac{\partial}{\partial t}\phi_0(\boldsymbol{x},t) &= \left[\frac{1}{2}\nabla^2 - V(\boldsymbol{x}) - (\beta_n+\beta_s)\left(|\phi_1|^2+|\phi_{-1}|^2\right) - \beta_n|\phi_0|^2\right]\phi_0 \\ &\quad -2\beta_s\,\phi_{-1}\,\bar{\phi}_0\,\phi_1, \qquad \boldsymbol{x}\in\mathbb{R}^d, \quad t_{n-1}\le t<t_n, \qquad n\ge 1, \qquad (4.24)\\ \frac{\partial}{\partial t}\phi_{-1}(\boldsymbol{x},t) &= \left[\frac{1}{2}\nabla^2 - V(\boldsymbol{x}) - (\beta_n+\beta_s)\left(|\phi_{-1}|^2+|\phi_0|^2\right) - (\beta_n-\beta_s)|\phi_1|^2\right]\phi_{-1} \\ &\quad -\beta_s\,\phi_0^2\,\bar{\phi}_1; \qquad\qquad (4.25)\end{aligned}$$

followed by a projection step as

$$\phi_1(\boldsymbol{x},t_n) := \phi_1(\boldsymbol{x},t_n^+) = \sigma_1^n\;\phi_1(\boldsymbol{x},t_n^-), \qquad (4.26)$$

$$\phi_0(\boldsymbol{x},t_n) := \phi_0(\boldsymbol{x},t_n^+) = \sigma_0^n\;\phi_0(\boldsymbol{x},t_n^-), \qquad \boldsymbol{x}\in\mathbb{R}^d, \qquad n\ge 1, \qquad (4.27)$$

$$\phi_{-1}(\boldsymbol{x},t_n) := \phi_{-1}(\boldsymbol{x},t_n^+) = \sigma_{-1}^n \ \phi_{-1}(\boldsymbol{x},t_n^-); \tag{4.28}$$

where $\phi_l(\boldsymbol{x},t_n^\pm) = \lim_{t\to t_n^\pm} \phi_l(\boldsymbol{x},t)$ $(l=-1,0,1)$ and σ_l^n $(l=-1,0,1)$ are the projection constants chosen such that

$$\|\Phi(\cdot,t_n)\|^2 = \sum_{l=-1}^{1} \|\phi_l(\cdot,t_n)\|^2 = 1, \qquad \|\phi_1(\cdot,t_n)\|^2 - \|\phi_{-1}(\cdot,t_n)\|^2 = M. \tag{4.29}$$

The gradient flow (4.23)–(4.25) can also be viewed as a result of applying the steepest decent method to the energy functional $E(\Phi)$ in (4.13) without constraints, and (4.26)–(4.28) project the solution back to the unit sphere S to satisfy the constraints in (4.15).

Substituting (4.26)–(4.28) into (4.29) yields

$$\sum_{l=-1}^{1} (\sigma_l^n)^2 \, \|\phi_l(\cdot,t_n^-)\|^2 = 1, \tag{4.30}$$

$$(\sigma_1^n)^2 \, \|\phi_1(\cdot,t_n^-)\|^2 - \left(\sigma_{-1}^n\right)^2 \, \|\phi_{-1}(\cdot,t_n^-)\|^2 = M. \tag{4.31}$$

There are three unknowns and only two equations in the above nonlinear system, so the solution is undetermined. In order to determine the projection constants σ_l^n $(l=-1,0,1)$, we need to find an additional equation which will be addressed in following section.

4.2.2 The third normalization condition

In order to find the third normalization equation to be used in the projection step of the normalized gradient flow, we first review the continuous normalized gradient flow (CNGF) constructed in [19] for computing the ground state of a spin-1 BEC in (4.14):

$$\begin{aligned}
\frac{\partial}{\partial t}\phi_1(\boldsymbol{x},t) &= \left[\frac{1}{2}\nabla^2 - V(\boldsymbol{x}) - (\beta_n+\beta_s)\left(|\phi_1|^2+|\phi_0|^2\right) - (\beta_n-\beta_s)|\phi_{-1}|^2\right]\phi_1 \\
&\quad -\beta_s\,\bar{\phi}_{-1}\,\phi_0^2 + \left[\mu_\Phi(t)+\lambda_\Phi(t)\right]\phi_1, && (4.32)\\
\frac{\partial}{\partial t}\phi_0(\boldsymbol{x},t) &= \left[\frac{1}{2}\nabla^2 - V(\boldsymbol{x}) - (\beta_n+\beta_s)\left(|\phi_1|^2+|\phi_{-1}|^2\right) - \beta_n|\phi_0|^2\right]\phi_0 \\
&\quad -2\beta_s\,\phi_{-1}\,\bar{\phi}_0\,\phi_1 + \mu_\Phi(t)\,\phi_0, && (4.33)\\
\frac{\partial}{\partial t}\phi_{-1}(\boldsymbol{x},t) &= \left[\frac{1}{2}\nabla^2 - V(\boldsymbol{x}) - (\beta_n+\beta_s)\left(|\phi_{-1}|^2+|\phi_0|^2\right) - (\beta_n-\beta_s)|\phi_1|^2\right]\phi_{-1} \\
&\quad -\beta_s\,\phi_0^2\,\bar{\phi}_1 + \left[\mu_\Phi(t)-\lambda_\Phi(t)\right]\phi_{-1}. && (4.34)
\end{aligned}$$

Here $\mu_\Phi(t)$ and $\lambda_\Phi(t)$ are chosen in a way that the above CNGF is mass (or normalization) and magnetization conserved. $\mu_\Phi(t)$ and $\lambda_\Phi(t)$ are given by [19]

$$\mu_\Phi(t) = \frac{R_\Phi(t)D_\Phi(t) - M_\Phi(t)F_\Phi(t)}{N_\Phi(t)R_\Phi(t) - M_\Phi^2(t)}, \qquad \lambda_\Phi(t) = \frac{N_\Phi(t)F_\Phi(t) - M_\Phi(t)D_\Phi(t)}{N_\Phi(t)R_\Phi(t) - M_\Phi^2(t)}, \tag{4.35}$$

with

$$N_\Phi(t) = \int_{\mathbb{R}^d} \left[|\phi_{-1}(\boldsymbol{x},t)|^2 + |\phi_0(\boldsymbol{x},t)|^2 + |\phi_1(\boldsymbol{x},t)|^2\right] d\boldsymbol{x}, \tag{4.36}$$

$$M_\Phi(t) = \int_{\mathbb{R}^d} \left[|\phi_1(\boldsymbol{x},t)|^2 - |\phi_{-1}(\boldsymbol{x},t)|^2\right]\ d\boldsymbol{x}, \tag{4.37}$$

$$R_\Phi(t) = \int_{\mathbb{R}^d} \left[|\phi_1(\boldsymbol{x},t)|^2 + |\phi_{-1}(\boldsymbol{x},t)|^2\right]\ d\boldsymbol{x}, \tag{4.38}$$

$$\begin{aligned} D_\Phi(t) \quad = \quad & \int_{\mathbb{R}^d}\Bigg\{\sum_{l=-1}^{1}\left(\frac{1}{2}|\nabla\phi_l|^2 + V(\boldsymbol{x})|\phi_l|^2\right) + 2(\beta_n - \beta_s)|\phi_1|^2|\phi_{-1}|^2 + \beta_n|\phi_0|^4 \\ & +(\beta_n+\beta_s)\Big[|\phi_1|^4 + |\phi_{-1}|^4 + 2|\phi_0|^2\left(|\phi_1|^2 + |\phi_{-1}|^2\right)\Big] \\ & +2\beta_s\left(\bar{\phi}_{-1}\phi_0^2\bar{\phi}_1 + \phi_{-1}\bar{\phi}_0^2\phi_1\right)\Bigg\}\ d\boldsymbol{x}, \end{aligned} \tag{4.39}$$

$$\begin{aligned} F_\Phi(t) \quad = \quad & \int_{\mathbb{R}^d}\Bigg\{\frac{1}{2}\left(|\nabla\phi_1|^2 - |\nabla\phi_{-1}|^2\right) + V(\boldsymbol{x})\left(|\phi_1|^2 - |\phi_{-1}|^2\right) \\ & +(\beta_n+\beta_s)\Big[|\phi_1|^4 - |\phi_{-1}|^4 + |\phi_0|^2\left(|\phi_1|^2 - |\phi_{-1}|^2\right)\Big]\Bigg\}\ d\boldsymbol{x}. \end{aligned} \tag{4.40}$$

For any given initial data

$$\Phi(\boldsymbol{x},0) = (\phi_1(\boldsymbol{x},0), \phi_0(\boldsymbol{x},0), \phi_{-1}(\boldsymbol{x},0))^T := \Phi^{(0)}(\boldsymbol{x}), \qquad \boldsymbol{x} \in \mathbb{R}^d, \tag{4.41}$$

satisfying

$$N_\Phi(t=0) := N_{\Phi^{(0)}} = 1, \qquad M_\Phi(t=0) := M_{\Phi^{(0)}} = M, \tag{4.42}$$

it was proven that the total mass and total magnetization are conserved in the CNGF (4.32)–(4.34), and at the same time the energy is diminishing [19], i.e.

$$N_\Phi(t) \equiv 1, \quad M_\Phi(t) \equiv M, \quad E\left(\Phi(\cdot,t\right) \le E\left(\Phi(\cdot,s)\right), \quad \text{for any } t \ge s \ge 0.$$

The normalized gradient flow (4.23)–(4.28) can be viewed as a result of applying a first order time-splitting scheme to the CNGF (4.32)–(4.34) and the projection step (4.26)–(4.28) is equivalent to solving the following nonlinear ordinary differential equations (ODEs):

$$\frac{\partial}{\partial t}\phi_1(\boldsymbol{x},t) = [\mu_\Phi(t) + \lambda_\Phi(t)]\,\phi_1, \tag{4.43}$$

$$\frac{\partial}{\partial t}\phi_0(\boldsymbol{x},t) = \mu_\Phi(t)\ \phi_0, \qquad t_{n-1} \le t \le t_n, \qquad n \ge 1, \tag{4.44}$$

$$\frac{\partial}{\partial t}\phi_{-1}(\boldsymbol{x},t) = [\mu_\Phi(t) - \lambda_\Phi(t)]\,\phi_{-1}. \tag{4.45}$$

The solution of the above ODEs can be expressed as

$$\phi_1(\boldsymbol{x},t_n) = \exp\left(\int_{t_{n-1}}^{t_n} [\mu_\Phi(\tau) + \lambda_\Phi(\tau)]\ d\tau\right)\phi_1(\boldsymbol{x},t_{n-1}), \tag{4.46}$$

$$\phi_0(\boldsymbol{x},t_n) = \exp\left(\int_{t_{n-1}}^{t_n} \mu_\Phi(\tau)\ d\tau\right)\phi_0(\boldsymbol{x},t_{n-1}), \tag{4.47}$$

$$\phi_{-1}(\boldsymbol{x},t_n) = \exp\left(\int_{t_{n-1}}^{t_n} [\mu_\Phi(\tau) - \lambda_\Phi(\tau)]\ d\tau\right)\phi_{-1}(\boldsymbol{x},t_{n-1}). \tag{4.48}$$

This solution gives the following relation between the coefficients

$$\exp\left(\int_{t_{n-1}}^{t_n} [\mu_\Phi(\tau) + \lambda_\Phi(\tau)]\ d\tau\right)\ \exp\left(\int_{t_{n-1}}^{t_n} [\mu_\Phi(\tau) - \lambda_\Phi(\tau)]\ d\tau\right)$$

$$= \exp\left(\int_{t_{n-1}}^{t_n} 2\mu_\Phi(\tau)\ d\tau\right) = \left[\exp\left(\int_{t_{n-1}}^{t_n} \mu_\Phi(\tau)\ d\tau\right)\right]^2. \tag{4.49}$$

This immediately suggests us to propose the third normalization equation,

$$\sigma_1^n\ \sigma_{-1}^n = \left(\sigma_0^n\right)^2, \tag{4.50}$$

to determine the projection parameters. In fact, equation (4.50) can be also obtained from the relation between the chemical potentials in (4.22) by physical intuition.

4.2.3 Normalization constants

The three normalization conditions (4.30), (4.31) and (4.50) form a nonlinear system of equations. They have to be solved to get an explicit expression for the normalization constants, σ_1, σ_0 and σ_{-1}.

Summing (4.30) and (4.31), we get

$$2(\sigma_1^n)^2\|\phi_1(\cdot,t_n^-)\|^2 = 1 + M - (\sigma_0^n)^2\|\phi_0(\cdot,t_n^-)\|^2. \tag{4.51}$$

This immediately implies

$$\sigma_1^n = \frac{\sqrt{1 + M - (\sigma_0^n)^2\|\phi_0(\cdot,t_n^-)\|^2}}{\sqrt{2}\ \|\phi_1(\cdot,t_n^-)\|}. \tag{4.52}$$

Subtracting (4.31) from (4.30) yields

$$2(\sigma_{-1}^n)^2\|\phi_{-1}(\cdot,t_n^-)\|^2 = 1 - M - (\sigma_0^n)^2\|\phi_0(\cdot,t_n^-)\|^2. \tag{4.53}$$

Again, this immediately implies

$$\sigma_{-1}^n = \frac{\sqrt{1 - M - (\sigma_0^n)^2\|\phi_0(\cdot,t_n^-)\|^2}}{\sqrt{2}\ \|\phi_{-1}(\cdot,t_n^-)\|}. \tag{4.54}$$

Multiplying (4.52) and (4.54) and noticing (4.50), we get

$$\begin{aligned}&\left[1 + M - (\sigma_0^n)^2\|\phi_0(\cdot,t_n^-)\|^2\right]\left[1 - M - (\sigma_0^n)^2\|\phi_0(\cdot,t_n^-)\|^2\right]\\ &\quad = 4\|\phi_{-1}(\cdot,t_n^-)\|^2\ \|\phi_1(\cdot,t_n^-)\|^2\ (\sigma_0^n)^4. \end{aligned}\tag{4.55}$$

The equation above can be simplified into

$$\begin{aligned}&\left[\|\phi_0(\cdot,t_n^-)\|^4 - 4\|\phi_{-1}(\cdot,t_n^-)\|^2\ \|\phi_1(\cdot,t_n^-)\|^2\right](\sigma_0^n)^4 - 2\|\phi_0(\cdot,t_n^-)\|^2\ (\sigma_0^n)^2\\ &\quad +(1 - M^2) = 0. \end{aligned}\tag{4.56}$$

Solving the above equation and noticing $(\sigma_0^n)^2\ \|\phi_0(\cdot,t_n^-)\|^2 \le (1 - M^2)$, we get

$$\begin{aligned}(\sigma_0^n)^2 &= \frac{\|\phi_0(\cdot,t_n^-)\|^2 - \sqrt{4(1-M^2)\|\phi_1(\cdot,t_n^-)\|^2\|\phi_{-1}(\cdot,t_n^-)\|^2 + M^2\|\phi_0(\cdot,t_n^-)\|^4}}{\|\phi_0(\cdot,t_n^-)\|^4 - 4\|\phi_{-1}(\cdot,t_n^-)\|^2\ \|\phi_1(\cdot,t_n^-)\|^2}\\ &= \frac{1 - M^2}{\|\phi_0(\cdot,t_n^-)\|^2 + \sqrt{4(1-M^2)\|\phi_1(\cdot,t_n^-)\|^2\|\phi_{-1}(\cdot,t_n^-)\|^2 + M^2\|\phi_0(\cdot,t_n^-)\|^4}}, \end{aligned}\tag{4.57}$$

as the only physical solution. It immediately implies that the normalization constant

$$\sigma_0^n = \frac{\sqrt{1-M^2}}{\left[\|\phi_0(\cdot,t_n^-)\|^2 + \sqrt{4(1-M^2)\|\phi_1(\cdot,t_n^-)\|^2\|\phi_{-1}(\cdot,t_n^-)\|^2 + M^2\|\phi_0(\cdot,t_n^-)\|^4}\right]^{1/2}}. \tag{4.58}$$

4.2.4 Backward-forward Euler sine-pseudospectral method

From numerical point of view, gradient flow (4.23)–(4.25) can be solved via any traditional technique, and the normalization of the gradient flow is simply achieved by a projection through the normalization constants (4.58), (4.52), and (4.54), at the end of each time step. Among all existing numerical schemes for solving the GPE for the BEC ground state, we choose the backward-forward Euler sine-pseudospectral method (BFSP) introduced in Chapter 2, and extend it to discretize the normalized gradient flow (4.23)–(4.25) and (4.26)–(4.28). The choice of the BFSP method is due to its efficiency in terms of spatial accuracy and computational time.

As the trapping potential $V(\boldsymbol{x})$ given by (4.5) is infinity at far-field, the solution $\Phi(\boldsymbol{x},t)$ decays to zero exponentially fast when $|\boldsymbol{x}| \to \infty$. Therefore the domain can be truncated into a bounded computational domain Ω with homogeneous Dirichlet boundary conditions. For simplicity of notation, we shall introduce the method for the case of one spatial dimension ($d = 1$) defined over the interval (a, b) with homogeneous Dirichlet boundary conditions. Generalization to higher dimension is straightforward for tensor product grids, and the results remain valid without modifications. For $d = 1$, we choose the spatial mesh size $h = \Delta x > 0$ with $h = (b-a)/L$ where L is an even positive integer, and let the grid points be

$$x_l := a + j\,h, \qquad j = 0, 1, \cdots, L.$$

Let $\Phi_j^n = (\phi_{1,j}^n, \phi_{0,j}^n, \phi_{-1,j}^n)^T$ be the approximation of $\Phi(x_j,t_n) = (\phi_1(x_j,t_n), \phi_0(x_j,t_n), \phi_{-1}(x_j,t_n))^T$ and Φ^n be the solution vector with component Φ_j^n. The sine-pseudospectral method is applied in the spatial discretization and the backward/forward Euler scheme is applied to the linear/nonlinear terms in the time discretization. The gradient flow (4.23)–(4.25) is discretized, for $j = 1, 2, \ldots, L-1$ and $n \geq 1$, as

$$\frac{\phi_{1,j}^* - \phi_{1,j}^{n-1}}{\Delta t} = \frac{1}{2}D_{xx}^s \phi_1^*|_{x=x_j} - \alpha_1 \phi_{1,j}^* + G_{1,j}^{n-1}, \tag{4.59}$$

$$\frac{\phi_{0,j}^* - \phi_{0,j}^{n-1}}{\Delta t} = \frac{1}{2}D_{xx}^s \phi_0^*|_{x=x_j} - \alpha_0 \phi_{0,j}^* + G_{0,j}^{n-1}, \tag{4.60}$$

$$\frac{\phi^*_{-1,j} - \phi^{n-1}_{-1,j}}{\Delta t} = \frac{1}{2} D^s_{xx} \phi^*_{-1}|_{x=x_j} - \alpha_{-1} \phi^*_{-1,j} + G^{n-1}_{-1,j}; \tag{4.61}$$

where

$$\begin{aligned} G^{n-1}_{1,j} &= \left[\alpha_1 - V(x_j) - (\beta_n + \beta_s)\left(|\phi^{n-1}_{1,j}|^2 + |\phi^{n-1}_{0,j}|^2\right) - (\beta_n - \beta_s)|\phi^{n-1}_{-1,j}|^2\right] \phi^{n-1}_{1,j} \\ &\quad -\beta_s\, \bar{\phi}^{n-1}_{-1,j}\, \left(\phi^{n-1}_{0,j}\right)^2, \qquad (4.62) \\ G^{n-1}_{0,j} &= \left[\alpha_0 - V(x_j) - (\beta_n + \beta_s)\left(|\phi^{n-1}_{1,j}|^2 + |\phi^{n-1}_{-1,j}|^2\right) - \beta_n |\phi^{n-1}_{0,j}|^2\right] \phi^{n-1}_{0,j} \\ &\quad -2\beta_s\, \phi^{n-1}_{-1,j}\, \bar{\phi}^{n-1}_{0,j}\, \phi^{n-1}_{1,j}, \qquad (4.63) \\ G^{n-1}_{-1,j} &= \left[\alpha_{-1} - V(x_j) - (\beta_n + \beta_s)\left(|\phi^{n-1}_{-1,j}|^2 + |\phi^{n-1}_{0,j}|^2\right) - (\beta_n - \beta_s)|\phi^{n-1}_{1,j}|^2\right] \phi^{n-1}_{-1,j} \\ &\quad -\beta_s\, \left(\phi^{n-1}_{0,j}\right)^2\, \bar{\phi}^{n-1}_{1,j}. \qquad (4.64) \end{aligned}$$

Here, D^s_{xx}, the pseudospectral differential operator approximation of $\frac{\partial^2}{\partial x^2}$, is defined as

$$D^s_{xx} U|_{x=x_j} = -\sum_{m=1}^{L-1} \mu_m^2 (\hat{U})_m \, \sin(\mu_m(x_j - a)), \qquad j = 1, 2, \cdots, L-1, \tag{4.65}$$

where $(\hat{U})_m$ $(m = 1, 2, \cdots, L-1)$, the sine transform coefficients of the vector $U = (U_0, U_1, \cdots, U_L)^T$ satisfying $U_0 = U_L = 0$, are defined as

$$\mu_m = \frac{\pi m}{b - a}, \qquad (\hat{U})_m = \frac{2}{L} \sum_{j=1}^{L-1} U_j \, \sin(\mu_m(x_j - a)), \quad m = 1, 2, \cdots, L-1; \tag{4.66}$$

and α_l $(l = -1, 0, 1)$ are the stabilization parameters, chosen in the optimal form (such that the time step can be taken as large as possible).

$$\alpha_1 = \frac{1}{2}\left(b_1^{\max} + b_1^{\min}\right), \quad \alpha_0 = \frac{1}{2}\left(b_0^{\max} + b_0^{\min}\right), \quad \alpha_{-1} = \frac{1}{2}\left(b_{-1}^{\max} + b_{-1}^{\min}\right); \tag{4.67}$$

with

$$\begin{aligned} b_1^{\max} &= \max_{1 \le j \le L-1} \left[V(x_j) + (\beta_n + \beta_s)\left(|\phi^{n-1}_{1,j}|^2 + |\phi^{n-1}_{0,j}|^2\right) + (\beta_n - \beta_s)|\phi^{n-1}_{-1,j}|^2\right], \\ b_1^{\min} &= \min_{1 \le j \le L-1} \left[V(x_j) + (\beta_n + \beta_s)\left(|\phi^{n-1}_{1,j}|^2 + |\phi^{n-1}_{0,j}|^2\right) + (\beta_n - \beta_s)|\phi^{n-1}_{-1,j}|^2\right], \\ b_0^{\max} &= \max_{1 \le j \le L-1} \left[V(x_j) + (\beta_n + \beta_s)\left(|\phi^{n-1}_{1,j}|^2 + |\phi^{n-1}_{-1,j}|^2\right) + \beta_n |\phi^{n-1}_{0,j}|^2\right], \\ b_0^{\min} &= \min_{1 \le j \le L-1} \left[V(x_j) + (\beta_n + \beta_s)\left(|\phi^{n-1}_{1,j}|^2 + |\phi^{n-1}_{-1,j}|^2\right) + \beta_n |\phi^{n-1}_{0,j}|^2\right], \\ b_{-1}^{\max} &= \max_{1 \le j \le L-1} \left[V(x_j) + (\beta_n + \beta_s)\left(|\phi^{n-1}_{-1,j}|^2 + |\phi^{n-1}_{0,j}|^2\right) + (\beta_n - \beta_s)|\phi^{n-1}_{1,j}|^2\right], \end{aligned}$$

$$b_{-1}^{\min} = \min_{1\le j\le L-1} \left[V(x_j) + (\beta_n+\beta_s)\left(|\phi_{-1,j}^{n-1}|^2 + |\phi_{0,j}^{n-1}|^2\right) + (\beta_n-\beta_s)|\phi_{1,j}^{n-1}|^2\right].$$

The homogeneous Dirichlet boundary conditions are discretized as

$$\phi_{1,0}^* = \phi_{1,L}^* = \phi_{0,0}^* = \phi_{0,L}^* = \phi_{-1,0}^* = \phi_{-1,L}^* = 0. \tag{4.68}$$

The projection step (4.26)–(4.28) is discretized, for $0 \le j \le L$ and $n \ge 1$, as

$$\phi_{1,j}^n = \sigma_1^n\ \phi_{1,j}^*, \quad \phi_{0,j}^n = \sigma_0^n\ \phi_{0,j}^*, \quad \phi_{-1,j}^n = \sigma_{-1}^n\ \phi_{-1,j}^*, \tag{4.69}$$

where

$$\sigma_0^n = \frac{\sqrt{1-M^2}}{\left[\|\phi_0^*\|^2 + \sqrt{4(1-M^2)\|\phi_1^*\|^2\|\phi_{-1}^*\|^2 + M^2\|\phi_0^*\|^4}\right]^{1/2}}, \tag{4.70}$$

$$\sigma_1^n = \frac{\sqrt{1+M-\alpha_0^2\|\phi_0^*\|^2}}{\sqrt{2}\ \|\phi_1^*\|}, \qquad \sigma_{-1}^n = \frac{\sqrt{1-M-\alpha_0^2\|\phi_0^*\|^2}}{\sqrt{2}\ \|\phi_{-1}^*\|}; \tag{4.71}$$

with

$$\|\phi_1^*\|^2 = h\sum_{j=1}^{L-1}|\phi_{1,j}^*|^2, \qquad \|\phi_0^*\|^2 = h\sum_{j=1}^{L-1}|\phi_{0,j}^*|^2, \qquad \|\phi_{-1}^*\|^2 = h\sum_{j=1}^{L-1}|\phi_{-1,j}^*|^2.$$

The initial data (4.41) is given by

$$\phi_{l,j}^0 = \phi_l(x_j,0), \qquad j=0,1,2,\cdots,L, \qquad l=-1,0,1.$$

The linear system (4.59)–(4.61) can be solved efficiently by making use of the fast sine transform. Taking discrete sine transform at both sides, we get

$$\frac{1}{\Delta t}\left[(\hat{\phi}_1^*)_m - (\hat{\phi}_1^{n-1})_m\right] = -\left[\frac{1}{2}\mu_m^2 + \alpha_1\right](\hat{\phi}_1^*)_m + (\hat{G}_1^{n-1})_m, \tag{4.72}$$

$$\frac{1}{\Delta t}\left[(\hat{\phi}_0^*)_m - (\hat{\phi}_0^{n-1})_m\right] = -\left[\frac{1}{2}\mu_m^2 + \alpha_0\right](\hat{\phi}_0^*)_m + (\hat{G}_0^{n-1})_m, \quad 1 \le m < L, \tag{4.73}$$

$$\frac{1}{\Delta t}\left[(\hat{\phi}_{-1}^*)_m - (\hat{\phi}_{-1}^{n-1})_m\right] = -\left[\frac{1}{2}\mu_m^2 + \alpha_{-1}\right](\hat{\phi}_{-1}^*)_m + (\hat{G}_{-1}^{n-1})_m. \tag{4.74}$$

Solving the above system in the phase space, we obtain

$$(\hat{\phi}_1^*)_m = \frac{1}{1+\Delta t\,[\alpha_1 + \mu_m^2/2]}\left[(\hat{\phi}_1^{n-1})_m + (\hat{G}_1^{n-1})_m\right], \tag{4.75}$$

$$(\hat{\phi}_0^*)_m = \frac{1}{1+\Delta t\,[\alpha_0 + \mu_m^2/2]}\left[(\hat{\phi}_0^{n-1})_m + (\hat{G}_0^{n-1})_m\right], \quad 1 \le m < L, \tag{4.76}$$

$$(\hat{\phi}^{*}_{-1})_m = \frac{1}{1+\Delta t\,[\alpha_{-1}+\mu_m^2/2]}\left[(\hat{\phi}^{n-1}_{-1})_m + (\hat{G}^{n-1}_{-1})_m\right]. \tag{4.77}$$

An inverse fast sine transform followed by the projection (4.69) yields the solution Φ^n.

4.2.5 Chemical potentials

After getting the ground state Φ numerically, the energy of the ground state can be computed from the discretization of (4.13) immediately. In order to compute the chemical potentials numerically, different formulations can be applied. We propose here a reliable way to compute them. Multiplying both sides of (4.17) by $\bar{\phi}_1$ and integrating over $\mathbb{R}^d$, we get

$$(\mu+\lambda)\|\phi_1\|^2 = \int_{\mathbb{R}^d} \bar{\phi}_1\; H_1\phi_1\; d\boldsymbol{x} := (\phi_1, H_1\phi_1). \tag{4.78}$$

Similarly, applying the same procedure to (4.18) and (4.19) by multiplying $\bar{\phi}_0$ and $\bar{\phi}_{-1}$, respectively, we obtain

$$\mu\|\phi_0\|^2 = \int_{\mathbb{R}^d} \bar{\phi}_0\; H_0\phi_0\; d\boldsymbol{x} := (\phi_0, H_0\phi_0), \tag{4.79}$$

$$(\mu-\lambda)\|\phi_{-1}\|^2 = \int_{\mathbb{R}^d} \bar{\phi}_{-1}\; H_{-1}\phi_{-1}\; d\boldsymbol{x} := (\phi_{-1}, H_{-1}\phi_{-1}). \tag{4.80}$$

Summing (4.78)–(4.80), noticing that the ground state Φ satisfy the constraints (4.15), we get

$$\mu + M\;\lambda = (\phi_1, H_1\phi_1) + (\phi_0, H_0\phi_0) + (\phi_{-1}, H_{-1}\phi_{-1}). \tag{4.81}$$

Subtracting (4.80) from (4.78) yields

$$M\;\mu + \left(\|\phi_1\|^2 + \|\phi_{-1}\|^2\right)\lambda = (\phi_1, H_1\phi_1) - (\phi_{-1}, H_{-1}\phi_{-1}). \tag{4.82}$$

Solving the linear system (4.81) and (4.82) for the chemical potentials μ and λ as unknowns and applying integration by parts to the right hand sides of the linear system, we get

$$\mu = \frac{\left(\|\phi_1\|^2+\|\phi_{-1}\|^2\right)D(\Phi) - M\;F(\Phi)}{\|\phi_1\|^2+\|\phi_{-1}\|^2-M^2}, \qquad \lambda = \frac{F(\Phi)-M\;D(\Phi)}{\|\phi_1\|^2+\|\phi_{-1}\|^2-M^2}, \tag{4.83}$$

where

$$\begin{aligned} D(\Phi) &= \int_{\mathbb{R}^d}\Bigg\{\sum_{l=-1}^{1}\left(\frac{1}{2}|\nabla\phi_l|^2+V(\boldsymbol{x})|\phi_l|^2\right)+2(\beta_n-\beta_s)|\phi_1|^2|\phi_{-1}|^2+\beta_n|\phi_0|^4 \\ &\quad+(\beta_n+\beta_s)\Big[|\phi_1|^4+|\phi_{-1}|^4+2|\phi_0|^2\left(|\phi_1|^2+|\phi_{-1}|^2\right)\Big] \\ &\quad+2\beta_s\left(\bar{\phi}_{-1}\phi_0^2\bar{\phi}_1+\phi_{-1}\bar{\phi}_0^2\phi_1\right)\Bigg\}\,d\boldsymbol{x}, \end{aligned} \tag{4.84}$$

$$\begin{aligned} F(\Phi) &= \int_{\mathbb{R}^d}\Bigg\{\frac{1}{2}\left(|\nabla\phi_1|^2-|\nabla\phi_{-1}|^2\right)+V(\boldsymbol{x})\left(|\phi_1|^2-|\phi_{-1}|^2\right) \\ &\quad+(\beta_n+\beta_s)\Big[|\phi_1|^4-|\phi_{-1}|^4+|\phi_0|^2\left(|\phi_1|^2-|\phi_{-1}|^2\right)\Big]\Bigg\}\,d\boldsymbol{x}. \end{aligned} \tag{4.85}$$

The chemical potentials μ and λ can then be computed numerically from the discretization of (4.83)–(4.85). Note that the expressions (4.83) are the same as (4.35) in which the Lagrange multipliers are chosen in such a way that the CNGF is normalization and magnetization conserved, and energy diminishing.

4.3 Numerical Results

In this section, we will first show that the spin-1 BEC ground state computed by our numerical method is independent of the choice of initial data in (4.41) and verify numerically the energy diminishing property of the method. Finally, we will apply the method to compute the ground state of spin-1 BECs with different interactions, in different trapping potentials. In the computations, the ground state is reached by using the numerical method (4.59)–(4.61), (4.69)–(4.71) when $\|\Phi_h^{n+1}-\Phi_h^n\|\le\varepsilon:=10^{-7}$. In addition, for the ground state of spin-1 BEC, we have $M\leftrightarrow -M \iff \phi_1\leftrightarrow\phi_{-1}$, thus we present only the results for $0\le M\le 1$.

4.3.1 Choice of initial data

In our tests, two typical physical experiments in harmonic potential are considered:

- Case I. Condensate with ferromagnetic interaction, e.g. ^{87}Rb confined in a cigar-shaped trapping potential with parameters: $m=1.443\times10^{-25}$[kg], $a_0=5.387$[nm], $a_2=5.313$[nm],

$\omega_x = 2\pi \times 20$[Hz], $\omega_y = \omega_z = 2\pi \times 400$[Hz]. These parameters give the dimensionless quantities in (4.6)–(4.8) for the computations as: $d = 1$, $V(x) = x^2/2$, $\beta_n \approx \frac{4\pi(a_0+2a_2)N}{3a_s}\frac{\sqrt{\omega_y\omega_z}}{2\pi\omega_x} = 0.0885N$ and $\beta_s \approx \frac{4\pi(a_2-a_0)N}{3a_s}\frac{\sqrt{\omega_y\omega_z}}{2\pi\omega_x} = -0.00041N$ with N being the total number of atoms in the condensate, the dimensionless length unit $a_s = \sqrt{\hbar/m\omega_x} = 2.4116 \times 10^{-6}$ [m] and time unit $t_s = 1/\omega_x = 0.007958$[s].

- Case II. Condensate with antiferromagnetic interaction, e.g. ^{23}Na confined in a cigar-shaped trapping potential with parameters: $m = 3.816 \times 10^{-26}$[kg], $a_0 = 2.646$[nm], $a_2 = 2.911$[nm], $\omega_x = 2\pi \times 20$[Hz], $\omega_y = \omega_z = 2\pi \times 400$[Hz]. These parameters give the following dimensionless quantities in the computations: $d = 1$, $V(x) = x^2/2$, $\beta_n \approx 0.0241N$ and $\beta_s \approx 0.00075N$ with the dimensionless length unit $a_s = 4.6896 \times 10^{-6}$ [m] and time unit $t_s = 0.007958$[s].

We first verify that the converged solution is independent of different choices of the initial data in (4.41), and that the normalized gradient flow is energy diminishing. In order to do so, we choose the initial data in (4.41) as

- Gaussian profiles satisfying the constraints in (4.15) initially, i.e.

$$\phi_1(x,0) = \frac{\sqrt{0.5(1+M-\kappa)}}{\pi^{1/4}}e^{-x^2/2}, \tag{4.86}$$

$$\phi_0(x,0) = \frac{\sqrt{\kappa}}{\pi^{1/4}}e^{-x^2/2}, \qquad -\infty < x < \infty, \tag{4.87}$$

$$\phi_{-1}(x,0) = \frac{\sqrt{0.5(1-M-\kappa)}}{\pi^{1/4}}e^{-x^2/2}, \tag{4.88}$$

  where κ is a constant satisfying $0 < \kappa < 1 - |M|$.

- Unnormalized Gaussian profiles, i.e.

$$\phi_1(x,0) = \phi_0(x,0) = \phi_{-1}(x,0) = e^{-x^2/2}, \qquad \infty < x < \infty. \tag{4.89}$$

The problem (4.14) is solved by the numerical method in the domain $[-16, 16]$ with time step $\Delta t = 0.005$ and mesh size $h = 1/64$. Figure 4.1 plots the time evolution of $N_l(t) := \|\phi_l(\cdot,t)\|^2$ ($l = 1, 0, -1$) for ^{87}Rb in Case I with $M = 0.5$ and $N = 10^4$ for different initial data (4.86)–(4.89), and Figure 4.2 shows similar results for ^{23}Na in Case II. Figure 4.3 depicts the time evolution of the energy for the two cases with $M = 0.5$ and $N = 10^4$ for different choices of initial data.

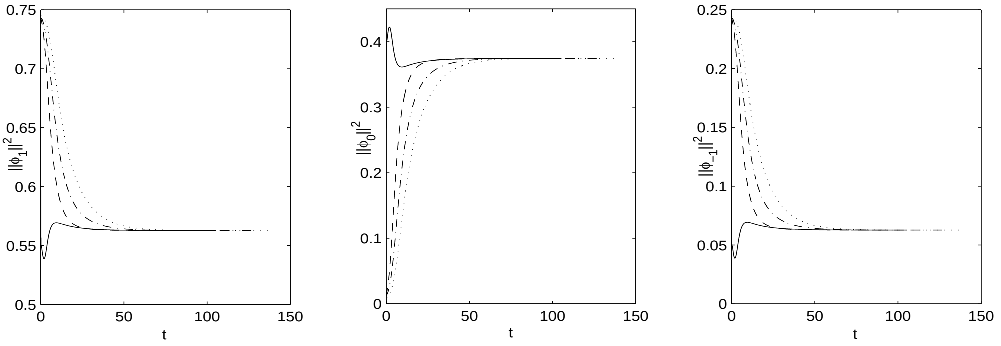

Figure 4.1: Time evolution of $N_1 = \|\phi_1(\cdot,t)\|^2$ (left), $N_0 = \|\phi_0(\cdot,t)\|^2$ (middle) and $N_{-1} = \|\phi_{-1}(\cdot,t)\|^2$ (right) described by normalized gradient flow (4.26)–(4.28) for ^{87}Rb in Case I with $M = 0.5$ and $N = 10^4$, with different initial data (4.89) (solid line) and (4.86)–(4.88) with $\kappa = 0.1$ (dotted line), $\kappa = 0.2$ (dash-dot line) and $\kappa = 0.4$ (dashed line), respectively.

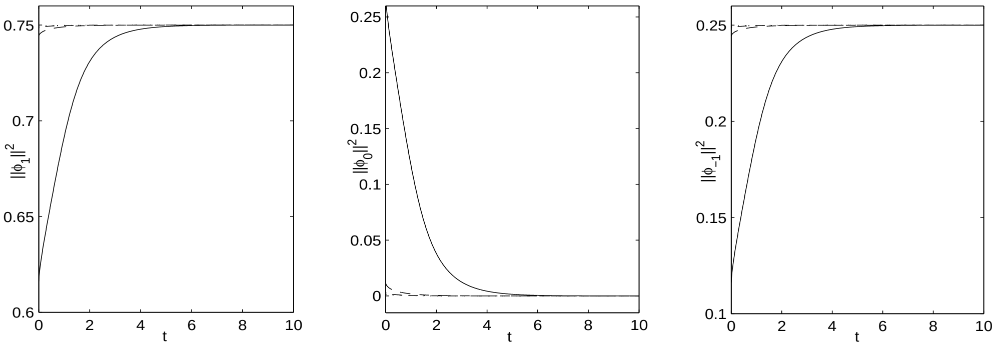

Figure 4.2: Time evolution of $N_1 = \|\phi_1(\cdot,t)\|^2$ (left), $N_0 = \|\phi_0(\cdot,t)\|^2$ (middle) and $N_{-1} = \|\phi_{-1}(\cdot,t)\|^2$ (right) described by normalized gradient flow (4.26)–(4.28) for ^{23}Na in Case II with $M = 0.5$ and $N = 10^4$, with different initial data (4.89) (solid line) and (4.86)–(4.88) with $\kappa = 0.1$ (dotted line), $\kappa = 0.2$ (dash-dot line) and $\kappa = 0.4$ (dashed line), respectively.

From Figures 4.1&4.2, we can see that the converged ground state is independent of the choice of initial data. In addition to that, based on our extensive numerical experiments on other types of initial data (not presented here for brevity), the numerical method always gives the ground state if all three components in the initial data are chosen as nonnegative functions. Furthermore, Figure 4.3 demonstrates the energy diminishing property of the normalized gradient flow and its full discretization when the time step Δt is small. Based on the numerical experiments, for $0 \le M \le 1$, we suggest the initial data in (4.41) to be chosen as: i) with ferromagnetic interaction ($\beta_s \le 0$),

$$\phi_1(\boldsymbol{x}) = \frac{1}{2}\sqrt{1+3M}\phi_g^{\rm ap}(\boldsymbol{x}), \quad \phi_0(\boldsymbol{x}) = \sqrt{\frac{1-M}{2}}\phi_g^{\rm ap}(\boldsymbol{x}), \quad \phi_1(\boldsymbol{x}) = \frac{1}{2}\sqrt{1-M}\phi_g^{\rm ap}(\boldsymbol{x});$$

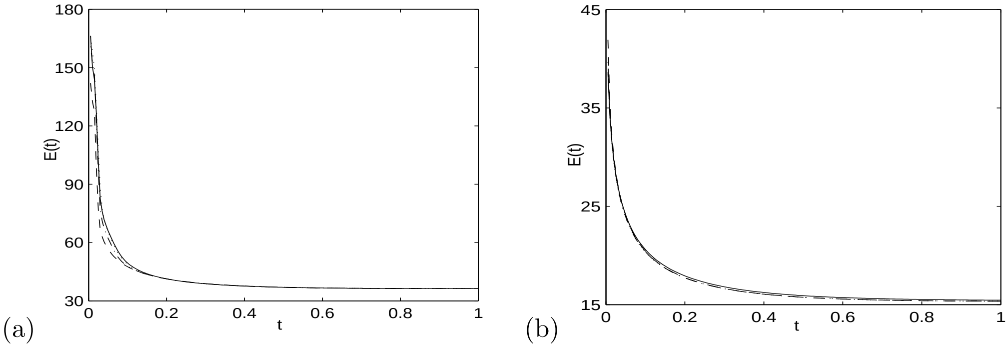

Figure 4.3: Time evolution of the energy of normalized gradient flow (4.26)–(4.28) with $M = 0.5$, and $N = 10^4$ for (a) ^{87}Rb in case I and (b) ^{23}Na in case II with different initial data (4.89) (solid line) and (4.86)–(4.88) with $\kappa = 0.1$ (dotted line), $\kappa = 0.2$ (dash-dot line) and $\kappa = 0.4$ (dashed line), respectively.

and ii) with antiferromagnetic interaction, ($\beta_s > 0$),

$$\phi_1(\boldsymbol{x}) = \sqrt{\frac{1+M}{2}}\phi_g^{\text{ap}}(\boldsymbol{x}), \quad \phi_0(\boldsymbol{x}) = 0, \quad \phi_1(\boldsymbol{x}) = \sqrt{\frac{1-M}{2}}\phi_g^{\text{ap}}(\boldsymbol{x});$$

where $\phi_g^{\text{ap}}(\boldsymbol{x})$ can be taken as the approximated ground state solution of a single component BEC, e.g. the harmonic oscillator approximation when β_n is small and the Thomas-Fermi approximation when $\beta_n \gg 1$ as discussed in Chapter 2. Based on these choices of initial data, we report the spin-1 BEC ground state solution computed by our numerical method.

Figure 4.4 shows the ground state solution of ^{87}Rb in Case I with $N = 10^4$ for different magnetization M and Table 4.1 lists the corresponding ground state energy and their Lagrange multipliers, as well as the weighted error defined as

$$e = \|\phi_1\|^2 \left[(\mu+\lambda) - \mu_1\right]^2 + \|\phi_0\|^2 \left[\mu - \mu_0\right]^2 + \|\phi_{-1}\|^2 \left[(\mu-\lambda) - \mu_{-1}\right]^2, \tag{4.90}$$

where μ_l ($l = 1, 0, -1$) are obtained from the numerical integration

$$\begin{aligned}
\mu_1 &= \frac{h}{\|\phi_1\|^2}\left\{\sum_{j=1}^{L-1} \frac{1}{L}\mu_j^2 (\widehat{\phi_1})_j^2 + \sum_{j=1}^{L-1} \left[\left(V(x_j) + \beta_n(|\phi_{1,j}|^2 + |\phi_{0,j}|^2 + |\phi_{-1,j}|^2)\right.\right.\right. \\
&+ \left.\left.\left.\beta_s\left(|\phi_{1,j}|^2 + |\phi_{0,j}|^2 - |\phi_{-1,j}|^2\right)\right)|\phi_{1,j}|^2 + \beta_s \phi_{0,j}^2 \bar{\phi}_{1,j}\bar{\phi}_{-1,j}\right]\right\}, \\
\mu_0 &= \frac{h}{\|\phi_0\|^2}\left\{\sum_{j=1}^{L-1} \frac{1}{L}\mu_j^2 (\widehat{\phi_0})_j^2 + \sum_{j=1}^{L-1} \left[\left(V(x_j) + \beta_n(|\phi_{1,j}|^2 + |\phi_{0,j}|^2 + |\phi_{-1,j}|^2)\right.\right.\right. \\
&+ \left.\left.\left.\beta_s\left(|\phi_{1,j}|^2 + |\phi_{-1,j}|^2\right)\right)|\phi_{0,j}|^2 + 2\beta_s \phi_{1,j}\phi_{-1,j}\bar{\phi}_{0,j}^2\right]\right\},
\end{aligned}$$

$$
\begin{aligned}
\mu_{-1} &= \frac{h}{\|\phi_{-1}\|^2}\left\{\sum_{j=1}^{L-1}\frac{1}{L}\mu_j^2(\widehat{\phi_{-1}})_j^2+\sum_{j=1}^{L-1}\left[\left(V(x_j)+\beta_n(|\phi_{1,j}|^2+|\phi_{0,j}|^2+|\phi_{-1,j}|^2\right)\right.\right.\\
&+\left.\left.\beta_s\left(|\phi_{-1,j}|^2+|\phi_{0,j}|^2-|\phi_{1,j}|^2\right)\right)|\phi_{-1,j}|^2+\beta_s\phi_{0,j}^2\bar{\phi}_{1,j}\bar{\phi}_{-1,j}\right]\Bigg\}.
\end{aligned}
$$

Figure 4.5 shows the results with $M = 0.5$ for different particle number N.

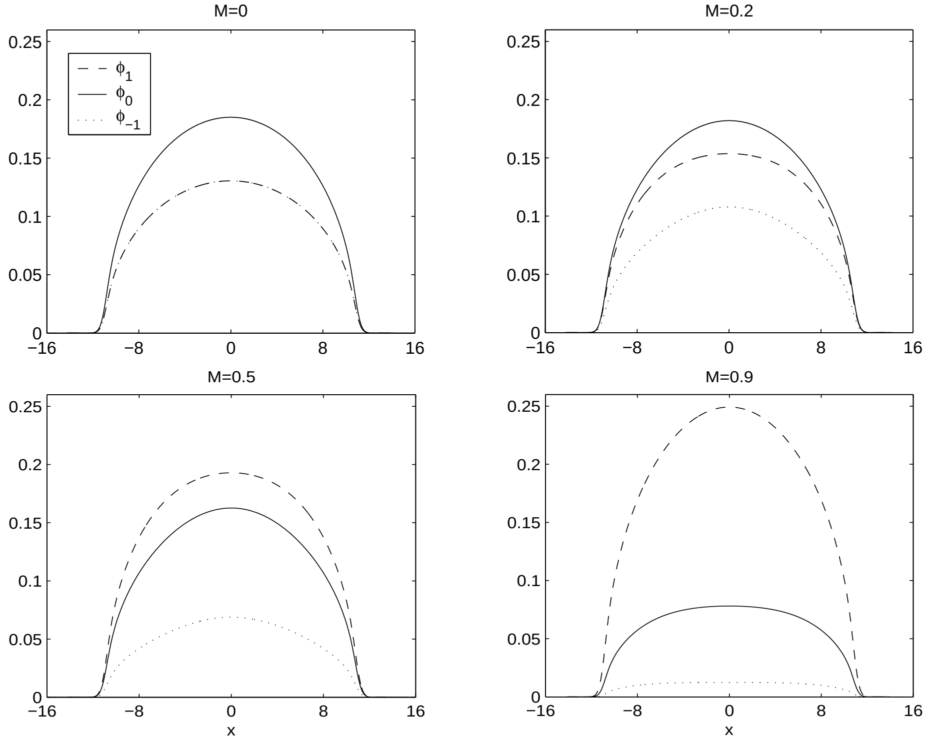

Figure 4.4: Wavefunctions of the ground state, i.e. $\phi_1(x)$ (dashed line), $\phi_0(x)$ (solid line) and $\phi_{-1}(x)$ (dotted line), of ^{87}Rb in Case I with $N = 10^4$ and $M = 0, 0.2, 0.5, 0.9$ in harmonic potential $V(x) = \frac{x^2}{2}$.

Similarly, Figure 4.6 shows the ground state solution of ^{23}Na in Case II with $N = 10^4$ for different magnetization M and Table 4.2 lists the corresponding ground state energy, their Lagrange multipliers, and the weighted error. In addition, Figure 4.7 shows the results with $M = 0.5$ for different particle number N.

Figure 4.8 plots the fractional mass of the three components in the spin-1 BEC ground state with $N = 10^4$ for different magnetization M, and Figure 4.9 depicts the energy and chemical potentials with $M = 0.5$ for different particle number N.

From Figures 4.4–4.9 as well as Tables 4.1–4.2, we can draw the following conclusions:

M	E	μ	$\lambda(\times 10^{-5})$	$\sqrt{e}(\times 10^{-4})$
0	36.1365	60.2139	0	0.4262
0.1	36.1365	60.2139	1.574	0.1456
0.2	36.1365	60.2139	1.621	0.5059
0.3	36.1365	60.2139	1.702	1.0432
0.4	36.1365	60.2139	1.827	1.6642
0.5	36.1365	60.2139	2.014	2.2853
0.6	36.1365	60.2139	2.218	2.7799
0.7	36.1365	60.2139	2.062	2.9815
0.8	36.1365	60.2139	2.081	2.7317
0.9	36.1365	60.2139	2.521	1.8199

Table 4.1: Ground state energy E and their chemical potentials μ and λ as well as the square root of weighted error e for ^{87}Rb in Case I with $N = 10^4$ in harmonic potential $V(x) = \frac{x^2}{2}$.

M	E	μ	λ	$\sqrt{e}(\times 10^{-5})$
0	15.2485	25.3857	0	4.882
0.1	15.2514	25.3847	0.0569	4.892
0.2	15.2599	25.3815	0.1142	4.913
0.3	15.2743	25.3762	0.1725	4.950
0.4	15.2945	25.3682	0.2325	5.019
0.5	15.3209	25.3572	0.2950	5.119
0.6	15.3537	25.3423	0.3611	5.270
0.7	15.3933	25.3220	0.4326	5.458
0.8	15.4405	25.2939	0.5121	5.720
0.9	15.4962	25.2527	0.6049	6.173

Table 4.2: Ground state energy E and their chemical potentials μ and λ as well as the square root of weighted error e for ^{23}Na in Case II with $N = 10^4$ in harmonic potential $V(x) = \frac{x^2}{2}$.

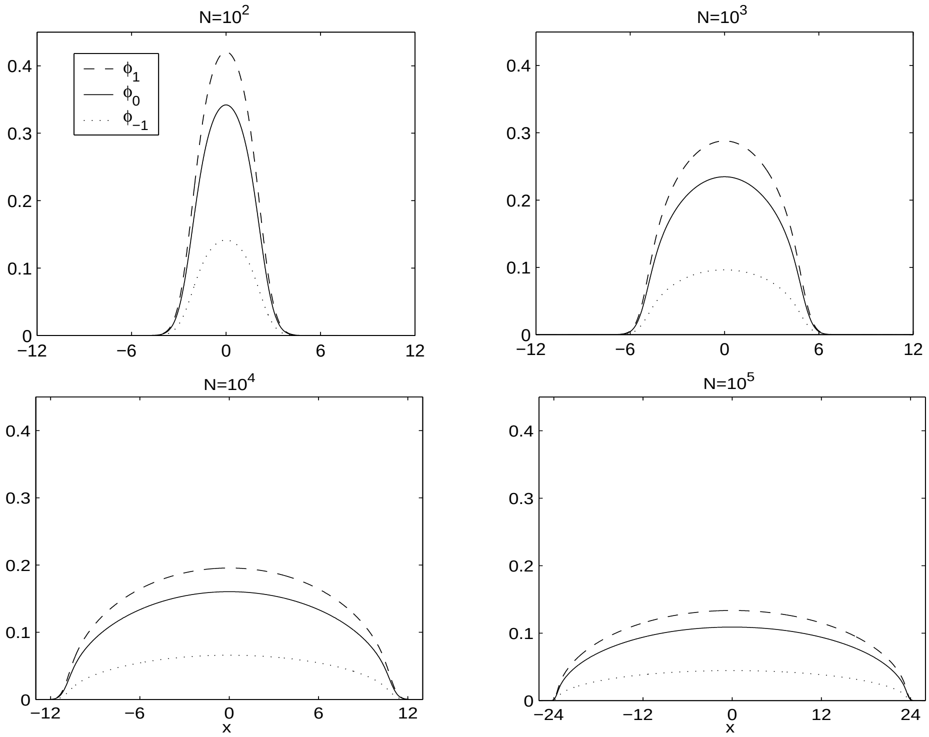

Figure 4.5: Wavefunctions of the ground state, i.e. $\phi_1(x)$ (dashed line), $\phi_0(x)$ (solid line) and $\phi_{-1}(x)$ (dotted line), of ^{87}Rb in Case I with $M = 0.5$ and $N = 10^2, 10^3, 10^4, 10^5$ in harmonic potential $V(x) = \frac{x^2}{2}$.

(i) For a spin-1 BEC with ferromagnetic interaction ($\beta_s \leq 0$), the three components in the ground state solution are all positive functions (c.f. Figures 4.4&4.5); while for a spin-1 BEC with antiferromagnetic interaction, i.e. $\beta_s \geq 0$, ϕ_1 and ϕ_{-1} are positive functions and $\phi_0 \equiv 0$ (c.f. Figures 4.6&4.7).

(ii) For a spin-1 BEC with ferromagnetic interaction ($\beta_s \leq 0$), for fixed number of particles N in the condensate, when the magnetization M increases from 0 to 1, the mass N_1 increases from 0.25 to 1, the mass N_{-1} decreases from 0.25 to 0 and the mass N_0 decreases from 0.5 to 0 (c.f. Figure 4.9(a)); while for a spin-1 BEC with antiferromagnetic interaction ($\beta_s \geq 0$), N_1 increases from 0.5 to 1, N_{-1} decreases from 0.5 to 0 and $N_0 = 0$ (c.f. Figure 4.9(b)).

(iii) For a spin-1 BEC with ferromagnetic interaction ($\beta_s \leq 0$), for fixed number of particles N in the condensate, the energy and chemical potentials are independent of the magnetization and the second chemical potential $\lambda = 0$ (c.f. Table 4.1, see [115] for detailed physical reasons); while for a spin-1 BEC with antiferromagnetic interaction ($\beta_s \geq 0$), when the magnetization M increases from 0 to 1, the energy E increases, the main chemical potential μ decreases and the

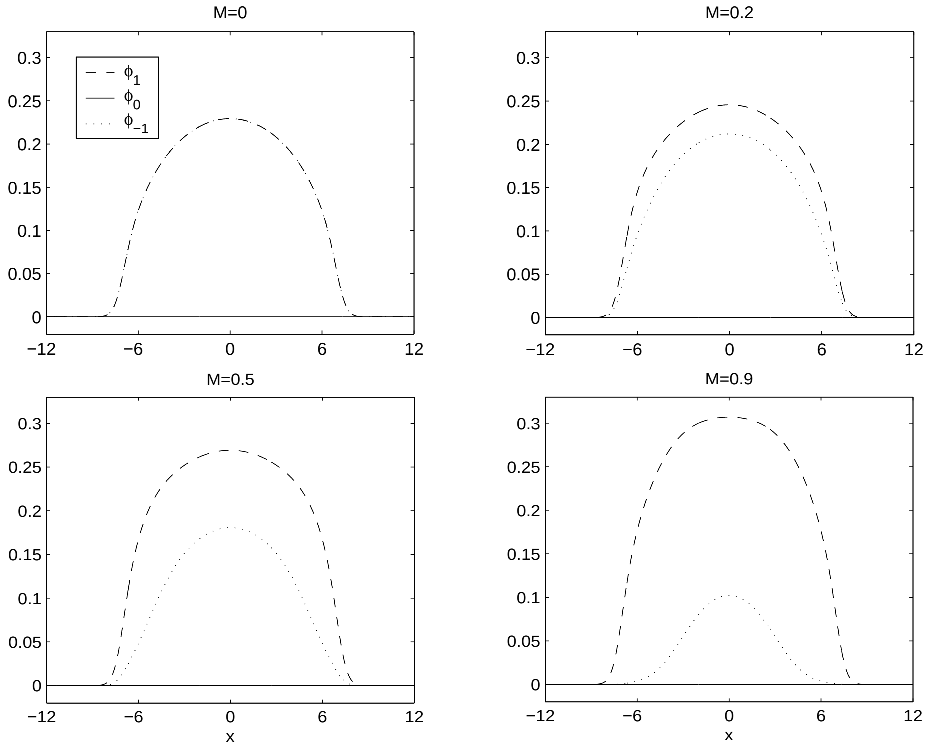

Figure 4.6: Wavefunctions of the ground state, i.e. $\phi_1(x)$ (dashed line), $\phi_0(x)$ (solid line) and $\phi_{-1}(x)$ (dotted line), of ^{23}Na in Case II with $N = 10^4$ and $M = 0, 0.2, 0.5, 0.9$ in harmonic potential $V(x) = \frac{x^2}{2}$.

second chemical potential λ increases (c.f. Table 4.2). In both cases, for fixed magnetization M, when the number of particles N increases, the energy and chemical potentials increase (c.f. Figure 4.8). These observations agree with those obtained in [19] and [118] by different numerical methods.

4.3.2 Application in 1D with optical lattice potential

The numerical method is applied to compute the ground state of spin-1 BEC in one dimension (1D) with an optical lattice potential. Again, two different interactions are considered:

- Case I. ^{87}Rb with the following dimensionless quantities: $d = 1$, $V(x) = x^2/2 + 25\sin^2\left(\frac{\pi x}{4}\right)$, $\beta_n = 0.0885N$ and $\beta_s = -0.00041N$, with N being the total number of atoms in the condensate. The dimensionless length unit $a_s = 2.4116 \times 10^{-6}$ [m] and time unit $t_s = 0.007958$[s].
- Case II. ^{23}Na with the following dimensionless quantities: $d = 1$, $V(x) = x^2/2 + 25\sin^2\left(\frac{\pi x}{4}\right)$, $\beta_n = 0.0241N$ and $\beta_s = 0.00075N$, with N being the total number of atoms in the condensate. The dimensionless length unit $a_s = 4.6896 \times 10^{-6}$ [m] and time unit $t_s = 0.007958$[s].

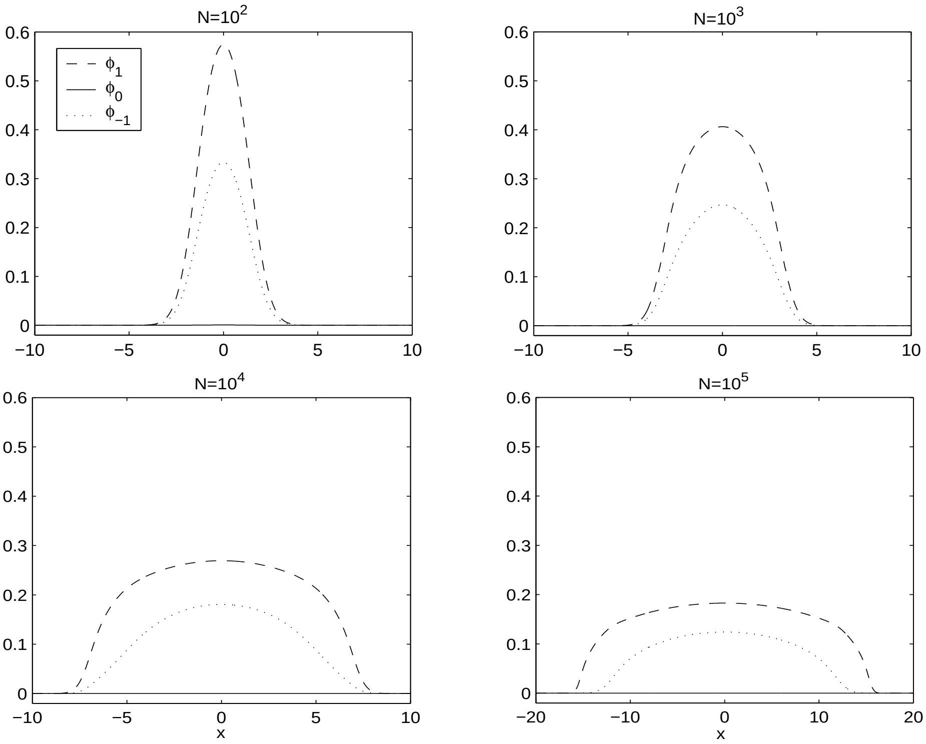

Figure 4.7: Wavefunctions of the ground state, i.e. $\phi_1(x)$ (dashed line), $\phi_0(x)$ (solid line) and $\phi_{-1}(x)$ (dotted line), of ^{23}Na in Case II with $M = 0.5$ and $N = 10^2, 10^3, 10^4, 10^5$ in harmonic potential $V(x) = \frac{x^2}{2}$.

Figure 4.10 shows the ground state solution of ^{87}Rb in Case I with $N = 10^4$ for different magnetization M and Table 4.3 lists the corresponding ground state energy and their Lagrange multipliers. Figure 4.11 and Table 4.4 show similar results for ^{23}Na in Case II. From Figures 4.10&4.11 and Tables 4.3&4.4, it can be seen that our method can be used in computing the ground state of a spin-1 BEC in a general potential. In addition to that, similar conclusions as those in the end of Section 4.3.1 can also be observed in the BEC ground state in the optical lattice potential.

4.3.3 Application in 3D with optical lattice potential

In this section, we apply the numerical method to compute the ground state of a spin-1 BEC in three dimensions (3D) with an optical lattice potential. Two different interactions are considered:

- Case I. ^{87}Rb with the following dimensionless quantities: $d = 3$, $V(x) = \frac{1}{2}\left(x^2 + y^2 + z^2\right) + 100\left[\sin^2\left(\frac{\pi x}{2}\right) + \sin^2\left(\frac{\pi y}{2}\right) + \sin^2\left(\frac{\pi z}{2}\right)\right]$, $\beta_n = 0.0880N$ and $\beta_s = -0.00041N$, with N being the total number of atoms in the condensate. The dimensionless length unit $a_s = \sqrt{\hbar/m\omega_x} =$

M	E	μ	$\lambda(\times 10^{-4})$
0	47.6944	73.0199	0
0.1	47.6944	73.0199	0.711
0.2	47.6944	73.0199	0.788
0.3	47.6944	73.0199	0.859
0.4	47.6944	73.0199	0.948
0.5	47.6944	73.0199	1.072
0.6	47.6944	73.0199	1.178
0.7	47.6944	73.0199	1.164
0.8	47.6944	73.0199	1.200
0.9	47.6944	73.0199	1.477

Table 4.3: Ground state energy E and their chemical potentials μ and λ for ^{87}Rb in Case I with $N = 10^4$ in optical lattice potential $V(x) = \frac{x^2}{2} + 25\sin^2\left(\frac{\pi x}{4}\right)$.

M	E	μ	λ
0	25.6480	37.4489	0
0.1	25.6509	37.4476	0.0593
0.2	25.6597	37.4400	0.1197
0.3	25.6753	37.4248	0.1931
0.4	25.6983	37.4025	0.2687
0.5	25.7291	37.3775	0.3458
0.6	25.7676	37.3492	0.4252
0.7	25.8144	37.3167	0.5079
0.8	25.8696	37.2305	0.6920
0.9	25.9340	37.2305	0.6920

Table 4.4: Ground state energy E and their chemical potentials μ and λ for ^{23}Na in Case II with $N = 10^4$ in optical lattice potential $V(x) = \frac{x^2}{2} + 25\sin^2\left(\frac{\pi x}{4}\right)$.

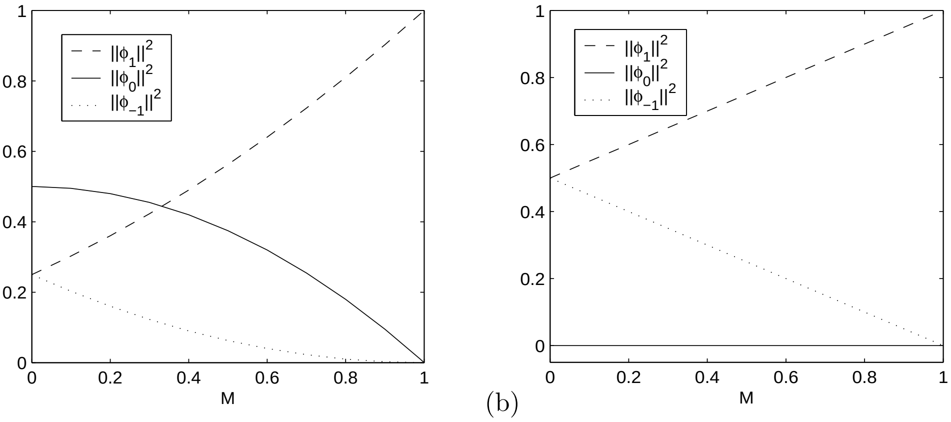

(a) (b)

Figure 4.8: Masses of the three components of the ground state, i.e. $N_l = \|\phi_l\|^2$ ($l = 1, 0, -1$), of spin-1 BEC with $N = 10^4$ and different magnetization $0 \leq M < 1$, for (a) ^{87}Rb in Case I and (b) ^{23}Na in Case II.

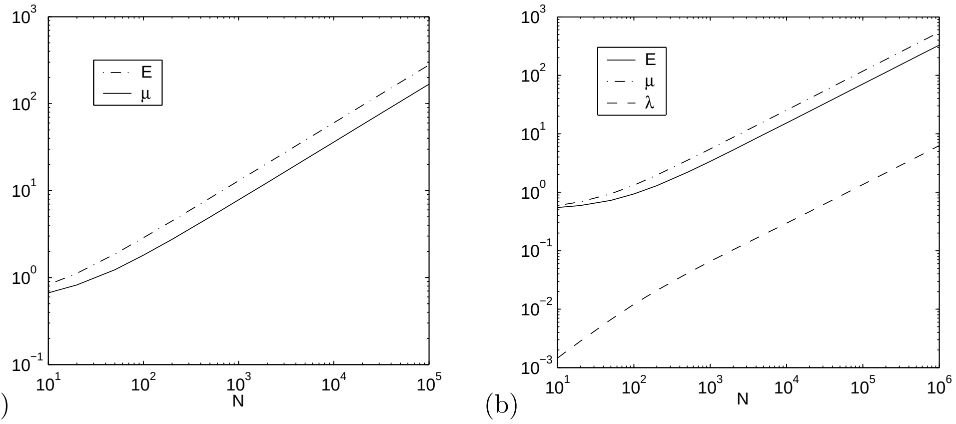

(a) (b)

Figure 4.9: Energy E and chemical potentials μ and λ of spin-1 BEC with $M = 0.5$ and different number of particles N, for (a) ^{87}Rb in Case I and (b) ^{23}Na in Case II.

7.6262×10^{-7} [m] and time unit $t_s = 1/\omega_x = 7.9577 \times 10^{-4}$[s] (corresponding to physical trapping frequencies $\omega_x = \omega_y = \omega_z = 2\pi \times 200$[Hz]).

- Case II. ^{23}Na with the following dimensionless quantities: $d = 3$, $V(x) = \frac{1}{2}\left(x^2 + y^2 + z^2\right) + 100\left[\sin^2\left(\frac{\pi x}{2}\right) + \sin^2\left(\frac{\pi y}{2}\right) + \sin^2\left(\frac{\pi z}{2}\right)\right]$, $\beta_n = 0.0239N$ and $\beta_s = 0.00075N$ with N being the total number of atoms in the condensate. The dimensionless length unit $a_s = 1.4830 \times 10^{-6}$ [m] and time unit $t_s = 7.9577 \times 10^{-4}$[s](corresponding to physical trapping frequencies $\omega_x = \omega_y = \omega_z = 2\pi \times 200$[Hz]).

Figure 4.12 shows the ground state solution with $N = 10^4$ and $M = 0.5$ for the two cases. From Figure 4.12, we can see that our numerical method can be used to compute the ground state of a spin-1 BEC in 3D with general trapping potential.

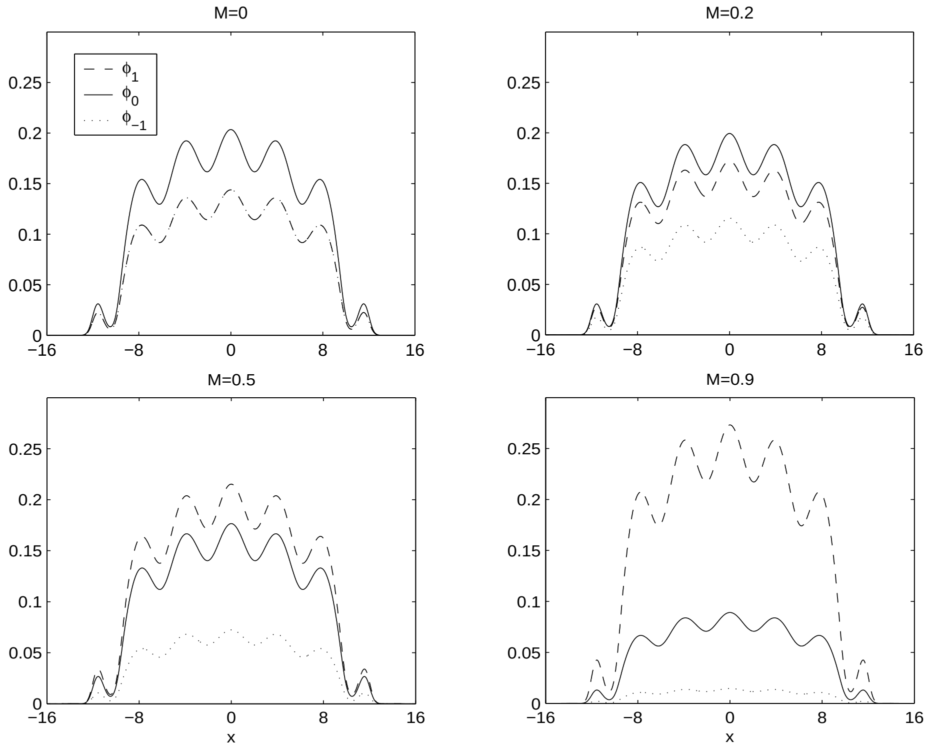

Figure 4.10: Wavefunctions of the ground state, i.e. $\phi_1(x)$ (dashed line), $\phi_0(x)$ (solid line) and $\phi_{-1}(x)$ (dotted line), of ^{87}Rb in Case I with $N = 10^4$ and $M = 0, 0.2, 0.5, 0.9$ in optical lattice potential $V(x) = \frac{x^2}{2} + 25\sin^2\left(\frac{\pi x}{4}\right)$.

4.4 Spin-1 BEC in Uniform Magnetic Field

While reporting the observation of equilibrium states of ^{23}Na spinor condensates in an optical trap, Ketterle et al. [105] had reported the ground state phase diagram of a uniform spin-1 condensate in the Thomas-Fermi regime, with the existence of external magnetic field. Recently, Murata et al. [86] also studied the broken axisymmetry phase of spin-1 ferromagnetic condensate subject to certain magnetic field. In numerical studies of spin-1 BEC, You et al. [118] had reported the ground state phase diagram for both ^{87}Rb and ^{23}Na confined in a harmonic oscillator trap subject to uniform magnetic field. In [118], the imaginary time method with several adjustable parameters was applied to solve the three-component coupled Gross-Pitaevskii equations (CGPEs) under the conservation of total mass and total magnetization.

In this section, we will first review the three-component CGPEs for spin-1 BEC in uniform magnetic field, followed by modifying the normalized gradient flow (NGF) method in section 4.2 to solve for the condensate ground state. Two different ways of incorporating the magnetic field in the normalized gradient flow will be presented. In order to identify the best scheme, comparison between

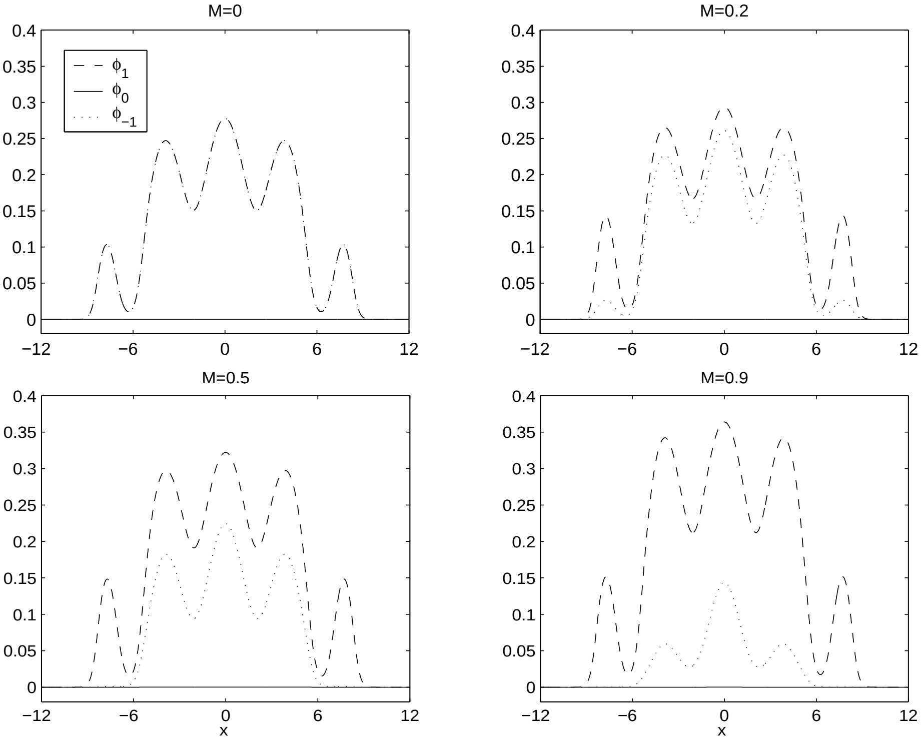

Figure 4.11: Wavefunctions of the ground state, i.e. $\phi_1(x)$ (dashed line), $\phi_0(x)$ (solid line) and $\phi_{-1}(x)$ (dotted line), of ^{23}Na in Case II with $N = 10^4$ and $M = 0, 0.2, 0.5, 0.9$ in optical lattice potential $V(x) = \frac{x^2}{2} + 25\sin^2\left(\frac{\pi x}{4}\right)$.

different numerical treatments will be made. Richer properties are expected for spin-1 condensate in magnetic field and they will be reported via our numerical simulation [16].

4.4.1 Coupled Gross-Pitaevskii equations (CGPEs) in uniform magnetic field

At temperature much lower than the critical temperature T_c, the three-component wavefunction, $\Psi(\boldsymbol{x},t) = (\psi_1(\boldsymbol{x},t), \psi_0(\boldsymbol{x},t), \psi_{-1}(\boldsymbol{x},t))^{\mathrm{T}}$, that gives the states of a spin-1 BEC subjected to a uniform external magnetic field B can be described by the following coupled Gross-Pitaevskii equations (CGPEs) [66, 90, 118]:

$$\begin{aligned} i\hbar\frac{\partial}{\partial t}\psi_1(\boldsymbol{x},t) &= \left[-\frac{\hbar^2}{2m}\nabla^2 + V(\boldsymbol{x}) + E_1 + (c_0+c_2)\left(|\psi_1|^2 + |\psi_0|^2\right) + (c_0-c_2)|\psi_{-1}|^2\right]\psi_1 \\ &\quad + c_2\,\bar{\psi}_{-1}\,\psi_0^2, \end{aligned} \tag{4.91}$$

$$\begin{aligned} i\hbar\,\frac{\partial}{\partial t}\psi_0(\boldsymbol{x},t) &= \left[-\frac{\hbar^2}{2m}\nabla^2+V(\boldsymbol{x})+E_0+(c_0+c_2)\left(|\psi_1|^2+|\psi_{-1}|^2\right)+c_0|\psi_0|^2\right]\psi_0 \\ &\quad +2c_2\,\psi_{-1}\,\bar{\psi}_0\,\psi_1, \qquad (4.92)\\ i\hbar\,\frac{\partial}{\partial t}\psi_{-1}(\boldsymbol{x},t) &= \left[-\frac{\hbar^2}{2m}\nabla^2+V(\boldsymbol{x})+E_{-1}+(c_0+c_2)\left(|\psi_{-1}|^2+|\psi_0|^2\right)+(c_0-c_2)|\psi_1|^2\right]\psi_{-1} \\ &\quad +c_2\,\psi_0^2\,\bar{\psi}_1. \qquad (4.93)\end{aligned}$$

We consider here a harmonic oscillator potential in the form of (4.5). E_l $(l=-1,0,1)$ is the Zeeman energy of the spin component $m_F=l$ in the uniform magnetic field. Two parameters which play important roles in the ground state phase diagram as well as the dynamics of the spin-1 BEC are the linear Zeeman energy

$$p_0=\frac{1}{2}(E_1-E_{-1})\approx-\frac{\mu_B B}{2}, \qquad (4.94)$$

and the quadratic Zeeman energy

$$q_0=\frac{1}{2}(E_1+E_{-1}-2E_0)\approx\frac{\mu_B^2B^2}{4\mathrm{E}_{\mathrm{hfs}}} \qquad (4.95)$$

[70, 98, 105]. The right hand sides of (4.94)–(4.95) are obtained when the Breit-Rabi formula is applied. μ_B is the Bohr magneton and $\mathrm{E}_{\mathrm{hfs}}$ is the hyperfine splitting.

In order to minimize any possible numerical error that can be caused by large Zeeman energy when (4.91)–(4.93) are solved numerically, we shift the energy level and set the zero energy to be E_0, which is equivalent to replacing $\psi_l\to\psi_l\exp(-\frac{iE_0t}{\hbar})$ $(l=1,0,-1)$ in (4.91)–(4.93). Furthermore, by introducing dimensionless variables: $t\to t/\omega_x$, $\boldsymbol{x}\to\boldsymbol{x}a_s$ with $a_s=\sqrt{\frac{\hbar}{m\omega_x}}$, $\psi_l\to\sqrt{N}\psi_l/a_s^{3/2}$ $(l=-1,0,1)$ with N being the total number of particles in the system, the dimensionless CGPEs are obtained from (4.91)–(4.93) as

$$\begin{aligned} i\frac{\partial}{\partial t}\psi_1(\boldsymbol{x},t) &= \left[-\frac{1}{2}\nabla^2+V(\boldsymbol{x})+q+p+(\beta_n+\beta_s)\left(|\psi_1|^2+|\psi_0|^2\right)+(\beta_n-\beta_s)|\psi_{-1}|^2\right]\psi_1 \\ &\quad +\beta_s\,\bar{\psi}_{-1}\,\psi_0^2, \qquad (4.96)\\ i\frac{\partial}{\partial t}\psi_0(\boldsymbol{x},t) &= \left[-\frac{1}{2}\nabla^2+V(\boldsymbol{x})+(\beta_n+\beta_s)\left(|\psi_1|^2+|\psi_{-1}|^2\right)+\beta_n|\psi_0|^2\right]\psi_0 \\ &\quad +2\beta_s\,\psi_{-1}\,\bar{\psi}_0\,\psi_1, \qquad (4.97)\\ i\frac{\partial}{\partial t}\psi_{-1}(\boldsymbol{x},t) &= \left[-\frac{1}{2}\nabla^2+V(\boldsymbol{x})+q-p+(\beta_n+\beta_s)\left(|\psi_{-1}|^2+|\psi_0|^2\right)+(\beta_n-\beta_s)|\psi_1|^2\right]\psi_{-1} \\ &\quad +\beta_s\,\psi_0^2\,\bar{\psi}_1, \qquad (4.98)\end{aligned}$$

where the dimensionless harmonic trapping potential $V(\boldsymbol{x})=\frac{1}{2}\left(x^2+\gamma_y^2y^2+\gamma_z^2z^2\right)$ with $\gamma_y=\frac{\omega_y}{\omega_x}$

and $\gamma_z = \frac{\omega_z}{\omega_x}$. The dimensionless mean field and spin-exchange interaction terms are given by the same form as in Section 4.1, i.e. $\beta_n = \frac{Nc_0}{a_s^3\hbar\omega_x} = \frac{4\pi N(a_0+2a_2)}{a_s}$ and $\beta_s = \frac{Nc_2}{a_s^3\hbar\omega_x} = \frac{4\pi N(a_2-a_0)}{a_s}$, while the linear and quadratic Zeeman terms are scaled according to

$$p = \frac{p_0}{\hbar\omega_x}, \quad q = \frac{q_0}{\hbar\omega_x}. \tag{4.99}$$

For a trapping potential which is tightly confined in 1 or 2 directions, the excitation energy along these tightly confined directions is very high and the BEC can be assumed to be in its ground state along these directions at all time. The problem can thus be effectively described by CGPEs in lower dimensions. We consider here dimensionless CGPEs in d dimensions, taking exactly the same form as (4.96)–(4.98), with effective trapping potential (4.9) and effective interaction parameters (4.10). The dimensionless Zeeman energies remain the same as (4.99) for 1D/2D CGPEs. Three conserved quantities associated with (4.96)–(4.98) are the normalization of the wavefunction

$$N(\Psi(\cdot,t)) := \|\Psi(\cdot,t)\|^2 = \int_{\mathbb{R}^d} \sum_{l=-1}^{1} |\psi_l(\boldsymbol{x},t)|^2 \, d\boldsymbol{x} = 1, \qquad t \geq 0, \tag{4.100}$$

the total magnetization

$$M(\Psi(\cdot,t)) := \int_{\mathbb{R}^d} \left[|\psi_1(\boldsymbol{x},t)|^2 - |\psi_{-1}(\boldsymbol{x},t)|^2\right] d\boldsymbol{x} = M, \qquad t \geq 0, \tag{4.101}$$

and the energy per particle

$$\begin{aligned} E(\Psi(\cdot,t)) \;=\; & \int_{\mathbb{R}^d} \Bigg\{ \sum_{l=-1}^{1} \left(\frac{1}{2}|\nabla\psi_l|^2 + V(\boldsymbol{x})|\psi_l|^2\right) + (\beta_n - \beta_s)|\psi_1|^2|\psi_{-1}|^2 \\ & + \frac{\beta_n}{2}|\psi_0|^4 + \frac{\beta_n + \beta_s}{2}\Big[|\psi_1|^4 + |\psi_{-1}|^4 + 2|\psi_0|^2\left(|\psi_1|^2 + |\psi_{-1}|^2\right)\Big] \\ & + \beta_s\left(\bar{\psi}_{-1}\psi_0^2\bar{\psi}_1 + \psi_{-1}\bar{\psi}_0^2\psi_1\right) \\ & + (q+p)|\psi_1|^2 + (q-p)|\psi_{-1}|^2 \Bigg\} \, d\boldsymbol{x} \equiv E(\Psi(\cdot,0)), \qquad t \geq 0. \end{aligned} \tag{4.102}$$

The ground state of a spin-1 BEC $\Phi_g(\boldsymbol{x})$ is given by the minimizer of the energy functional (4.102) subjected to constraints (4.100) and (4.101). By defining a Lagrangian in a similar way as in Section 4.1, it is easy to show that the ground state is also the lowest energy solution of the time-independent CGPEs,

$$\begin{aligned}
(\mu+\lambda)\phi_1(\boldsymbol{x}) &= \left[-\frac{1}{2}\nabla^2 + V(\boldsymbol{x}) + q + p + (\beta_n+\beta_s)\left(|\phi_1|^2+|\phi_0|^2\right) + (\beta_n-\beta_s)|\phi_{-1}|^2\right]\phi_1 \\
&\quad +\beta_s\,\bar{\phi}_{-1}\,\phi_0^2, \qquad (4.103)\\
\mu\phi_0(\boldsymbol{x}) &= \left[-\frac{1}{2}\nabla^2 + V(\boldsymbol{x}) + (\beta_n+\beta_s)\left(|\phi_1|^2+|\phi_{-1}|^2\right) + \beta_n|\phi_0|^2\right]\phi_0 \\
&\quad +2\beta_s\,\phi_{-1}\,\bar{\phi}_0\,\phi_1, \qquad (4.104)\\
(\mu-\lambda)\phi_{-1}(\boldsymbol{x},t) &= \left[-\frac{1}{2}\nabla^2 + V(\boldsymbol{x}) + q - p + (\beta_n+\beta_s)\left(|\phi_{-1}|^2+|\phi_0|^2\right) + (\beta_n-\beta_s)|\phi_1|^2\right]\phi_{-1} \\
&\quad +\beta_s\,\phi_0^2\,\bar{\phi}_1, \qquad (4.105)
\end{aligned}$$

with μ and λ the Lagrange multipliers of the minimization problem.

4.4.2 Numerical methods

Since p and q in (4.96)–(4.98) are constants, it is straightforward to apply the normalized gradient flow (4.23)–(4.28) to solve for the spin-1 BEC ground state in a uniform magnetic field. However, the linear Zeeman effect term is always much greater than the quadratic Zeeman term, i.e. $p \gg q$, and it causes high instability in the numerical scheme. The numerical scheme does not converge for almost all physically realistic parameter values. For this reason, we have to modify the numerical scheme (4.23)–(4.28) for the computation.

We first construct the continuous normalized gradient flow (CNGF) for the spin-1 BEC in uniform magnetic field:

$$\begin{aligned}
\frac{\partial}{\partial t}\phi_1(\boldsymbol{x},t) &= \left[\frac{1}{2}\nabla^2 - V(\boldsymbol{x}) - (\beta_n+\beta_s)\left(|\phi_1|^2+|\phi_0|^2\right) - (\beta_n-\beta_s)|\phi_{-1}|^2\right]\phi_1 \\
&\quad -\beta_s\,\bar{\phi}_{-1}\,\phi_0^2\,[\mu_\Phi(t)+(\lambda_\Phi(t)-p)]\,\phi_1 - q\phi_1, \qquad (4.106)\\
\frac{\partial}{\partial t}\phi_0(\boldsymbol{x},t) &= \left[\frac{1}{2}\nabla^2 - V(\boldsymbol{x}) - (\beta_n+\beta_s)\left(|\phi_1|^2+|\phi_{-1}|^2\right) - \beta_n|\phi_0|^2\right]\phi_0 \\
&\quad -2\beta_s\,\phi_{-1}\,\bar{\phi}_0\,\phi_1 + \mu_\Phi(t)\,\phi_0, \qquad (4.107)\\
\frac{\partial}{\partial t}\phi_{-1}(\boldsymbol{x},t) &= \left[\frac{1}{2}\nabla^2 - V(\boldsymbol{x}) - (\beta_n+\beta_s)\left(|\phi_{-1}|^2+|\phi_0|^2\right) - (\beta_n-\beta_s)|\phi_1|^2\right]\phi_{-1} \\
&\quad -\beta_s\,\phi_0^2\,\bar{\phi}_1 + [\mu_\Phi(t)-(\lambda_\Phi(t)-p)]\,\phi_{-1} - q\phi_{-1}. \qquad (4.108)
\end{aligned}$$

where $\mu_\Phi(t)$ and $\lambda_\Phi(t)$ are functionals of $\Phi = (\phi_1,\phi_0,\phi_{-1})^{\mathrm{T}}$. Similarly to (4.32)–(4.34), they can be chosen such that the above CNGF is normalization and magnetization conserved, and can be proved to be energy diminishing for any given initial data. The linear Zeeman term p is grouped together with λ_Φ, acting as a Lagrange multiplier in the energy minimization process. A first order time-splitting scheme will be applied to the CNGF (4.106)–(4.108), to form the standard normalized gradient flow for ground state computation, as well as to find the third normalization condition. There are two ways to deal with the quadratic Zeeman energy q during the time-splitting procedure and we call the two numerical treatments as projection with magnetic field (PWMF) and projection without magnetic field (POMF), respectively.

4.4.2.1 Projection with magnetic field (PWMF)

The first way to deal with the Zeeman energy is to apply a first order time-splitting to the CNGF (4.106)–(4.108) in discrete time interval $t_{n-1} \le t \le t_n$, where $t_n = n\Delta t$ with time step Δt, in the following way:

Step 1:

$$\begin{aligned}
\frac{\partial}{\partial t}\phi_1(\boldsymbol{x},t) &= \left[\frac{1}{2}\nabla^2 - V(\boldsymbol{x}) - (\beta_n+\beta_s)\left(|\phi_1|^2+|\phi_0|^2\right) - (\beta_n-\beta_s)|\phi_{-1}|^2\right]\phi_1 \\
&\quad -\beta_s\,\bar{\phi}_{-1}\,\phi_0^2, \qquad (4.109)\\
\frac{\partial}{\partial t}\phi_0(\boldsymbol{x},t) &= \left[\frac{1}{2}\nabla^2 - V(\boldsymbol{x}) - (\beta_n+\beta_s)\left(|\phi_1|^2+|\phi_{-1}|^2\right) - \beta_n|\phi_0|^2\right]\phi_0 \\
&\quad -2\beta_s\,\phi_{-1}\,\bar{\phi}_0\,\phi_1, \qquad \boldsymbol{x}\in\mathbb{R}^d, \quad t_{n-1}\le t<t_n, \qquad n\ge 1, \qquad (4.110)\\
\frac{\partial}{\partial t}\phi_{-1}(\boldsymbol{x},t) &= \left[\frac{1}{2}\nabla^2 - V(\boldsymbol{x}) - (\beta_n+\beta_s)\left(|\phi_{-1}|^2+|\phi_0|^2\right) - (\beta_n-\beta_s)|\phi_1|^2\right]\phi_{-1} \\
&\quad -\beta_s\,\phi_0^2\,\bar{\phi}_1; \qquad (4.111)
\end{aligned}$$

Step 2:

$$\frac{\partial}{\partial t}\phi_1(\boldsymbol{x},t) = \left[\mu_\Phi(t) + (\lambda_\Phi(t)-p)\right]\phi_1 - q\phi_1, \qquad (4.112)$$

$$\frac{\partial}{\partial t}\phi_0(\boldsymbol{x},t) = \mu_\Phi(t)\phi_0, \qquad t_{n-1}\le t\le t_n, \qquad n\ge 1, \qquad (4.113)$$

$$\frac{\partial}{\partial t}\phi_{-1}(\boldsymbol{x},t) = \left[\mu_\Phi(t) - (\lambda_\Phi(t)-p)\right]\phi_{-1} - q\phi_{-1}. \qquad (4.114)$$

The nonlinear ordinary differential equations (ODEs) (4.112)–(4.114) are equivalent to the projection step (4.26)–(4.28). Following the similar procedures in Section 4.2.2 and 4.2.3, a third normalization condition for the normalization constants can be derived from the solution of the nonlinear ODEs

(4.112)–(4.114), as

$$\sigma_1^n \sigma_{-1}^n = \mathrm{e}^{-2\mathrm{q}\Delta\mathrm{t}}(\sigma_0^{\mathrm{n}})^2. \tag{4.115}$$

The normalization condition (4.115), together with the two physical conditions of the conservation of mass and conservation of magnetization, determines the three normalization constants as

$$\sigma_0^n = \frac{\sqrt{1-M^2}}{\left[\|\phi_0(\cdot,t_n^-)\|^2 + \sqrt{4e^{-4q\Delta t}(1-M^2)\|\phi_1(\cdot,t_n^-)\|^2\|\phi_{-1}(\cdot,t_n^-)\|^2 + M^2\|\phi_0(\cdot,t_n^-)\|^4}\right]^{1/2}}, \tag{4.116}$$

$$\sigma_1^n = \frac{\sqrt{1+M-(\sigma_0^n)^2\|\phi_0(\cdot,t_n^-)\|^2}}{\sqrt{2}\ \|\phi_1(\cdot,t_n^-)\|}, \tag{4.117}$$

$$\sigma_{-1}^n = \frac{\sqrt{1-M-(\sigma_0^n)^2\|\phi_0(\cdot,t_n^-)\|^2}}{\sqrt{2}\ \|\phi_{-1}(\cdot,t_n^-)\|}. \tag{4.118}$$

4.4.2.2 Projection without magnetic field (POMF)

Another approach to deal with the magnetic field is to retain q in the gradient flow equations instead of including it in the normalization step. This yields the gradient flow (Step 1),

$$\begin{aligned}
\frac{\partial}{\partial t}\phi_1(\boldsymbol{x},t) &= \left[\frac{1}{2}\nabla^2 - V(\boldsymbol{x}) - (\beta_n+\beta_s)\left(|\phi_1|^2+|\phi_0|^2\right) - (\beta_n-\beta_s)|\phi_{-1}|^2\right]\phi_1 \\
&\quad -\beta_s\,\bar{\phi}_{-1}\,\phi_0^2 - q\phi_1, &&(4.119)\\
\frac{\partial}{\partial t}\phi_0(\boldsymbol{x},t) &= \left[\frac{1}{2}\nabla^2 - V(\boldsymbol{x}) - (\beta_n+\beta_s)\left(|\phi_1|^2+|\phi_{-1}|^2\right) - \beta_n|\phi_0|^2\right]\phi_0 \\
&\quad -2\beta_s\,\phi_{-1}\,\bar{\phi}_0\,\phi_1, \qquad \boldsymbol{x}\in\mathbb{R}^d, \quad t_{n-1}\le t<t_n, \qquad n\ge 1, &&(4.120)\\
\frac{\partial}{\partial t}\phi_{-1}(\boldsymbol{x},t) &= \left[\frac{1}{2}\nabla^2 - V(\boldsymbol{x}) - (\beta_n+\beta_s)\left(|\phi_{-1}|^2+|\phi_0|^2\right) - (\beta_n-\beta_s)|\phi_1|^2\right]\phi_{-1} \\
&\quad -\beta_s\,\phi_0^2\,\bar{\phi}_1 - q\phi_{-1}; &&(4.121)
\end{aligned}$$

and the ODEs (Step 2),

$$\frac{\partial}{\partial t}\phi_1(\boldsymbol{x},t) = \left[\mu_\Phi(t) + (\lambda_\Phi(t)-p)\right]\phi_1, \tag{4.122}$$

$$\frac{\partial}{\partial t}\phi_0(\boldsymbol{x},t) = \mu_\Phi(t)\phi_0, \qquad t_{n-1}\le t\le t_n, \qquad n\ge 1, \tag{4.123}$$

$$\frac{\partial}{\partial t}\phi_{-1}(\boldsymbol{x},t) = \left[\mu_\Phi(t) - (\lambda_\Phi(t)-p)\right]\phi_{-1}, \tag{4.124}$$

which are equivalent to projection step (4.26)–(4.28). The normalization constants in this case are, of course, given by (4.58), (4.52) and (4.54).

4.4.3 Numerical comparison

In this section, we will compute the ground state of a spin-1 BEC confined in a cigar-shaped harmonic oscillator potential and perform comparison between the accuracy of the ground state solution obtained via the PWMF and POMF methods. The atoms are tightly confined in two directions and can be effectively described by 1D CGPEs. Both gradient flows (4.109)–(4.111) and (4.119)–(4.121) can be discretized by the backward-forward Euler sine-pseudospectral method (BFSP). However, in order to perform a complete comparison between different numerical schemes, we apply also the backward Euler sine-pseudospectral (BESP) discretization to the two gradient flows. Thus two different projections, i.e. PWMF&POMF, and two different discretizations, i.e. BFSP&BESP, give four combinations of numerical schemes:

1. PWMF + BFSP
2. PWMF + BESP
3. POMF + BFSP
4. POMF + BESP

In the following, we will compare the accuracy and the efficiency of the four schemes. Numerical results obtained using different time steps are compared to the estimated exact solutions, which are obtained using the time step $\Delta t = 5 \times 10^{-5}$. For the parameter sets we used, all four numerical schemes give the same results under this time step. In studying the numerical accuracy, we use the following notations to indicate the numerical errors:

$\epsilon_{N_1}^{\Delta t}$: error in the fractional mass of component $m_F = 1$ computed with time step Δt;

$\epsilon_{E}^{\Delta t}$: error in the total energy computed with time step Δt.

4.4.3.1 Ferromagnetic interaction

For the case of condensate with ferromagnetic interaction, we consider 10^4 ^{87}Rb atoms in a cigar-shaped harmonic potential with trapping frequencies $\omega_x = 2\pi \times 20$[Hz], and $\omega_y = \omega_z = 2\pi \times 400$[Hz]. The atomic parameters are given by $m = 1.443 \times 10^{-25}$[kg], $a_0 = 5.387$[nm], $a_2 = 5.313$[nm], and

	Method	$\epsilon_{N_1}^{0.01}$	$\epsilon_{E}^{0.01}$	$\epsilon_{N_1}^{0.001}$	$\epsilon_{E}^{0.001}$
$M = 0.2$	PWMF+BFSP	0.018	0.0006	0.002	0.0001
	PWMF+BESP	$\underline{0.007}$	$\underline{0}$	$\underline{0.001}$	0.0001
$N_1 = 0.306$	POMF+BFSP	0.015	0.0005	0.003	0
$E = -1132.9770$	POMF+BESP	0.015	0.0005	0.002	0
$M = 0.5$	PWMF+BFSP	0.007	0.0002	0.001	0.0001
	PWMF+BESP	$\underline{0.004}$	$\underline{0.0001}$	$\underline{0}$	0.0001
$N_1 = 0.535$	POMF+BFSP	0.007	0.0004	0.001	0.0001
$E = -2886.7040$	POMF+BESP	0.015	0.0013	0.002	0.0001
$M = 0.8$	PWMF+BFSP	$\underline{0.001}$	0.0002	0	0.0001
	PWMF+BESP	0.003	$\underline{0.0001}$	0	0.0001
$N_1 = 0.805$	POMF+BFSP	$\underline{0.001}$	0.0002	0	0.0001
$E = -4640.4221$	POMF+BESP	0.005	0.0009	0	0.0001

Table 4.5: Comparison of numerical schemes for computing the spin-1 ^{87}Rb ground state in uniform magnetic field with Zeeman energies $p = 5845.80$ and $q = 0.5$ (the smallest error is underlined).

	Method	$\epsilon_{N_1}^{0.01}$	$\epsilon_{E}^{0.01}$	$\epsilon_{N_1}^{0.001}$	$\epsilon_{E}^{0.001}$
$M = 0.2$	PWMF+BFSP	0.006	0.0009	0.001	0
	PWMF+BESP	$\underline{0.002}$	$\underline{0.0001}$	$\underline{0}$	0
$N_1 = 0.211$	POMF+BFSP	0.014	0.0025	0.002	0
$E = -2578.0254$	POMF+BESP	0.014	0.0024	0.001	0
$M = 0.5$	PWMF+BFSP	0.002	0.0005	0	0.0001
	PWMF+BESP	$\underline{0}$	$\underline{0.0001}$	0	0
$N_1 = 0.505$	POMF+BFSP	0.004	0.0008	0.001	0.0001
$E = -6499.3979$	POMF+BESP	0.007	0.0017	0.001	0.0001
$M = 0.8$	PWMF+BFSP	0	0.0002	0	0
	PWMF+BESP	0	$\underline{0.0001}$	0	0
$N_1 = 0.801$	POMF+BFSP	0	0.0002	0	0
$E = -10420.7489$	POMF+BESP	0.001	0.0005	0	0

Table 4.6: Comparison of numerical schemes for computing the spin-1 ^{87}Rb ground state in uniform magnetic field with Zeeman energies $p = 13071.61$ and $q = 0.5$ (the smallest error is underlined).

$E_{\text{hfs}} = 4.5287 \times 10^{-24}$[J]. The uniform magnetic field B[G] is applied in the z-direction and the effective one-dimensional potential and parameters are found to be $V(x) = \frac{1}{2}x^2$, $\beta_n = \frac{2(a_0+2a_2)N}{3a_s}\frac{\sqrt{\omega_y\omega_z}}{\omega_x} = 885.4$, $\beta_s = \frac{2(a_2-a_0)N}{3a_s}\frac{\sqrt{\omega_y\omega_z}}{\omega_x} = -4.1$, $p = -34990.6346B$ and $q = 3.5827B^2$, where the dimensionless length scaling unit $a_s = 2.4116[\mu\text{m}]$ and time scaling unit $t_s = 7.958$[ms].

Tables 4.5&4.6 compare the accuracy of different numerical schemes in computing the spin-1 ^{87}Rb ground state in uniform magnetic field $B = 1.6707 \times 10^{-1}$[G] ($p = 5845.80$, $q = 0.5$) and $B = 3.7357 \times 10^{-1}$[G] ($p = 13071.61$, $q = 0.5$), respectively. As shown in the two tables, scheme 2, i.e. PWMF with BESP discretization, gives the most accurate results under large time step $\Delta t \sim 0.01$. When a smaller time step, e.g. $\Delta t \sim 0.001$, is used, all four numerical schemes give good results. In term of efficiency, the BFSP method is preferable in the case of smaller time step since it is explicit.

4.4.3.2 Antiferromagnetic interaction

	Method	$\epsilon_{N_1}^{0.01}$	$\epsilon_E^{0.01}$	$\epsilon_{N_1}^{0.001}$	$\epsilon_E^{0.001}$
$M = 0.2$	PWMF+BFSP	0.022	0.0008	0.003	0
	PWMF+BESP	0.03	0.0012	0.005	0
$N_1 = 0.277$	POMF+BFSP	$\underline{0.007}$	$\underline{0.0002}$	$\underline{0.001}$	0
$E = -579.9371$	POMF+BESP	0.046	0.0022	0.007	0
$M = 0.55$	PWMF+BFSP	0.072	0.0032	0.034	0.0002
	PWMF+BESP	0.092	0.0057	0.026	0.0005
$N_1 = 0.760$	POMF+BFSP	$\underline{0.007}$	$\underline{0.0001}$	$\underline{0}$	$\underline{0}$
$E = -1621.5122$	POMF+BESP	0.081	0.0042	0.022	0.0003
$M = 0.6$	PWMF+BFSP	0.052	0.0033	0.020	0.0009
	PWMF+BESP	0.085	0.0077	0.060	0.0042
$N_1 = 0.800$	POMF+BFSP	$\underline{0}$	$\underline{0.0001}$	$\underline{0}$	$\underline{0}$
$E = -1770.3084$	POMF+BESP	0.074	0.0060	0.051	0.0031
$M = 0.8$	PWMF+BFSP	0	0.0002	0	0.0001
	PWMF+BESP	0.004	0.0013	0	0.0001
$N_1 = 0.900$	POMF+BFSP	0	$\underline{0.0001}$	0	$\underline{0}$
$E = -2365.4656$	POMF+BESP	0	0.0100	0	0.0100

Table 4.7: Comparison of numerical schemes for computing the spin-1 ^{23}Na ground state in uniform magnetic field with Zeeman energies $p = 2976.27$ and $q = 0.1$ (the smallest error is underlined).

	Method	$\epsilon_{N_1}^{0.01}$	$\epsilon_{E}^{0.01}$	$\epsilon_{N_1}^{0.001}$	$\epsilon_{E}^{0.001}$
$M = 0.2$	PWMF+BFSP	0.004	0.0008	0	0
	PWMF+BESP	0.005	0.0011	0	0
$N_1 = 0.209$	POMF+BFSP	$\underline{0.001}$	$\underline{0.0003}$	0	0
$E = -1315.6122$	POMF+BESP	0.012	0.0037	0.001	0
$M = 0.5$	PWMF+BFSP	0.009	0.0019	0.001	0.0001
	PWMF+BESP	$\underline{0.003}$	$\underline{0.0003}$	0	0
$N_1 = 0.522$	POMF+BFSP	$\underline{0.003}$	0.0004	0	0
$E = -3311.9032$	POMF+BESP	0.013	0.0020	0.001	0
$M = 0.95$	PWMF+BFSP	0.012	0.0017	0.002	0
	PWMF+BESP	0.010	0.0012	0.002	0
$N_1 = 0.966$	POMF+BFSP	0.006	$\underline{0.0002}$	$\underline{0.001}$	0
$E = -6306.3645$	POMF+BESP	$\underline{0.004}$	$\underline{0.0002}$	0	0
$M = 0.99$	PWMF+BFSP	0.002	0.0006	0	0
	PWMF+BESP	$\underline{0.001}$	0.0004	0	0
$N_1 = 0.995$	POMF+BFSP	0	$\underline{0.0001}$	0	0
$E = -6572.5433$	POMF+BESP	0	0	0	0

Table 4.8: Comparison of numerical schemes for computing the spin-1 ^{23}Na ground state in uniform magnetic field with Zeeman energies $p = 6655.15$ and $q = 0.5$ (the smallest error is underlined).

For the case of condensate with antiferromagnetic interaction, we consider 10^4 ^{23}Na atoms in the cigar-shaped harmonic potential with trapping frequencies $\omega_x = 2\pi \times 20$[Hz], and $\omega_y = \omega_z = 2\pi \times 400$[Hz]. The atomic parameters are $m = 3.816 \times 10^{-26}$[kg], $a_0 = 2.646$[nm], $a_2 = 2.911$[nm], and $E_{\rm hfs} = 1.1739 \times 10^{-24}$[J]. The effective one-dimensional potential and parameters are found to be $V(x) = \frac{1}{2}x^2$, $\beta_n = 240.8$, $\beta_s = 7.5$, $p = 34990.6346B$, and $q = 13.8216B^2$, where the dimensionless length scaling unit $a_s = 4.6896[\mu$m] and time scaling unit $t_s = 7.958$[ms].

Tables 4.7&4.8 compare the accuracy of different numerical schemes in computing the spin-1 ^{23}Na ground state in uniform magnetic field $B = 8.5059 \times 10^{-2}$[G] ($p = 2976.27$, $q = 0.5$) and $B = 1.9020 \times 10^{-1}$[G] ($p = 13071.61$, $q = 0.5$), respectively. From the two tables, numerical scheme 3, i.e. POMF with BFSP discretization always gives the results with the smallest error, in particular for the case when the total magnetization is close to the critical magnetization, which will be discussed later. Therefore, we conclude that POMF with BFSP discretization is the best for computing antiferromagnetic condensate ground state, for its high accuracy and efficiency in terms of computational time.

4.4.4 Application

The numerical solution of spin-1 BEC ground state in a harmonic potential have been discussed in literature [118]. In this section, we will apply the POMF method with BFSP discretization to compute the spin-1 BEC ground state in a harmonic plus optical lattice potential. The ground state solution in a harmonic potential is used as a reference frame to investigate the influence of periodic potential, as well as the effect of interatomic interaction in the mean field ground state solution.

4.4.4.1 Ferromagnetic interaction

Simulations for ^{87}Rb, with the same set of parameters as in Section 4.4.3.1, are carried out for a harmonic plus optical lattice potential,

$$V(x) = \frac{1}{2}x^2 + V_0 \sin^2(\frac{\pi x}{2}), \tag{4.125}$$

where V_0 is the depth of the optical lattice. Figures 4.13(a)&(b) show the ground state solutions of spin-1 ^{87}Rb ($M = 0.3$) in the harmonic potential, while Figures 4.13(c) &(d) show the ground state solutions when the periodic potential with $V_0 = 50$ is added. The ground state in the potential (4.125) can be viewed as the ground state in a harmonic potential modulated by a periodic function. Figure 4.14 shows a few ^{87}Rb ground states in potential (4.125) with $V_0 = 50$ for the fixed $q = 0.1$ and different M. The relative population of each spinor component, as shown in Figure 4.15, is found to be almost unaffected by the existence of the optical lattice except for the case of small magnetization.

We investigated also the effect of spin-independent mean field interaction β_n on the ground state phase diagram. Figure 4.20 (right column) shows the relative population of each component for several β_n. The interaction is repulsive and increasing β_n has the similar effect as increasing the magnitude of magnetic field, or equivalently, increasing the quadratic Zeeman energy q.

4.4.4.2 Antiferromagnetic interaction

Simulations for ^{23}Na, with the same set of parameters as in Section 4.4.3.2, are carried out for harmonic plus optical lattice potential (4.125) with $V_0 = 50$. Figures 4.16(a)&(b) show the ground state solutions of spin-1 ^{23}Na ($M = 0.3$) in a harmonic potential, while Figures 4.16(c)&(d) show the solutions when the periodic potential exists. For both potentials, ϕ_0 is immiscible with ϕ_1 and ϕ_{-1}. For constant M, the immiscibility property is better defined for larger q, with thinner overlapping layer. When a periodic potential exists, the immiscibility property of the three components is further enhanced. Figure 4.17 shows a few ^{23}Na ground states in potential (4.125) with $V_0 = 50$ for fixed $q = 0.1$ and different M.

Figure 4.18 depicts the relative population of each hyperfine component as function of M and as function of q. In the ground state phase diagram of BEC with antiferromagnetic interaction subjected to weak magnetic field, there exists a critical value for magnetization (M_c) such that when $M < M_c$, all three hyperfine components co-exist, and when $M > M_c$, only components $m_F = \pm 1$ exist. At $M = M_c$, the ground state is not unique and two stationary solutions, one with the three co-existing components and the other one with zero particle in component $m_F = 0$, share the same energy level. As shown in Figure 4.18, the existence of optical lattice has the effect of shifting M_c to a smaller value, or equivalently, shifting the critical value of magnetic field q_c to a larger value when M is held as constant. Computations are also carried out for optical lattice of different depths V_0 in (4.125) and M_c as a function of q is plotted in Figure 4.19. The critical magnetization M_c is found to decrease when the lattice depth increases.

The effect of spin-independent mean field interaction on the ground state phase diagram is also investigated for the antiferromagnetic interaction case. Figure 4.20(left column) shows the relative population of each component for several β_n. Similarly to the ferromagnetic case, increasing β_n has the similar effect as increasing the magnitude of the magnetic field. Large β_n gives larger critical magnetization. The relation between M_c and β_n is depicted in Fig. 4.21

4.5 Discussion

We have proposed an efficient and accurate normalized gradient flow method to compute the ground state of spin-1 Bose-Einstein condensates, through the introduction of a third normalization condition, in addition to the conservation of total particle number and the conservation of total magnetization. The condition is derived from the relations between the chemical potentials of the three spinor components together with a first-order time splitting scheme applied to the continuous normalized gradient flow used in the computation of the spin-1 BEC ground state. The backward-forward sine-pseudospectral method is applied to discretize the normalized gradient flow for practical computation.

Based on our extensive numerical results, we conjecture that when $\beta_n \geq 0$, $\beta_n \geq |\beta_s|$, $V(\boldsymbol{x}) \geq 0$, and $\lim_{|\boldsymbol{x}|\to\infty} V(\boldsymbol{x}) \to \infty$, there exists a solution of the nonconvex minimization problem (4.14). In addition, when $\beta_s < 0$, the positive minimizer (the three wavefunctions are positive functions) is unique; when $\beta_s > 0$, the nonnegative minimizer (ϕ_1 and ϕ_{-1} are positive and $\phi_0 \equiv 0$) is unique.

The method was then extended to compute the ground state of spin-1 BEC in uniform magnetic field. Using a similar kind of approach, we found two ways to incorporate the Zeeman energies with the coupled Gross-Pitaevskii equations numerically: (i) PWMF method: both linear and quadratic Zeeman terms are treated in the normalization step, and (ii) POMF method: the quadratic Zeeman term is retained in the gradient flow while the linear Zeeman term is included in the normalization step. In both treatments, the effect of the linear Zeeman term will be finally canceled out in the third normalization condition and it has no effect on the ground state solution. Numerical results show that the POMF approach with the backward-forward Euler sine-pseudospectral method is the best numerical scheme for the ground state computation, in terms of accuracy and efficiency.

The condensate ground state in harmonic plus optical lattice potential, for the cases of different quadratic Zeeman energy, was also studied. For a condensate with ferromagnetic interaction, the existence of optical lattice makes no significant difference in the ground state phase diagram except for small M, as compared to the condensate ground state in a harmonic trap. For a condensate with antiferromagnetic interaction, the optical lattice tends to reduce the critical value of magnetization and M_c can be further reduced by increasing lattice depth.

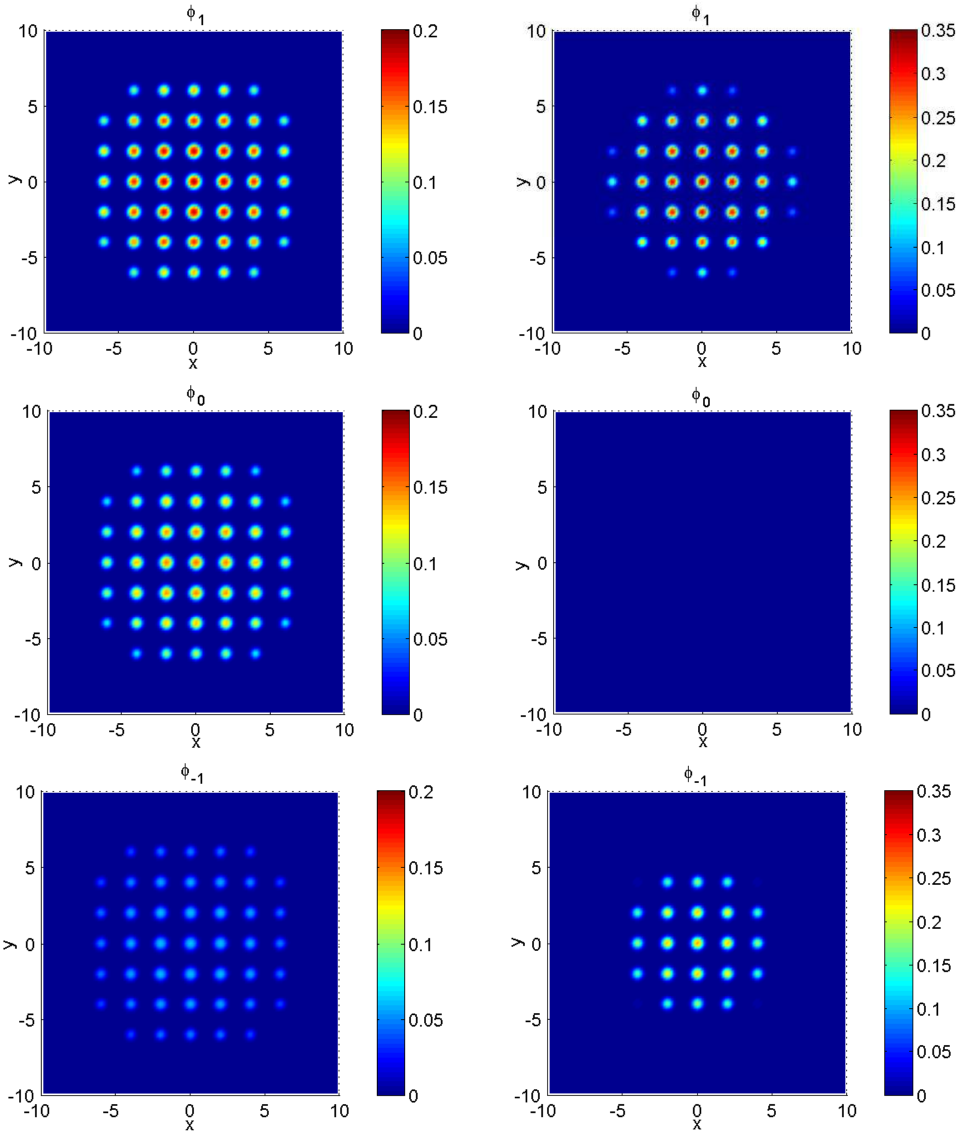

Figure 4.12: Contour plots of the wavefunctions of the ground state, i.e. $\phi_1(x, y, 0)$ (top row), $\phi_0(x, y, 0)$ (middle row) and $\phi_{-1}(x, y, 0)$ (bottom row) with $N = 10^4$ and $M = 0.5$ in an optical lattice potential for ^{87}Rb in Case I (left column), and for ^{23}Na in Case II (right column).

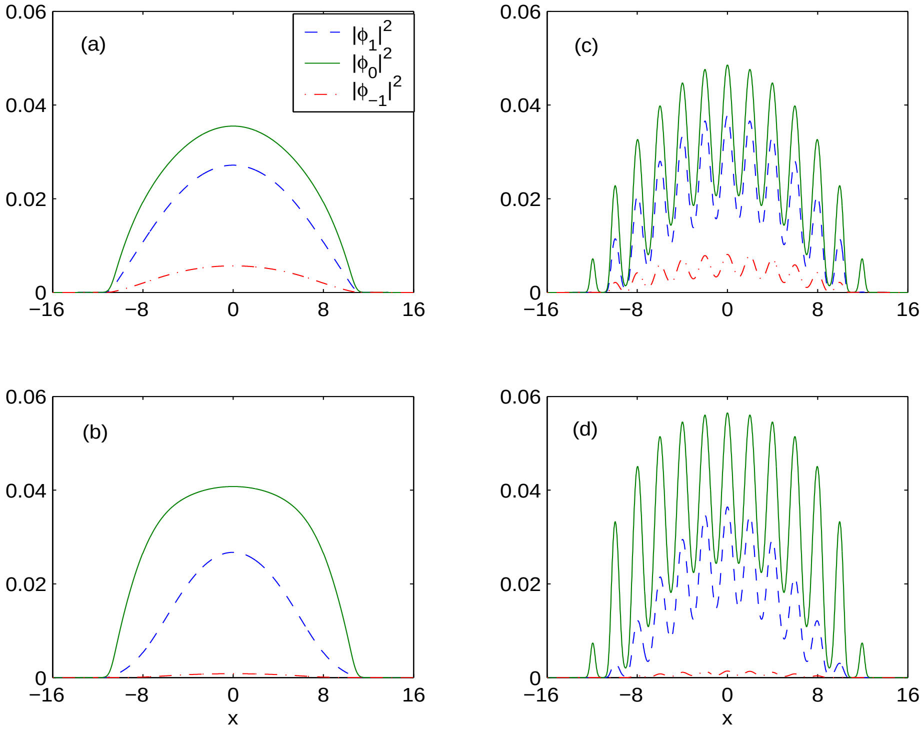

Figure 4.13: Ground state of ^{87}Rb with $M = 0.3$ in harmonic potential (left column) and harmonic plus optical lattice potential (right column), subjected to magnetic field (a,c) $q = 0.1$ and (b,d) $q = 0.5$.

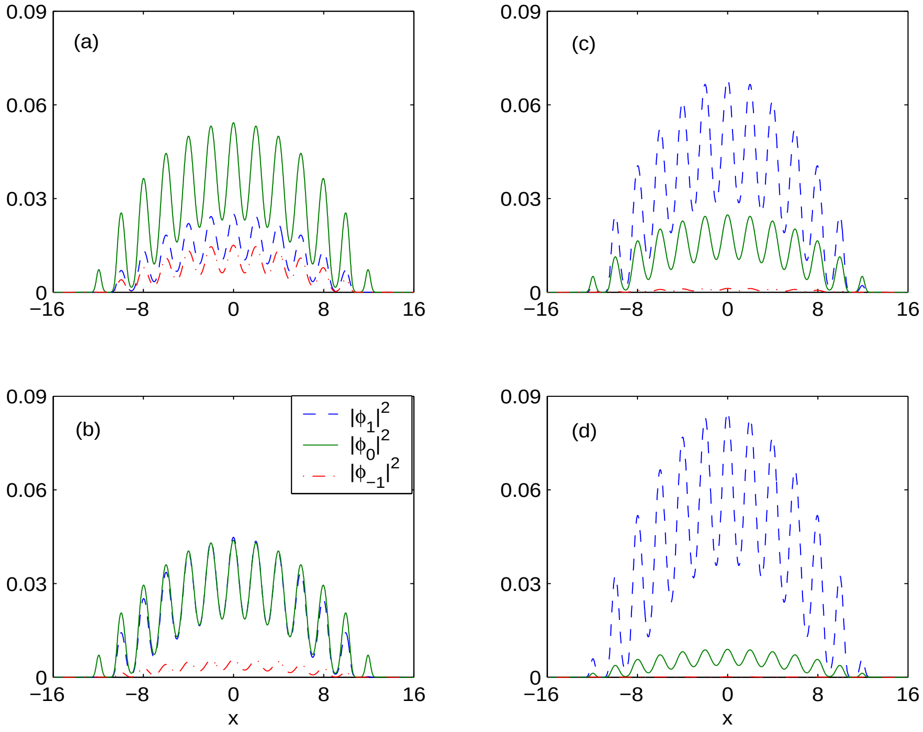

Figure 4.14: Ground state of ^{87}Rb in harmonic plus optical lattice potential with (a) $M = 0.1$, (b) $M = 0.4$, (c) $M = 0.7$, and (d) $M = 0.9$ subjected to $q = 0.1$.

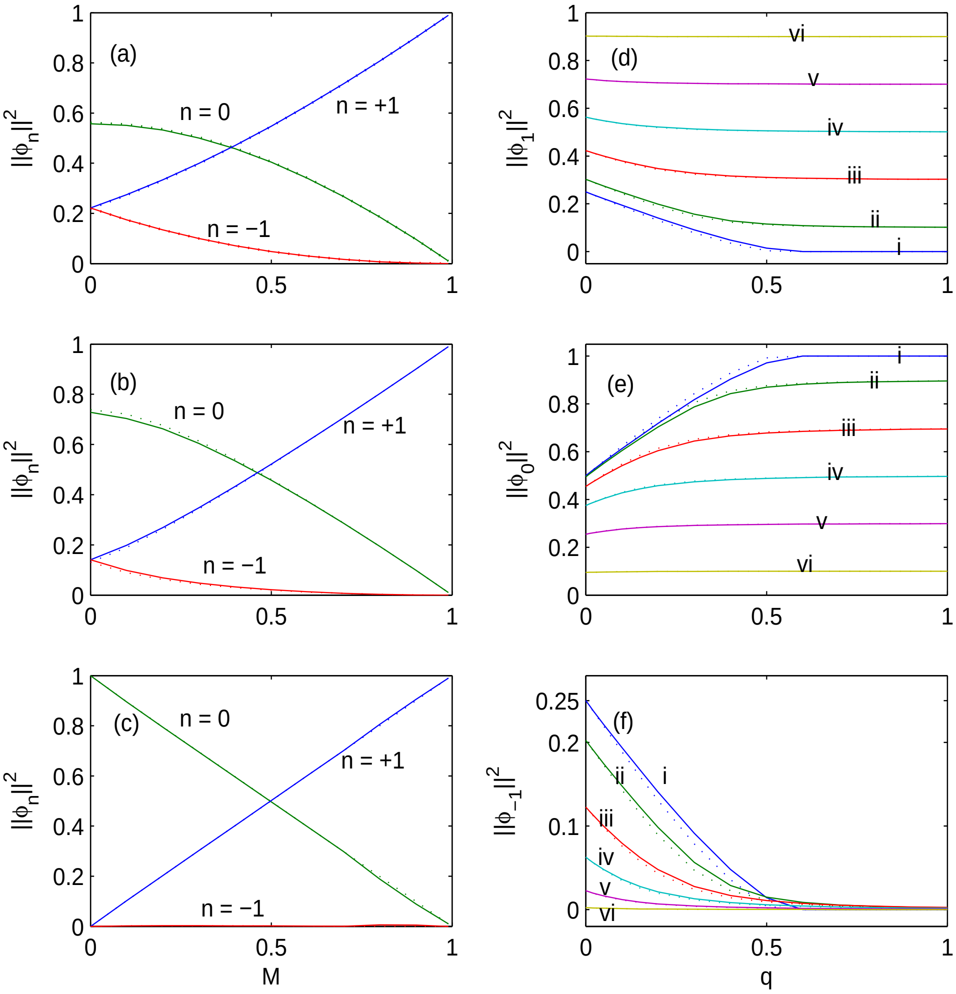

Figure 4.15: Relative population of each hyperfine component of ^{87}Rb in a harmonic potential (dotted line) and a harmonic plus optical lattice potential (solid line), (left column) with respect to magnetization, for (a) $q = 0.05$, (b) $q = 0.2$, and (c) $q = 1.0$; (right column) with respect to quadratic Zeeman energy for (i) $M = 0$, (ii) $M = 0.1$, (iii) $M = 0.3$, (iv) $M = 0.5$, (v) $M = 0.7$, and (vi) $M = 0.9$.

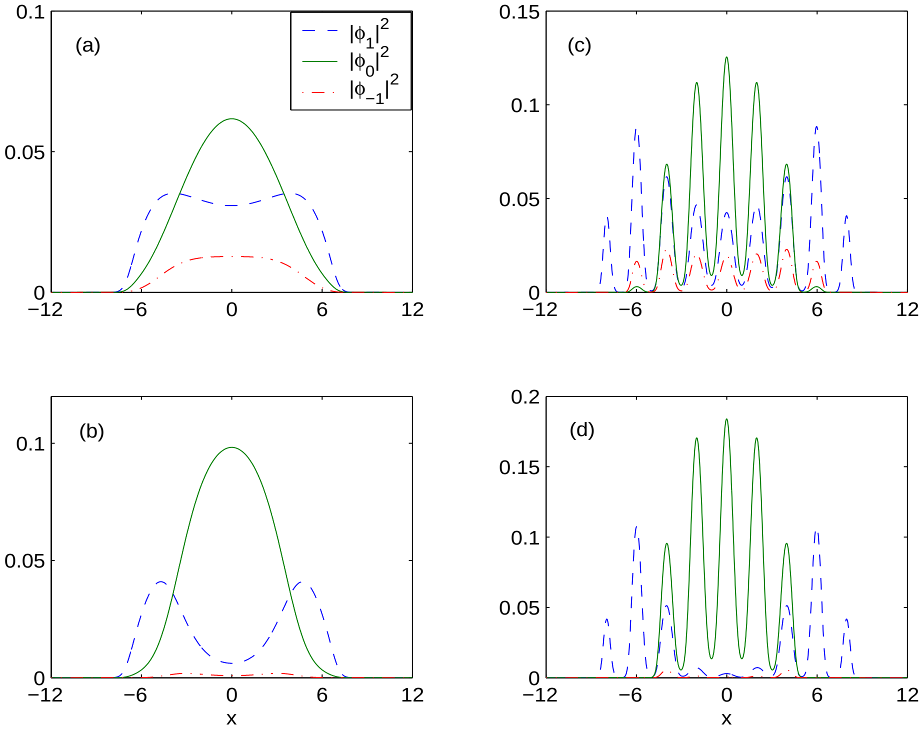

Figure 4.16: Ground state of ^{23}Na with $M = 0.3$ in harmonic potential (left column) and harmonic plus optical lattice potential (right column), subjected to magnetic field (a,c) $q = 0.1$, and (b,d) $q = 0.5$.

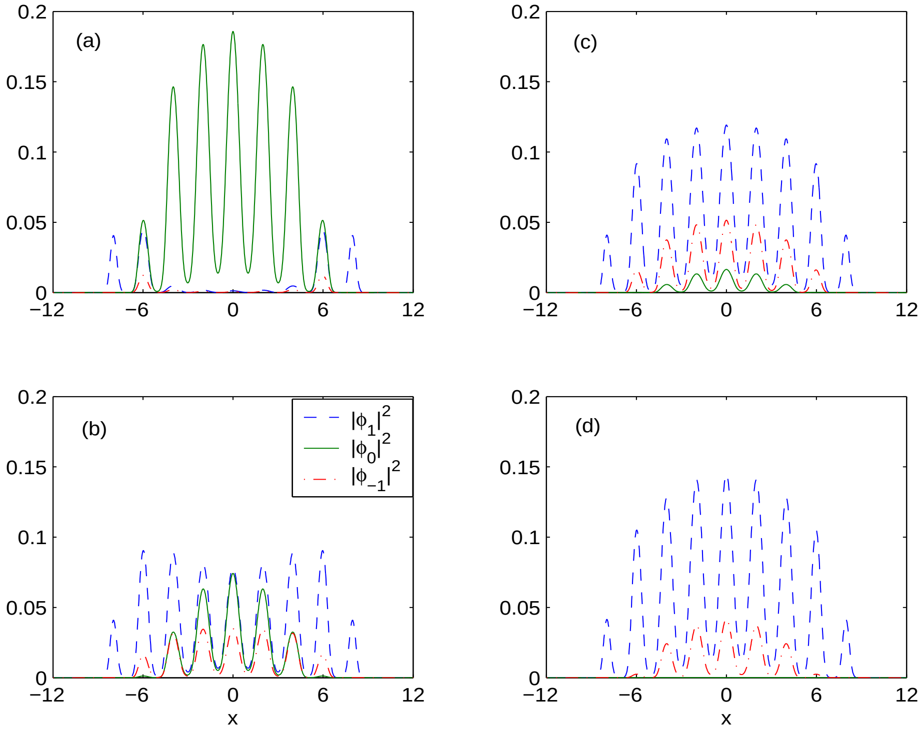

Figure 4.17: Ground state of ^{23}Na in harmonic plus optical lattice potential with (a) $M = 0.1$, (b) $M = 0.4$, (c) $M = 0.5$, and (d) $M = 0.7$ subjected to $q = 0.1$.

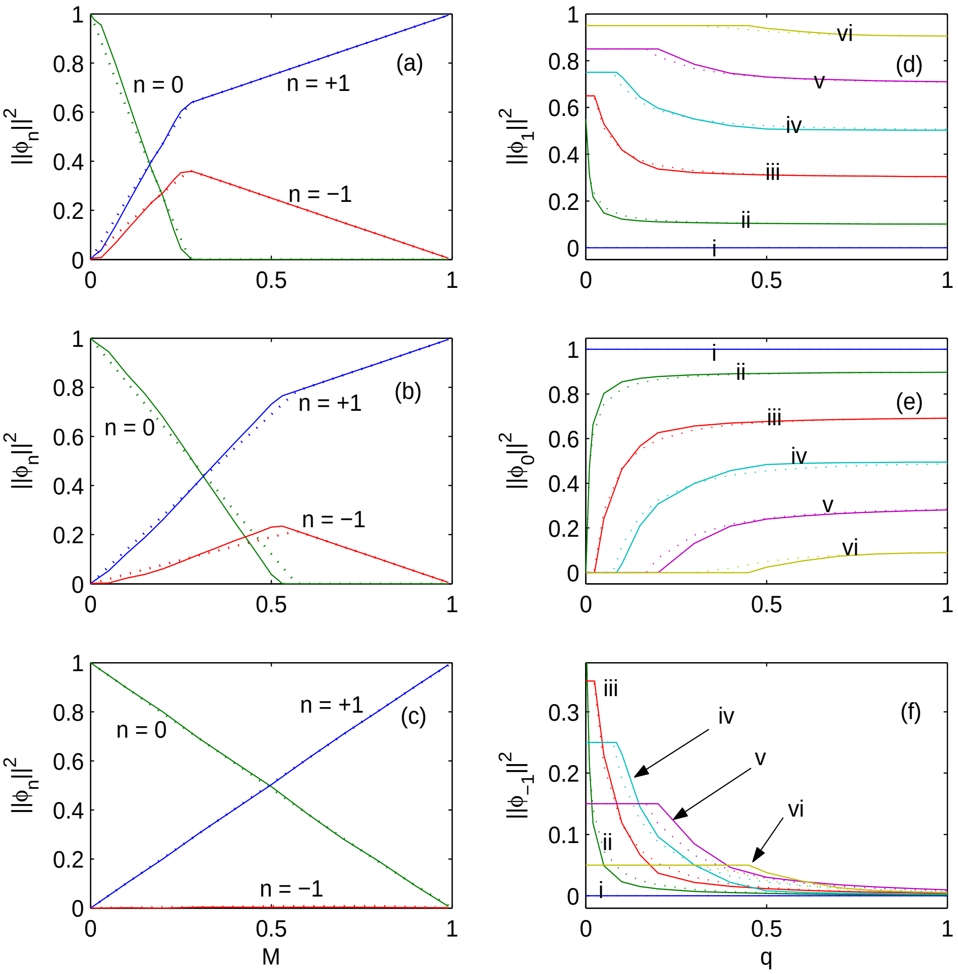

Figure 4.18: Relative population of each hyperfine component of ^{23}Na in a harmonic potential (dotted line) and a harmonic plus optical lattice potential (solid line), (left column) with respect to magnetization for (a) $q = 0.02$, (b) $q = 0.1$, and (c) $q = 1.0$; (right column) with respect to quadratic Zeeman energy for (i) $M = 0$, (ii) $M = 0.1$, (iii) $M = 0.3$, (iv) $M = 0.5$, (v) $M = 0.7$, and (vi) $M = 0.9$.

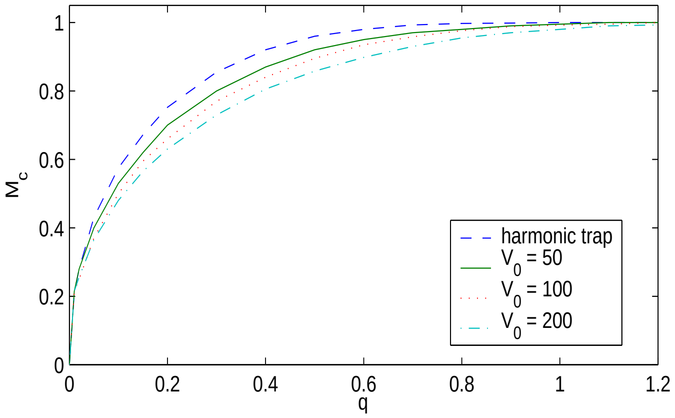

Figure 4.19: Critical magnetization M_c with respect to the quadratic Zeeman energy q for 10^4 spin-1 ^{23}Na atoms in different trapping potentials.

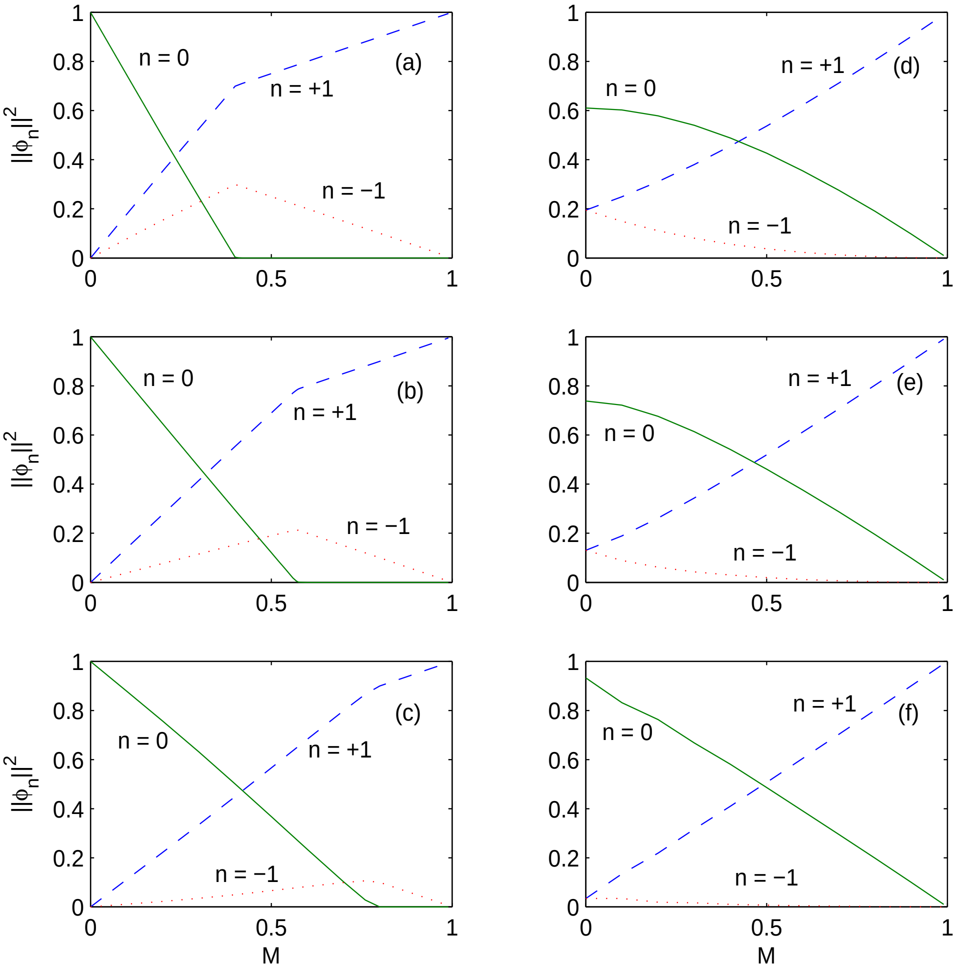

Figure 4.20: Relative population of each hyperfine component of (left column) ^{23}Na with $\beta_s = 7.5$ and (a) $\beta_n = 24.08$, (b) $\beta_n = 240.8$, and (c) $\beta_n = 2408$; and of (right column) ^{87}Rb with $\beta_s = -4.1$ and (d) $\beta_n = 88.54$, (e) $\beta_n = 885.4$, and (f) $\beta_n = 8854$, in harmonic potential $V(x) = \frac{1}{2}x^2$.

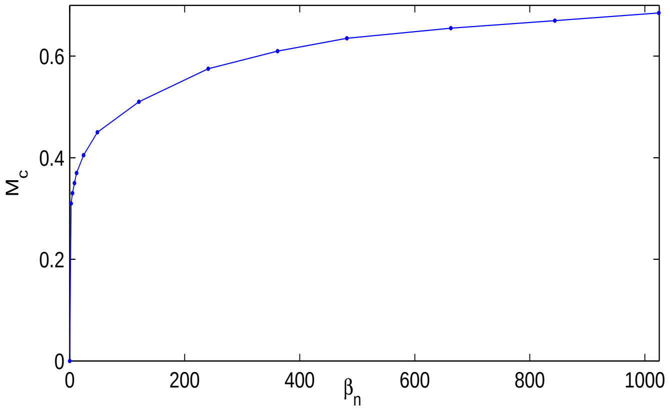

Figure 4.21: Critical magnetization M_c with respect to the spin-independent mean-field interaction β_n for spin-1 ^{23}Na atoms with spin-exchange interaction $\beta_s = 7.5$.

Chapter 5

Dynamical Self-Trapping of BEC in Shallow Optical Lattices

The transport properties of BECs through optical lattices have sparked interest in recent years after a series of experiments revealed dissipative dynamics and instabilities [24, 32, 84, 100]. Early experiments with BECs in optical lattices showed characteristic effects of such a periodic potential on atoms, namely, Bloch oscillations [46] and Josephson junctions [7, 36]. In later years the research focus shifted towards the study of nonlinear effects arising due to the interaction of the atoms [43]. In a deep lattice it was found that increasing the nonlinearity leads to a self-trapped state within the lattice [9]. A theoretical framework of this self-trapping was derived in [5]. In this chapter, we study the transport of a strongly interacting, one-dimensional BEC partially exposed to a shallow optical lattice of finite width. A sudden breakdown of the transport of atoms is observed for high enough interaction strength and we attribute this behaviour to the development of a self-trapped state. An analytical description of the self-trapped states will be provided in terms of nonlinear Bloch waves [96].

5.1 The Model

A typical experiment in this field is conducted by trapping the atoms in a parabolic trap, i.e. a harmonic oscillator trap, and then switching on a moving optical lattice. Alternatively, one can displace the parabolic trap in a stationary lattice, which leads to acceleration of the atoms through the lattice. We model these experiments by a simplified setup where two flat-bottom potentials are connected via the optical lattice as shown in Figure 5.1. Instead of a moving lattice, we make use of the inherent expansion of the BEC. In contrast to experiments such as [9], in the present work we focus on the very shallow lattice regime, where the lattice depth is strictly less than the photon recoil energy. The theoretical study in [5] suggests that self-trapping is possible even at lower lattice depths, but it does not take into account a short, finite optical lattice. We extend previous works in this field by assuming a finite optical lattice connecting two reservoirs.

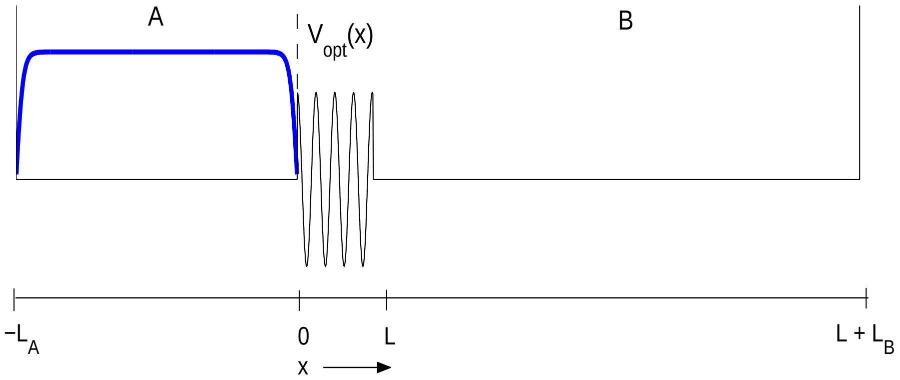

Figure 5.1: Schematic setup of the system. The BEC is initially located in the flat-bottom box reservoir A. The shutter to its right (dashed vertical line) can be removed instantaneously so that the atoms expand into the optical lattice $V_{\text{opt}}(x)$ of size L. A wide potential-free region B serves as a second reservoir for the atoms. In our numerical calculations, we used the dimensionless lengths $L_A = 160\pi, L_B = 326\pi$ and $L = 10\pi$.

The full setup is sketched in Figure 5.1. The flat-bottom reservoirs A and B serve as a source and a sink of the BEC, respectively. The BEC is initially confined in a potential-free box A. We use the flat-bottom trap geometry as a model to describe experiments with harmonic oscillator potentials, but it can also be realized more precisely as demonstrated, for example, in the experiment by Meyrath et al. [80]. The difference in the chemical potentials on the left- and right-hand side of the lattice leads to an expansion of the atoms into the lattice and eventually into reservoir B.

We consider a BEC at zero temperature in the elongated trap $V(\boldsymbol{x}) = \frac{1}{2m}\left[V_{\text{ax}}(x) + \omega_\perp(y^2+z^2)\right]$. The radial frequency $\omega_\perp$ is chosen to be $\hbar\omega_\perp \gg gn_0$, where g is the interaction strength of the atoms and n_0 is the average density of the BEC. In this chapter, we assume $g > 0$, which corresponds to repulsive atomic interaction. The above choice of the frequency $\omega_\perp$ results in freezing of the atomic motion in the radial directions. Hence, the BEC can be treated as an effectively one-dimensional condensate with a trapping potential $V_{\text{ax}}(x)$ along the axial direction. In our model, this potential has the form

$$V_{\text{ax}}(x) = \begin{cases} 0 & \text{for } -L_A \le x < 0, \\ V_{\text{opt}}(x) & \text{for } 0 \le x \le L, \\ 0 & \text{for } L < x \le L + L_B, \end{cases} \tag{5.1}$$

which is illustrated in Figure 5.1. The condensate is initialized in its ground state in the box potential of size L_A. After the initialization of the BEC in reservoir A, the shutter confining the BEC (dashed line in Figure 5.1) is removed. The BEC then penetrates a short optical lattice

$$V_{\text{opt}}(x) = V_0 + V_1 \cos(2\kappa x), \tag{5.2}$$

of size $L \ll L_A$. The periodicity κ is given by the geometry and the wavenumber of the lasers producing the standing wave, and determines the number of lattice sites $L\kappa/\pi$. The lattice height V_1 and the constant bias V_0 are assumed to be independently adjustable. The size of the sink reservoir B is $L_B \gg L$.

In order to obtain the dimensionless 1D GPE we introduce the following dimensionless quantities. Times are rescaled according to $\tilde{t} = t2E_R/\hbar$ and lengths according to $\tilde{x} = \kappa x$, where $E_R = \hbar^2\kappa^2/2m$ is the photon recoil energy. Furthermore, the wavefunction yields $\tilde{\psi}(\tilde{x}, \tilde{t}) = \kappa^{-1/2}\psi(x,t)$. For the convenience of the analysis in the later part of this chapter, the scaling units are chosen to be different from those introduced in Chapter 2. In the experimental setup, potential (5.1) is scaled into

$$v_{\text{ax}}(x) = \begin{cases} 0 & \text{for } -L_A \le x < 0, \\ v_{\text{opt}}(x) = v + s\cos(2x) & \text{for } 0 \le x \le L, \\ 0 & \text{for } L < x \le L + L_B, \end{cases} \tag{5.3}$$

where the tildes have been removed for clarity. The dimensionless constant offset is $v = V_0/2E_R$ and the lattice depth $s = V_1/2E_R$. At $T = 0$, the BEC can then be described by the dimensionless 1D GPE

$$i\frac{\partial}{\partial t}\psi(x,t) = \left[-\frac{1}{2}\frac{\partial^2}{\partial x^2} + v_{\text{ax}}(x) + \beta|\psi(x,t)|^2\right]\psi(x,t), \quad -L_A < x < L + L_B, \tag{5.4}$$

$$\psi(x, t=0) = \psi^0(x), \quad -L_A \le x \le L + L_B, \tag{5.5}$$

$$\psi(-L_A, t) = \psi(L + L_B, t) = 0, \quad t \ge 0. \tag{5.6}$$

The dimensionless interaction strength is $\beta = Na_s k\hbar\omega_\perp/E_R$, which is expressed in terms of the number of atoms N and the s-wave scattering length a_s. The wavefunction $\psi = \psi(x,t)$ is normalized according to $\int_{-L_A}^{L+L_B} |\psi(x,t)|^2 \, dx = 1$ for all times t. As an indicator of the dynamics of the system, we define the dimensionless current

$$j(x,t) = \frac{1}{2i}\left[\bar{\psi}(x,t)\frac{\partial}{\partial x}\psi(x,t) - \psi(x,t)\frac{\partial}{\partial x}\bar{\psi}(x,t)\right], \tag{5.7}$$

where $\bar{\psi}$ denotes the complex conjugate of the wavefunction ψ. As the sizes of both reservoir A and reservoir B are much larger than the lattice length, the current within the lattice is expected to stay more or less constant throughout a finite simulation time. As will become apparent in the numerical analysis, it is advantageous to define a more qualitative quantity, namely, the stationary current within the lattice. The stationary current is computed by taking the time derivative of the particle number in reservoir B, N_B, at times where the particle number within the lattice, N_{opt}, is nearly constant. Given at time t_0 with such a nearly constant particle number in the lattice, we define the stationary current as

$$j_0 = \left.\frac{dN_B}{dt}\right|_{t_0}. \tag{5.8}$$

In general, the stationary current will depend on all parameters of the system such as the lattice depth s or the interaction strength β.

5.2 Numerical Method

The BEC in reservoir A is initialized in its ground state, which can be computed with the normalized gradient flow with backward/backward-forward Euler sine-pseudospectral method. For the numerical treatment of the dynamics of the condensate passing through the optical lattice into reservoir B, we simulate the 1D GPE (5.4) by the time-splitting sine-pseudospectral (TSSP) method [13, 14]. We choose the spatial mesh size $h = \Delta x > 0$ with $h = (L + L_A + L_B)/M$ for M being an even positive integer, the time step size $k = \Delta t > 0$, and let the spatial and temporal grid points be

$$x_j = L_A + jh, \quad j = 0, 1, 2, ..., M, \quad t_n = nk, \quad n = 0, 1, 2, ...$$

Let ψ_j^n be the approximation of $\psi(x_j, t_n)$ and ψ^n be the solution vector with components ψ_j^n.

From time $t = t_n$ to $t = t_{n+1}$, the GPE (5.4) is solved in two splitting steps. The first step consists in solving

$$i\frac{\partial}{\partial t}\psi(x,t) = -\frac{1}{2}\frac{\partial^2}{\partial x^2}\psi(x,t), \tag{5.9}$$

for $t = t_n$ to $t = t_{n+1}$, followed by solving

$$i\frac{\partial}{\partial t}\psi(x,t) = \upsilon_{ax}(x)\psi(x,t) + \beta|\psi(x,t)|^2\psi(x,t), \tag{5.10}$$

for the same time step. The diffusion equation (5.9) subject to zero boundary conditions (5.6) can be discretized in space by the sine-spectral method and integrated in time exactly. For $t \in [t_n, t_{n+1}]$, the ODE (5.10) leaves the density invariant in time, i.e.

$$\frac{\partial}{\partial t}|\psi(x,t)|^2 = 0, \quad t_n \le t \le t_{n+1}.$$

Therefore, (5.10) is reduced to

$$i\frac{\partial}{\partial t}\psi(x,t) = \upsilon_{ax}(x)\psi(x,t) + \beta|\psi(x,t_n)|^2\psi(x,t), \quad t_n \le t \le t_{n+1}, \tag{5.11}$$

which can be integrated in time exactly. A second order Strang splitting is applied to combine the splitting steps (5.9) and (5.11) as follows

$$\psi_j^* = \exp\left[-\frac{i}{2}\left(\upsilon_{ax}(x_j) + \beta|\psi_j^n|^2\right)k\right]\psi_j^n, \tag{5.12}$$

$$\psi_j^{**} = \frac{2}{M}\sum_{m=1}^{M-1}\exp\left(-\frac{i}{2}\mu_m^2 k\right)\hat{\psi}_m^* \sin\left(\mu_m(x_j + L_A)\right), \quad j = 1, 2, \cdots, M-1, \tag{5.13}$$

$$\psi_j^{n+1} = \exp\left[-\frac{i}{2}\left(\upsilon_{ax}(x_j) + \beta|\psi_j^n|^2\right)k\right]\psi_j^{**}, \tag{5.14}$$

where $(\hat{U})_m$ $(m = 1, 2, \cdots, M-1)$, the sine transform coefficients of the vector $U = (U_0, U_1, \cdots, U_M)^T$ satisfying $U_0 = U_M = 0$, are defined as

$$\mu_m = \frac{\pi m}{b-a}, \qquad (\hat{U})_m = \sum_{j=1}^{M-1} U_j \ \sin(\mu_m(x_j + L_A)), \quad m = 1, 2, \cdots, M-1. \tag{5.15}$$

The overall time discretization error comes from the time-splitting error, which in this case is $O(k^2)$ while the spatial discretization is of spectral accuracy. The fast sine transform is applied in order to reduce the computational time.

5.3 Dynamical Self-Trapped States

In this section we will numerically investigate the transport of the BEC initially trapped in region A through the optical lattice. Various numerical findings, in particular the development of self-trapped states with finite life time, will be illustrated and explanation in terms of nonlinear band structure will be given.

5.3.1 Nonlinear band structure

If we assume a stationary state $\psi(x,t) = \exp(-i\mu t)\phi_q(x)$ and ignore the finite width of the optical lattice, the GPE (5.4) leads to the well-known Mathieu equation

$$\frac{d^2}{dx^2}\phi_q x + \left(-2v - 2s\cos(2x)\right)\phi_q = 0, \tag{5.16}$$

in the limit of vanishing interaction ($\beta = 0$). Here, μ is the chemical potential. The chemical potential of a BEC in the strongly repulsively interacting limit can be determined by utilizing the Thomas-Fermi approximation, which results in $\mu = \beta/L_A$. Our numerical calculations of the chemical potential of the initial 1D BEC are in good agreement with the Thomas-Fermi approximation for the parameters used in this chapter. In this limit, the energy eigenvalues of (5.16) develop the characteristic linear band structure of periodic potentials. The solutions $\phi_q(x)$ are the Bloch functions

$$\phi_q(x) = \exp(iqx)\sum_{l=1}^{\infty} c_l \exp(i2lx). \tag{5.17}$$

The parameter q is the quasi-momentum of the condensate.

Inclusion of the nonlinear term $\beta|\phi_q|^2$ with $\beta > 0$ in the GPE introduces a new energy scale into the system and thereby modifies the band structure of the Mathieu eigenvalues. To model the resulting wavefunction of the interacting case, we similarly assume a Bloch function representation of the state. In order to simplify the analytical model, we further truncate the Bloch waves according to [78]

$$\phi_q(x) = \sqrt{n}e^{iqx}\left(c_0 + c_{-1}e^{-2ix} + c_1 e^{2ix}\right). \tag{5.18}$$

The density n is defined as the averaged relative density of the BEC within the lattice, i.e.

$$n = \frac{N_{\text{opt}}}{L}. \tag{5.19}$$

The normalization of the full wavefunction $\psi(x)$ requires the coefficients to satisfy

$$|c_0|^2 + |c_{-1}|^2 + |c_1|^2 = 1. \tag{5.20}$$

The normalization condition allows us to parameterize the coefficients in terms of two angles η and θ according to the spherical coordinates, as pointed out in [78],

$$\begin{aligned} c_0 &= \cos\theta, &(5.21)\\ c_{-1} &= \sin\theta\sin\eta, &(5.22)\\ c_1 &= \sin\theta\cos\eta. &(5.23) \end{aligned}$$

Stationary states can be found by plugging the ansatz (5.18) together with (5.21)–(5.23) into the energy functional

$$\frac{\epsilon_d(\eta,\theta)}{n} = \frac{1}{n\pi}\int_0^\pi \left(\frac{1}{2}|\frac{d}{dx}\phi_q(x)|^2 + s\cos(2x)|\phi_q(x)|^2 + \frac{\beta}{2}|\phi_q(x)|^4\right) dx, \tag{5.24}$$

which represents the energy density within the lattice. Solving the integral analytically yields

$$\begin{aligned} \frac{\epsilon_d(\eta,\theta)}{n} &= \frac{q^2}{2} + 2\sin^2\theta[1 + q\cos(2\eta)]\\ &+ \frac{s}{2}\sin(2\theta)(\cos\eta + \sin\eta)\\ &+ \frac{n\beta}{64}\{43 - \cos(4\eta)[3+\cos(4\eta)] - \cos(4\theta)[7 + 8\sin(2\eta)]\\ &+ 8\sin(2\eta)[1 - \cos(2\theta)\sin(2\eta)]\}. \end{aligned} \tag{5.25}$$

The first line of (5.25) represents the kinetic energy, the second line represents the potential energy and the last two lines represent the interaction energy. Minimizing the energy density (5.25) with respect to η and θ, we get

$$\begin{aligned} 0 = \frac{\partial\epsilon}{n\partial\eta} &= -4q\sin^2\theta\sin(2\eta) + \frac{s}{2}\sin(2\theta)\left(\cos\eta - \sin\eta\right)\\ &\quad + \frac{n\beta}{16}\left[3 + \sin(8\eta) - 4\cos(2\theta)\sin(4\eta) + 8\sin^2(2\theta)\cos(2\eta)\right], &(5.26)\\ 0 = \frac{\partial\epsilon}{n\partial\theta} &= 2\sin(2\theta)\left(1 + q\cos(2\eta)\right) + s\cos(2\theta)\left(\cos\eta + \sin\eta\right)\\ &\quad + \frac{n\beta}{16}\left[4\sin^2(2\eta)\sin(2\theta) + 7\sin(4\theta) + 8\sin(2\eta)\sin(4\theta)\right]. &(5.27) \end{aligned}$$

By fixing different values of quasi-momentum q and solve (5.26)–(5.27) numerically, we obtain the band structure for given parameters $n\beta$ and s.

A net effect of the interparticle interaction in the energy spectrum is an overall mean field shift of the energies by $n\beta$. This effect is shown in Figure 5.2(a) for typical parameters used in our simulations. For $n\beta > s$ the band structure additionally develops a loop at the band edge, which gradually decreases the width of the first band gap [53, 78, 114]. These loops can be observed in Figure 5.2(b). The insets show a close-up of the band edges, where a loop has developed. Note that we only plot $|q|$ in a reduced zone scheme, which means that the loop closes symmetrically at $|q| > 1$. The relative position of the chemical potential (dashed line in the figure) and the band gap will be important for the explanation of the self-trapped state given in the next section.

Figure 5.3 shows a few energy contour plots of (5.25) for $n\beta > s$, where a loop is developed at the band edge. The band structures (Figure 5.2) are obtained by first identifying the stationary points in the energy contour plots, followed by solving (5.26)–(5.27) via Newton's method with an initial guess to the stationary points.

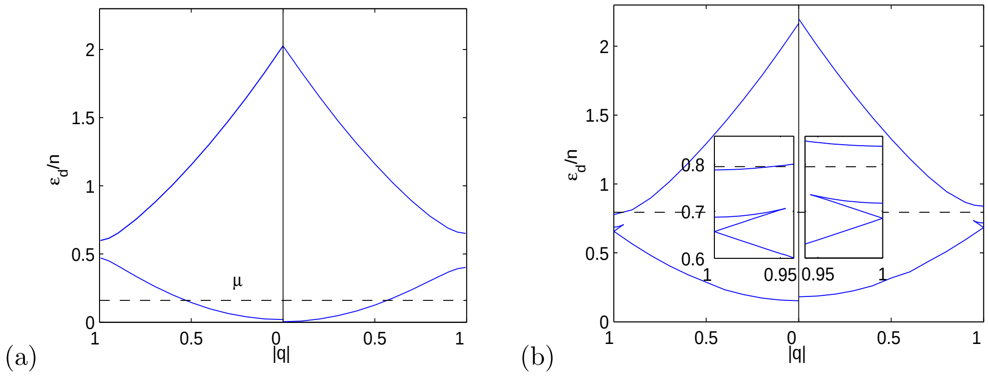

Figure 5.2: Band structure for four sets of parameters μ, s, and $n\beta$. The vertical line separates two sets with the same chemical potential (dashed line) but different s and $n\beta$. Each set is symmetric around $q = 0$, hence we plot $|q|$. The offset υ is kept at zero. The other parameters are (a) $\mu = 0.16, \beta = 79.58$ with $s = 0.13, n\beta = 0.05$ (left part) and $s = 0.25, n\beta = 0.04$ (right part); (b) $\mu = 0.795, \beta = 397.89$ with $s = 0.095, n\beta = 0.329$ (left part) and $s = 0.127, n\beta = 0.393$ (right part). The left and right insets in (b) show a zoom of the loops near the left and right band edges, respectively.

5.3.2 Numerical results

Applying the TSSP method, we calculate the stationary current (5.8) numerically. Figures 5.4(a)&(b) show two typical time-dependent plots of the particle number within the lattice and within reservoir B, for two sets of parameters with fixed interaction strength β but different optical lattice depth

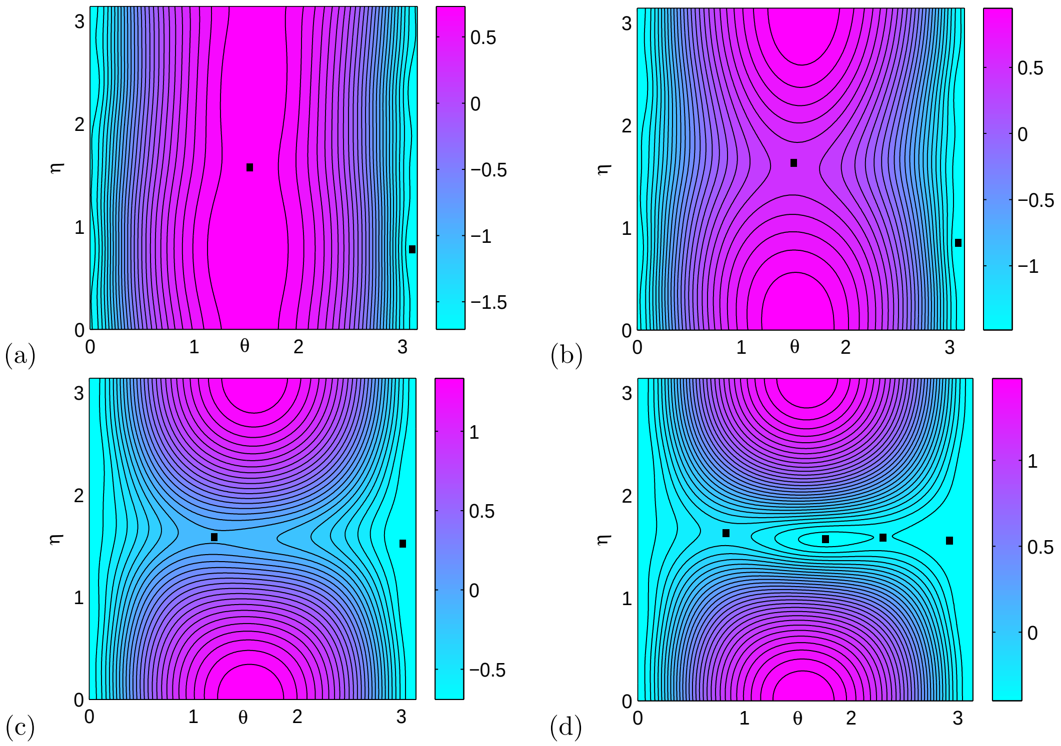

Figure 5.3: Contour plots of energy density with parameters $s = 0.127, n\beta = 0.393$, for (a) $q = 0$, (b) $q = 0.3$, (c) $q = 0.8$ and (d) $q = 0.99$. Black dots shown in the plots correspond to the stationary points, whose energies correspond to the band structure shown in Figure 5.2 (b) (right part).

s. From the particle number plots within the lattice, we can recognize plateaux at different times, which can be used to compute the stationary current. For example, in Figure 5.4(b) such plateaux exist at the three time intervals [80,190], [210,400] and [400,1100]. The stationary current is then computed according to (5.8). In Figure 5.4(c)&(d), two typical results for the time-dependent current (5.7) are shown at different positions within the lattice. The dashed horizontal line indicates the stationary current. It can be seen in the figure that the stationary current coincides well with the actual current within the lattice for an extended amount of time. The actual current undergoes small oscillations around the value of the stationary current. Figure 5.5 shows similar plots for another two sets of parameters, with the same lattice depth s but different interaction strength β. The stationary current indicates the gross expansion speed of the BEC. We will analyze its dependence on the parameters s and β below.

Intuitively one would expect the BEC in the setup of Figure 5.1 to expand into the optical lattice where its transport properties are subjected to the modified band structure discussed in Section 5.3.1. Numerical calculations are conducted in the regime of weak lattices ($s \ll 1$) and

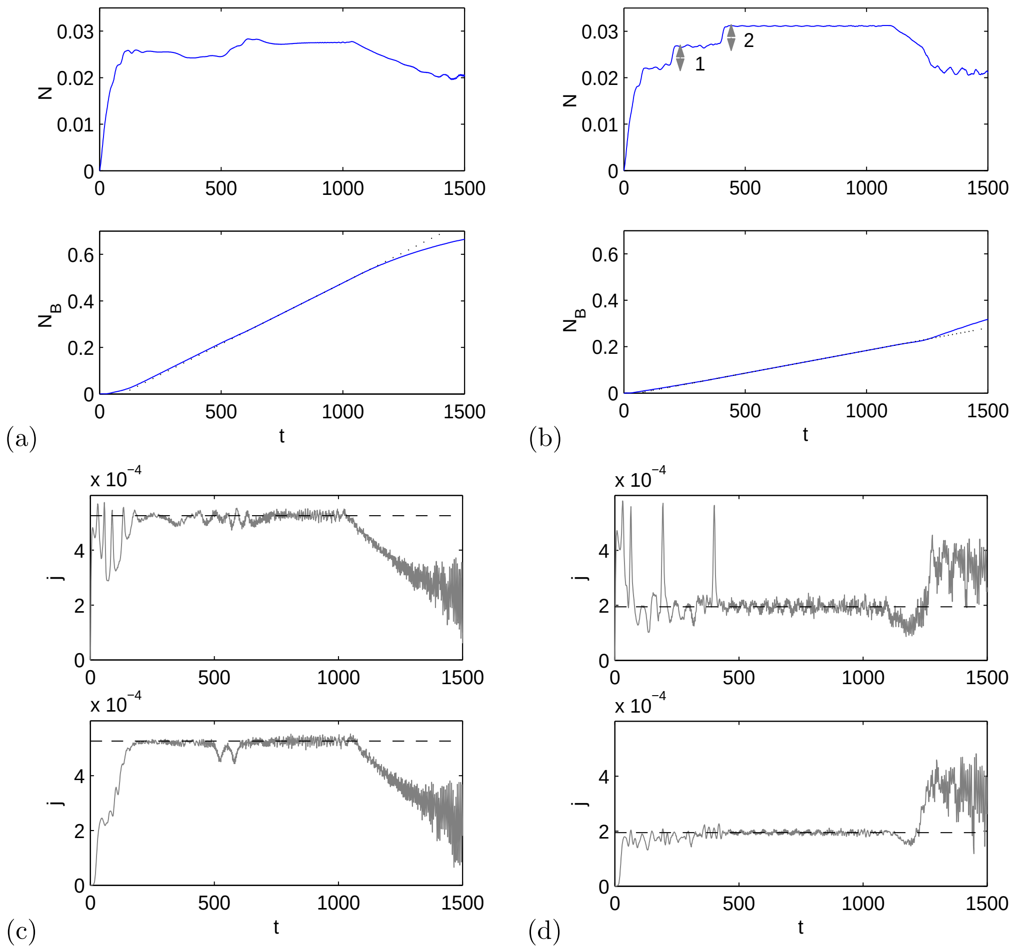

(a) (b) (c) (d)

Figure 5.4: (a,b) Time-dependent particle number within the lattice (upper panel) and within reservoir B (lower panel). The gradient of the dotted line gives the stationary current. (c,d) Time-dependent currents at the first lattice site (upper panel) and the last lattice site (lower panel). The dashed horizontal line indicates the stationary current. The parameters are $\beta = 397.89, \upsilon = 0$ for all plots and (a,c) $s = 0.095$ and (b,d) $s = 0.127$. The vertical bars in (b) indicates the analytical results for the particle number difference ΔN (see text and Table 5.1).

strong interaction ($\beta \gg 1$). If we plot the stationary current for different interaction strengths β as function of the optical lattice depth s, we notice a sharp drop in the curves for large β. In Figure 5.6(a) this drop is clearly visible, whereas for the lower interactions in Figure 5.6(c) it is absent in the shallow lattice regime. The value of stationary current at $s = 0$ increases with increasing β. This behaviour is expected since a higher repulsive interaction leads to a higher potential difference between the reservoirs, which drives more atoms through the lattice region. An increase of the lattice depth s does not influence the stationary current in Figure 5.6(a) at first, instead it stays constant up to the drop. After the drop it decreases when the lattice depth increases.

We can relate the sudden drop in the stationary current to the development of an extended

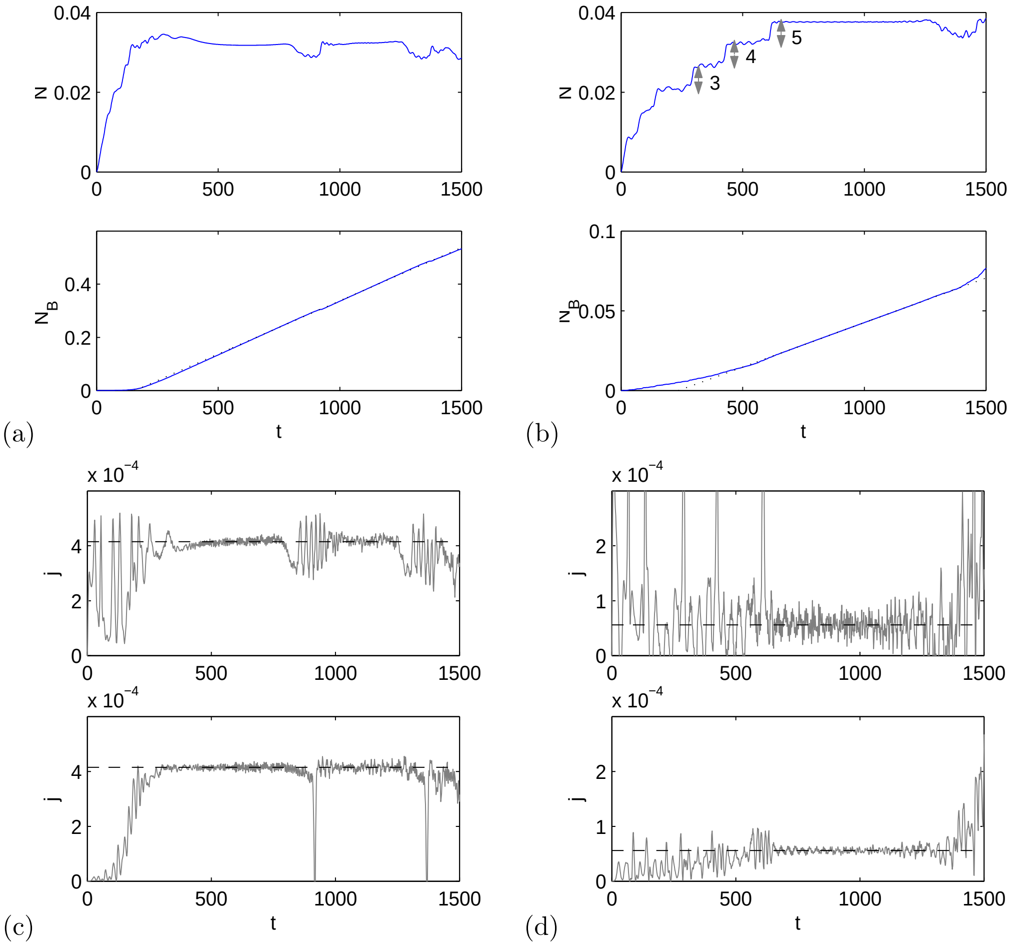

(a) (b) (c) (d)

Figure 5.5: (a,b) Time-dependent particle number within the lattice (upper panel) and within reservoir B (lower panel). The gradient of the dotted line gives the stationary current. (c,d) Time-dependent currents at the first lattice site (upper panel) and the last lattice site (lower panel). The dashed horizontal line indicates the stationary current. The parameters are $s = 0.253, \upsilon = 0$ for all plots and (a,c) $\beta = 251.46$ and (b,d) $\beta = 318.31$. The vertical bars in (b) indicates the analytical results for the particle number difference ΔN (see text and Table 5.1).

plateau in the time-dependent particle density within the lattice. In Figure 5.4(b) upper panel, we clearly recognize such a plateau for times from 400 to 1100, as well as shorter plateaux at earlier times. For the parameters of this plot, $\beta = 397.89$ and $s = 0.127$, a drop in the stationary current has occurred (cf. Figure 5.6(a)). The drop can also be observed in the time dependent current plotted in Figure 5.4(d), which is lower than the current in Figure 5.4(c) with $s = 0.095$. The existence of the plateau indicates that after the drop, the BEC density within the lattice stays constant for an extended amount of time and there is only a small residual current flowing through the lattice. The BEC has effectively stopped its expansion despite its high repulsion and despite the lattice being very shallow. Similar phenomenon is observed in Figure 5.5(b)&(d), when the interaction is strong.

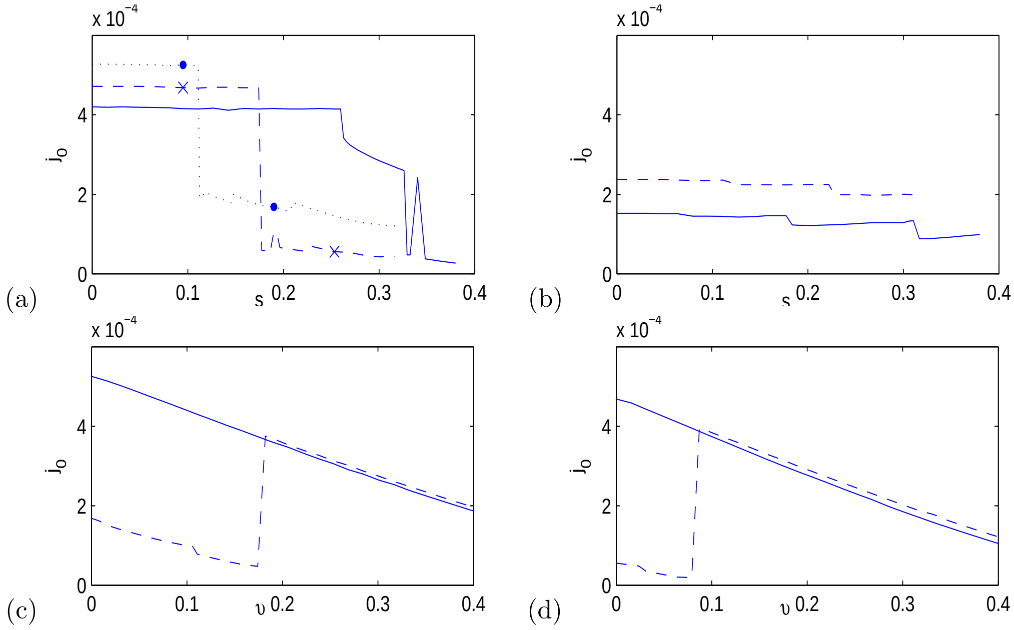

Figure 5.6: Stationary current for varying s at $\upsilon = 0$ (a,b) and varying constant offset υ at fixed s (c,d). The parameters are (a) $\beta = 251.46$ (solid line), $\beta = 318.31$ (dashed line), and $\beta = 397.89$ (dotted line); (b) $\beta = 31.83$ (solid line) and $\beta = 79.58$ (dashed line); (c) $\beta = 397.31$ for fixed $s = 0.095$ (solid line) and $s = 0.19$ (dashed line); (d) $\beta = 318.31$ with $s = 0.095$ (solid line) and $s = 0.253$ (dashed line). The values for the lattice amplitude s used in (c,d) are marked in (a) on the curves with the respective interaction strengths.

For a fixed optical lattice depth s but a weaker interaction case, e.g. Figure 5.5(a)&(c), the stopping of BEC expansion is absent.

This fact can also be observed in a density plot of $|\psi(x,t)|^2$. Figure 5.7(a) shows the density of a BEC with an interaction strength which does not show a drop in the stationary current. In contrast, the density for a higher β which features a drop in the stationary current is plotted in Figure 5.7(b). The value of s in this plot is chosen to be larger than the value for the drop (cf. Figure 5.6(a)). By comparing Figure 5.7(b) with the particle number in Figure 5.4(b), we also relate the steps in the plateau structure of the particle number within the lattice to the tunneling of the BEC across the lattice sites as a lump of atoms. Every time a lump of atoms tunnels to the next lattice site, the average particle density increases by a fixed amount ΔN until it reaches a final lattice site where the expansion stops and a quasi-stationary state develops. For a fixed lattice height υ, the final lattice site is determined by the values of $n\beta$ and s.

Compare the chemical potential in Figure 5.2 (dashed horizontal line) with the position of the first band gap for a given set of parameters. For $\beta = 79.58$, where the stationary current does not exhibit a drop, the chemical potential lies deep in the first energy band (cf. Figure 5.2(a)). The atoms can populate the first band when being injected into the lattice region and move through the lattice. For very high β, however, the chemical potential initially lies above the first band gap (cf. Figure 5.2(b) (left part)). As s is increased, the local chemical potential within the lattice $n\beta$ also increases slightly and shifts the band structure in such a way that the overall chemical potential μ falls into the first band gap (cf. Figure 5.2(b) (right part)). With its chemical potential lying inside the band gap, the wavefunction cannot expand anymore because there is no state available. This causes the BEC to manifest itself in the development of the quasi-stationary state in Figure 5.7(b). Increasing s further broadens the gap and the stationary current decreases steadily. Alexander et al. [5] showed that such a gap wave in a different setup remains stable. However, due to the shortness of the lattice in our setup, there is still a small current flowing through the lattice. This current leakage eventually causes the self-trapped state to disappear after a finite time. In Figure 5.7(b), this breakdown can be observed for $t > 1300$, when the BEC dissipates over the whole lattice. Such phenomenon of a finite life-time of the self-trapped state has also been observed in a different optical lattice setup [112].

More numerical results are shown in Figure 5.8, demonstrating similar phenomenon for a fixed parameter β but different lattice depth s. For $s = 0.127$, the chemical potential lies within an energy band and the atoms flow through the lattice quite smoothly. For $s = 0.253$ the chemical potential falls within the energy band gap and self-trapping is developed in the transport of BEC through the lattice. The expansion of the condensate stops at the sixth lattice site for an extended amount of time.

We further study the case of a fixed lattice depth s with a varying offset potential v confined to the optical lattice region. The two curves in each of Figure 5.6(b)&(d) depict the results obtained for two fixed values of β. The solid and dashed lines in each plot correspond to two different values of s. The lattice depths are chosen to lie before and after the drop in the stationary current. As expected, for a system whose chemical potential is located below the first band gap at $v = 0$, the stationary current decreases with increasing offset potential (solid lines). In this case the offset shifts the whole band structure by a constant value. However, if the lattice depth is chosen in such a way that the chemical potential lies in a band gap at $v = 0$, a sudden jump is observed in the stationary current (dashed lines). This counter-intuitive behaviour, an increasing current for a higher potential barrier, can again be explained by noting that the constant offset v shifts the band structure. Increasing the offset will eventually result in a band structure in which the chemical potential does not lie in a gap

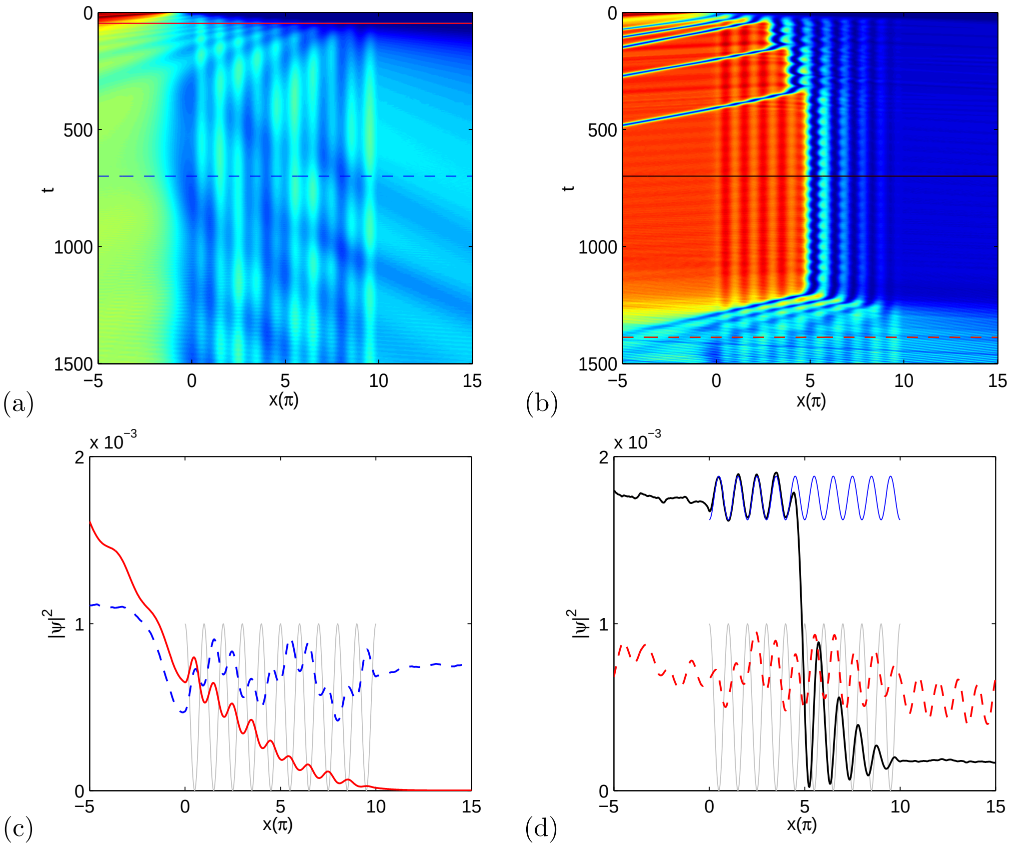

Figure 5.7: Density plots of the BEC near the optical lattice. (Upper panel) Time evolution of the condensate density. Red color indicates high density and blue color indicates low density. (Lower panel) Profile of the BEC at times indicated by the corresponding horizontal lines in the upper panel. The solid blue line in (d) indicates the analytical result (5.33) for the corresponding nonlinear Bloch wave and the thin solid gray line indicates the position of the optical lattice. For both plots $s = 0.127, \upsilon = 0$ and (a,c) $\beta = 79.58$, (b,d) $\beta = 397.89$.

anymore. Therefore the jump in the stationary current occurs when the chemical potential rejoins a band.

5.3.3 Nonlinear Bloch waves

In order to understand the quasi-stationary nature of the state after the drop in Figure 5.6, we consider truncated Bloch waves (5.18) with parameters $\sqrt{n}c_{-1} = \sqrt{n}c_1 =: d_1/2$ and $d_0 := \sqrt{n}c_0$, with n being the average particle density within the lattice, given by (5.19). For the ground state with $q = 0$, this results in the state

$$\phi(x) = d_0 + d_1 \cos(2x). \tag{5.28}$$

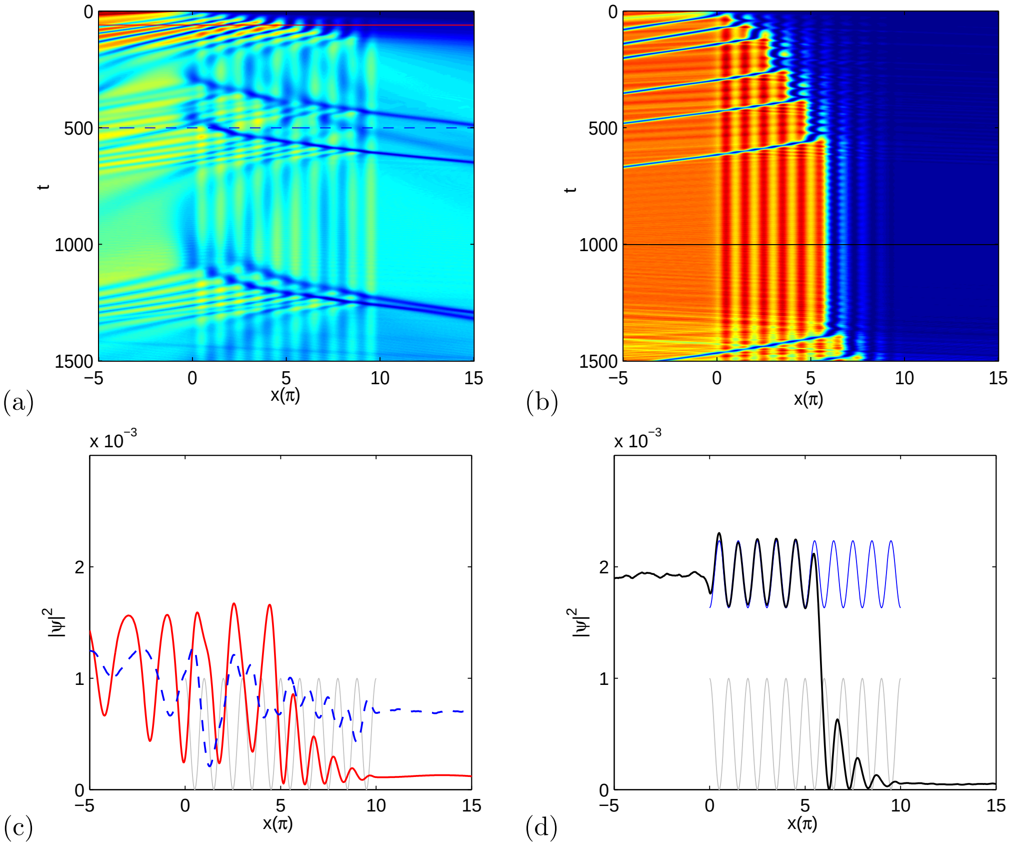

(a) (b) (c) (d)

Figure 5.8: Density plots of the BEC near the optical lattice. (Upper panel) Time evolution of the condensate density. (Lower panel) Profile of the BEC at times indicated by the corresponding horizontal lines in the upper panel. The solid blue line in (d) indicates the analytical result (5.33) for the corresponding nonlinear Bloch wave and the thin solid gray line indicates the position of the optical lattice. For both plots $\beta = 318.31, v = 0$ and (a,c) $s = 0.127$, (b,d) $s = 0.253$.

The normalization condition (5.20) has to be rewritten as

$$|d_0|^2 + \frac{1}{2}|d_1|^2 = n. \tag{5.29}$$

The coefficients d_0 and d_1 can be determined by minimizing the energy functional under the constraint (5.29). Minimizing the Lagrangian

$$L(\phi,\mu) = \frac{1}{\pi}\int_0^{\pi}\left[\frac{1}{2}\left|\frac{d}{dx}\phi\right|^2 + s\cos(2x)|\phi|^2 + \frac{\beta}{2}|\phi|^4\right]dx - \mu\left(d_0^2 + \frac{1}{2}d_1^2 - n\right) \tag{5.30}$$

yields two algebraic equations

$$2\beta d_0^3 + d_0(3\beta d_1^2 - 2\mu) + s d_1 \quad = \quad 0, \tag{5.31}$$

$$3\beta d_1^3 + 4d_1(2 + 3\beta d_0^2 - \mu) + 4sd_0 \quad = \quad 0, \tag{5.32}$$

which can be solved analytically. Here μ is the chemical potential. The real-valued solution of equations (5.31)–(5.32) describes a nonlinear Bloch wave [5, 30]. For the case of $q = 0$, this wavefunction describes an oscillation of $|\phi(x)|^2$ with the period of the lattice around a finite value. To see this, we assume a real-valued solution of equations (5.31)–(5.32) and calculate the density $|\phi(x)|^2$ from (5.28) as follows

$$|\phi(x)|^2 = d_0^2 + \frac{d_1^2}{2} + 2d_0 d_1 \cos(2x) + \frac{d_1^2}{2} \sin(4x). \tag{5.33}$$

The constant offset in the solution (5.33) is the particle density n given in (5.29). The oscillation with the double period $4x$ can be neglected since for our parameter range $d_1^2/2 \ll 2|d_0 d_1|$.

In our numerical simulations, we observe that for s above the threshold of the drop in the stationary current, a quasi-stationary state develops. Figures 5.7(b) and 5.8(b) show the development of such a nonlinear Bloch wave and its disappearance over time for high interaction strength. As an example, in Figure 5.7(d), this behaviour is demonstrated at two time slices. At early times the BEC tunnels across the lattice sites as it expands into the lattice. At time $t \approx 700$, we recognize the nonlinear Bloch wave in Figure 5.7(d). The line overlapping with the numerically calculated density is the analytical density (5.33) with the parameters same as in the numerical result. To obtain the analytical solution, we use the reduced chemical potential of the BEC that is still left in reservoir A and the lattice. The analytical description of a nonlinear Bloch wave is found to coincide well with the numerical results. At a later time $t \approx 1400$, the BEC is spread uniformly with a periodic modulation. In Figure 5.8(d), at $t \approx 1000$ the analytical solution (5.33) is again shown to agree well with the numerical solution.

In contrast, for values of s and β where the stationary current does not show a drop, the BEC spreads almost uniformly with time. In Figure 5.7(c) at $t \approx 45$ and in Figure 5.8(c) at $t \approx 60$, the BEC has expanded into the optical lattice but the atomic density is only slightly modulated within the lattice region and otherwise is uniformly distributed. A quasi-stationary nonlinear Bloch wave is not developed.

We further calculate the size of the steps between the plateaux in the particle number plot in Figures 5.4(b) and 5.5(b). Integrating the particle density (5.29) over one lattice site yields

$$\Delta N = \pi \left(|d_0|^2 + \frac{1}{2}|d_1|^2 \right). \tag{5.34}$$

When the BEC advances by one lattice site, the particle number within the lattice should grow by ΔN. The vertical bars in Figure 5.4(b) and Figure 5.5(b) indicate the particle difference between the plateaux. Table 5.1 shows the analytically calculated particle number difference (5.34) for the parameters used in the plots with a reduced chemical potential as discussed above. These results agree with the difference of the numerically obtained particle number plateaux. Given the above agreements of analytical and numerical results, we conclude that indeed the formation of a nonlinear Bloch wave causes the breakdown of the stationary current.

Label	$\Delta N_{analysis}$	$\Delta N_{numerical}$
1	0.0058	0.0048
2	0.0055	0.0044
3	0.0067	0.0058
4	0.0066	0.0056
5	0.0065	0.0052

Table 5.1: Analytically and numerically computed particle difference between plateaux shown in Figure 5.4(b) and Figure 5.5(b), each corresponds to the growth in particle number within the lattice when a lump of BEC advances by one lattice site.

5.3.4 Dark solitons

The GPE supports soliton solutions for non-zero interaction β. These solutions are shape-preserving notches or peaks in the density, which do not disperse over time. In the case of repulsive interaction without an optical lattice, solitons are typically of the dark type [31, 34] but both dark and bright solitons can exist in BECs in optical lattices [6, 107, 122]. Our numerical results of the condensate density in Figure 5.7(b) and Figure 5.8(b) show the creation of moving dark solitons when the condensate jumps to a neighboring lattice site. For example, in Figure 5.7(b), dark notches can be seen moving to the left, away from the lattice region. These excitations move slower than the local speed of sound ($c = \sqrt{\beta|\psi|^2}$) and do not change their shape considerably over the simulation time. Other typical features of solitons such as the repulsion of two solitons approaching each other or the phase shift across a soliton, are also observed in the numerical results. Furthermore, we notice that the solitons emit sound waves traveling at the speed of sound. This happens when the center of mass of the solitons enters a region of different mean density, which causes a change in speed. A detailed analysis of soliton trajectories and their deformations in a non-uniform potential has been presented in [91]. It is worth noting that their exact dynamics and stability also depends on the ratio $v/\omega_\perp$ [87]. In our simulation, we do not take into account the radial confinement, assuming that it is very tight and the overall BEC dynamics can be described by an effective 1D model. Hence, we do not undertake a thorough analysis of the soliton dynamics in our system as their creation can be considered as a side product of the development of the quasi-stationary state in the lattice, which is the main focus of this work.

5.4 Discussion

We have investigated the effects of a finite width lattice on the transport properties of a strongly interacting BEC. The corresponding 1D GPE was solved numerically and relevant quantities such as the atomic current and density were extracted. We also compared the numerical results with the analytical results in terms of nonlinear Bloch waves. We found that even for low lattice depths, a quasi-stationary state may develop after an initial expansion of the BEC into the lattice. This results in a sharp drop of the current in the lattice when the lattice depth and interaction reaches a critical value. However, the atoms can tunnel out of this state due to the finiteness of the lattice, which eventually leads to the breakdown of the stationarity. The development of such a self-trapped state can be explained with partial nonlinear Bloch waves, which builds up over only a few lattice sites and blocks further atomic flow through the optical lattice. When a constant offset potential was introduced into the system, increasing the offset can trigger the previously suppressed flow of the atoms again and eventually destroy the self-trapped state. Finally, we reported on the creation of moving dark solitons during the development of the nonlinear Bloch waves. Every time when a lump of condensate particles advances to a neighboring lattice site, a soliton is emitted. Therefore, the number of solitons present in the BEC indicates the number of occupied lattice sites.

Chapter 6

Conclusion

The ground state solutions of single component Bose-Einstein condensates (BECs) in traps have been studied both analytically and numerically. For analytical studies, asymptotic approximations were derived for strongly repulsively interacting system by neglecting the kinetic energy term in the Gross-Pitaevskii equation (GPE), and for strongly attractively interacting system by neglecting the potential energy term. Good agreements with numerical solutions were obtained. One dimensional weakly attractively interacting BEC system in double well potential was also studied through variational approach and a Gaussian approximation to the wavefunction. The ground state in this case is not unique for certain interaction strength, when a symmetry breaking state, in which the BEC is strongly localized only in one well, starts to possess lower energy than the usual symmetric state. The Gaussian approximation was shown to provide a good prediction to the solution when the double well is deep. The studies for attractively interacting BEC system have been limited to one dimensional case in which the condensate described by the GPE does not collapse even in a strongly interacting regime, which does occur in higher dimensions. For numerical studies, two efficient numerical schemes were developed on the basis of the widely used imaginary time method and the normalized gradient flow. Sine-pseudospectral method is utilized for the discretization in space to achieve a spectral accuracy in the solutions. The introduction of the stabilization parameter greatly improves the overall convergence rate of solving linear system in the backward Euler sine-pseudospectral method (BESP) and greatly increases the upper bound for the time step constraint in the backward-forward Euler sine-pseudospectral method (BFSP). The numerical schemes were shown to be effective even in 3D modelling of the BEC ground state that exhibits multiscale structures.

The normalized gradient flow method developed for computing the single component BEC ground state was extended to three-component spin-1 BECs. The two available physical constraints for a spin-1 BEC, the conservation of total particle number and the conservation of total magnetization, are not enough to normalize the three wavefunctions for applying the normalized gradient flow method directly to the three-component coupled GPEs. For the reason, a third normalization condition was introduced into the numerical scheme. The third condition was derived from the continuous normalized gradient flow, which is total mass conserved and total magnetization conserved, via a first order time-splitting scheme. The method was further modified to be applied to a spin-1 BEC subjected to uniform magnetic field. Due to the additional Zeeman energy terms, the stability and accuracy of the method vary with different treatments of the Zeeman energies as well as with different discretization schemes. The projection without magnetic field (POMF) approach discretized by the BFSP method was found to be more effective than other numerical schemes.

Finally, the dynamics of BEC, in particular the transport of a strongly repulsively interacting condensate through a shallow optical lattice of finite width, was studied. The study was first carried out via solving the time-dependent GPE numerically with the time-splitting sine-pseudospectral method (TSSP). Self-trapped states were observed for some sets of parameters, indicated by stopping in the expansion of BEC at certain lattice site. The finiteness of the lattice is found to result in the dissipation of the self-trapping after a finite time. The self-trapped state was then studied analytically in terms of nonlinear Bloch waves, approximated by a truncated Bloch function. The approximation gave a good qualitative agreement with the numerical observation.

Despite the fact that all of the present study is based on the simplest zero temperature mean field model, the numerical methods developed for the model are applicable to the finite temperature mean field equations to yield efficient numerical schemes, provided that an efficient numerical method is also developed for solving the Bogoliubov-de-Gennes (BdG) equations. The BdG equations coupled with the GPE at finite temperature are solved via a self-consistent iterative scheme in literature. The convergence of the self-consistent scheme remains an open question up to date. Solving the BdG equations, in particular in three dimensions, involves solving a large scale eigenvalue problem. Similar type of eigenvalue problems have been widely studied in electronic structure calculation as well as in condensed matter physics. Those methods developed for such large scale eigenvalue problems could be applied to the BdG equations with an appropriate modification to attain a desired efficiency. Other than these problems, BEC with long-range interaction, e.g. dipolar BEC gases, is also a recent interest in the research. The numerical methods developed here can also be applied to the corresponding nonlinear Schrödinger equation by taking the long-range dipolar interacting potential into account, in which the nonlocal interaction presents a certain difficulty in the computational implementation. As a conclusion, this thesis presented part of the zero temperature BEC study within the mean field theory which is itself part of the studies of the Bose-Einstein condensation. Researchers are exploring for more interesting properties of BECs as well as the applications of BECs for example in quantum computation. Numerical modelling plays an important role in the exploration of the condensate properties, and plenty of challenges are still existing in terms of numerical modelling of the Bose-Einstein condensation. Further studies beyond the context of this thesis are expected to be done in the future.

Bibliography

[1] S. Adhikari. Numerical solution of the two-dimensional Gross-Pitaevskii equation for trapped interacting atoms. *Phys. Lett. A*, **265,** 91, 2000.

[2] S. Adhikari and P. Muruganandam. Mean-field model for the interference of matter-waves from a three-dimensional optical trap. *Phys. Lett. A*, **310,** 229, 2003.

[3] A. Aftalion and Q. Du. Vortices in a rotating Bose-Einstein condensate: Critical angular velocities and energy diagrams in the Thomas-Fermi regime. *Phys. Rev. A*, **64,** 063603, 2001.

[4] M. Albiez, R. Gati, J. Fölling, S. Hunsmann, M. Cristiani, and M. K. Oberthaler. Direct observation of tunneling and nonlinear self-trapping in a single bosonic Josephson junction. *Phys. Rev. Lett.*, **95,** 010402, 2005.

[5] T. J. Alexander, E. A. Ostrovskaya, and Y. S. Kivshar. Self-trapped nonlinear matter waves in periodic potential. *Phys. Rev. Lett.*, **96,** 040401, 2006.

[6] G. L. Alfimov, V. V. Konotop, and M. Salerno. Matter solitons in Bose-Einstein condensates with optical lattices. *Europhys. Lett.*, **58,** 7, 2002.

[7] B. P. Anderson and M. A. Kasevich. Macroscopic quantum interference from atomic tunnel arrays. *Science*, **282,** 1686, 1998.

[8] M. H. Anderson, J. R. Ensher, M. R. Matthewa, C. E. Wieman, and E. A. Cornell. Observation of Bose-Einstein condensation in a dilute atomic vapor. *Science*, **269,** 198, 1995.

[9] T. Anker, M. Albiez, R. Gati, S. Hunsmann, B. Eiermann, A. Trombettoni, and M. K. Oberthaler. Nonlinear self-trapping of matter waves in periodic potentials. *Phys. Rev. Lett.*, **94,** 020403, 2005.

[10] W. Bao. Ground states and dynamics of multi-component Bose-Einstein condensates. *Multiscale Modeling and Simulation*, **2,** 210, 2004.

[11] W. Bao, I.-L. Chern, and F. Y. Lim. Efficient and spectrally accurate numerical methods for computing ground and first excited states in Bose-Einstein condensates. *J. Comput. Phys.*, **219,** 836, 2006.

[12] W. Bao and Q. Du. Computing the ground state solution of Bose-Einstein condensates by a normalized gradient flow. *SIAM J. Sci. Comput.*, **25,** 1674, 2004.

[13] W. Bao, D. Jaksch, and P. Markowich. Numerical solution of the Gross-Pitaevskii equation for Bose-Einstein condensation. *J. Comput. Phys.*, **187,** 318, 2003.

[14] W. Bao, S. Jin, and P. A. Markowich. Numerical study of time-splitting spectral discretizations of nonlinear Schrodinger equations in the semi-classical regimes. *SIAM J. Sci. Comput.*, **25,** 27, 2003.

[15] W. Bao and F. Y. Lim. Computing ground state of spin-1 Bose-Einstein condensates by the normalized gradient flow. *SIAM J. Sci. Comput.*, **30,** 1925, 2008.

[16] W. Bao and F. Y. Lim. Numerical methods for computing the ground state of spin-1 Bose-Einstein condensates in uniform magnetic field. *Phys. Rev. E*, **78,** 066704, 2008.

[17] W. Bao, F. Y. Lim, and Y. Zhang. Energy and chemical potential asymptotics for the ground state of Bose-Einstein condensates in the semiclassical regime. *Bulletin of the Institute of Mathematics, Academia Sinica*, **2,** 495, 2007.

[18] W. Bao and W. Tang. Ground state solution of trapped interacting Bose-Einstein condensate by directly minimizing the energy functional. *J. Comput. Phys.*, **187,** 230, 2003.

[19] W. Bao and H. Wang. A mass and magnetization conservative and energy diminishing numerical method for computing ground state of spin-1 Bose-Einstein condensates. *SIAM J. Numer. Anal.*, **45,** 2177, 2007.

[20] W. Bao, H. Wang, and P. Markowich. Ground, symmetric and central vortex states in rotating Bose-Einstein condensates. *Commun. Math. Sci.*, **3,** 57, 2005.

[21] W. Bao and Y. Zhang. Dynamics of the ground state and central vortex states in Bose-Einstein condenstation. *Math. Models Meth. Appl. Sci.*, **15,** 1863, 2005.

[22] M. D. Barrett, J. A. Sauer, and M. S. Chapman. All-optical formation of an atomic Bose-Einstein condensate. *Phys. Rev. Lett.*, **87,** 010404, 2001.

[23] S. T. Beliaev. Application of the methods of quantum field theory to a system of bosons. *Sov. Phys. JETP*, **7,** 289, 1958.

[24] C. F. Bharucha, K. W. Madison, P. R. Morrow, S. R. Wilkinson, B. Sundaram, and M. G. Raizen. Observation of atomic tunneling from an accelerating optical potential. *Phys. Rev. A*, **55,** R587, 1997.

[25] N. N. Bogoliubov. On the theory of superfluidity. *J. Phys. USSR*, **11,** 23, 1947.

[26] S. N. Bose. Plancks gesetz und lichtquantenhypothese. *Zeitschrift fr Physik*, **3,** 178, 1924.

[27] C. C. Bradley, C. A. Sackett, and R. G. Hulet. Bose-Einstein condensation of Lithium: observation of limited condensate number. *Phys. Rev. Lett.*, **78,** 985, 1997.

[28] C. C. Bradley, C. A. Sackett, J. J. Tollett, and R. G. Hulet. Evidence of Bose-Einstein condensation in an atomic gas with attractive interaction. *Phys. Rev. Lett.*, **75,** 1687, 1995.

[29] J. Bronski, L. Carr, B. Deconinck, J. Kutz, and K. Promislow. Stability of repulsive Bose-Einstein condensates in a periodic potential. *Phys. Rev. E*, **63,** 036612, 2001.

[30] J. C. Bronski, L. D. Carr, B. Deconinck, and J. N. Kutz. Bose-Einstein condensates in standing waves: The cubic nonlinear Schrödinger equation with a periodic potential. *Phys. Rev. Lett.*, **86,** 1402, 2001.

[31] S. Burger, K. Bongs, S. Dettmer, W. Ertmer, K. Sengstock, A. Sanpera, G. V. Shlyapnikov, and M. Lewenstein. Dark solitons in Bose-Einstein condensates. *Phys. Rev. Lett.*, **83,** 5198, 1999.

[32] S. Burger, F. S. Cataliotti, C. Fort, F. Minardi, and M. Inguscio. Superfluid and dissipative dynamics of a Bose-Einstein condensate in a periodic optical potential. *Phys. Rev. Lett*, **86,** 4447, 2001.

[33] P. Capuzzi and S. Hernandez. Bose-Einstein condensation in harmonic double wells. *Phys. Rev. A*, **59,** 1488, 1999.

[34] L. D. Carr, J. Brand, S. Burger, and A. Sanpera. Dark-soliton creation in Bose-Einstein condensates. *Phys. Rev. A*, **63,** 051601, 2001.

[35] L. D. Carr, C. W. Clark, and W. Reinhardt. Stationary solutions of the one-dimensional nonlinear Schroedinger equation: I. case of repulsive nonlinearity. *Phys. Rev. A*, **62,** 063610, 2000.

[36] F. S. Cataliotti, S. Burger, C. Fort, P. Maddaloni, F. M. A. Trombettoni, A. Smerzi, and M. Inguscio. Josephson junction arrays with Bose-Einstein condensates. *Science*, **293,** 843, 2001.

[37] M. Cerimele, M. Chiofalo, F. Pistella, S. Succi, and M. Tosi. Numerical solution of the Gross-Pitaevskii equation using an explicit finite-difference scheme: An application to trapped Bose-Einstein condensates. *Phys. Rev. E*, **62,** 1382, 2000.

[38] S.-M. Chang, C.-S. Lin, T.-C. Lin, and W.-W. Lin. Segregated nodal domains of two-dimensional multispecies Bose-Einstein condensates. *Physica D*, **196,** 341, 2004.

[39] S.-M. Chang, W.-W. Lin, and S.-F. Shieh. Gauss-Seidel-type methods for energy states of a multi-component Bose-Einstein condensate. *J. Comput. Phys.*, **202,** 367, 2005.

[40] M. Chiofalo, S. Succi, and M. Tosi. Ground state of trapped interacting Bose-Einstein condensates by an explicit imaginary-time algorithm. *Phys. Rev. E*, **62,** 7438, 2000.

[41] D.-I. Choi and Q. Niu. Bose-Einstein condensates in an optical latice. *Phys. Rev. Lett.*, **82,** 2022, 1999.

[42] C. V. Ciobanu, S. K. Yip, and T.-L. Ho. Phase diagrams of $F = 2$ spinor Bose-Einstein condensates. *Phys. Rev. A*, **61,** 033607, 2000.

[43] M. Cristiani, O. Morsch, J. H. Müller, D. Ciampini, and E. Arimondo. Experimental properties of Bose-Einstein condensates in one-dimensional optical lattices: Bloch oscillations, Landau-Zener tunneling, and mean-field effects. *Phys. Rev. A*, **65,** 063612, 2002.

[44] B. J. Dabrowska-Wüster, E. A. Ostrovskaya, T. J. Alexander, and Y. S. Kivshar. Multicomponent gap solitons in spinor Bose-Einstein condensates. *Phys. Rev. A*, 75, 2007.

[45] R. D'Agosta and C. Presilla. States without a linear counterpart in Bose-Einstein condensates. *Phys. Rev. A*, **65,** 043609, 2002.

[46] M. B. Dahan, E. Peik, J. Reichel, Y. Castin, and C. Salomon. Bloch oscillations of atoms in an optical potential. *Phys. Rev. Lett.*, **76,** 4508, 1996.

[47] F. Dalfovo, S. Giorgini, L. P. Pitaevskii, and S. Stringari. Theory of Bose-Einstein condensation in trapped gases. *Rev. Mod. Phys.*, **71,** 463, 1999.

[48] K. B. Davis, M. O. Mewes, M. R. Andrews, N. J. van Druten, D. S. Durfee, D. M. Kurn, and W. Ketterle. Bose-Einstein condensation in a gas of sodium atoms. *Phys. Rev. Lett.*, **75,** 3969, 1995.

[49] M. J. Davis, R. J. Ballagh, and K. Burnett. Dynamics of thermal Bose-fields in the classical limit. *J. Phys. B*, **34,** 4487, 2001.

[50] M. J. Davis and P. B. Blakie. Critical temperature of a trapped Bose gas: comparison of theory and experiment. *Phys. Rev. Lett.*, **96,** 060404, 2006.

[51] M. J. Davis, S. A. Morgan, and K. Burnett. Simulations of Bose-fields at finite temperature. *Phys. Rev. Lett.*, **87,** 160402, 2001.

[52] M. J. Davis, S. A. Morgan, and K. Burnett. Simulations of thermal Bose-fields in the classical limits. *Phys. Rev. A*, **66,** 053618, 2002.

[53] D. Diakonov, L. M. Jensen, C. J. Pethick, and H. Smith. Loop structure of the lowest Bloch band for a Bose-Einstein condensate. *Phys. Rev. A*, **66,** 013604, 2002.

[54] R. Dodd. Approximate solutions of the nonlinear Schrödinger equation for ground and excited states of Bose-Einstein condensates. *J. Res. Natl. Inst. Stan.*, **101,** 545, 1996.

[55] R. J. Dodd, M. Edwards, and C. W. Clark. Two-gas description of dilute Bose-Einstein condensates at finite temperature. *J. Phys. B*, **32,** 4107, 1999.

[56] R. J. Dodd, M. Edwards, C. W. Clark, and K. Burnett. Collective excitations of Bose-Einstein condensed gases at finite temperatures. *Phys. Rev. A*, **57,** R32, 1998.

[57] M. Edwards and K. Burnett. Numerical solution of the nonlinear Schrödinger equation for small samples of trapped neutral atoms. *Phys. Rev. A*, **51,** 1382, 1995.

[58] A. Einstein. Quantentheorie des einatomigen idealen gases. *Sitzungsberichte der Preussischen Akademie der Wissenschaften*, **22,** 261, 1924.

[59] A. Einstein. Quantentheorie des einatomigen idealen gases, zweite abhandlung. *Sitzungsberichte der Preussischen Akademie der Wissenschaften*, **1,** 3, 1925.

[60] A. L. Fetter. Theory of a dilute low-temperature trapped Bose condensate. *cond-mat/9811366*, 1998.

[61] D. G. Fried, T. C. Killian, L. Willmann, D. Landhuis, S. C. Moss, D. Kleppner, and T. J. Greytak. Bose-Einstein condensation of atomic hydrogen. *Phys. Rev. Lett*, **81,** 3811, 1998.

[62] G. Golub and C. V. Loan. *Matrix Computations.* Johns Hopkins University Press, 1989.

[63] A. Görlitz, T. L. Gustavson, A. E. Leanhardt, E. Löw, A. P. Chikkatur, S. Gupta, S. Inouye, D. E. Pritchard, and W. Ketterle. Sodium Bose-Einstein condensates in the $F = 2$ state in a large-volume optical trap. *Phys. Rev. Lett.*, **90,** 090401, 2003.

[64] A. Griffin. Conserving and gapless approximations for an inhomogeneous Bose gas at finite temperatures. *Phys. Rev. B*, **53,** 9341, 1996.

[65] E. P. Gross. Structure of a quantized vortex in boson systems. *Nuovo. Cimento.*, **20,** 454, 1961.

[66] T. L. Ho. Spinor Bose condensates in optical traps. *Phys. Rev. Lett.*, **81,** 742, 1998.

[67] M. Holthaus. Towards coherent control of a Bose-Einstein condensate in a double well. *Phys. Rev. A*, 64, 2001.

[68] D. A. W. Hutchinson, K. Burnett, R. J. Dodd, S. A. Morgan, M. Rusch, E. Zaremba, N. P. Proukakis, M. Edwards, and C. W. Clark. Gapless mean-field theory of Bose-Einstein condensates. *J. Phys. B*, **33,** 3825, 2000.

[69] D. A. W. Hutchinson, E. Zaremba, and A. Griffin. Finite temperature excitations of a trapped Bose gas. *Phys. Rev. Lett.*, **78,** 1842, 1997.

[70] T. Isoshima and S. Yip. Effect of quadratic Zeeman energy on the vortex of spinor Bose-Einstein condensates. *J. Phys. Soc. Jpn.*, **75,** 074605, 2006.

[71] R. Kanamoto, H. Saito, and M. Ueda. Quantum phase transition in one-dimensional Bose-Einstein condensates with attractive interactions. *Phys. Rev. A*, **67,** 013608, 2003.

[72] P. Kapitza. Viscocity of liquid helium below the λ-point. *Nature*, **141,** 74, 1938.

[73] G. M. Kavoulakis. Bose-Einstein condensates with attractive interactions on a ring. *Phys. Rev. A*, **67,** 011601(R), 2003.

[74] L. D. Landau. The theory of superfluidity of helium II. *J. Phys. USSR*, **5,** 71, 1941.

[75] P. Leboeuf and N. Pavloff. Bose-Einstein beams: coherent propagation through a guide. *Phys. Rev. A*, **64,** 033602, 2001.

[76] E. Lieb, R. Seiringer, and J. Yugvason. Bosons in a trap: a rigorous dervation of the Gross-Pitaevskii energy functional. *Phys. Rev. A*, **61,** 3602, 2000.

[77] F. London. The λ-phenomenon of liquid helium and the Bose-Einstein degeneracy. *Nature*, **141,** 643, 1938.

[78] M. Machholm, C. J. Pethick, and H. Smith. Band structure, elementary excitations, and stability of a Bose-Einstein condensate in a periodic potential. *Phys. Rev. A*, **67,** 053613, 2003.

[79] K. W. Mahmud, J. N. Kutz, and W. P. Reinhardt. Bose-Einstein condensates in a one-dimensional double square well: analytical solutions of the nonlinear Schrödinger equation. *Phys. Rev. A*, **66,** 063607, 2002.

[80] T. P. Meyrath, F. Schreck, J. L. Hanssen, C.-S. Chuu, and M. G. Raizen. Bose-Einstein condensate in a box. *Phys. Rev. A*, **71,** 041604, 2005.

[81] H. J. Miesner, D. M. Stamper-Kurn, J. Stenger, S. Inouye, A. P. Chikkatur, and W. Ketterle. Observation of metastable states in spinor Bose-Einstein condensates. *Phys. Rev. Lett.*, **82,** 2228, 1999.

[82] G. Milburn, J. Corney, E. Wright, and D. Walls. Quantum dynamics of an atomic Bose-Einstein condensate in a double-well potential. *Phys. Rev. A*, **55,** 4318, 1997.

[83] T. Mizushima, N. Kobayashi, and K. Machida. Coreless and singular vortex lattices in rotating spinor Bose-Einstein condensates. *Phys. Rev. A*, **70,** 043613, 2004.

[84] O. Morsch, J. H. Müller, M. Cristiani, D. Ciampini, and E. Arimondo. Bloch oscillations and mean-field effects of Bose-Einstein condensates in 1D optical lattices. *Phys. Rev. Lett.*, **87,** 140402, 2001.

[85] J. Mur-Petit, M. Guilleumas, A. Polls, A. Sanpera, and M. Lewenstein. Dynamics of $F = 1$ ^{87}Rb condensates at finite temperatures. *Phys. Rev. A*, **73,** 013629, 2006.

[86] K. Murata, H. Saito, and M. Ueda. Broken axisymmetry phase of a spin-1 ferromagnetic Bose-Einstein condensate. *Phys.Rev. A*, **75,** 013607, 2007.

[87] A. Muryshev, G. V. Shlyapnikov, W. Ertmer, K. Sengstock, and M. Lewenstein. Dynamics of dark solitons in elongated Bose-Einstein condensates. *Phys. Rev. Lett.*, **89,** 110401, 2002.

[88] O. E. Müstecaplıoğlu, M. Zhang, and L. You. Tunneling of condensate magnetization in a double-well potential. *Phys. Rev. A*, **71,** 053616, 2005.

[89] T. Nikuni, E. Zaremba, and A. Griffin. Two-fluid dynamics for a Bose-Einstein condensate out of local equilibrium with the noncondensate. *Phys. Rev. Lett.*, **83,** 10, 1999.

[90] T. Ohmi and K. Machida. Bose-Einstein condensation with internal degrees of freedom in alkali atom gases. *J. Phys. Soc. Jpn.*, **67,** 1822, 1998.

[91] N. G. Parker, N. P. Proukakis, M. Leadbeater, and C. S. Adams. Deformation of dark solitons in inhomogeneous Bose-Einstein condensates. *J. Phys. B*, **36,** 2891, 2003.

[92] A. Parola, L. Salanich, and L. Reatto. Structure and stability of bosonic clouds: alkali-metal atoms with negative scattering length. *Phys. Rev. A*, **57,** R3180, 1998.

[93] V. M. Pérez-García, H. Michinel, J. I. Cirac, M. Lewenstein, and P. Zoller. Dynamics of Bose-Einstein condensates: variational solutions of the Gross-Pitaevskii equations. *Phys. Rev. A*, **56,** 1424, 1997.

[94] L. Pitaevskii and S. Stringari. *Bose-Einstein condensation.* Clarendon Press, 2003.

[95] L. P. Pitaevskii. Vortex lines in an imperfect Bose gas. *Soviet Phys. JETP*, **13,** 451, 1961.

[96] M. Rosenkranz, D. Jaksch, F. Y. Lim, and W. Bao. Self-trapping of Bose-Einstein condensates expanding into shallow optical lattices. *Phys. Rev. A*, **77,** 063607, 2008.

[97] P. Ruprecht, M. Holland, K. Burrett, and M. Edwards. Time-dependent solution of the nonlinear Schrodinger equation for Bose-condensed trapped neutral atoms. *Phys. Rev. A*, **51,** 4704, 1995.

[98] H. Saito and M. Ueda. Spontaneous magnetization and structure formation in a spin-1 ferromagnetic Bose-Einstein condensate. *Phys. Rev. A*, **72,** 023610, 2005.

[99] B. Schneider and D. Feder. Numerical approach to the ground and excited states of a Bose-Einstein condensated gas confined in a completely anisotropic trap. *Phys. Rev. A*, **59,** 2232, 1999.

[100] R. G. Scott, A. M. Martin, S. Bujkiewicz, and T. M. Fromhold. Transport and disruption of Bose-Einstein condensates in optical lattices. *Phys. Rev. A*, **69,** 033605, 2004.

[101] H. Shi and W.-M. Zheng. Bose-Einstein condensation in an atomic gas with attractive interactions. *Phys. Rev. A*, **55,** 2930, 1997.

[102] L. Simon. Asymptotics for a class of nonlinear evolution equations, with applications to geometric problems. *Ann. of Math.*, **118,** 525, 1983.

[103] D. M. Stamper-Kurn, M. R. Andrews, A. P. Chikkatur, S. Inouye, H.-J. Miesner, J. Stenger, and W. Ketterle. Optical confinement of a Bose-Einstein condensate. *Phys. Rev. Lett.*, **80,** 2027, 1998.

[104] D. M. Stamper-Kurn and W. Ketterle. Spinor condensates and light scattering from Bose-Einstein condensates. In *Coherent Atomic Matter Waves, Les Houches Summer School Session LXXII in 1999.* Springer, NewYork.

[105] J. Stenger, S. Inouye, D. M. Stamper-Kurn, H.-J. Miesner, A. P. Chikkatur, and W. Ketterle. Spin domains in ground state Bose-Einstein condensates. *Nature*, **396,** 345, 1998.

[106] H. T. C. Stoof. Macroscopic quantum tunneling of a Bose condensate. *J. Stat. Phys.*, **87,** 1353, 1997.

[107] K. E. Strecker, G. B. Partridge, A. G. Truscott, and R. G. Hulet. Formation and propagation of matter-wave soliton trains. *Nature*, **417,** 150, 2002.

[108] L. Tisza. Transport phenomena in helium II. *Nature*, **141,** 913, 1938.

[109] M. Uchiyama, J. Ieda, and M. Wadati. Dark solitons in $F = 1$ spinor Bose-Einstein condensate. *J. Phys. Soc. Jpn*, **75,** 064002, 2006.

[110] M. Ueda and M. Koashi. Theory of spin-2 Bose-Einstein condensates: Spin correlations, magnetic response, and excitation spectra. *Phys. Rev. A*, **65,** 063602, 2002.

[111] S. M. M. Virtanen and M. M. Salomaa. Effect of the thermal gas component on the stability of vortices in trapped Bose-Einstein condensates. *J. Phys. B*, **35,** 3967, 2002.

[112] B. Wang, P. Fu, J. Liu, and B. Wu. Self-trapping of Bose-Einstein condensates in optical lattices. *Phys. Rev. A*, **74,** 063610, 2006.

[113] G.-F. Wang, L.-B. Fu, and J. Liu. Periodic modulation effect on self-trapping of two weakly coupled Bose-Einstein condensates. *Phys. Rev. A*, **73,** 013619, 2006.

[114] B. Wu and Q. Niu. Nonlinear Landau-Zener tunnelling. *Phys. Rev. A*, **61,** 023402, 2000.

[115] S. Yi, O. E. Müstecaplioğlu, C. P. Sun, and L. You. Single-mode approximation in a spinor-1 atomic condensate. *Phys. Rev. A*, **66,** 011601, 2002.

[116] E. Zaremba, A. Griffin, and T. Nikuni. Two-fluid hydrodynamics for a trapped weakly interacting Bose gas. *Phys. Rev. A*, **57,** 4695, 1998.

[117] E. Zaremba, T. Nikuni, and A. Griffin. Dynamics of trapped Bose gases at finite temperature. *J. Low Temp. Phys.*, **116,** 277, 1999.

[118] W. Zhang, S. Yi, and L. You. Mean field ground state of a spin-1 condensate in a magnetic field. *New J. Phys.*, **5,** 77, 2003.

[119] W. Zhang, S. Yi, and L. You. Bose-Einstein condensation of trapped interacting spin-1 atoms. *Phys. Rev. A*, **70,** 043611, 2004.

[120] W. Zhang and L. You. An effective quasi-one-dimensional description of a spin-1 atomic condensate. *Phys. Rev. A*, **71,** 025603, 2005.

[121] P. Zín, E. Infeld, M. Matuszewski, G. Rowlands, and M. Trippenbach. Method for obtaining exact solutions of the nonlinear Schrödinger equation for a double-square-well potential. *Phys. Rev. A*, **73,** 022105, 2006.

[122] O. Zobay, S. Pötting, P. Meystre, and E. M. Wright. Creation of gap solitons in Bose-Einstein condensates. *Phys. Rev. A*, **59,** 643, 1999.

List of Publications

1. Efficient and spectrally accurate numerical methods for computing ground and first excited states in Bose-Einstein condensates (with W. Bao and I-L. Chern), *J. Comput. Phys.*, **219**, 836, 2006.

2. Energy and chemical potential asymptotics for the ground state of Bose-Einstein condensates in the semiclassical regime (with W. Bao and Y. Zhang), *Bulletin of the Institute of Mathematics, Academia Sinica*, **2**, 495, 2007.

3. Computing ground states of spin-1 Bose-Einstein condensates by the normalized gradient flow (with W. Bao), *SIAM J. Sci. Comput.*, **30**, 1925, 2008.

4. Self-trapping of Bose-Einstein condensates expanding into shallow optical lattices (with M. Rosenkranz, D. Jaksch and W. Bao), *Phys. Rev. A*, **77**, 063607, 2008.

5. Numerical methods for computing the ground state of spin-1 Bose-Einstein condensates in uniform magnetic field (with W. Bao), *Phys. Rev. E*, **78**, 066704, 2008.